University of Southampton Research Repository

UNIVERSITY OF SOUTHAMPTON

Faculty of Engineering and Physical Sciences

Chemistry

Investigating Cobalt Zeolitic Imidazolate Frameworks as Catalysts for Cross-Dehydrogenative Couplings; Exploring Mesoporous Silicas as Scaffolds for an Organocatalyst

by

Cameron Ross

Thesis for the degree of Doctor of Philosophy

December 2019

University of Southampton

Abstract

Faculty of Engineering and Physical Sciences
Chemistry
Thesis for the degree of Doctor of Philosophy
Investigating Cobalt Zeolitic Imidazolate Frameworks as Catalysts for Cross-Dehydrogenative Couplings; Exploring Mesoporous Silicas as Scaffolds for an Organocatalyst
by
Cameron Ross

One of the greatest challenges for homogeneous catalysis is the difficulty in recovering and reusing the catalyst following a reaction. In order for applications to be carried out industrially, it is highly desirable to choose a system with a tuneable design, higher stability, and easy recyclability. This report presents novel applications of heterogeneous catalysts in reactions which have previously relied upon homogeneous systems. The heterogeneous alternatives reported here look to incorporate the growing fields of visible-light photocatalysis and organocatalysis in an ever more environmentally focused world.

Two zeolitic imidazolate frameworks (ZIFs) have been identified as solid photocatalysts for the cross-dehydrogenative coupling (CDC) of isoquinolines and nitromethane. There are few reports of Co-ZIFs in catalysis, with fewer still utilising photoactivation, here high yields have been achieved with ZIF-9 and ZIF-67 in the aza-Henry reaction using a solar simulator. A combination of UV-Vis and XAS spectroscopy, alongside theoretical simulations, was used to elucidate the nature of the framework's activity. The catalysts were then trialled in C-O bond formations to produce functionalised benzoxazoles. Comparing and contrasting their mode of action, oxidation state transitions, and applicability to wider research.

The immobilisation of organic catalysts onto mesoporous supports is an exciting evolution of the recent insurgence of organocatalysis. The aim was to adopt highly attractive properties of the homogeneous parent catalysts, such as high enantioselectivity and low toxicity, with a solid support to aid recyclability. By harnessing pendant silanols, a pyrrolidine silyl ether was successfully anchored onto a range of mesoporous silicas, as confirmed by elemental analysis, NMR and BET. The materials were then trialled in the cyclopropanation of a benzyl halide with an α,β-unsaturated aldehyde, revealing the support has a significant effect on the yield and enantioselectivity achieved.

Table of Contents

List of Tables

List of Figures

List of Schemes

Definitions and Abbreviations

BET	Brunauer-Emmett-Teller
BDDT	Brunauer-Deming-Deming-Teller
CB	Conduction Band
CDC	Cross-Dehydrogenative Coupling
CS	Charge Separation
CTAB	Cetrimonium Bromide
DDQ	2,3-Dichloro-5,6-dicyano-1,4-benzoquinone
DR	Diffuse Reflectance
d.r.	Diastereomeric Ratio
EDA	Electron Donor-Acceptor
e.e.	Enantiomeric Excess
eq.	Equivalents
FTIR	Fourier Transform Infrared Spectroscopy
GO	Graphene Oxide
rGO	Reduced Graphene Oxide
ICP-OES	Inductively Coupled Plasma-Optical Emission Scanning
J-H	Jørgensen-Hayashi
LG	Leaving Group
LMCT	Ligand-Metal Charge Transfer
MAS	Magic Angle Spin
MIm	Methylimidazole
MLCT	Metal-Ligand Charge Transfer

MOF	Metal-Organic Framework
NMR	Nuclear Magnetic Spectroscopy
PEG	Polyethylene Glycol
PhIm	Benzimidazole
SAXS/WAXS	Short/Wide Angle X-Ray Scattering
SDA	Structure Directing Agent
SEM	Scanning Electron Microscopy
SET	Single Electron Transfer
SS	Solar Simulator
TBHP	*tert*-Butyl Hydroperoxide
TGA	Thermogravimetric Analysis
TM	Transition Metal
(Ph)THIQ	(*N*-Phenyl-)1,2,3,4-Tetrahydroisoquinoline
UV-Vis	Ultraviolet-Visible
VB	Valence Band
(p)XRD	(Powder) X-Ray Diffraction
ZIF	Zeolitic Imidazolate Framework

Research Thesis: Declaration of Authorship

Print name: Cameron Ross

Title of thesis: Investigating Cobalt Zeolitic Imidazolate Frameworks as Catalysts for Cross-Dehydrogenative Couplings; Exploring Mesoporous Silicas as Scaffolds for an Organocatalyst

I declare that this thesis and the work presented in it are my own and has been generated by me as the result of my own original research.

I confirm that:

1. This work was done wholly or mainly while in candidature for a research degree at this University;
2. Where any part of this thesis has previously been submitted for a degree or any other qualification at this University or any other institution, this has been clearly stated;
3. Where I have consulted the published work of others, this is always clearly attributed;
4. Where I have quoted from the work of others, the source is always given. With the exception of such quotations, this thesis is entirely my own work;
5. I have acknowledged all main sources of help;
6. Where the thesis is based on work done by myself jointly with others, I have made clear exactly what was done by others and what I have contributed myself;
7. None of this work has been published before submission

Signature: .... Date:..........................

Acknowledgements

During my PhD I have experienced many ups and downs. I have plenty of people to thank for celebrating the good times with me and helping me to overcome the bad.

Firstly, my Southampton supervisors Ramon Rios and Robert Raja, from that initial undergrad project you saw the potential I had, and I will forever be grateful that you offered me this incredible opportunity. I also benefitted from the guidance of Abdul Majeed Seayad and Jean-Alexandre Richard who supervised me in Singapore, as well as funding from the A*STAR Graduate Academy which enabled me to truly experience a world outside of Southampton.

My research was supported by several people who I would like to thank for their valuable contributions. Matthew Potter and Diego Gianolio helped decipher the XAS data, which was made possible thanks to Diamond Light Source. I wish to thank Marina Carravetta for offering her time with solid-state NMR, Elpi Georgiou and James Hay for their work alongside the CDC project, and India Willimott for the hours she spent helping me with SEM and TGA. There are many other PhD students who I have spoken to along the way and have helped guide me along the right path, many of whom are past and present members of the Raja group, I hope my legacy of colour coded weeks on the oven board lives on.

Both in Southampton and Singapore I found the support and friendship of my fellow PhD students to be instrumental in making it through these four years. To Steph Chapman, Luke Shirley, Will Webb and India Willimott, I always appreciated our lunch breaks, and the trip to Budapest was pretty neat too. My housemates along the way, special mention to Sam Fitch and Pepe Recatala for their moral judgement helping to steer me in the right direction. Yet I still have to thank Alice Oakley, Jordan Gill and Tom Frank for leading me astray every now and then. Claire Scott for everything animal related she has ever sent me. And fellow Heathers Lauren Reid and Jo Howson.

They haven’t all been PhD students, there seems to be very little I can’t talk about with Aaisha Anis. I was also reunited with old school friends Hannah Gibson and Katie Sweed, who reminded me where I’ve been without holding me back from where I’m going. Then there is Ash Hartridge, we may have only met in the final stages of my PhD but I am so grateful for all the love and support you’ve given me in that time.

Joining the hockey club was one of the greatest decisions I made at university, being able to plan my week around something that wasn’t chemistry based certainly helped keep me sane. To every stick wielding knight of Wessex and the rhinos of Tornadoes, thank you for the matches, the socials, and turning me into someone athletic?!

I would like to give a special thanks to three incredible friends I made out in Singapore, who even when they are thousands of miles away, can still be relied upon to give me the best advice and a smile on my face. So thank you to Ebru Aksanoglu, Joel Lim, and Henrick Ayala for becoming a home for me when I felt so lost.

Lastly, the unconditional love and support of my family has helped keep me afloat through even the darkest times. Simply knowing they are there for me, and always have been, is all I need. But the supply of food and other essentials is certainly appreciated too.

Chapter 1: Introduction

1.1 Green Chemistry

The advancements in our understanding of chemistry and its applications has dramatically improved life over the past two centuries. Everything from lifesaving medicines, production of fuels for transport and energy, to the development of clean water supplies, owes its progress to chemistry. However, as our chemical industry has boomed over the last few decades we have become more aware of the environmental challenges that face us, the Earth's finite resources, pollutants, and worsening climate change. This has led to the concept of green chemistry which heralds sustainability and efficiency within the sector. Designing processes which follow the 12 principles of Green Chemistry listed below, as outlined by Anastas and Warner,[1] has become of increasing significance.

1) ***Prevention*** *- of waste over remediation afterwards*
2) ***Atom Economy*** *- maximise the incorporation of all materials to the final product*
3) ***Less Hazardous Syntheses*** *- minimal toxicity to health and the environment*
4) ***Designing Safer Chemicals*** *- performing desired function with minimal toxicity*
5) ***Safer Solvents and Auxiliaries*** *- auxiliaries unnecessary or innocuous where possible*
6) ***Design for Energy Efficiency*** *- for example using ambient temperatures and pressures*
7) ***Use of Renewable Feedstocks*** *- rather than deplete current resources further*
8) ***Reduce Derivatives*** *- additional steps avoided where possible*
9) ***Catalysis*** *- selective catalytic reagents over use of stoichiometric reagents*
10) ***Design for Degradation*** *- once function complete, break down into harmless products*
11) ***Real-time Analysis for Pollution Prevention*** *- in-process monitoring and control before the formation of hazardous substances*
12) ***Inherently Safer Chemistry for Accident Prevention*** *- minimise the potential for chemical accidents*

1.2 Fundamentals of Catalysis

Further developing the ninth principle, the drive for sustainable processes is intrinsically linked with catalysis. The chemical industry, including the production of fuels, fine chemicals, pharmaceuticals and plastics, has seen a huge growth over the past two centuries, in part due to the rise of catalysis. A catalyst is defined as *a substance which increases the rate of reaction without itself being consumed*.[2] They function by lowering activation energies and improving selectivity, thus minimising both the energy required and waste produced. It is unsurprising they have found applications across the whole chemical industry.

In any given reaction, the rate at which it proceeds, and indeed if it proceeds at all, is determined by both kinetics and thermodynamics. This can be further understood by Gibbs free energy:

$$\Delta G = \Delta H - T\Delta S$$

Equation 1: Gibbs free energy, where G corresponds to the Gibbs free energy, H is enthalpy, T is temperature and S is entropy.

For a reaction to be thermodynamically favoured, the Gibbs free energy for the products must be lower than that for the reactants at a given temperature, resulting in a negative change in Gibbs free energy. This is visualised in Figure 1, which also displays the activation energy (E_a) that must be overcome for the reaction to occur.

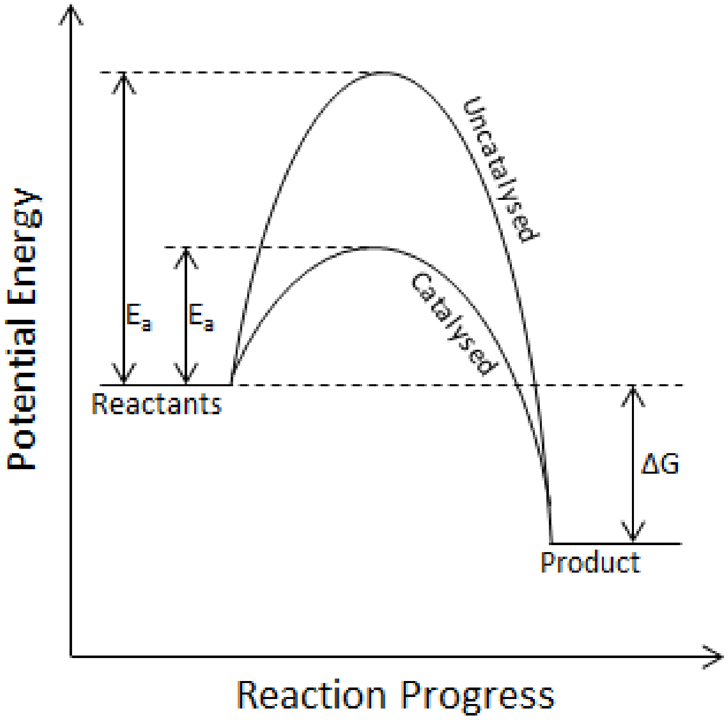

Figure 1: Energy level diagram for an uncatalysed and catalysed reaction.

The kinetics for the reaction is inherently linked to this E_a, and by altering this, the rate of reaction can also be changed. A catalyst provides a lower energy pathway for the reaction to occur by generating one or more transition states of lower energy. Although the Gibbs free energy is unaffected, Figure 1 shows how a catalyst can provide a more energy efficient route, for example by decreasing the temperature required for the reaction to proceed. This lower energy pathway can be achieved by the catalyst interacting in a number of ways, including but not limited to: stabilisation of the intermediate/transition state; holding reactants in close proximity/correct configurations; donating/accepting electrons; and providing efficient energy transfers.[3]

There are two main classes of catalysts, those in the same or a different phase, each with their own advantages and disadvantages. Homogeneous catalysts are typically metal complexes, but recently organocatalysts have also thrived. They tend to offer high selectivity and activity, with the option to tune the chemo-, regio- and/or enantio-selectivity depending on the complex employed. However, homogeneous systems often struggle with commercialisation because of their difficult separation from reaction mixtures, meaning the catalyst can rarely be reused. On the other hand, heterogeneous catalysts tend to have a much easier and cheaper recovery, and often benefit from increased stability. Catalyst design is also a key advantage, where modification on an atomic or molecular level can provide a unique reaction field, similar to that observed with enzymes. A limitation to using heterogeneous catalysts is that once the surface has been completely saturated with reactant molecules, the reaction cannot proceed until products leave the surface to make room for a new reactant molecule. Therefore, desorption is often the rate-limiting step in a heterogeneously catalysed reaction. More and more research is going into discovering heterogeneous systems which can replace already established homogeneous examples in an effort to adhere to the principles of green chemistry.

Two key areas of modern catalysis, in the search for new and more sustainable methods in the production of fine chemicals, are photocatalysis and organocatalysis.

1.3 Photocatalysis

1.3.1 Photochemistry

Photoexcitation to promote a reaction is often regarded as the next step to modifying a synthesis in order to achieve a more sustainable process. It’s easy to see why as it follows many of the principles for green chemistry, the use of light itself produces no waste, it is non-toxic, and energy efficient, particularly if harnessing sunlight. For photochemical processes to be fulfilled, the first law of photochemistry must be satisfied. The Grotthuss-Draper law states that a molecule must absorb light to have sufficient energy to break or reorganise a covalent bond. The energy supplied by each wavelength can be calculated using the Planck-Einstein relation:

$$E = \frac{hc}{\lambda}$$

Equation 2: Planck-Einstein relation, where E corresponds to the energy, h is Planck's constant, c is speed of light and λ is the wavelength.

This relation demonstrates how wavelengths such as visible light (400-800 nm) are less energetic than shorter wavelengths, as seen in the UV range (200-400 nm). Thus UV light can promote photochemical reactions more easily than visible light. This becomes a major drawback, when considering that organic molecules can rarely absorb longer wavelengths. So despite visible light being thought of as an infinitely available promoter, the application of it has required deeper study. Photosensitisers and photocatalysts offer a way around this problem.[4]

1.3.2 Methods of Photocatalysis

While classical photochemical steps have found notable applications in synthesis,[5,6] efforts in photocatalysis have focused on water splitting in the aim to convert solar energy into storable chemical fuels.[7,8] Our understanding of this process is improving, allowing further applications to be developed. When irradiated with light of sufficient energy, a molecule is converted to its photoexcited state, a far more reactive species due to the altered electronic distribution. These photoexcited states can follow physical decay pathways or chemical deactivation processes. Energy-transfer and electron-transfer reactions hold the most significance in photocatalysis as they both play a crucial role as indirect initiators.

The excited state of a photocatalyst can be used to promote a reaction substrate directly, as shown in Scheme 1a. Alternatively, and most common, is a photoredox catalytic process relying on the excited states to be more easily reduced or oxidised than their corresponding ground states, such that the photocatalyst is able to serve as an electron donor or acceptor. This is illustrated in Scheme 1b, which also shows the quenching and regenerating of the photocatalyst, enabling a chemical transformation to take place. Ideally, the single electron transfer (SET) processes would involve substrates or intermediates to avoid the use of sacrificial electron donors/acceptors.

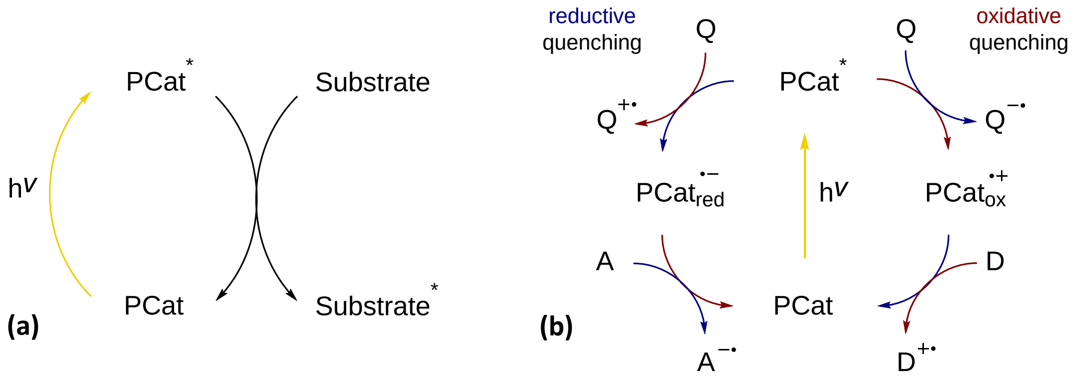

Scheme 1: (a) Photoinduced energy transfer. (b) Photoinduced electron transfer. Where PCat corresponds to the photocatalyst, Q is a quencher, D is a donor and A an acceptor. Reduction steps shown in blue, oxidation in red, photoexcitation in yellow.

These photocatalytic reactions are frequently undertaken at room temperature with commercially available light sources, further adhering to the principles of green chemistry, and preferable over the use of high/low temperatures or UV lamps. Additionally, organic molecules do not usually absorb visible light, thus discouraging side-reactions that might otherwise occur.[9] Reactions previously successful using other methods of activation are being investigated with catalysts exhibiting a photoresponse, as the process becomes more desirable from a sustainability perspective.

1.3.3 Classes of Photocatalysts

There are three main classes of photocatalysts: iridium and ruthenium complexes, organic dyes, and semiconductors.

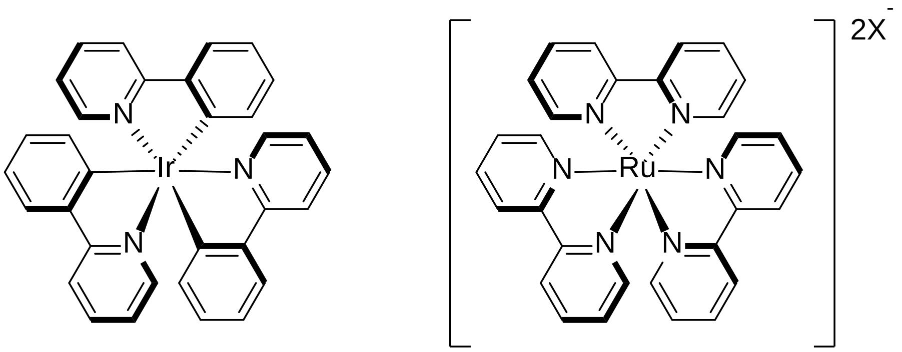

Figure 2: Ir(ppy)$_3$ and Ru(bpy)$_3$X$_n$.

Iridium and ruthenium complexes such as those in Figure 2, are arguably the most commonly used at the present time. Recent research has focused on the ruthenium(II) polypyridine complex [Ru(bpy)$_3$]$^{2+}$, having proven itself as an exceptional photoredox catalyst because of its chemical stability, and long lifetime of the photoexcited state. Usually these complexes are reduced from their photoexcited state by an electron donor, the general mechanism for this activity is displayed in Scheme 2. However, the disadvantages to these transition metal complexes are typically the high cost, toxicity, and their limited availability in the future.

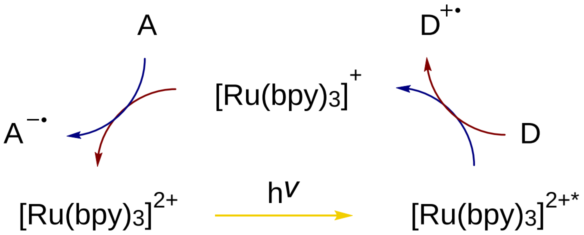

Scheme 2: General mechanism for the photoactivity of Ru^{II} species. Reduction steps shown in blue, oxidation in red, photoexcitation in yellow.

An attractive alternative are organic dyes, these highly conjugated molecules can absorb a photon of visible light, and their excited state lasts long enough to act as reductants or oxidants. These molecules are less toxic, less expensive and generally more stable than the transition metal complexes. A few examples of the most commonly employed are shown in Figure 3, which have been extensively studied for their ability to form singlet oxygen from the transfer of triplet state energy.

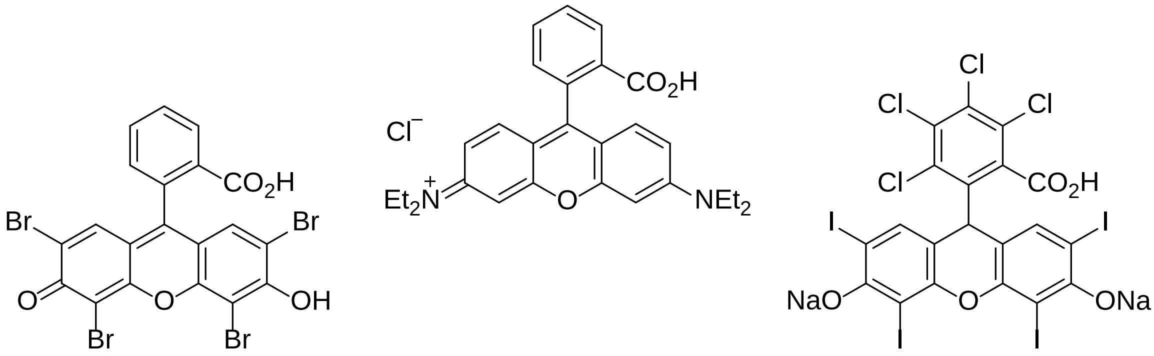

Figure 3: Organic dyes (from left to right), Eosin Y, Rhodamine B, Rose Bengal.

The final class of photocatalysts to discuss are semiconductors, which are easily available, cheap and non-toxic. Following photoexcitation with a wavelength corresponding to the band gap energy (E_b), electrons are promoted from the valence band (VB) to the conductance band (CB), and an electron-hole pair is formed. A fraction of these electrons/holes are able to migrate and eventually reach the external surface of the particles to allow a SET to take place, as shown in Scheme 3.

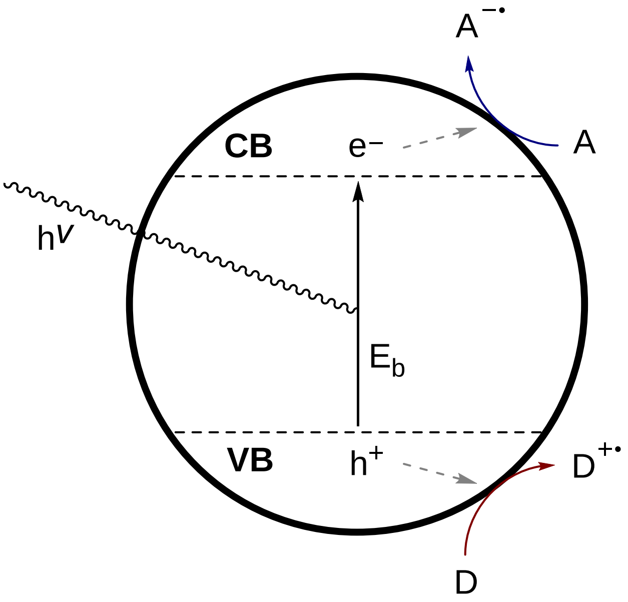

Scheme 3: Photoinduced electron-hole formation in a semiconductor, where E_b corresponds to the band gap energy, D is a donor and A an acceptor.

Many semiconductors have been held back by a lack of response to visible light. One such example is arguably the most widely studied semiconductor titanium dioxide (TiO_2). It is attractive as a stable, reactive and relatively cheap material. However, the large band gap requires absorbance in the UV range, limiting potential applications. The need to develop photocatalysts with visible light activity has driven research into adapting these materials, as well as identifying new ones. Whilst doping TiO_2 with organic or inorganic compounds is a popular strategy to reduce the band gap, they often suffer from decreased stability and increased charge-carrier recombination.[10,11] Other semiconductors with visible light responses have since been identified, including Fe_2O_3,[12] WO_3,[13] and $BiVO_4$.[14]

1.4 Organocatalysis

1.4.1 Development of Organocatalysis

The advent of asymmetric catalysis meant chemists no longer had to rely on natural sources as a starting point for a synthetic protocol towards a chiral product. Instead they could employ a chiral motif as a catalyst that would effectively transfer their chirality to prochiral substrates. For the last two decades organocatalysis has emerged as a powerful alternative to established asymmetric catalysts such as enzymes and synthetic metal complexes.[15,16] Organocatalysis is the acceleration of chemical reactions by utilising a substoichiometric quantity of a typically small organic molecule.[17] Whilst there have been sporadic reports of organic molecules behaving as catalysts for over a century, it wasn't until the year 2000 when the term 'Organocatalysis' was born.[18,19] Following the work of List and Macmillan, great advances have been made with the design of new organocatalysts, and the strategies and methodologies for enantioselective synthesis. These organocatalytic reactions are meeting the standards of already established protocols in terms of efficiency and selectivity.

There are drawbacks to organocatalysts, such as the high loading required for most reactions, and the limited substrate scope. However, there are also great advantages to the utilisation of simple and readily available organic compounds to catalyse demanding organic transformations. Their higher chemical stability compared to enzymes, better resistance to moisture and oxygen than metal complexes, absence of metal residues and their related toxicity, and ultimately lower cost are all very attractive. Reactions can be performed in an aerobic atmosphere, where the presence of water can often be beneficial to the reaction. They can be anchored onto solid supports, thus offering methods to reuse. They are generally easy to design and synthesise, as they are often based upon non-toxic compounds such as sugars, peptides or amino acids – which also contain natural chirality. The importance of chirality is well-known, considering nearly all natural products are chiral, with their respective properties reliant on how they interact with chiral receptors. Thus the use of organic molecules in catalytic quantities as chiral controllers, has been noted as having high potential in finding synthetic methods to produce enantiopure compounds, inspiring a greener and more sustainable route to the synthesis of fine chemicals. Their homogeneous nature also admits easy manipulation, to functionalise the molecule and tune the enantioselectivity. However, what is probably most appealing is simply that they are organic molecules.

Over the years various examples of asymmetric carbon-carbon bond formation through organocatalysis have been identified. The first such instance shown in Scheme 4 was detailed by Bredig in 1913, obtaining mandelonitrile, albeit with a very small enantiomeric excess (e.e.) of less than 10 %.[20]

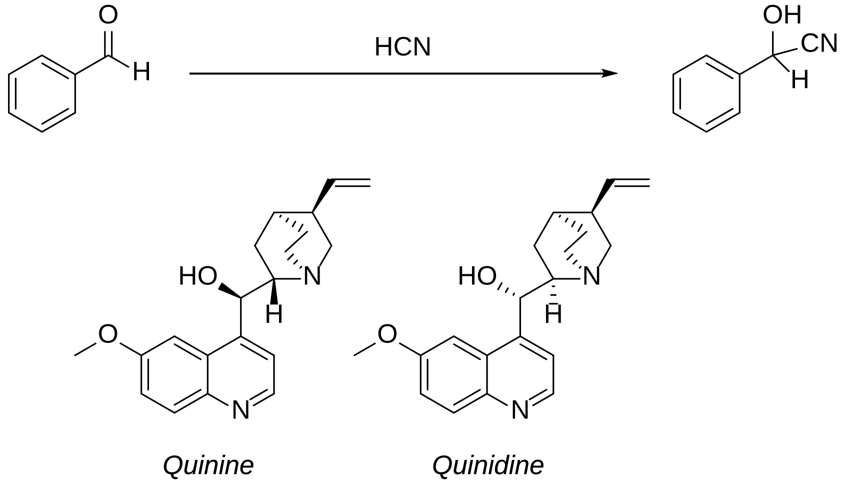

Scheme 4: Bredig's asymmetric catalysis.

By the early 1970s much higher enantioselectivity of 93 % could be achieved using (S)-proline as a catalyst in the reaction shown in Scheme 5. One of the most notable observations during this time, paving the way for asymmetric organocatalysis.[21]

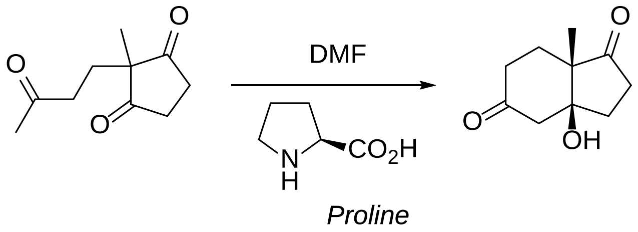

Scheme 5: Hajos-Parrish-Eder-Sauer-Wiechert reaction.

Then in 2000 the pioneering works of List and MacMillan were published for the intermolecular asymmetric aldol reaction[22] and an enantioselective Diels-Alder reaction[18] (Scheme 6), beginning a period of increasing interest in organocatalysis.

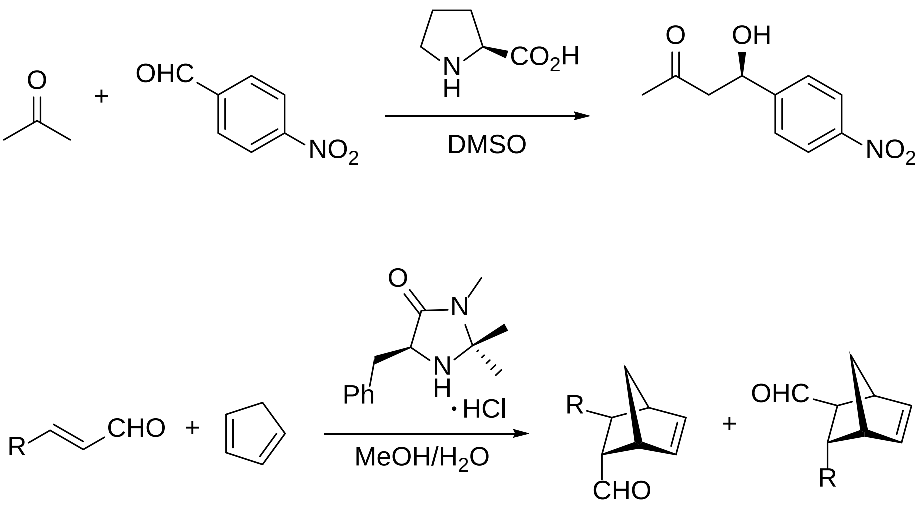

Scheme 6: List and MacMillan's founding reactions.

From this explosion of interest, there was a variety of asymmetric carbon-carbon and carbon-heteroatom bond-forming reactions including Diels-Alder, Mannich, Michael, 1,3-dipolar cycloadditions, aldol condensations, and epoxidations to name a few.[23–25] There is a long-standing goal to identify a general catalyst, one which could promote a large number of enantioselective reactions, through multiple modes of activation, with good substrate tolerance.

1.4.2 Aminocatalysis

Organic molecules are capable of catalysing reactions through various mechanisms, but one popular course is the utilisation of nucleophilic/electrophilic properties. The molecule is not consumed nor requires regeneration through a parallel reaction, but rather behaves as a conventional Lewis acid/base, as displayed in Scheme 7. The majority of organocatalysts are Lewis bases where a carbon, nitrogen, oxygen, phosphorus, or sulphur atom converts substrates to activated nucleophiles or electrophiles. Most common are nitrogen containing organocatalysts forming iminium, enamine or enolate intermediates, examples of aminocatalysis.

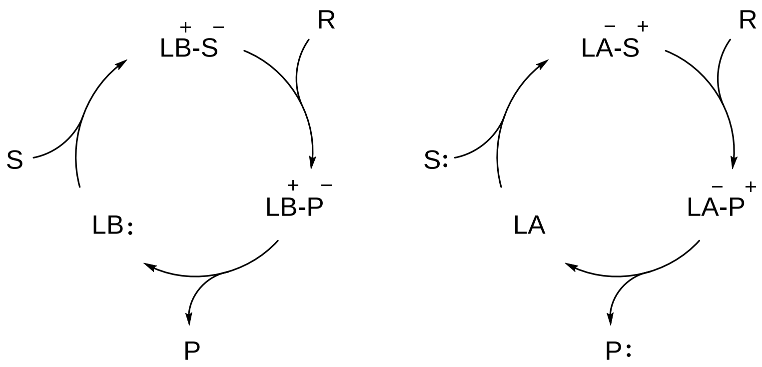

Scheme 7: Organocatalytic cycles, where S corresponds to the substrate, R is a reactant, P is a product and LB and LA are a Lewis base and acid respectively.

Aminocatalysis was first used by List in 2001[26] to describe reactions catalysed by primary and secondary amines *via* enamine and iminium intermediates. Whilst enamine activation increases electron density at the α-position, the iminium ion decreases the electron density, instead activating the β-position into reacting further. This is shown in Scheme 8 where the amine is behaving as a catalyst, to amplify reactivity at the desired positions.

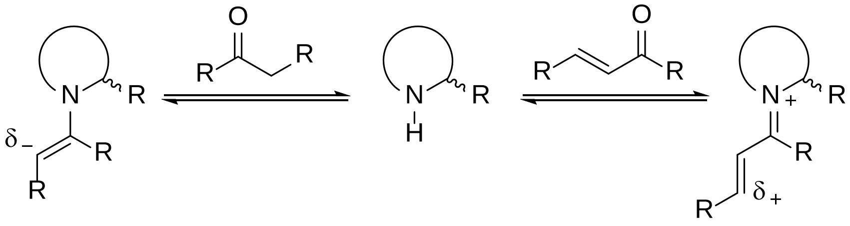

Scheme 8: Enamine and iminium intermediate formation.

In order to achieve stereoselectivity, a well-organised transition state must form with either passive or dynamic interactions such as those in biological systems. Whilst dynamic binding refers to the interactions between the catalysts and substrates at the reaction centre, passive binding includes the hydrophobic, van der Waals, and electrostatic interactions. Crucially, hydrogen bonding has been shown to influence the conformational preferences and stabilise the reactive intermediates, much like enzyme catalysis. Amino acids, such as *L*-proline, have been particularly successful. As a natural product with chirality it is a cheap source for an asymmetric organocatalyst, one that can easily be functionalised further to tailor the compound towards different reactions/products.[22,27,28]

Enamine catalysis is arguably the most frequent example of organocatalysis, permitting functionalisation at the α-position of enolisable aldehydes/ketones with electrophiles.[29] Scheme 9 shows the transition states that can occur after enamine formation with the popular pyrrolidine. If the substituent on the amine has a hydrogen-bond directing group, typically carboxylic acid, then this can direct the electrophile to the *Re*-face. Alternatively, the opposite enantiomer can be formed by employing steric effects of a large bulky group, this effect is also observed with iminium intermediates.

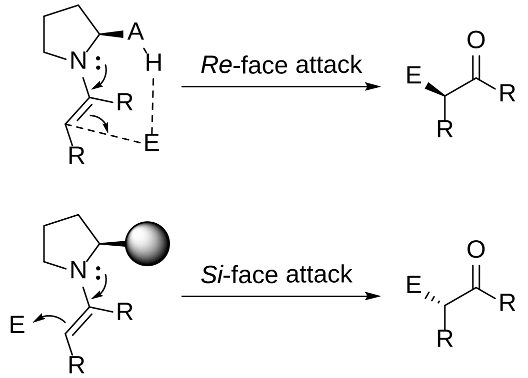

Scheme 9: Transition states for the addition of an electrophile to the enamine.

Iminium catalysis has now been established as an efficient route for the asymmetric addition of nucleophiles at the β-position on enals. In order to achieve high stereoselectivity, a chiral pyrrolidine with a bulky substituent, like the one shown in Scheme 10 can be employed.[30] The *trans*-conformer is favoured, whilst steric effects direct attack to the opposite face of the enal. The larger the group, the more selective, but in turn a decrease in rate of reaction. However, one drawback is that the addition to enals requires a good nucleophile, typically a malonate, and as such there are limited reports of other systems being used.

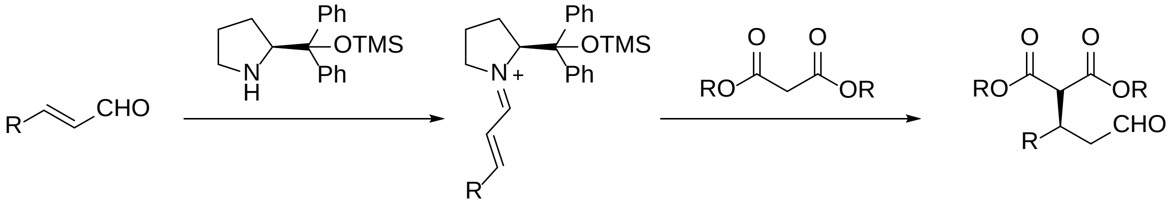

Scheme 10: Jørgensen organocatalytic nucleophilic addition of malonates to enals.

Sequential iminium-enamine catalysis has also been observed, where the addition of a nucleophile to the β-position results in an enamine intermediate, which can further undergo the addition of an electrophile to the α-position. The advantage to this mechanism is that the addition to both positions can occur in one step, and the stereoselectivity can be predicted through the choice of chiral catalyst. However, a great limitation is that the electrophile and nucleophile must both be present, whilst simultaneously not reacting with one another.

1.5 Aims and Objectives

As green chemistry continues to grow in prominence, there is increasing interest and importance in discovering novel catalysts which deliver on those principles. Photocatalysts enable the initiation of reactions with an innocuous source of energy. Further benefits can be achieved by utilising a heterogeneous material, including easy recovery and recyclability. Utilising large quantities of organocatalysts such as proline has been demonstrated to achieve excellent yields and enantioselectivity. Thus the logical next step is to trial their heterogenisation onto a support in order to reduce waste and provide a route towards more sustainable processes

The investigations in this thesis seek to identify novel photocatalysts for use in cross-dehydrogenative couplings, exploring their catalytic ability under a variety of conditions. By comparing and contrasting the chosen materials, their activity and characterisation, this work aims to improve our understanding of their mode of action and scope of use. Additionally, probing the scope for implementing organocatalysis on heterogeneous supports, examining the consequences of different pore sizes and surface effects. This work aims to identify heterogeneous materials which can join a growing field of more sustainable catalysts to consider for larger scale syntheses.

1.6 References

1 P. Anastas and J. Warner, *Green Chemistry: Theory and Practice*, Oxford University Press, 1998.

2 P. Atkins, T. Overton, J. Rourke, M. Weller and F. Armstrong, *Inorganic Chemistry*, Oxford University Press, 5th edn., 2010.

3 R. Masel, *Chemical Kinetics and Catalysis*, John Wiley & Sons, 1st edn., 2001.

4 K. Zeitler, *Angew. Chemie - Int. Ed.*, 2009, **48**, 9785–9789.

5 N. Hoffmann, *Chem. Rev.*, 2008, **108**, 1052–1103.

6 A. Griesbeck and J. Mattay, Eds., *Synthetic Organic Photochemistry*, Taylor & Francis Group, 2004.

7 A. J. Esswein and D. G. Nocera, *Chem. Rev.*, 2007, **107**, 4022–4047.

8 X. Sala, I. Romero, M. Rodríguez, L. Escriche and A. Llobet, *Angew. Chemie - Int. Ed.*, 2009, **48**, 2842–2852.

9 C. K. Prier, D. A. Rankic and D. W. C. MacMillan, *Chem. Rev.*, 2013, **113**, 5322–5363.

10 S. Rehman, R. Ullah, A. M. Butt and N. D. Gohar, *J. Hazard. Mater.*, 2009, **170**, 560–569.

11 R. Asahi, T. Morikawa, T. Ohwaki and Y. Taga, *Science*, 2001, **293**, 269–271.

12 S. K. Mohapatra, S. E. John, S. Banerjee and M. Misra, *Chem. Mater.*, 2009, **21**, 3048–3055.

13 A. Sclafani, L. Palmisano, G. Marcí and A. M. Venezia, *Sol. Energy Mater. Sol. Cells*, 1998, **51**, 203–219.

14 S. Kohtani, M. Koshiko, A. Kudo, K. Tokumura, Y. Ishigaki, A. Toriba, K. Hayakawa and R. Nakagaki, *Appl. Catal. B Environ.*, 2003, **46**, 573–586.

15 B. List and J. W. Yang, *Science*, 2006, **313**, 1584–1586.

16 D. W. C. MacMillan, *Nature*, 2008, **455**, 304–308.

17 P. I. Dalko and L. Moisan, *Angew. Chemie - Int. Ed.*, 2004, **43**, 5138–5175.

18 K. A. Ahrendt, C. J. Borths and D. W. C. Macmillan, *J. Am. Chem. Soc.*, 2000, **122**, 4243–4244.

19 W. S. Jen, J. J. M. Wiener and D. W. C. MacMillan, *J. Am. Chem. Soc.*, 2000, **122**, 9874–9875.

20 G. Bredig and P. S. Fiske, *Biochem. Z.*, 1913, **46**, 7–23.

21 Z. G. Hajos and D. R. Parrish, *J. Org. Chem.*, 1974, **39**, 1615–1621.

22 B. List, R. a Lerner and C. F. Barbas III, *J. Am. Chem. Soc.*, 2000, **122**, 2395–2396.

23 P. I. Dalko, *Enantioselective Organocatalysis*, Wiley-VCH Verlag GmbH & Co. KGaA, Weinheim, 2007.

24 P. I. Dalko and L. Moisan, *Angew. Chemie Int. Ed.*, 2001, **40**, 3726–3748.

25 A. Dondoni and A. Massi, *Angew. Chemie - Int. Ed.*, 2008, **47**, 4638–4660.

26 B. List, *Synlett*, 2001, **11**, 1675–1686.

27 D. B. Ramachary, N. S. Chowdari and C. F. Barbas, *Tetrahedron Lett.*, 2002, **43**, 6743–6746.

28 B. List, *J. Am. Chem. Soc.*, 2000, **122**, 9336–9337.

29 S. Mukherjee, J. W. Yang, S. Hoffmann and B. List, *Chem. Rev.*, 2007, **107**, 5471–5569.

30 S. Brandau, A. Landa, J. Franzén, M. Marigo and K. A. Jørgensen, *Angew. Chemie - Int. Ed.*, 2006, **45**, 4305–4309.

Chapter 2: Experimental Methods

2.1 Instrumentation

A range of characterisation techniques were employed to ensure the materials had been synthesised as expected, to rationalise the activity observed, and to make steps to optimise the performance. Understanding structure-property correlations is of crucial importance to the application of heterogeneous catalysts. These go from analytical methods which confirm the material obtained is that which we expect (NMR, XRD), to methods which look at the structural properties (BET, SEM), stability and composition (TGA, ICP) and then those which further elucidate the active site (UV-Vis, IR, XAS). Herein is presented a brief description of each technique used as well as the specific instrumentation details.

2.1.1 Nuclear Magnetic Resonance (NMR)

NMR examines how nuclei absorb and re-emit electromagnetic radiation. The energy is at a specific resonance frequency, dependent on the strength of magnetic field and properties of the atom.

2.1.1.1 Solution-Phase

Typically studying ^1H or ^{13}C, by detecting these frequencies, a well-resolved, unique spectra can be collected with peaks corresponding to specific nuclei. The shape and intensity of peaks can elucidate the environment of the atom, and its highly predictable nature allows for the easy characterisation of organic molecules. This technique will be used to characterise final products to determine structure and purity, and with the use of an internal standard, calculate conversion, yield and mass balance for crude reaction mixtures. NMR spectra were recorded on Bruker AV400 FT-NMR spectrometers in $CDCl_3$. Chemical shifts for proton and carbon spectra are reported on the delta scale in ppm, referenced to tetramethylsilane (TMS).

2.1.1.2 Solid-State

As a result of the more static nature of nuclei within a solid, the NMR spectra of solids do not show the high resolution of solution NMR. However, by spinning at the magic angle of 54.7 ° where chemical shift anisotropy becomes zero, resolution is improved and the location of peaks become very helpful in determining an atom's environment. This technique will be used to characterise the immobilised catalysts on solid supports. Analysis using solid-state NMR was performed using a Varian NMR System 600 MHz, with a 3.2 m probe and 3.2 mm rotor.

2.1.2 Powder X-Ray Diffraction (pXRD)

XRD studies long range ordering to confirm purity and crystallinity of a structure. A monochromatic beam of X-rays interacts with atomic electrons and scatters from atoms in the top layer, and layers below. To observe the scattered X-rays they must be in phase with constructive interference, which will only occur if the extra distance travelled by the second photon is an integral number of wavelengths. This principle is shown in Figure 4, enabling the derivation of Bragg's law (Equation 3)

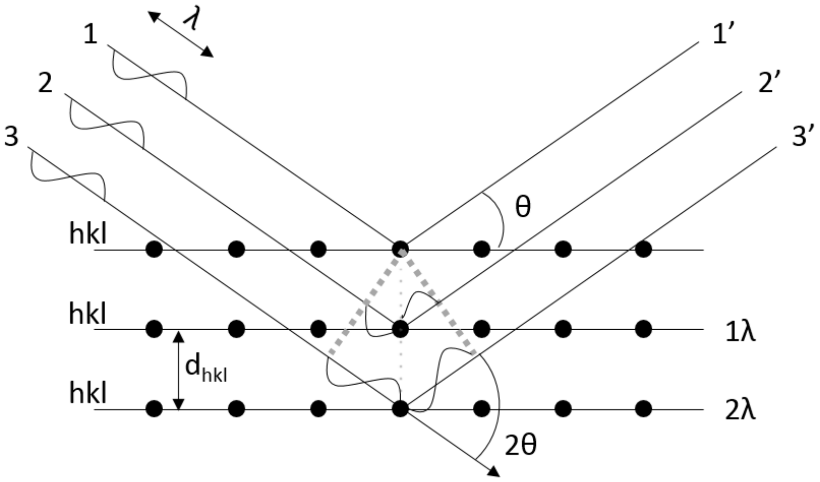

Figure 4: Derivation of Bragg's law.

$$n\lambda = 2d\sin\theta$$

Equation 3: Bragg's law, where the angle of incidence (θ), of known wavelength irradiation (λ) determines the spacing (d) between planes of a crystal.

With a powdered sample, numerous crystallites can fulfil the Bragg equation at a given angle and wavelength, producing a cone of diffracted X-rays. An X-ray detector moves around the circumference, cutting through the cones at various diffraction maxima, recording the intensity as a function of the angle. The resulting spectrum is a simple diffraction pattern that can be indexed to determine phase purity. pXRD was undertaken on a Bruker AXS D2 Phaser with Cu radiation (wavelength = 1.5406 Å). The range scanned was dependent on the expected framework, whilst a step of 0.02 ° was used for all scans.

If the XRD peaks are well resolved, structure refinement can be achieved with the Rietveld method.[1] Typically starting from an exemplary structure, an overall line profile is calculated for the diffraction pattern by a least-squares approach, varying parameters such as atomic positions. The variables are modified iteratively to achieve the best fit of the calculated pattern to the experimental data. Once complete, the nature of the crystal structure can be ascertained as in Table 1 for two Co-ZIFs.

Table 1: Crystallographic data of Co-ZIFs achieved using Rietveld analysis.

	Crystal System	Lattice Parameters / Å	Unit Cell Volume / Å^3
ZIF-9[2]	Hexagonal	a = b = 22.9437, c = 15.747	7178.8
ZIF-67[3]	Cubic	a = b = c = 16.9589(3)	4877.45(15)

The Scherrer equation (Equation 4) can provide further quantitative analysis by relating the broadening of a peak in a diffraction pattern to the size of the crystallite.[1] There are limitations to the equation, it assumes that after the incoming radiation is scattered by an atom, it doesn't interact with the others. It also doesn't take into account the type or scattering power of the atoms, crystal symmetry or reflection used. The width of the diffraction peak can also be influenced by other factors including instrumental effects, inhomogeneous strain, and lattice imperfections. Accuracy can be heavily dependent on the crystallinity of the sample. However, despite these simplifications, it can provide acceptable results when compared with other techniques such as electron microscopy.

$$D = \frac{K\lambda}{\varphi \cos\theta}$$

Equation 4: Scherrer equation, where the shape factor (K), X-ray wavelength (λ), full width of the peak at half maximum (ϕ), and Bragg angle (θ) determines the size of the crystallite (D).

2.1.3 Nitrogen Adsorption/Desorption

Gas adsorption/desorption experiments can study the quantity of gas adsorbed on a solid material at a given temperature and pressure, yielding information regarding its surface area and porosity. The Brunauer-Emmett-Teller (BET) model is widely used to determine surface area of materials, including zeolites and MOFs, typically by monitoring nitrogen adsorption at -196 ^{o}C. Following the Langmuir isotherm theory, the rate of gas adsorption is measured against change in pressure to determine surface area. The Brunauer-Deming-Deming-Teller (BDDT) classification also describes how the shape of the isotherm is indicative of the material's porosity, detailed further in Figure 5, where representative plots of quantity adsorbed *vs.* relative pressure are shown. Although a simplified model of physisorption, BET theory can elucidate the surface area and porosity of solid materials, which has useful applications during this project as the frameworks studied are expected to have high surface areas and porosity. BET N_2 adsorption measurements were performed at liquid nitrogen temperature, by first degassing the samples under vacuum. Surface area was determined by nitrogen adsorption-desorption isotherms using Micromeritics ASAP 2020, calculated using the BET method.

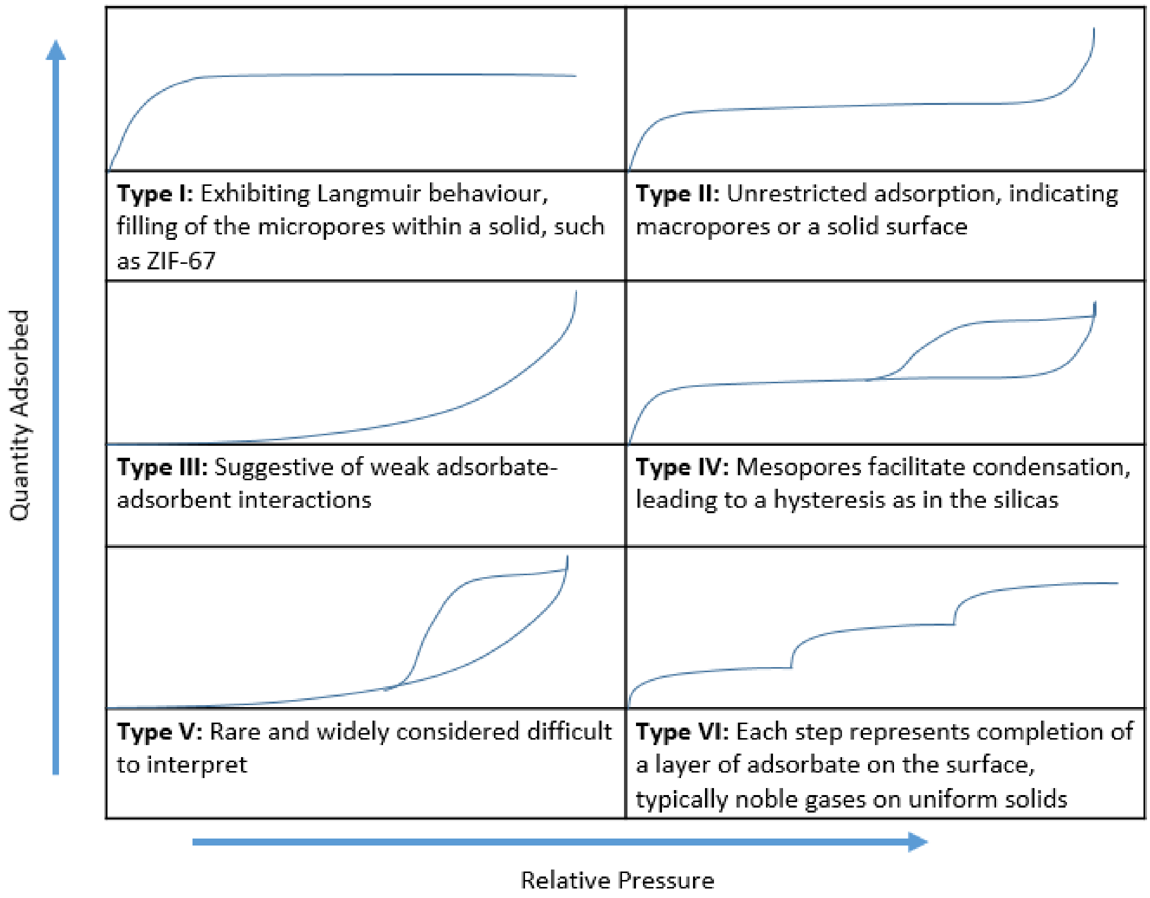

Figure 5: BDDT classification of isotherms.

2.1.4 Scanning Electron Microscopy (SEM)

SEM provides an insight to the surface and particulate properties, by scanning an electron beam over the sample under vacuum. Electrons or X-rays are in turn emitted from the sample, which are detected and analysed to generate an image. Of these, secondary electrons are most commonly detected by SEM, which are generated from the collision of incoming electrons and loosely bound outer electrons. These low energy electrons are only generated close to the surface of the sample in order to reach the detector, thus being able to reveal the topology of the material. SEM micrographs can be compared to literature dimensions and shapes to ensure phase purity and crystallinity have been achieved. Particle size can also be observed and checked for uniformity. SEM images were obtained by gold sputter coating MOF samples loaded onto silica wafers, and visualising with a JEOL JSM-6500F Field Emission Scanning Electron Microscope.

2.1.5 Thermogravimetric Analysis (TGA)

TGA measures the changes of physical and chemical properties as a function of temperature or time. Most commonly, characteristics are determined by simply monitoring the mass loss or gain over a broad temperature range at a constant heating rate. The resulting thermogram can indicate any desolvation, decomposition or oxidation that occurs and give an insight to the thermal stability of the material. Composition of guest molecules and metal/organic components can also be calculated through observation of the mass loss profile. Analysis was completed using a Netzsch Libra TG 209 F1 with a ramp rate of 10 ^{o}Cmin^{-1}, air (Chapter 3 and 4) or N_2 (Chapter 5) flow of 50 mLmin^{-1}, and a temperature range of 30-900 ^{o}C.

2.1.6 Inductively Coupled Plasma Optical Emission Spectroscopy (ICP-OES)

In most ICP analyses the sample is introduced as a liquid following digestion of the sample, typically using strong acids such as HNO_3/H_2SO_4 or even HF. The liquid is sprayed as an aerosol into the centre of a high temperature plasma (8000 K). The atoms within this aerosol are excited, once relaxed they emit photons which are element specific. A spectrometer measures this output for both element identification and concentration, particularly useful to determine metal content of a framework and CHN analysis. Measurements were conducted on a Varian Vista MPX CCD simultaneous axial ICP-OES instrument, based at MEDAC Ltd. Laboratories.

2.1.7 Ultra-Violet Visible (UV-Vis) Spectroscopy

Diffuse reflectance (DR) UV-Vis spectroscopy can be used to determine the redox capabilities of transition metals, and their coordination environments. By observing the wavelengths of electromagnetic radiation absorbed by a sample, the energy of transition between electronic energy levels can be ascertained. Typically d-d electron transfers as well as ligand to metal/metal to ligand charge transfers (LMCT/MLCT) are observed. The presence of certain bands at characteristic frequencies can provide evidence for the incorporation of transition metals in a framework, as well as their oxidation state and coordination geometry. These results can then also be used to tune which wavelength of light to use during photocatalysis. (DR) UV-Vis measurements were conducted using a Shimadzu 2600 spectrometer with integrated sphere. Reference standard was $BaSO_4$, obtaining a range from 200-850 nm.

2.1.8 Fourier Transform Infrared Spectroscopy (FTIR)

IR spectroscopy exposes a sample to IR radiation in the region of 4000-400 cm^{-1}, resulting in excitation of vibrations of covalent bonds. This vibrational mode is only observed by FTIR spectroscopy if it accompanies a change in dipole moment. The vibration frequency depends on the mass of the two bonded atoms and the force constant (strength) of the bond. The frequency is higher when the bond is stiff and the mass is low, thus frequencies are indicative of particular functional groups, and can aid the characterisation of materials. FTIR spectra plot absorption at a given wavenumber. Solid samples were studied using a Thermo Scientific Nicolet iS10.

2.1.9 X-Ray Absorption Spectroscopy (XAS)

XAS is a powerful technique for the bulk analysis of active sites in heterogeneous catalysts, by monitoring the transmittance of X-rays through a sample, the local environment and structure of specific elements can be examined. In XAS, electromagnetic radiation is used to excite core electrons, it is possible to selectively probe a specific element as the energy required for this is particular to individual elements, and has been well-defined and accurately documented. An incident X-ray beam is scanned though an energy range, when absorption events occur - leading to the generation of secondary electrons and photoelectrons - a reduction in intensity is observed in the transmitted beam at discrete energy values. The adsorption of X-rays is measured using Equation 5, which compares the intensities of the X-rays before the sample (incident X-rays), with those after the sample (transmitted X-rays).

$$I_t = I_0 e^{-\mu x}$$

Equation 5: Beer's law, where I_t is the intensity of the transmitted X-ray, I_0 is the intensity of the incident X-ray, μ is the absorption coefficient, and x is the thickness of the sample.

The absorption coefficient is dictated by the composition of the sample, as each element has differing absorption potentials, with heavier elements generally absorbing more X-rays than lighter elements. As such, the absorption coefficient can be more generally described as the probability for an X-ray to be absorbed by the sample, with data plotted as this value against the energy of the incident beam. A typical spectrum is displayed in Figure 6, where the regions representing X-ray absorption near-edge structure (XANES) and extended X-ray absorption fine structure (EXAFS) have been highlighted. The distinction is made relative to E_0, where $E \leq E_0 + 50$ eV corresponds to XANES, while EXAFS extends beyond.

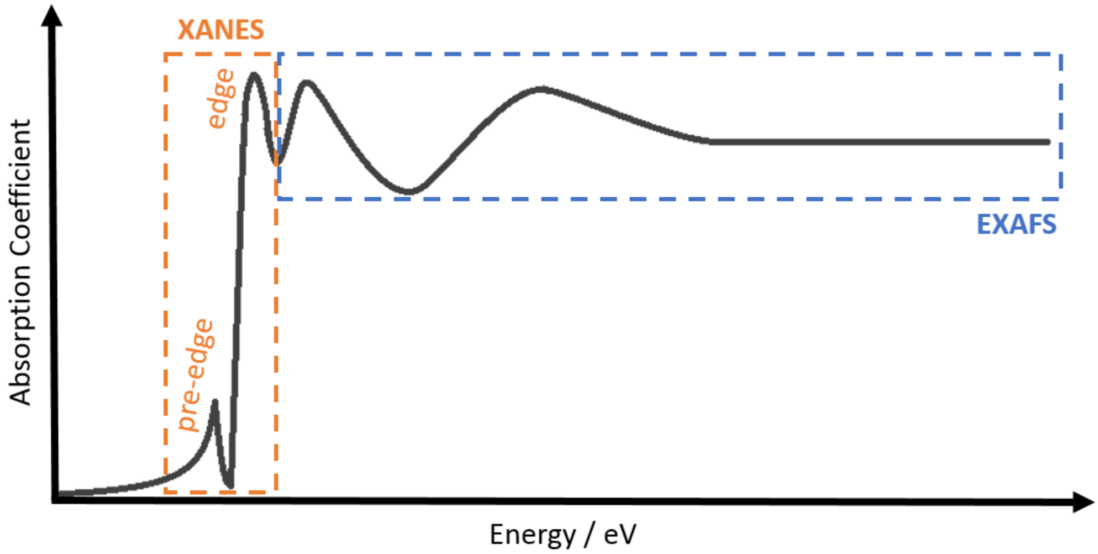

Figure 6: Representation of a typical spectrum produced using XAS.

Once obtained the experimental data is fitted to theoretical models. A range of parameters are used to find a model which best fits the data, whilst still being chemically feasible. How much information that can be gained depends on the quality of the data, although the first coordination sphere is commonly satisfactorily modelled.

XAS was used in this work to further explore the potential for photocatalytic activity, and investigate how the cobalt centres are effected by illumination from the solar simulator. Comparing the spectra from each catalyst can offer explanations on how their performance may differ, as well as increased understanding of their role in the reaction mechanism.

XAS data was collected with B18 at the Diamond Light Source, Harwell. The ZIF photocatalysts were diluted with cellulose to form a pellet 13 mm in diameter, mounted on a sample holder. The experimental hutch was darkened and XAS data collected at a scan rate of 3 minutes per scan for 10 scans to give the 'dark' scans. The solar simulator was placed 25 cm away and turned on when collecting data for a further 10 scans. The light source was then switched off, and 'dark' data collected, confirming in both cases the system was reversible. Measurements were referenced to a metallic Co(0) foil. Data processing and analysis were performed using IFEFFIT with the Horae package (Athena and Artemis).[4] The amplitude reduction factor, S_0^2, was derived from EXAFS data analysis of the known reference compound, Co(0) metallic foil.

2.1.9.1 X-Ray Absorption Near-Edge Structure (XANES)

The XANES region reveals electronic information, such as oxidation state and geometry. Features include a strong peak labelled 'edge', characteristic of the absorption of incident X-rays for excitation of a photoelectron into the continuum. The 'pre-edge' consists of shoulders and small isolated peaks related to the density of unoccupied orbitals that an electron can be excited to, these are at slightly lower energies than required for complete excitation and ejection from the atom. The sharp rise to the edge is attributed to the larger number of available high energy orbitals below the continuum of ionisation. Changes in the chemical environment, such as the oxidation state of the chosen element, can result in a shift of the peaks in this region to a higher or lower energy, due to a change in the binding energy (BE). However, as the core electrons are buried close to the nucleus, their energy levels are only subtly modified by coordination geometry, neighbouring atoms, and oxidation state. Accordingly, the energy required to promote the core electron (E_0) will exhibit only slight variations based on these factors.

2.1.9.2 Extended X-Ray Absorption Fine Structure (EXAFS)

In contrast, EXAFS yields information on bond lengths and neighbouring atoms. Occurring after the initial absorption edge, and able to extend up to 1000 eV further, this region has an oscillatory appearance stemming from the back-scattering of the initial photoelectric wave by the neighbouring atoms. The oscillatory features contain information on the local environment around the atoms within the sample, revealing the types and numbers of neighbouring atoms and their bonding.

When a sample is irradiated with a monochromatic X-ray beam with sufficient energy to eject a photoelectron, it will interact with neighbouring atoms, constructively or destructively, resulting in an oscillating signal. The photoelectrons propagate from the atom as spherical waves, and are scattered from neighbouring atoms, as displayed in Figure 7. The phase of scattering can positively or negatively influence the absorbing capabilities of the sample. If the scattered waves are in-phase with the original waves, where the interatomic distances are equal to an integer value of the photoelectron wavelength, then accordingly a maxima will be observed for absorption coefficient μ. However, if the waves are out-of-phase, then a minima will be observed, thus presenting the oscillatory nature of the EXAFS region.

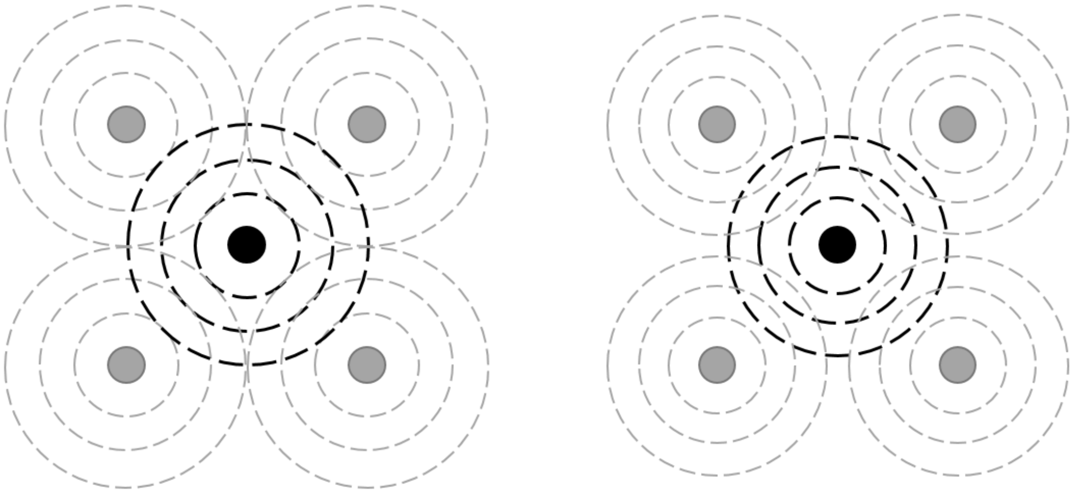

Figure 7: Scattering of photoelectrons upon excitation, shown on the left is in-phase, and on the right is out-of-phase.

Neighbouring atoms equidistant from the absorbing atom will all contribute to the same signal in the EXAFS plot, and are thus considered part of the same shell. A system may have multiple shells, especially in bulk materials, with the number of atoms in each shell referred to as the coordination number (CN). It is important to note that signals generated for a specific element are an average of the local chemistry and structure across the bulk of the sample, therefore it is preferable to have no more than one type of coordination geometry, as it can be difficult to separate the contribution of each metal centre.

2.1.10 High-Performance Liquid Chromatography (HPLC)

HPLC is used to separate, identify, and quantify each component in a mixture, even in minute quantities. Pumping pressurised solvent containing the sample mixture through a column of a solid adsorbent material. Each component will interact differently to the column contents, with different retention times, thus separating the components as they flow through. Typically chromatograms are obtained showing peaks over time relating to each component, which can be compared to literature values to help identify. Chiral columns are employed to separate enantiomers, the comparison of peaks then allows the enantioselectivity to be quantified. Analysis was performed on an Agilent 1220 Infinity LC System HPLC.

2.1.11 Light Sources

Two light sources were employed, initially JSG 5M 300 LED’s 3528 SMD day white/neutral white colour at 4.8 Wm^{-1}. Then moving towards an Oriel 150 W Xe short arc lamp, equipped with an AM1.5G solar simulator filter, placed 25 cm away from the reaction mixture, with a power output of 50 mWcm^{-2}. The reaction setups are displayed in Figure 8. Spectra for the light sources were collected using a USB4000-VIS-NIR-ES spectrometer between a range of 350-1000 nm.

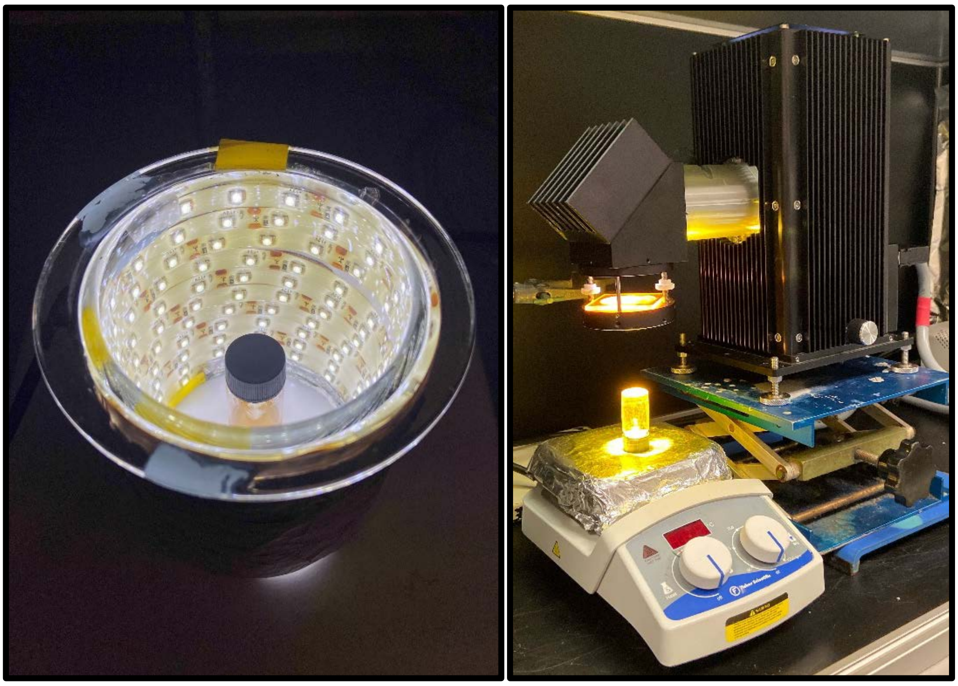

Figure 8: Reaction setup for the LEDs (left) and solar simulator (right).

2.2 Quantifying Activity

When reporting catalytic data, it is important to accurately quantify the results to draw conclusions on a catalyst's activity. This is typically done by calculating conversion, selectivity and yield. Where by-products appear but are unknown, selectivity can also be indicated by the mass balance, which calculates the amount of material accounted for at the end of the reaction, compared to the amount initially added. In this work, conversion and yield are calculated by comparing the starting material (SM) and product to a known quantity of an internal standard.

$$Conversion\ (\%) = \frac{Moles\ of\ SM_{t=0} - Moles\ of\ SM_{t=x}}{Moles\ of\ SM_{t=0}} \times 100$$

$$Yield\ (\%) = \frac{Moles\ of\ Product_{t=x}}{Moles\ of\ SM_{t=0}} \times 100$$

$$Mass\ Balance\ (\%) = \frac{Moles\ of\ SM_{t=x} + \sum Moles\ of\ Product(s)_{t=x}}{Moles\ of\ SM_{t=0}} \times 100$$

In reactions which produce molecules with chiral centres, diastereoselectivity and enantioselectivity is also considered. Diastereomers are more easily discernible, and within this work each presented different peaks in their ^{1}H NMR. The integral ratio of these peaks were used to give a diastereomeric ratio (d.r.).

Enantioselectivity was quantified through the use of an HPLC, by comparison of the two peaks relating to the enantiomers in question, the enantiomeric excess (e.e.) was calculated.

$$Enantiomeric\ Excess\ (\%) = \frac{Area\ of\ E_{major} - Area\ of\ E_{minor}}{Area\ of\ E_{major} + Area\ of\ E_{minor}} \times 100$$

2.3 References

1 E. J. Mittemeijer and U. Welzel, *Modern Diffraction Methods*, John Wiley & Sons, Weinheim, 2012.

2 K. S. Park, Z. Ni, A. P. Cote, J. Y. Choi, R. Huang, F. J. Uribe-Romo, H. K. Chae, M. O'Keeffe and O. M. Yaghi, *Proc. Natl. Acad. Sci.*, 2006, **103**, 10186–10191.

3 R. Banerjee, A. Phan, B. Wang, C. Knobler, H. Furukawa, M. O'Keeffe and O. M. Yaghi, *Science.*, 2008, **319**, 939–944.

4 B. Ravel and M. Newville, *J. Synchotron Radiat.*, 2005, **12**, 537–541.

Chapter 3: Novel Heterogeneous Photocatalysts for Cross-Dehydrogenative Couplings

3.1 Introduction

3.1.1 Significance of Cross-Dehydrogenative Couplings

Recently, green practices have attracted much attention from organic chemists, presenting an exciting challenge with the discovery of benign, green, and atom economic processes.[1] Coupling reactions are favourable for the predictable regioselectivity of the newly formed C-C bond, typically determined by the leaving groups on each substrate. However, the use of any leaving group inevitably results in undesirable stoichiometric waste also being produced. Each leaving group also tends to be installed in preceding steps, which is both ecologically and economically undesirable.[2] Therefore, the direct transformation of C-H bonds in organic molecules to form the new C-C bond, leads to more efficient syntheses.[3] Substantial research has gone into increasing the catalogue of reactions that minimise waste production in this way, leading to a large number of procedures for the selective construction of C-C bonds from two different C-H bonds.[4–6]

As such, cross-dehydrogenative couplings (CDCs) have emerged as one of the most important strategies for C-C bond formation. Where hypothetically one C-H bond is activated by a catalyst/mediator to form a nucleophile *in situ*, followed by coupling with an electrophile also generated *in situ* by oxidation of the second C-H bond. These are typically highly efficient, atom economic processes, which mitigate the need for prefunctionalisation of the substrates, reducing the number of synthetic steps undertaken and thus waste generated. This process adheres to the principles of Green Chemistry, in particular the prevention of waste, and reducing derivatives.[7] When under ideal conditions – such as using molecular oxygen as the terminal oxidant – water is produced as the only by-product. This is displayed in Scheme 11, alongside a classic cross-coupling mechanism which produces stoichiometric amounts of waste.

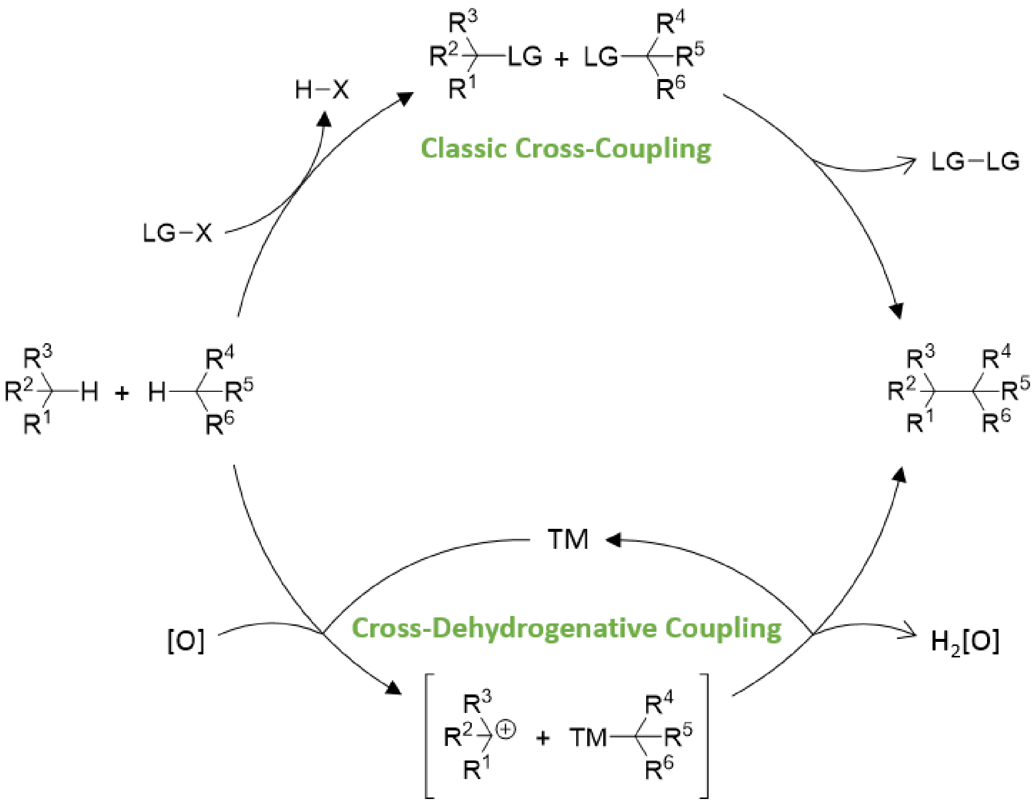

Scheme 11: Popular methodologies for C-C bond formation.

Nitrogen containing compounds, such as those with a tetrahydroisoquinoline (THIQ) motif or vicinal diamines, are commonly found in nature and are important structural features for pharmaceuticals.[8] Vicinal diamines are not just present in biologically active compounds but have also been applied as chiral auxiliaries and ligands in asymmetric catalysis.[9] Accordingly, the syntheses of such compounds have generated both industrial and academic interest. The reaction in Scheme 12 has been established as a reference system for benchmarking the performance of new catalytic systems for use in CDCs. A direct result of the interest behind nitrogen-containing compounds, combined with the experimental advantages of the CDC with THIQs. The carbon adjacent to the nitrogen and aromatic ring is easily activated, leading to selective coupling at this position with a variety of nucleophiles, including terminal alkynes, indoles, arenes, nitroalkanes, malonates and ketones.[10] The addition of aromatic rings to the nitrogen also allows us to test the system with a range of functional groups present, some examples of which are displayed in Scheme 12.

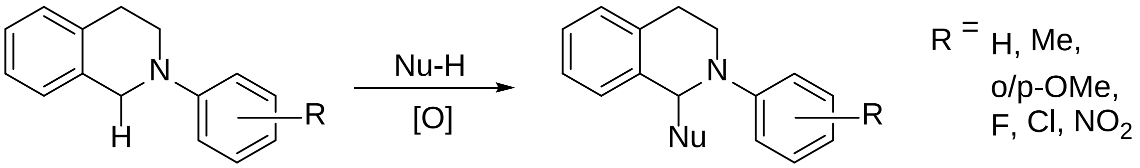

Scheme 12: Reaction of tetrahydroisoquinoline with a nucleophile.

It was previously believed the strength of a C-H bond made it too difficult to cleave *via* oxidative addition. As a result, stoichiometric amounts of transition metal complexes were used to perform such reactions.[11] However, in the past few decades, numerous catalytic systems have been found to successfully perform a CDC. These include catalytic amounts of transition metal complexes of vanadium,[12] iron,[13] copper,[10] zinc,[14] ruthenium[15] and palladium,[16] typically using TBHP or DDQ as an oxidant. Whilst they were all capable of achieving good yields, most appealing was CuBr which did not require excessive temperatures, and showed an ability to work with many differing substrates. The literature review in Appendix A shows a variety of products from the reaction in Scheme 12, and the conditions required, using CuBr as a catalyst.

Photocatalysts were later found to be effective, including iridium/ruthenium complexes and organic dyes, such as those discussed in Chapter 1,[17,18] along with the classic photocatalyst TiO_2.[19] Although organic dyes and TiO_2 appear to require longer reaction times, their low cost and low toxicity make them attractive catalysts. Magnetic iron oxide nanoparticles,[20] metal-organic frameworks (MOFs) containing copper,[21,22] and Zr-based MOFs doped with selenium[23] or iridium/ruthenium,[24] have been identified as active heterogeneous catalysts. Although the iron nanoparticles required heating to 100 °C, their method of separation is unique. In contrast, the MOFs worked well at room temperature. The doped zirconium materials were also active photocatalysts.

Whilst the homogeneous systems offer their own benefits, such as the metal-free organic dyes, the separation of organic moieties at the end of the process, in order to reuse, remains time consuming and energy intensive. In contrast, heterogeneous catalysts tend to have a much easier and cheaper recovery, facilitating recyclability. However, many of the materials reported thus far are costly and suffer a complicated synthesis. Selecting inexpensive and easily available metal complexes to develop would help to meet the demands of green chemistry. Copper and cobalt are both cheaper and more abundant metals to use than the frequently reported iridium/ruthenium, and are well known in the catalysis of coupling reactions due to their easily accessible oxidation states. Homogeneous systems of copper salts and peroxides have been used to test a wide variety of CDCs, as exemplified in the literature review (Appendix A), spurred on by the desire to establish how many different products can be formed through this methodology.[10] Whereas, the reports of cobalt in CDCs are very limited. To the author's knowledge, only one report has utilised cobalt as a photocatalyst, $CoCl_2$ formed a cobaloxime with dimethylglyoxime (dmgH) *in situ*, before going on to aid the nucleophilic attack of a THIQ with an indole, as displayed in Scheme 13.[25]

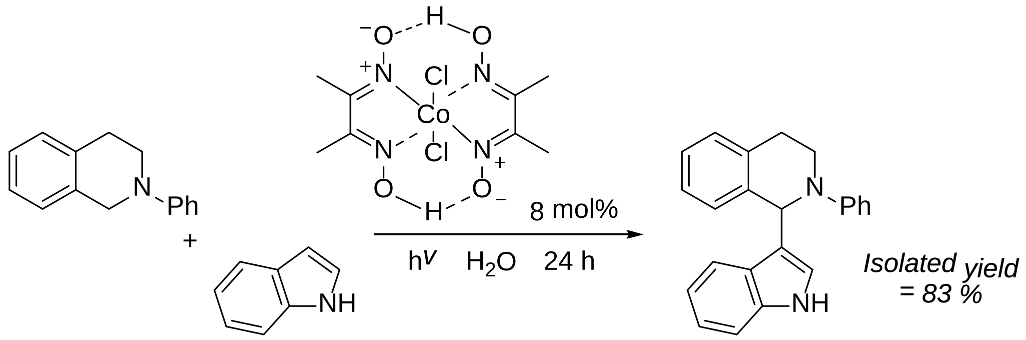

Scheme 13: Reaction of PhTHIQ with indole, catalysed by a cobalt complex.

It is proposed that upon photoexcitation, the cobalt complex partakes in a SET with PhTHIQ, exploiting the facile redox nature of cobalt by going from Co^{III} to Co^{II}, before regenerating the catalyst with molecular oxygen from the air. The solvent system used was water, demonstrating the environmentally friendly properties of the catalytic system, but its homogeneous nature still restricts potential applications.

When considering green chemistry, it is important to review the whole catalytic process, not just the catalytic material. The environmental and economic impact of reagents, oxidants and conditions are key to achieve a genuinely sustainable change. Herein, the aim is to identify a catalyst that itself is not only a step forward on current options, but can attain excellent yields under benign conditions. A promising environmental move, offering renewability, and a non-toxic, cheap source of energy, is the use of light in combination with a photosensitiser to catalyse organic reactions.[26] During this work, white light will be employed to review all materials unilaterally. Initially this will be a set of white LEDs, followed by a more sophisticated xenon lamp solar simulator, to emulate more industrial techniques. Similar systems of both setups have been investigated to photocatalyse CDCs.[25,27–29] UV-Vis spectroscopy will be used to identify which prospective materials exhibit absorption in the visible range and could be active under these light sources as a photocatalyst.

The use of environmentally harmful oxidants often produces stoichiometric waste, an aspect many groups try to eliminate from CDCs. Even the more desirable alkyl peroxides are problematic over molecular oxygen which would produce water as a singular by-product, achieving high atom efficiency, one of the principles of green chemistry.[30,31] Air is the cheapest oxidant available, but avoiding dilution and using pure oxygen often leads to faster reactions, improved yields, and lower energy consumption. The research carried out here looks to combine ideas from these examples, using a photocatalytic heterogeneous framework, and molecular oxygen as the terminal oxidant. It is hoped to achieve a catalytic system that uses less energy, with a cheaper and recyclable solid material, following the resounding principles of CDCs.

Scheme 12 showed nucleophilic addition to a THIQ. The aza-Henry reaction uses nitromethane as the nucleophile to generate a β-nitroamine, providing a route to vicinal diamines or α-amino carbonyl compounds by reduction of the nitro group.[32,33] Facile and selective, the reaction is widely studied to efficiently discover which catalytic complexes are promising for CDCs. Consequently, the reaction shown in Scheme 14 is ideal for screening the synthesised catalysts, and was chosen to explore during this project.

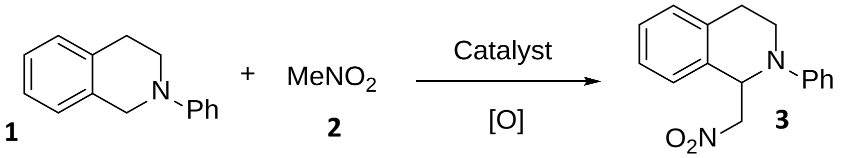

Scheme 14: Aza-Henry reaction.

For a review of photocatalysts in the aza-Henry reaction, including yields and conditions, Table 33 has been provided in Appendix A. One report of particular note is that of Bartling et al.,[34] which reviewed the mechanism for the aza-Henry reaction with a ruthenium photocatalyst. They determined that visible light was able to initiate a SET from the N-atom in PhTHIQ to the ruthenium complex, reducing it from its +2 state, before regenerating the catalyst with an oxidant in the system.

3.1.2 Identifying Potential Photocatalytic Materials

Whilst the first photochemical studies were carried out in solution, the power of surfaces and confined spaces soon became apparent with their improved selectivity.[35] Consequently, porous materials became of interest, enabling mass transfer from the external to the internal surfaces of a solid particle. This allows for a reaction to take place within the confines of a rigid cavity that has control over specific properties such as polarity and the presence of acid/basic or redox sites. The influential zeolites were deemed favourable due to their high porosity and surface areas. However, they generally hold a passive role, being unable to undergo direct photoexcitation themselves. By immobilising organic substrates, or incorporating transition metals, a route to photoactivity can be achieved, whilst the additional component benefits from the increased stability found with zeolites.[36] MOFs can be considered the logical evolution from zeolites in photocatalysis, combining many of the sought after properties as a result of their structures and compositions.

3.1.2.1 Metal-Organic Frameworks (MOFs)

MOFs have been highlighted previously as active catalysts in CDCs. They are metal ions or clusters linked together with bi- or multidentate organic ligands, a simplistic view of this is shown in Figure

9. A MOF's photoresponse can occur *via* light absorption by the metal node or organic linker. Such photoexcitation often generates a ligand-metal charge separation state, which in turn can result in photocatalytic activity.

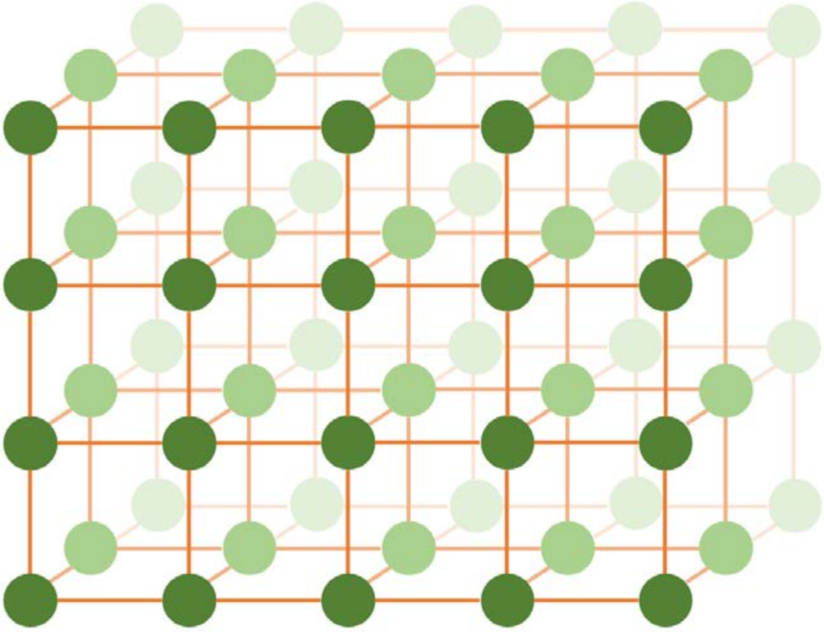

Figure 9: Diagrammatic representation of a MOF, where the green circles correspond to metal nodes, and the orange lines as bridging organic ligands.

Whilst few MOFs have had their applications commercialised, the interest in these materials has grown immensely over the past few decades. Their flexible nature and ease of design show potential in a wide range of applications including gas storage, separation, magnetism, and catalysis.[37] This is in part due to their desirable properties, including: high surface areas; pore volumes; crystallinity; low densities; and uniformly structured pores and cavities. Whilst these properties have determined MOFs main applications as gas adsorbents and in gas separation, they also lend themselves to catalysis. For a review regarding the design of MOFs for heterogeneous catalysis see the work of Corma, García and Llabrés I Xamena.[38] The review highlights the great diversity in metals and ligands that can be incorporated, and the various methods which can be used in synthesis that allow the design of frameworks with tuneable porosity, particle sizes, crystallinity and catalytic activity.[39,40]

MOFs use in photocatalysis is an emerging field, with reports appearing on their applications in the degradation of dyes,[41] CO_2 reduction,[42] as well as water splitting and H_2 production.[43] MOFs can play an active role in absorbing photons, in contrast to zeolites which are transparent to most UV-visible light radiations without the incorporation of impurities. Whilst it is well known many transition metals have the ability to elicit a photoresponse, the organic linker can also come into play. Utilising the facile transfer of electrons between metals and ligands, absorption by the organic ligands can be followed by conversion of the ligand-localised excitation to a charge separation state (CS), *via* SET to the metal nodes. The most common ligands in MOFs often have an excess of electron density, such as the aromatic 1,3,5-benzenetricarboxylate (btc) used in HKUST-1 (Figure 10).[44] The nature of the framework means that upon photon absorption, the electron rich ligands can be considered electron donors to the positive metal ions (electron acceptors) bound to them. Aromatic compounds have intense absorption bands, typically in the UV range, though substituents can shift this into the visible region. It is also possible to introduce a new band in the visible region when using common ligands such as 1,4-benzenedicarboxylic acid (bdc) by incorporating functional groups with a strong bathochromic influence, such as the NH_2 in Figure 10. The MOF remains isostructural with its unsubstituted counterpart, thus the same synthesis conditions may be used. In addition, it is not uncommon for MOFs to be synthesised using a mix of these potential linkers, which offers more opportunities to introduce or amplify interesting photophysical properties.

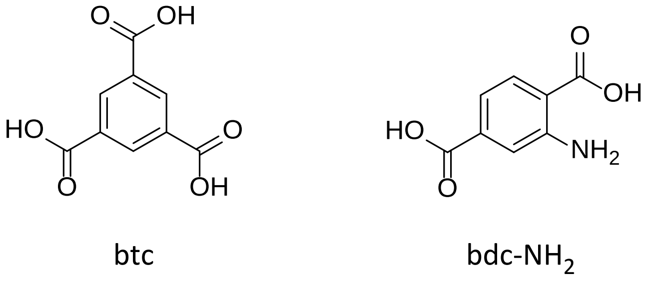

Figure 10: Electron rich ligands frequently used to construct MOFs.

The technique of selecting appropriate metal nodes, aromatic linkers or dyes when designing a MOF for a visible-light photoresponse is easily implemented, but not suitable for adjusting the photoresponse of conventional inorganic semiconductors. Semiconductors are characterised by their photoinduced CS and charge mobility, as mentioned MOFs also experience a photoinduced CS state. However, only in certain cases do the charge carriers have some mobility, which itself is a result of the long-lived CS states, therefore most MOFs should not be considered semiconductors.[45] A limited number of MOFs have chains of transition metal atoms connected by oxygen bridges, exhibiting semiconductor behaviour such as increased charge mobility. Although charge mobility may still occur in MOFs without this motif if there is sufficient orbital overlap to create a conduction band (CB) in which charge carriers may migrate.

A major drawback for the application of MOFs, particularly across industrial processes, is their lack of thermal stability. MOFs typically breakdown around 250 °C as a result of the metal-ligand forces which construct the frameworks. Water and other polar solvents are known to cause structural damage to certain MOFs by metal-ion solvation. Strong nucleophilic reagents such as hydroxide, amines and alkoxides can also coordinate strongly with metal ions, destroying MOF structures. Photochemical stability is a major issue, as some organic molecules are known to undergo rapid degradation upon illumination. Oxygen is able to quench electronic excited states which can form singlet oxygen, or it may undergo electron transfer to form superoxide, and then onto hydroperoxides, those reactive species can go on to attack multiple bonds within a MOF. These pathways can accelerate oxidative degradation or transformation of the organic linkers. Accordingly, the photostability should be carefully examined when proposing a MOF for photocatalysis. This should include extended irradiation under similar conditions to those in which the MOF will be employed. Stability of the MOF can then be confirmed using XRD, surface area measurements, and other techniques such as UV-Vis and TGA. Leaching of any metal or organic linker from the framework to the solution during the reaction can be determined by chemical analysis of the liquid phase, following separation of the solid catalyst. Recyclability tests are also important to determine if the MOF has been sufficiently affected to be unable or inefficient at completing the process upon repeated cycles. The cause of deactivation can then be hypothesised by comparison of data on the fresh and used samples. The two most common causes for MOF deactivation are a decrease in crystallinity and porosity. Although crystallinity is not directly related to efficient photocatalysis.[46]

As mentioned previously, a major advantage that MOFs have over other materials is the great diversity in metals and ligands that can be incorporated, and the activity/structural properties that can be tuned accordingly. Thus it should be easy to design a MOF which fits the requirements of an efficient photocatalyst. Firstly, and most obvious, is to absorb light to undergo excitation, from the available light source. For many applications, such as the degradation of pollutants and fuel production, sunlight is employed. Once solar energy reaches the Earth's surface it contains approximately 4 % UV radiation and 46 % visible light, which is why there is such a demand for visible light photoresponsive catalysts, and why there are numerous studies which employ artificial visible light to give an indication of performance under solar light. The second requirement for an efficient photocatalyst is charge separation (CS), favourable in MOFs due to the close contact and rigid positioning of organic linkers and metal nodes. However, charge recombination, a typical deactivation pathway, will compete with any photocatalytic activity. Unfortunately, there is a lack of information regarding the significance of charge recombination in MOFs.

Presently, it is a recurrent theme to modify MOFs which have already been described for other applications, repurposing them for photocatalysis. The two most common modifications are the use of NH_2-containing linkers mentioned previously, and the deposition of Pt nanoparticles (NPs).[47] Noble-metal NPs can enhance the CS efficiency of MOFs by allowing the migration of electrons from the MOF where they were initially generated to the metal NP. Thus increasing the lifetime of the CS state, as charge recombination becomes more difficult. Metal NPs are also able to act as co-catalysts by efficiently transferring electrons to the substrates. Although these modifications have been successful, they do not fully exploit the vast flexibility of MOFs in their design. Light harvesting could be accomplished by organic dyes or metal centres that as discrete molecules in solution absorb visible light, circumventing the need for expensive noble metals. The CS step should take into consideration the redox potential of metal clusters, and their orientation with respect to the LUMO orbitals of the linker.[48] Crystal size and surface modification should also be considered for enhancing photocatalytic activity. The approach of application-driven synthesis is somewhat unique to MOFs, with methodology for other conventional photocatalysts not as reliable or flexible.

HKUST-1 is a widely studied MOF constructed from Cu^{2+} and 1,3,5-benzenetricarboxylate paddlewheel units, forming 3D channels with a pore aperture of 6 Å, as displayed in Figure 11.[44] The nature of the paddlewheel leaves open copper sites with Lewis acidic character, typically absorbing moisture from the atmosphere, which can be easily removed upon heating under vacuum, this distinctive feature has driven research in the material. HKUST-1 has been identified as an effective and reusable catalyst in the oxidation of benzylic alcohols,[49] and was highly efficient in the photocatalytic degradation of organic dyes.[50] It has also been investigated in the aza-Henry reaction with TBHP, achieving 76 % after 6 hours.[22]

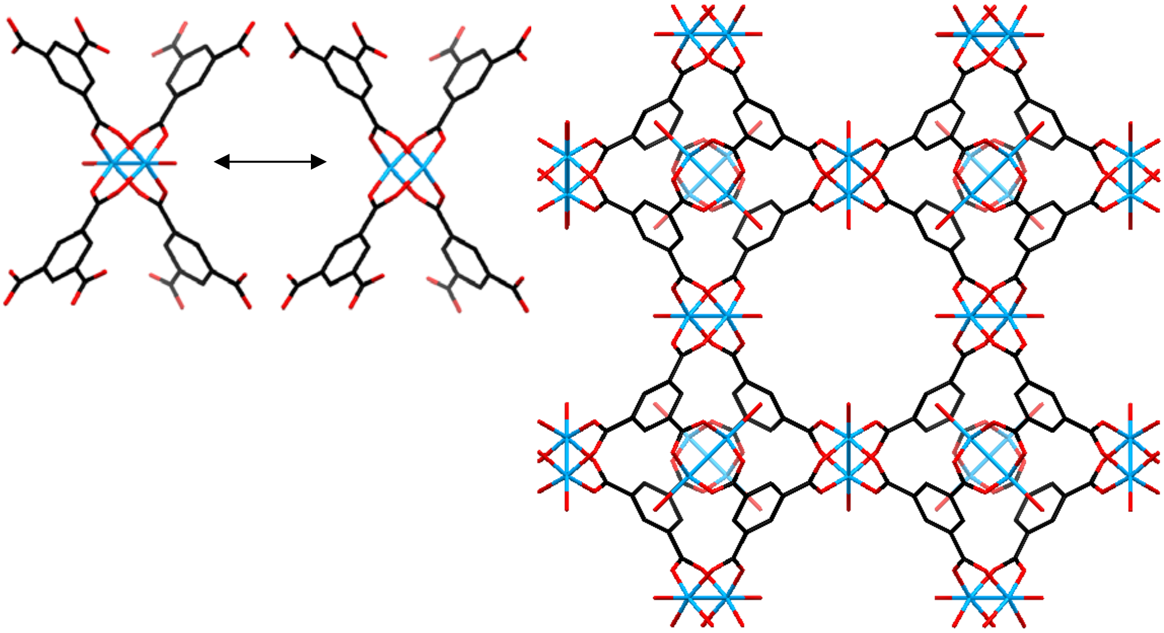

Figure 11: Chemical structure of HKUST-1,[44] packing diagrams showing the paddlewheel units, their change in coordination, and how they come together to form channels. Hydrogen atoms omitted for clarity. Cu blue, C black, O red.

Other solely copper MOFs tested as catalysts in CDCs have only been used with peroxide,[21,22] achieving 97 % after 6 hours at room temperature for the aza-Henry reaction. Whilst under the irradiation of light, selenium doped UiO-68 and ruthenium doped UiO-67 achieved 90 % after 4 hours, and 86 % after 12 hours respectively.[23,24] However, a disadvantage to these materials is the more complex syntheses compared to conventional MOFs, which make them less desirable on an industrial scale.

3.1.2.2 Zeolitic-Imidazolate Frameworks (ZIFs)

Although it has so far been difficult to achieve, there is great potential in the catalytic applications of a zeolite which incorporates transition metal ions and an organic unit within the pore, and as an integral part of the framework.[51] ZIFs are a sub-class of MOFs consisting of metal ions and imidazolate linkers. They typically incorporate cobalt or zinc nodes due to their higher proficiency for tetrahedral geometries in the 2+ oxidation state, over the likes of copper which tends to favour an octahedral coordination sphere. Figure 12 shows how the components arrange themselves with a bond angle analogous to that of zeolites, allowing the resulting framework to adopt crystalline architectures which mimic the well-known zeotype materials. They are attracting significant attention, combining the chemical and thermal stability of zeolites with the unique properties of MOFs.[52,53] Unlike zeolites, ZIFs have much greater flexibility in structural design, being able to tune the framework, pore aperture, cavities and surface area, as a result of which over 150 ZIF structures have been reported.[51,52] Although compared to conventional MOFs, there are limited reports of ZIFs in catalysis.

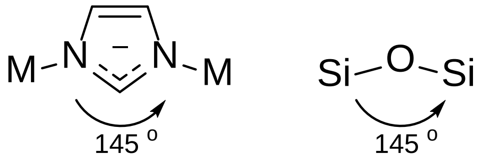

Figure 12: Analogous bond angles of ZIFs and zeolites.

ZIF-8 is a prototypical ZIF material, widely studied as a result of its high stability and facile synthesis, often in aqueous conditions.[54] Consisting of tetrahedral Zn^{2+} nodes with 2-methylimidazole linkers to form a sodalite framework, it has been reported to catalyse transesterifications,[55] the Knoevenagel condensation,[56] and the synthesis of styrene carbonate.[57] ZIF-8 helped open doors for ZIFs to be considered as alternatives to current solid catalysts, demonstrating high activity, little degradation upon repeated use, and minimal leaching.

Reports of cobalt ZIFs as active catalysts are increasing in number. ZIF-9 consists of tetrahedral Co^{2+} nodes with benzimidazole linkers, which construct the sodalite cages shown in Figure 13. The bulky linkers restrict the pore apertures to 3.0 Å,[58] but high activity on the surface generates promising results in organic transformations. For example, in the oxidation of several small aromatic molecules under molecular oxygen,[59] and ZIF-9 achieved excellent conversions under mild conditions in the Knoevenagel reaction with no significant loss in activity after multiple cycles.[60] As such, the ZIF-based material represents an exciting alternative to homogeneous and current industrial catalysts too. ZIF-9 has also been identified as a co-catalyst for supporting the photocatalytic splitting of CO_2 into CO under mild conditions, combining the advantages of its high porosity for CO_2 capture, with the catalytic function of cobalt and imidazole entities in CO_2 reduction catalysis. The framework is believed to promote the electron transfers required, when used alongside a ruthenium photosensitiser[61] or cadmium sulphide semiconductor.[62] However, to the author's knowledge, there are no reports of ZIF-9 as a photocatalyst on its own merit.

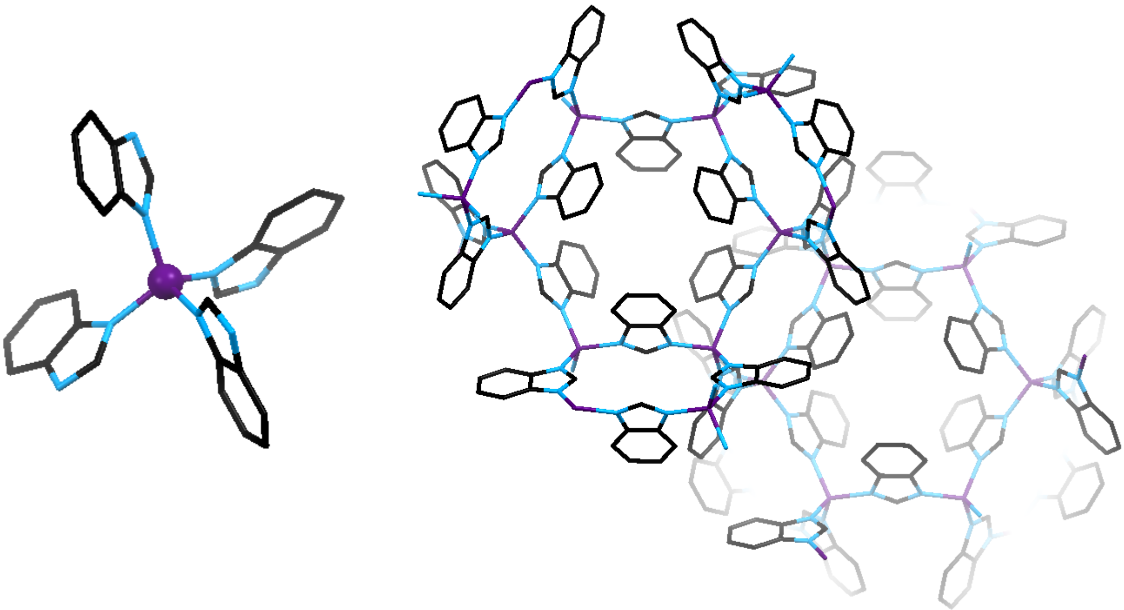

Figure 13: Chemical structure of ZIF-9. Left, Representation of the secondary building units showing the tetrahedral environment around cobalt. Right, Packing diagram of ZIF-9 showing the sodalite cage. Hydrogen atoms omitted for clarity. Co purple, C black, N blue.

The flexible nature of ZIFs was clearly demonstrated by the guest-induced phase transitions of ZIF-7, reported by Redfern et al. and illustrated in Figure 14 with the isomorphous ZIF-9.[63] They observed that upon the loss of the guest molecule DMF from within the pores, a structural transformation took place to a more condensed phase termed ZIF-7-II. The process is reversible by stirring the framework in solvent, whether it be DMF, ethanol or hypothetically nitromethane, to achieve ZIF-7-I. A third irreversible transition to a much denser phase of ZIF-7-III has potential applications in more extreme environments.

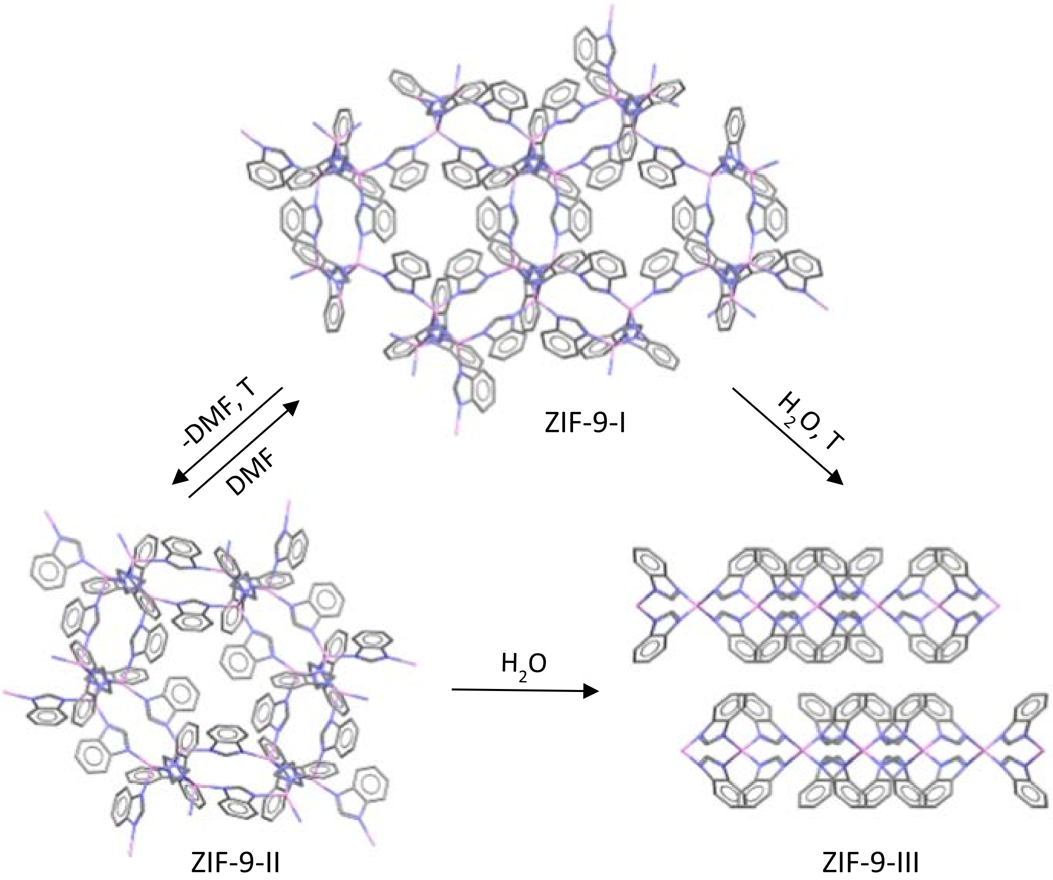

Figure 14: Phase transitions for ZIF-9, adapted from a figure by Sun, Li and Tan.[64]

ZIF-67 shares the same Co^{2+} tetrahedra as ZIF-9 with the 2-methylimidazole linkers of ZIF-8, thus adopting similar characteristics to both, such as a sodalite topology. The replacement of Zn^{2+} (ionic radii of 0.60 Å) with Co^{2+} (ionic radii of 0.58 Å) makes very little metrical difference to the structure adopted, thus ZIF-7 (Zn^{2+} and benzimidazole) and ZIF-9 also share many structural similarities, as observed with the method of synthesis, pXRD, and SEM.[51] The less bulky linker of ZIF-67 leads to a larger pore aperture of 3.4 Å, as displayed in Figure 15.[65] An advantage to using ZIF-67 over ZIF-9 is that the synthesis does not involve a toxic solvent and it can also be formed quickly under ambient conditions. This is believed to be a result of an electron withdrawing effect from the aromatic ring in the benzimidazole linker, reducing the availability of the nitrogen lone pair, thus requiring more forceful conditions to build the framework. ZIF-67 has been used as a heterogeneous redox catalyst, reporting excellent yields in the cyclisation to form quinazoline products.[66] As is typical of these ZIF-based materials, it was recovered and reused without significant degradation. The material is used to activate peroxymonosulfate,[67] or doped with copper[68] for the degradation of organic dyes. Once again, ZIF-67 is also reported as facilitating photocatalytic processes, but to this author’s knowledge, has not been demonstrated as being effective on its own merit.

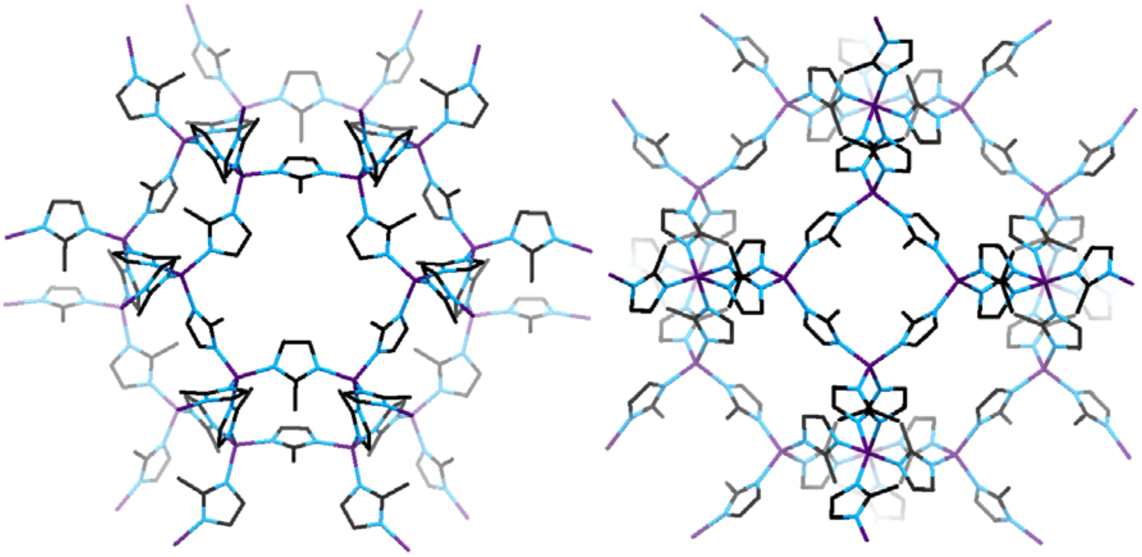

Figure 15: Chemical structure of ZIF-67. Packing diagrams of ZIF-9 showing the sodalite cage. Hydrogen atoms omitted for clarity. Co purple, C black, N blue.

The literature suggests performance could be improved using techniques such as doping copper into the framework, or utilising a photosensitiser. However, XAS spectra for ZIF-67 before and after exposure to light suggest those additional elements are not necessary.[69] The subtle differences showed the edge of cobalt centre shifting to lower energy, indicating the Co-N bond elongation and reduction of cobalt due to photoexcitation. It can then be deduced that the imidazolate ligand, as the only other component, must be oxidised in return, confirming the CS state with LMCT character. This long-lived CS state and absorption peaks in UV-Vis spectra, along with the hybrid porous nature of Co-ZIFs, strongly imply the photocatalytic potential these materials have without alteration.

The increasing global interest in visible light photocatalysis has driven this exploration into the application of ZIFs. Current reports focus on photoactive nanostructures/molecules being incorporated into the highly porous ZIF, where the structure is simply a host or passive medium for dispersing this photocatalytic species.[61,70–72] Whilst this technique has been widely used to develop zeolite-based photocatalysts,[36] they often suffer from guest material aggregation and lack of control over spatial distribution and homogeneity.[73–75] This work delves into the preferable route of utilising the framework to exhibit an intrinsic photochemical response, as the XAS suggests is possible, and be directly applied as a photocatalyst to bypass these complications. This has been successfully realised with some photoactive MOFs.[46,76]

3.1.3 Mechanistic Insights

3.1.3.1 Mode of Action

There are limited reports on the Co-ZIFs typical mode of action, so in order to understand how they might promote the aza-Henry reaction, it's important to look at how similar materials behave. By combining FTIR-monitored carbon monoxide adsorption and DFT calculations, the work of Chizallet et al.[55] came up with three hypotheses for the mechanism in which ZIF-8 acts as a transesterification catalyst:

I. The saturated node acts as a Lewis acid, temporarily increasing its coordination number.

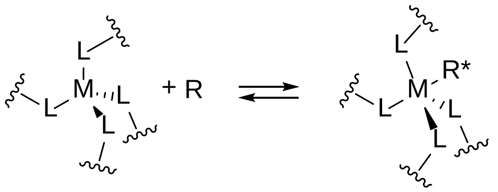

II. One of the node-linker bonds temporarily de-coordinates, generating a transient species that can activate the reactants by either the Lewis acidic unsaturated node, the basic unsaturated linker, or as shown below, both.

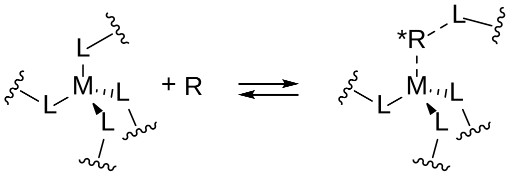

III. The active site is located on the external surface or at structural defects due to the presence of dangling bonds, in this example the metal is shown completing its coordination shell.

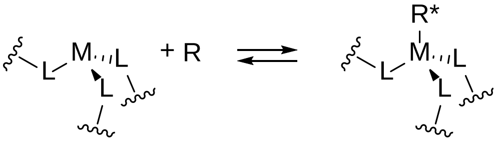

These findings can be translated to the microporous ZIF-9 and ZIF-67. With pore apertures of 3.0-3.4 Å restricting the admission of substrates, hypothesis III is considered the most probable route to catalyse the aza-Henry reaction on the outer surface. The environments which could be found on the surface of ZIF-8 were studied by use of DFT calculations for the IR-frequency shifts of adsorbed CO.[55] By comparing these shifts with experimental recordings, the acid-basic sites appear to be located at the external surface or structural defects, rather than within the micropores. The nature of these are also diverse, including: strong Lewis acid sites (low coordinated metal atoms); Brønsted acids (NH groups); and basic sites (free N^- moieties of the linkers). If external surface area is where the reaction is occurring and smaller particles result in larger surface areas, then SEM can be employed to view particle size and distribution and determine how this may be having an effect on activity.

3.1.3.2 Aza-Henry Mechanism

The work of Bartling et al. proposed a comprehensive mechanism for the photocatalysed aza-Henry reaction, in which the intermediates could be identified using ^{1}H NMR. Scheme 15 shows how this could be applied with Co^{2+}, as well as the light-induced reaction in the absence of a photocatalyst, and the background reaction in the dark.[34]

The formation of an electron donor-acceptor (EDA) transition state is believed to form upon first addition of nitromethane to the substrate. This can form the product **3** in a very slow background reaction, potentially following the **4**-**6**-**10**-**3** pathway detailed later on. A light-induced exchange can also occur, believed possible because light excitation facilitates the charge transfer in the EDA transition state. The back electron transfer is prevented by electron transfer of the nitromethane species with dissolved oxygen. The superoxo radical is then able to drive the $H^\bullet$-abstraction and iminium pathway. Reports detailed in Appendix A give high yields in the dark after a week of stirring, with intense blue light and oxygen, it has been found to reach full conversion in 24 hours.[34] This is in contrast to just 2 % yield after 20 hours without light and just 7 % yield after 20 hours without oxygen. Whilst this does raise the question why a photocatalyst is necessary, being able to employ one that works at a different wavelength allows us to scope for potential photocatalysts in other CDCs which do not have such an efficient background reaction.

When utilising the photocatalyst, in this scheme represented by the metal ion Co^{2+}, it is proposed a photoexcitation leads to a SET and the radical intermediate **4**. The catalyst is then renewed by oxygen or nitromethane oxidising Co(I). Although the Co(II)-Co(III) transition is more commonly known, the photochemical reduction of Co^{2+} has previously been reported.[69,77] The subsequent step is somewhat dependent on which species was used as the terminal oxidant. Under anaerobic conditions, the radical intermediate is deprotonated to form **6**, potentially by the nitromethane radical, or the basic sites expected on the external surface of the Co-ZIFs.[55] Two potential radical pathways are then initiated, both of which eventually lead to the desired product. One of these utilises a stepwise reduction of nitromethane, which can occur by picking up electrons from the metal catalyst in the photocatalytic cycle. Under aerobic conditions, oxygen can also act as the terminal oxidant, the superoxo species facilitates $H^\bullet$-abstraction towards the highly effective iminium ion pathway. These mechanisms justify why even in the absence of light, catalyst, oxygen, or even all three, product may still be detected.

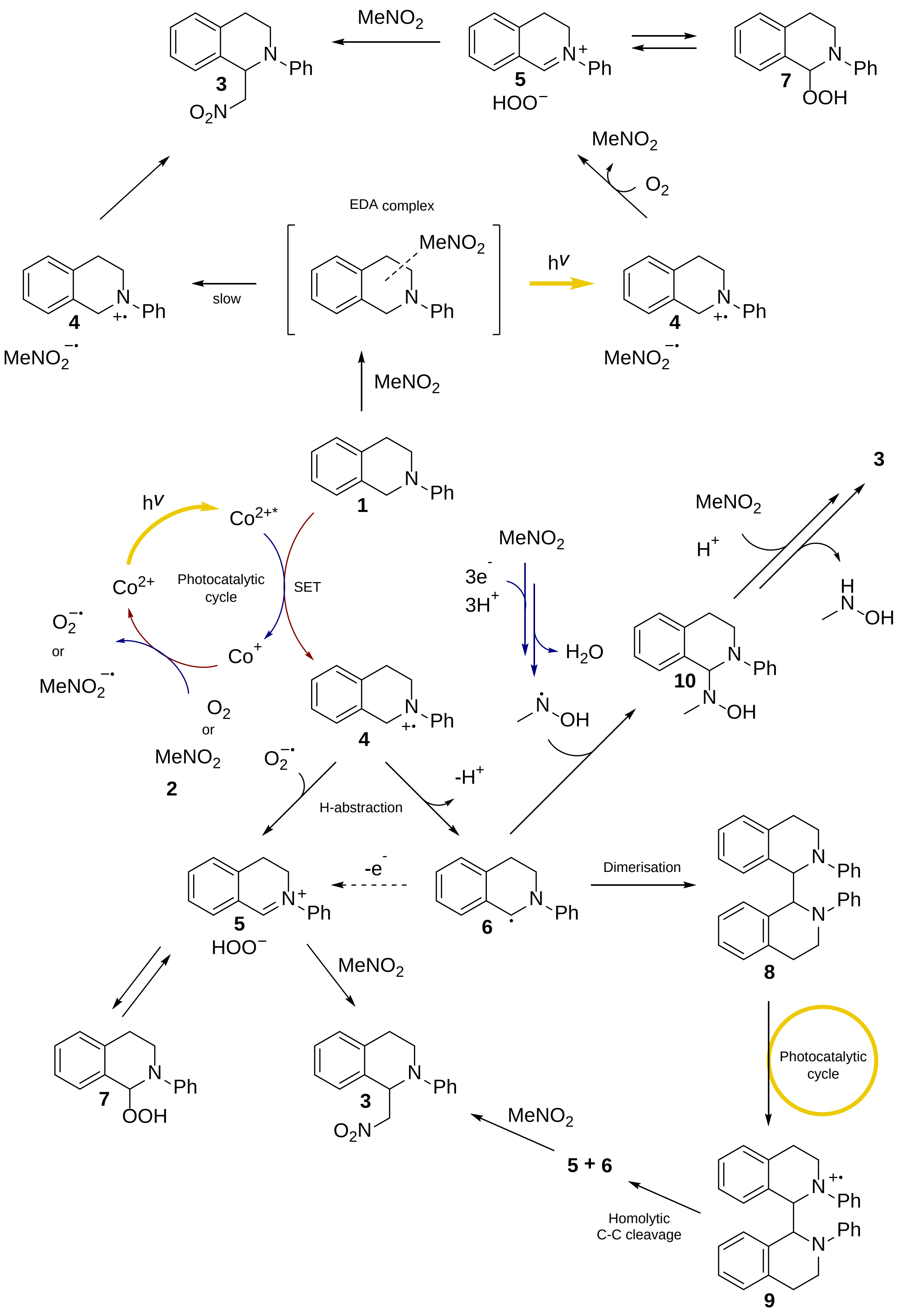

Scheme 15: Proposed mechanism for the aza-Henry reaction, in this example using Co^{2+} as the photocatalyst. Reduction steps shown in blue, oxidation in red and photoexcitation in yellow.

3.1.4 Potential Developments to Optimise MOFs towards Catalysis

One of the advantages of working with MOFs is the ease of modifying the framework, which is not simply limited to varying the metal node or altering the organic linker, but can also be achieved through subtle changes to the synthesis. This flexibility allows us to enhance aspects which could be of significance in a material's catalytic performance: crystallinity, mesoporosity, and particle size. Higher crystallinity tends to accompany higher stability, broadening the potential applications. A decrease in particle size could mean more accessible active sites for the reaction to occur. For example, the aza-Henry reaction with the Co-ZIFs would occur on the external surface, thus improved catalytic activity could in theory be achieved by decreasing particle sizes, or engineering a hierarchical framework. Either approach would decrease the cobalt within the bulk, inaccessible to the substrates, and would theoretically increase the number of available active sites the substrates can interact with. Another benefit would be that lower quantities of catalyst could be added, while still maintaining the same surface area for which a reaction can occur. Whilst both techniques are promising, increasing the porosity may be less beneficial as photoexcitation will more readily occur on the outer surface, thus increasing the external surface area is more likely to provide a notable effect on photocatalytic activity. Particle size has also been a recurrent theme in photocatalysis as it is believed to be commensurate with the mobility of charge carriers. For example, quantum dots exhibit interesting emissions and photocatalytic activity, as a result of their small particle sizes.

Although the modulation of particle sizes has been investigated with many different MOFs and achieved in numerous ways, there are limited reports of this type of study with Co-ZIFs. The order of solvating the reactants has been shown to influence particle sizes, with a reduction from 2000 nm to 300 nm being observed by SEM.[78] Dissolving the metal salt first allows time to establish a solvation shell before interacting with the organic linker. The number of nucleation points is thus believed to increase, forming a larger number of smaller particles when the ligand is added. Diluting the reaction mixture slows down the rate at which components and growing particles interact, allowing more nucleation points to occur, and again building a larger number of smaller particles. Khan et al. observed a reduction in particle sizes calculated by SEM from 800 nm down to 200 nm, simply by increasing the amount of water used in the synthesis.[79] On the other hand, increasing the concentration of the organic linker overloads the system but has the same overall effect.[80] Finally, a monodentate ligand, with similar properties to the organic linker, can be employed as a capping agent if it can bond with the metal node, or a modulating agent if it interacts favourably but is ultimately removed. Either additive would slow further growth of the particle as it behaves as a competitive inhibitor.[80] However, as the only method which introduces a different reactant into the mix, these capping agents could also alter the surface chemistry, which may present difficulties considering that the exact pathway by which the aza-Henry reaction occurs is unclear. One such example of how surface chemistry must be carefully considered is the nature of the exposed crystallite phase, as different atomic arrangements offered by different lattice planes of the same material can have great impacts on the catalytic outcome.[81] This phenomenon has been extensively observed with platinum nanoparticles. Bratlie et al. discovered that the hydrogenation of benzene produced different selectivity profiles depending on whether the substrates were exposed to the Pt(100) plane, or a combination of the (100) and (111) planes.[82] The different planes have been proposed to have contrasting affinities towards oxygen, and therefore affect how the substrates will later react.[83]

Discouraging the aggregation of particles would increase the number of available active sites. There are commonly accepted practices to achieve this such as increased dilution, reducing the likelihood of particles interacting with each other whilst forming, controlling particle growth by the use of capping agents for example, and increasing the reaction time. ZIF-8 is an excellent example of how the final case, increasing reaction time, can lead to improved properties. Short/Wide Angle X-ray Scattering (SAXS/WAXS) studies have given direct insight to the homogeneous nucleation and early growth events.[84] It was discovered that ZIF-8 is formed almost immediately with prenucleation clusters upon first addition of the ligand to the metal in solution, leading on to nanoparticle/nanocrystal growth, which suggests a complex crystallisation process. It is common practice to leave ZIF-8 stirring for 24 hours despite this initial interaction, which can be thought of as developing the thermodynamic morphology over kinetic crystal growth.

To analyse whether any of these modifications are successful, XRD can be employed to confirm phase purity and give an indication of crystallinity/particle size. This can later be confirmed by viewing the particles with SEM, and using BET to determine changes in surface area and porosity, before reviewing other characterisation techniques to observe what other effects may have occurred. This analysis in conjunction with catalysis results can be compared with the original samples to determine which methodology offers the most promise as a viable option in CDCs.

3.2 Aims and Objectives

Two Co-ZIFs will be trialled as photocatalysts in the aza-Henry reaction with a tetrahydroisoquinoline and nitromethane. Their response to different light sources will be probed, including a solar simulator to mimic more industrial methods for activation. In order to compare favourably with examples in the literature, the catalysts should achieve excellent yields within 6 hours, and be reusable through multiple cycles. Characterisation of the materials will be conducted to rationalise the displayed activity and identify areas requiring further investigation, this will include modifying the synthesis to exploit traits such as large surface areas.

To recommend a novel photocatalyst for further research in the sustainable formation of new bonds *via* a CDC, a wide range of characterisation and strong catalytic results are to be collected. It is expected that the challenging reduction of Co(II) proposed in the mechanism will be justified by studying their response to visible light with a combination of UV-Vis and XAS spectroscopy, as well as theoretical simulations, while further analysis such as TGA and BET will help build a profile for where the strengths lie for these Co-ZIFs.

3.3 Results and Discussion

3.3.1 Initial Findings

The first step was to build upon previous work which investigated MOFs in the aza-Henry reaction. As a guide to assess which were worth developing further, experiments with the key materials were repeated under differing conditions to confirm conversion to product. The results of these are shown in Table 2.

Table 2: Control experiments for the aza-Henry reaction under varying conditions.

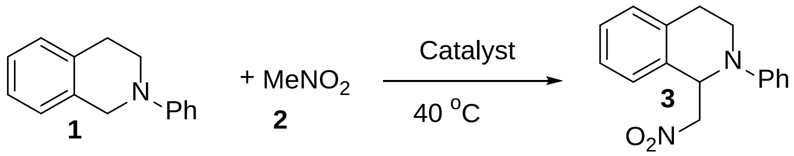

	Conversion / %			
	Dark	LEDs[a]	TBHP[b] (Dark)	TBHP (LEDs)[a,b]
Blank	*trace*	20	28	47
ZIF-9	17	88	64	100
$Co(OAc)_2.4H_2O$	12	22	100	100
$Co(NO_3)_2.6H_2O$	12	19	75	93
PhIm	*trace*	13	23	40

Reaction conditions: *N*-phenyl-tetrahydroisoquinoline (0.11 mmol) and catalyst (9 wt%) stirring in nitromethane (1 mL) for 6 h at 40 °C. [a] White LED illumination. [b] Addition of TBHP (0.15 mmol). Conversions determined by ^1H NMR of reaction mixture.

Apprehensive about the high background reaction using LEDs, this experiment was repeated multiple times with due caution. As discussed in 3.1.3 Mechanistic Insights, this effect has been observed before, with intense blue light recognised as facilitating an electron transfer between the two substrates.[34] The work of Wu et al.[25] also uses white LEDs and observes 9 % yield after 3 hours, and 0 % with no light at room temperature, correlating well with the observations here.

As expected from reviewing the literature, the cobalt salts perform well with TBHP.[10,25] However, under the ideal conditions of LEDs and atmospheric oxygen, they were no better than the blank and outperformed by the heterogeneous ZIF-9.

The components of ZIF-9 were tested with the reaction to observe what background effects may be occurring. Benzimidazole is comparable to the blank, no apparent photocatalytic effect, whilst with TBHP it even appears to hamper conversion. A combination of cobalt salts and benzimidazole were also tested multiple times, the results of which varied wildly. This was likely due to the small-scale of the reaction making it difficult to accurately study the ratio of the two components. When the yield was low, dark solids had formed, suggestive of an aggregate which is ineffective at catalysing the reaction. This is an effect often seen with homogeneous catalysts,[85] where the aggregate formed reduces the quantity of available active sites. Suggesting it is the specific way in which ZIF-9 is constructed, and the structure it adopts, that gives such high conversion.

3.3.2 Probing the Response to Different Wavelengths of Light

Following the success of ZIF-9, another cobalt ZIF was chosen to compare and evaluate. ZIF-67 shares the same Co^{2+} tetrahedra as ZIF-9 but with 2-methylimidazole linkers instead of benzimidazole. In order to examine the regions of light which promote photocatalytic activity with the two Co-ZIFs, specific wavelengths of light were used to study the reaction. In Table 3, these results are compared to the reaction in the dark, and with the white LEDs. Regardless of the specific wavelength employed, ZIF-9 still achieved between 10-21 % yields. As expected, blue light is the largest contributor to the background reaction with white LEDs. Yields using ZIF-67 remained low throughout, with the ZIF even appearing to hinder the background reaction under blue light and the white LEDs. This is likely to be a result of the loss of transparency when the catalyst is added to the reaction. The suspension of the catalyst lowers the amount of light reaching the substrates, therefore fewer electron transfers are induced between nitromethane and PhTHIQ, as described in the introduction. ZIF-9 displays activity even in the dark, as was noted with the cobalt salts tested in Table 2, but unlike the analogous ZIF-67. Thus even without a photoresponse, the ZIF-9 sample is already demonstrating the capability to perform the CDC, as it plays a role beyond the photocatalytic cycle. What would be interesting to discover is why the very similar structures of ZIF-9 and ZIF-67 do not both share this feature, what is it about the different linker that causes this activity?

Table 3: Control experiments for the aza-Henry reaction under different wavelengths of light.

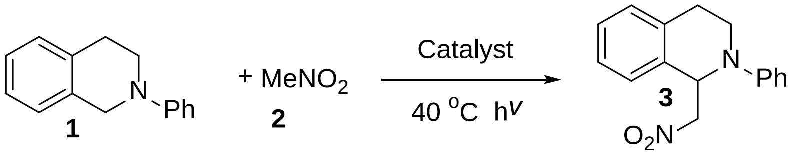

Wavelength / nm	Catalyst	Conversion / %	Yield / %	Mass Balance / %
Dark	Blank	0	*trace*	100
	ZIF-9	16	17	101
	ZIF-67	0	*trace*	101
White LEDs	Blank	20	20	100
	ZIF-9	89	84	95
	ZIF-67	13	13	10
450 (Blue) [a]	Blank	18	18	100
	ZIF-9	21	21	100
	ZIF-67	4	5	101
515 (Green) [a]	Blank	*trace*	*trace*	101
	ZIF-9	19	16	97
	ZIF-67	*trace*	*trace*	101
589 (Orange) [b]	Blank	5	0	95
	ZIF-9	20	19	98
	ZIF-67	8	5	97
630 (Red) [a]	Blank	0	*trace*	101
	ZIF-9	15	10	95
	ZIF-67	0	*trace*	101

Reaction conditions: *N*-phenyl-tetrahydroisoquinoline (0.11 mmol) and catalyst (9 wt%) stirring in nitromethane (1 mL) for 6 h at 40 °C under [a] LED, or [b] Na lamp illumination. Conversion/yield determined by ^{1}H NMR of reaction mixture using mesitylene as an internal standard.

Considering the great similarities between the two Co-ZIFs, it is surprising how significant the difference in activity is under white LEDs. As such, both Co-ZIFs were tested with the more sophisticated solar simulator. A glass filter was used to block wavelengths of light below 515 nm being emitted by the solar simulator, this was to prevent Co-ZIF catalytic activity being masked by a high background reaction. Figure 16 shows the results of these experiments, other than the light source the conditions were kept the same, with the distance from the solar simulator being tuned so as to achieve the same ambient temperature of 40 ^{o}C observed under the LEDs.

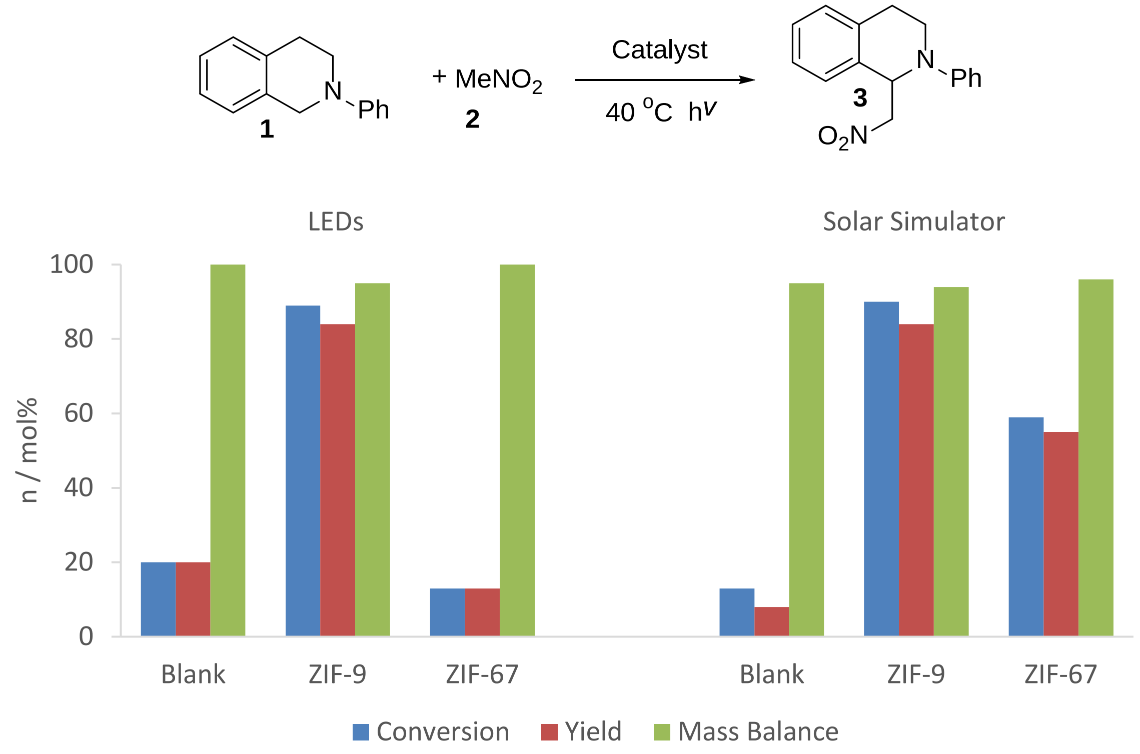

Figure 16: Photocatalytic activity of Co-ZIFs for the aza-Henry reaction, calculated by ^{1}H NMR with an internal standard.

ZIF-9 still achieves its high yield of 84 %, with the potential to go further as full conversion has not yet been reached. The yield when using ZIF-67 has improved over 40 % with the solar simulator. Evidently, there is a wavelength of light missing from the white LEDs which ZIF-67 capitalises on. A gap in the blue light region from the LEDs can be clearly seen in the emission spectra displayed in Figure 17 for both light sources. However, with the overlain d-d ligand field transitions from the UV-Vis spectra of both Co-ZIFs, it appears the gap is near to, but not encompassing, this significant range of absorbance. The full UV-Vis spectra is displayed later in Figure 19, page 53. These results highlight the importance of tuning the wavelength of light used during photocatalysis.

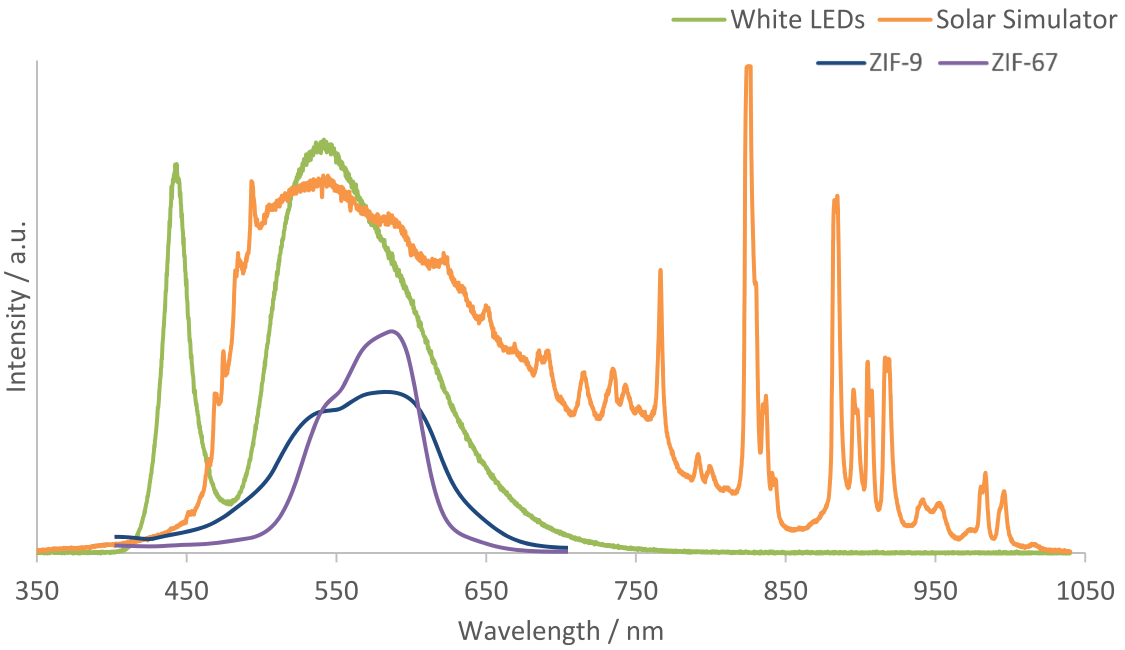

Figure 17: Emission spectra for the light sources, overlain with the UV-Vis spectra for the Co-ZIFs.

Plotted in Figure 18 are the conversions and yields over the course of the reaction, when these reached over 20 % after 6 hours, hourly samples were collected. Full conversion is achieved in both plots for ZIF-9, with increased yields of 91 % under both the LEDs and the solar simulator. This is attributed to the closed vial holding approximately 0.2 mmol of oxygen inside, with 0.11 mmol of substrate present. Thus opening the vial and disturbing the system to take a sample replaces the spent oxygen, preventing the retardation of product formation, which reveals a linear rate for the LEDs. The same effect is seen with ZIF-67, which went on to achieve full conversion after 10 hours with a 99 % yield.

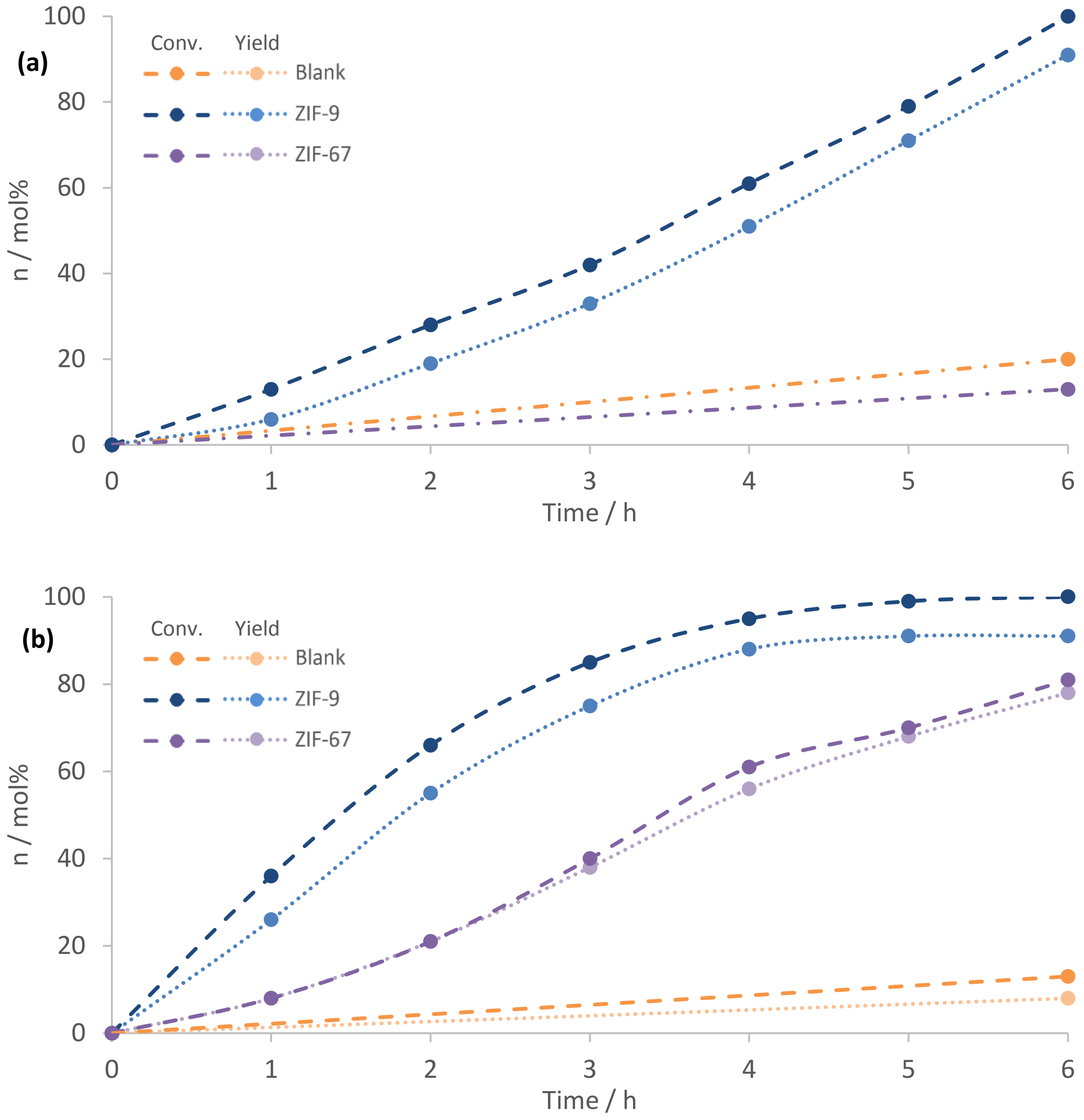

Figure 18: Rate plots showing the conversion and yield in the aza-Henry reaction using Co-ZIFs under (a) white LEDs, (b) solar simulator with 515 nm filter.

In order to study the trends seen in Figure 18 further, argon was used to saturate the system prior to reaction, the results of which are shown in Table 4. A yield of 23 % could still be achieved, demonstrating how nitromethane can also act as an oxidant, as detailed earlier with the reaction mechanism. An additional test with the LEDs was to check whether the increased temperature of 40 ^{o}C was significant in the performance of the catalyst. Although a high yield was still observed at room temperature, the yield and mass balance are slightly reduced. Cobalt formate is a by-product formed during the ZIF-9 synthesis and removed through centrifugation. XRD is used to determine the relative purity of the final product by observing the disappearance of the cobalt formate peaks. To ensure that if the impurity remained, it was not responsible for the increased activity of ZIF-9, the isolated cobalt formate was also tested in the CDC reaction. A yield of 41 % was comfortably lower than the values achieved for ZIF-9.

Table 4: Control experiments for the aza-Henry reaction with ZIF-9, under varying conditions.

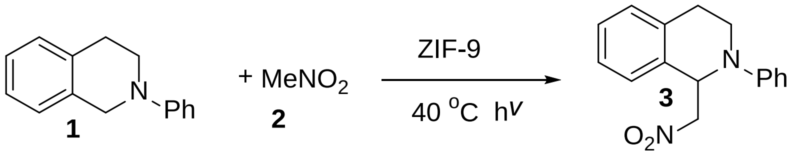

Entry	Catalyst	Conversion / %	Yield / %	Mass Balance / %
1	Blank	20	20	100
2	ZIF-9	89	84	95
3[a]	ZIF-9	88	78	90
4[b]	ZIF-9	28	23	95
5	Cobalt formate	51	41	90

Reaction conditions: *N*-phenyl-tetrahydroisoquinoline (0.11 mmol) and catalyst (9 wt%) stirring in nitromethane (1 mL) for 6 h at 40 °C under white LED illumination. Conversion/yield determined by ^{1}H NMR of reaction mixture using mesitylene as an internal standard. [a] Reaction left running at r.t., [b] Mixture bubbled through with argon for 15 minutes prior to stirring under light.

3.3.3 Rationalising Co-ZIF Activity

To understand the demonstrated activity further, characterisation for the two Co-ZIFs were compared. UV-Vis spectra are shown in Figure 19 and exhibit three absorption features, the first is a broad absorption in the UV region (<350 nm) which can be assigned to the LMCT. The second feature relates to the higher-lying [$^4A_2(F)$–$^4T_2(P)$]. The peak positions in this visible band, with maxima at 540, 570 and 590 nm, do not appear to vary between the two Co-ZIFs. Beginning to show in the near-IR region is the third feature, attributed to the lower-lying [$^4A_2(F)$–$^4T_1(F)$]. Both the second and third features are well known d-d ligand field transitions for tetrahedral Co^{2+}.[86,87] The intensity is a result of the metal-ligand interactions present in Co-ZIFs and other MOF materials, aided by the electron-rich nature of the ligands, which make them attractive as photocatalysts.

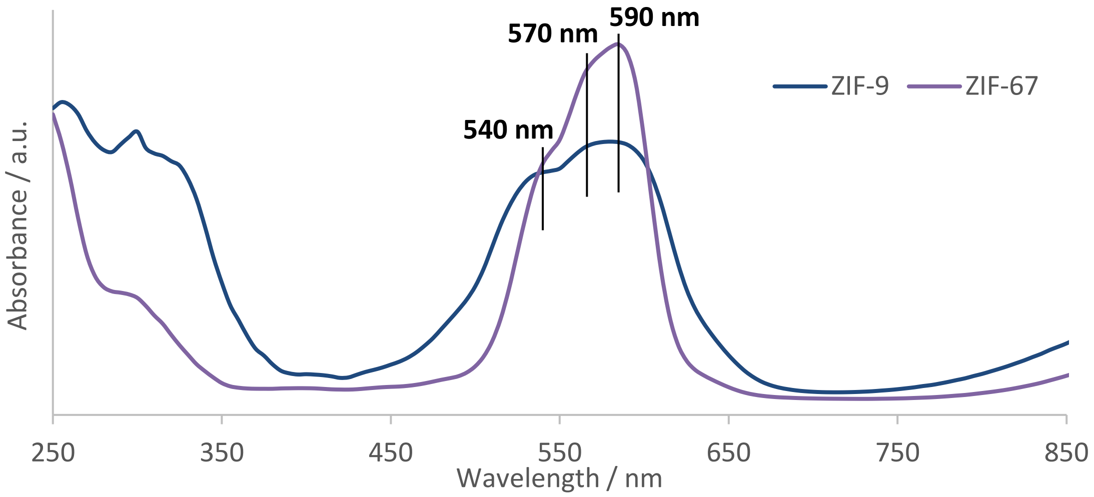

Figure 19: (DR) UV-Vis of the Co-ZIFs.

Framework integrity of the two Co-ZIFs was probed with XRD, BET, TGA and SEM. Figure 20 compares the XRD of the Co-ZIFs with their simulated data. While both materials were phase pure and form sodalite frameworks, the patterns differ markedly as a result of the additional electrons found in the system for ZIF-9, originating from the extra aromatic ring of the linker.

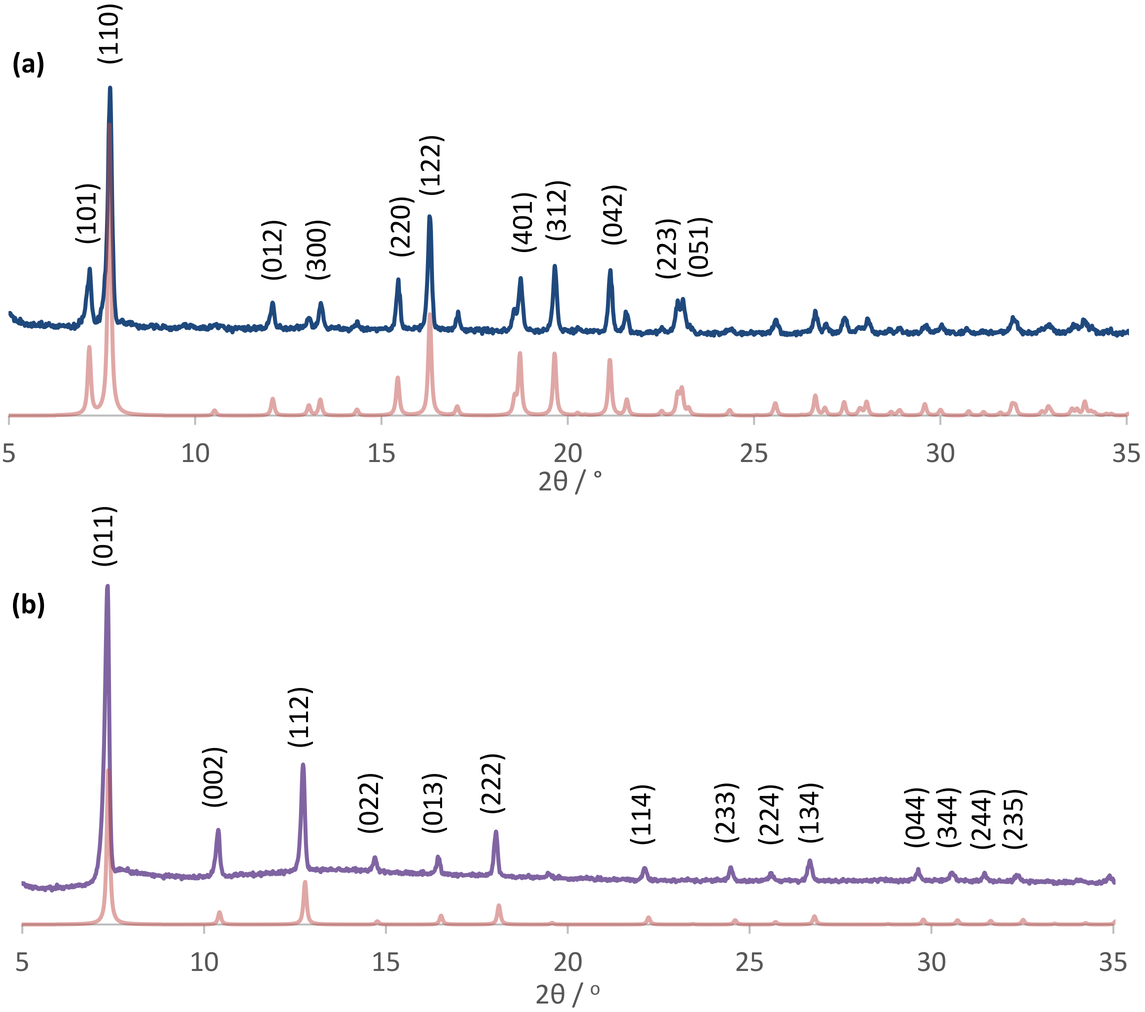

Figure 20: pXRD of (a) ZIF-9 and (b) ZIF-67, with their respective simulated pattern.

The crystal structure was determined by Rietveld analysis, the lattice parameters and unit cell volume displayed in Table 5 compare well to the literature.[51,88] Crystallite sizes are similar between the two ZIFs, although ZIF-67 is slightly smaller, characteristic of the nanoparticle procedure that was followed.

Table 5: Crystal structure analysis for Co-ZIFs.

	Crystal System	Lattice Parameters / Å	Unit Cell Volume / Å^3	Crystallite Size / Å
ZIF-9	Hexagonal	a = 22.935(17) b = 22.926(14) c = 15.783(10)	7198(8)	528(10)
ZIF-67	Cubic	a = b = c = 17.067(3)	4971.0(18)	480(15)

Analysis for the surface area of the two ZIFs gave vastly different results. In Figure 21, ZIF-9 displays a Type III isotherm, with only weak adsorbate-adsorbent interactions rather than any significant porosity. Whereas ZIF-67 adopts a Type I isotherm, typical for microporous materials. As a microporous material, and as MOFs are generally regarded, ZIF-9 should display high surface area like that of ZIF-67 at 1303 m^{2}g^{-1}. Yet this is not a unique observation, with ZIF-9 previously reporting a surface area of 4 m^{2}g^{-1}, as it did here, under the same synthetic procedure.[89]

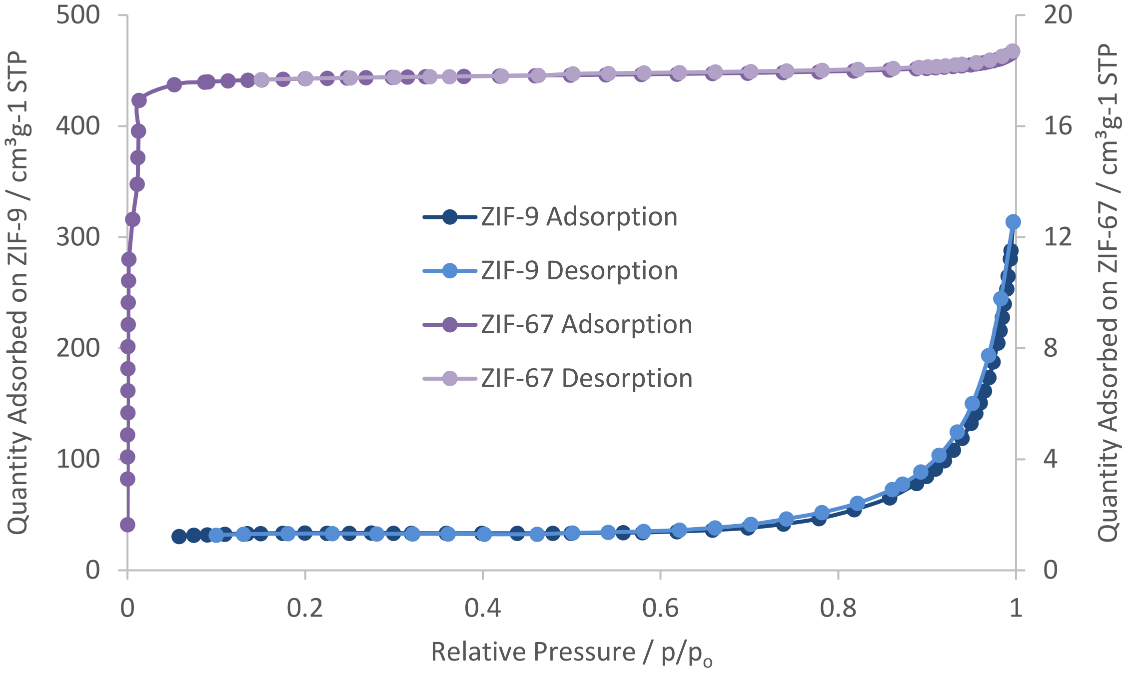

Figure 21: Nitrogen adsorption-desorption isotherm for ZIF-9 and ZIF-67.

The reason for ZIF-9's low surface area is believed to be that despite drying the solid at 120 °C under vacuum, the bulky benzimidazole linkers continue to trap the strongly physisorbed DMF molecules within the pores. Nonetheless, it does not appear to affect the activity as it is understood the reaction occurs on the surface, thus strengthening the argument to investigate materials/methods that maximise the outer surface area. IR spectroscopy was used to help confirm whether DMF remained with the sample.

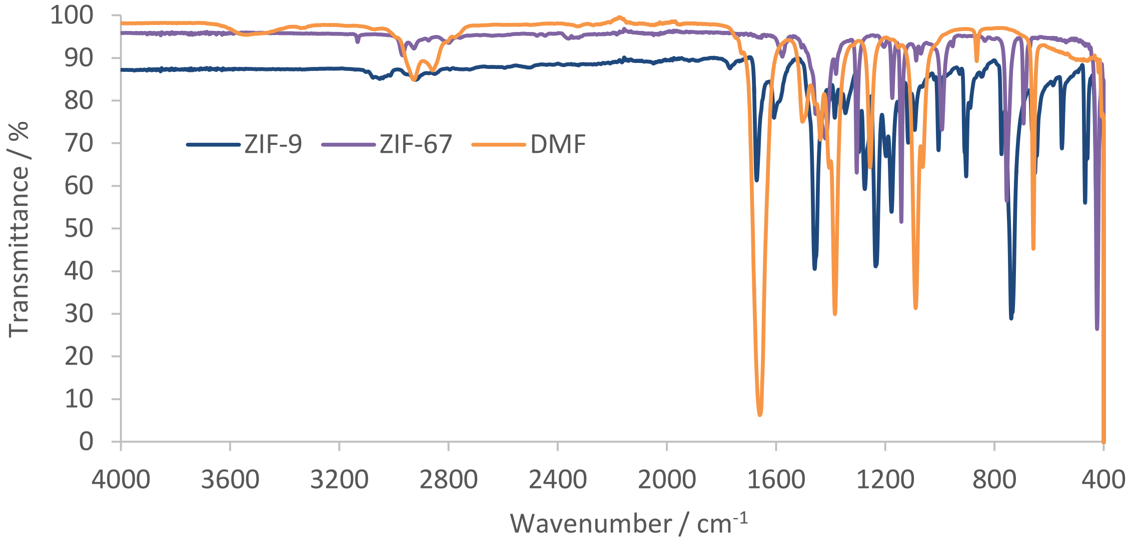

Figure 22: IR spectra for the Co-ZIFs and DMF.

The IR spectra in Figure 22 are consistent with those reported in the literature.[67,89] A distinct lack of a broad absorption peak around 2600-2800 cm^{-1}, which would usually indicate an N-H bond, suggests that the imidazole has been deprotonated in order to form the framework. Since these MOFs consist of cobalt nodes with imidazolate linkers, the bands observed in the IR spectrum are primarily attributed to the ligand. However, trapped DMF is indicated by the presence of a clear carbonyl moiety in the ZIF-9 spectrum, at roughly 1660 cm^{-1}. TGA was used to analyse the quantity of trapped DMF, as well as elemental composition of the framework, by observing drops in mass which could be associated with the loss of solvent or ligand.

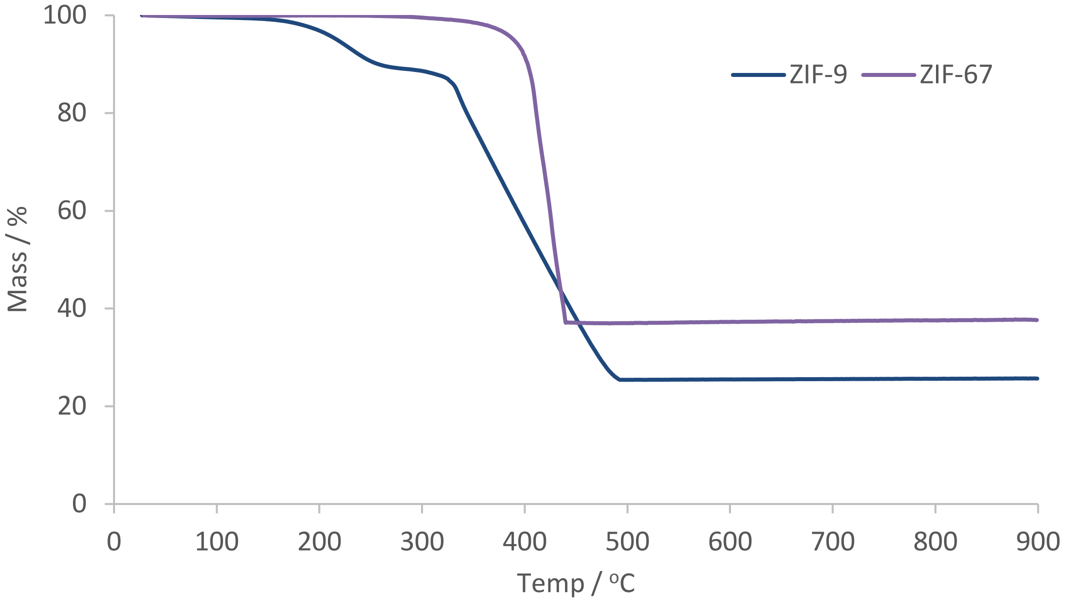

Figure 23: TGA curves of the Co-ZIFs.

In Figure 23, two weight loss steps are observed for ZIF-9, the first of 11.1 % was attributed to the loss of DMF. The second weight loss of 63.2 % between 300-500 °C, is the breakdown of the framework and decomposition of organic components, leading to the formation of cobalt oxide. ZIF-9 is typically stable to near 600 °C,[59,60,89] a lower value and more gentle slope could suggest lower and varied levels of crystallinity. The TGA has also indicated heating the sample to 200 °C under vacuum would remove the remaining DMF. Although the pore apertures are too small (3.0 Å) to admit the THIQ substrate investigated during this project, thus it is unlikely removing the DMF would affect activity. In contrast, ZIF-67 does not appear to host any guest molecules. The plateau observed with both Co-ZIFs before eventual breakdown demonstrate stability without guest molecules. The ZIF-67 sample used during this work was stable to 400 °C, much higher than most MOF materials.[90] Typically with ZIF-67, a slight drop in mass is seen at 200 °C, followed by the decomposition of the framework anywhere from 300-550 °C.[88,98,100] The paper reporting the procedure followed for this sample showed a more gradual slope, with breakdown beginning between 400-450 °C.[91] Table 6 shows how the TGA agrees with the proposed molecular formulas [Co(PhIm)$_2$] and [Co(2-MIm)$_2$], and compliments the ICP analysis. The calculations for these values are included in Appendix A.

Table 6: Composition of Co-ZIF samples as determined by TGA and ICP.

	ZIF-9				ZIF-67		
	Theoretical Mass / %	Calculated Mass / %		ICP Analysis / %	Theoretical Mass / %	Calculated Mass / %	ICP Analysis / %
		No DMF	With DMF				
Cobalt	20.1	20.5	18.2	18.6	26.7	26.7	26.2
Linker	79.9	79.7	-	-	73.3	73.3	-

Although the literature tends to refrain from defining ZIF-9's morphology, consistent crystalline particles are generally achieved.[60,89] The SEM results reveal an average particle size for ZIF-9 of 4.3 µm, much larger than the crystallite size calculated from the XRD of 53 nm. The particles for ZIF-9 appeared crystalline, but with little definition in its morphology. However, there were some crystals, such as the one displayed in Figure 24a, which compare well to the polyhedral formed for the isomorphous ZIF-7 (zinc nodes with benzimidazole linkers).[58,92] Figure 24b on the other hand shows consistent truncated rhombic dodecahedral particles, as expected from ZIF-67 and the isomorphous ZIF-8. The average particle size was 315 nm, much smaller than ZIF-9, and larger than the crystallite size reported earlier at 48 nm. The differences between the two Co-ZIFs could be a result of the time spent during synthesis; ZIF-9 is prepared at 130 °C for 48 hours, compared to 6 hours at room temperature for ZIF-67. The much longer crystal growth time for ZIF-9 promotes larger crystals, and more random arrangements. The SEM results suggest particle size is less significant to catalytic activity than the composition of the framework, as ZIF-67 still performs comparably with ZIF-9 under the solar simulator. This may change upon altering the scale of the reaction, the reaction may not require all of the 9 wt% of catalyst used.

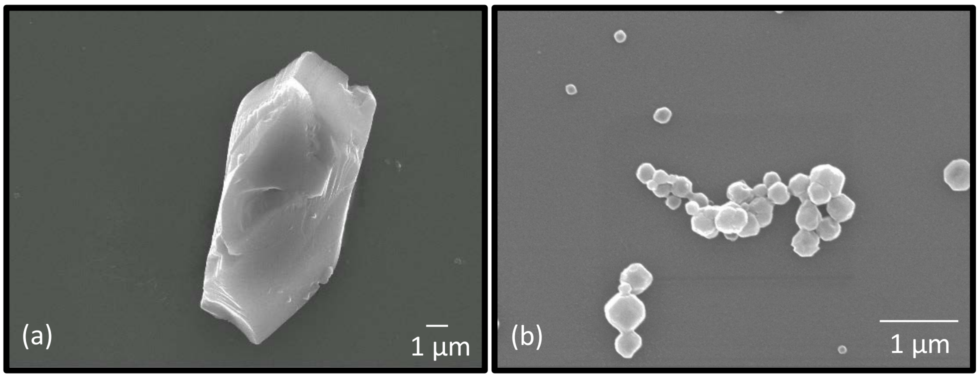

Figure 24: SEM images of (a) ZIF-9, (b) ZIF-67.

The highly crystalline nature of zeolites contributes to their high chemical and thermal stability. The SEM and XRD results for ZIF-9 indicate a crystalline material, but the wider SEM view does not display consistent particles. This is in agreement with the TGA, the more gradual degradation of the framework beginning at a lower temperature was indicative of lower crystallinity.

3.3.4 X-Ray Absorption Spectroscopy

To explore the photocatalytic response of the Co-ZIFs in more detail, *in situ* XAS data was collected before and after illumination from the solar simulator. Although within error, when under illumination, changes do occur in the XANES region displayed in Figure 25. Due to the similarities between the "dark" and "hv" spectra, they appear super-imposed on this scale. The difference spectra are calculated by subtracting the "dark" spectra from the "hv", they have been exaggerated to effectively observe the changes.

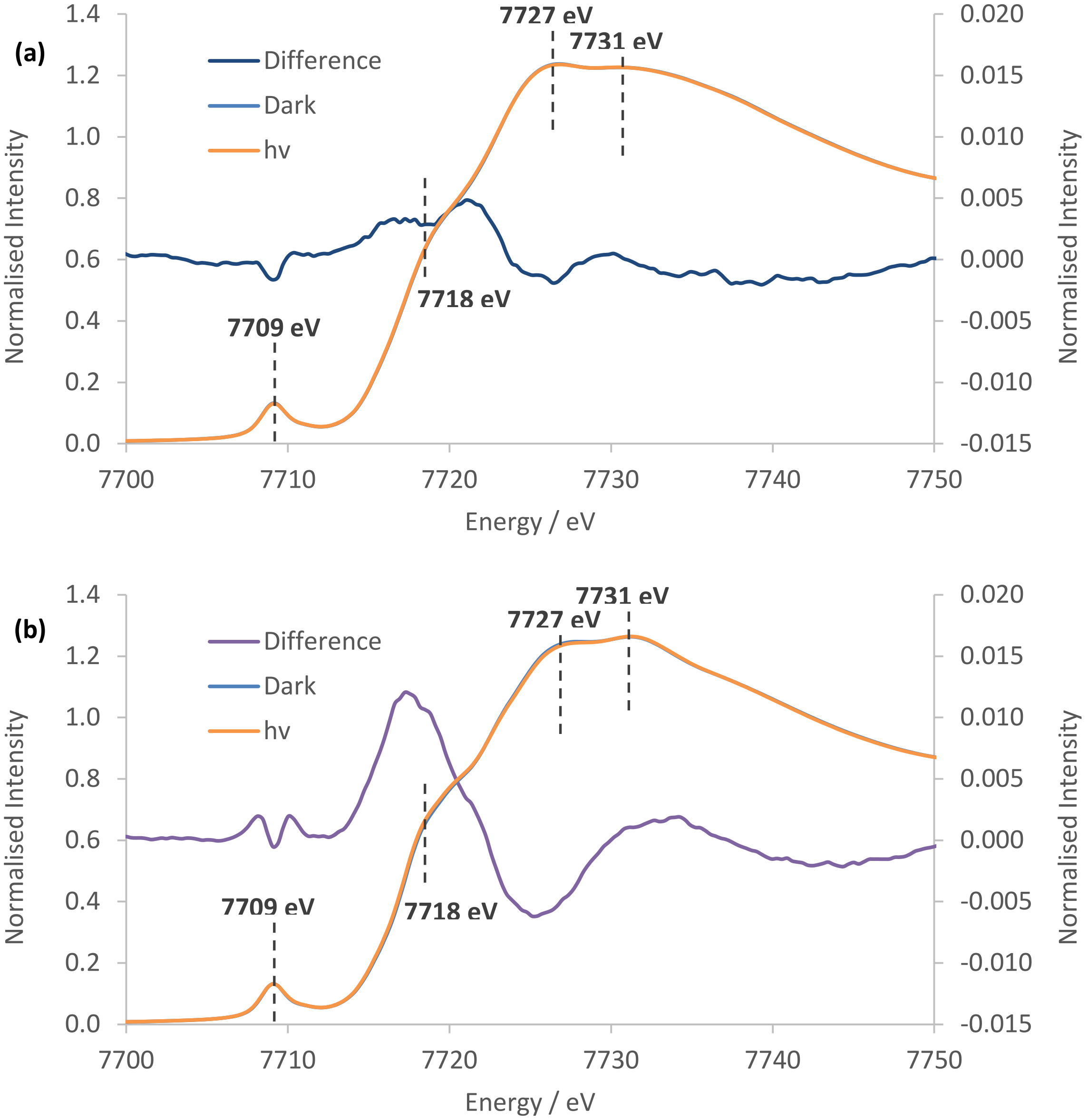

Figure 25: Normalised XANES data, highlighting the difference in the cobalt environment under both "dark" and "hv" conditions for (a) ZIF-9 and (b) ZIF-67.

Density of States (DoS) theoretical simulations, combined with published literature, confirms the origin of the four features seen in both ZIF-9 and ZIF-67 XANES region. The initial pre-edge feature at 7709 eV is due to a Co(1s) -> Co(3d) transition with tetrahedral symmetry, as seen by the significant Co(d) contribution in Figure 26.[93–95]

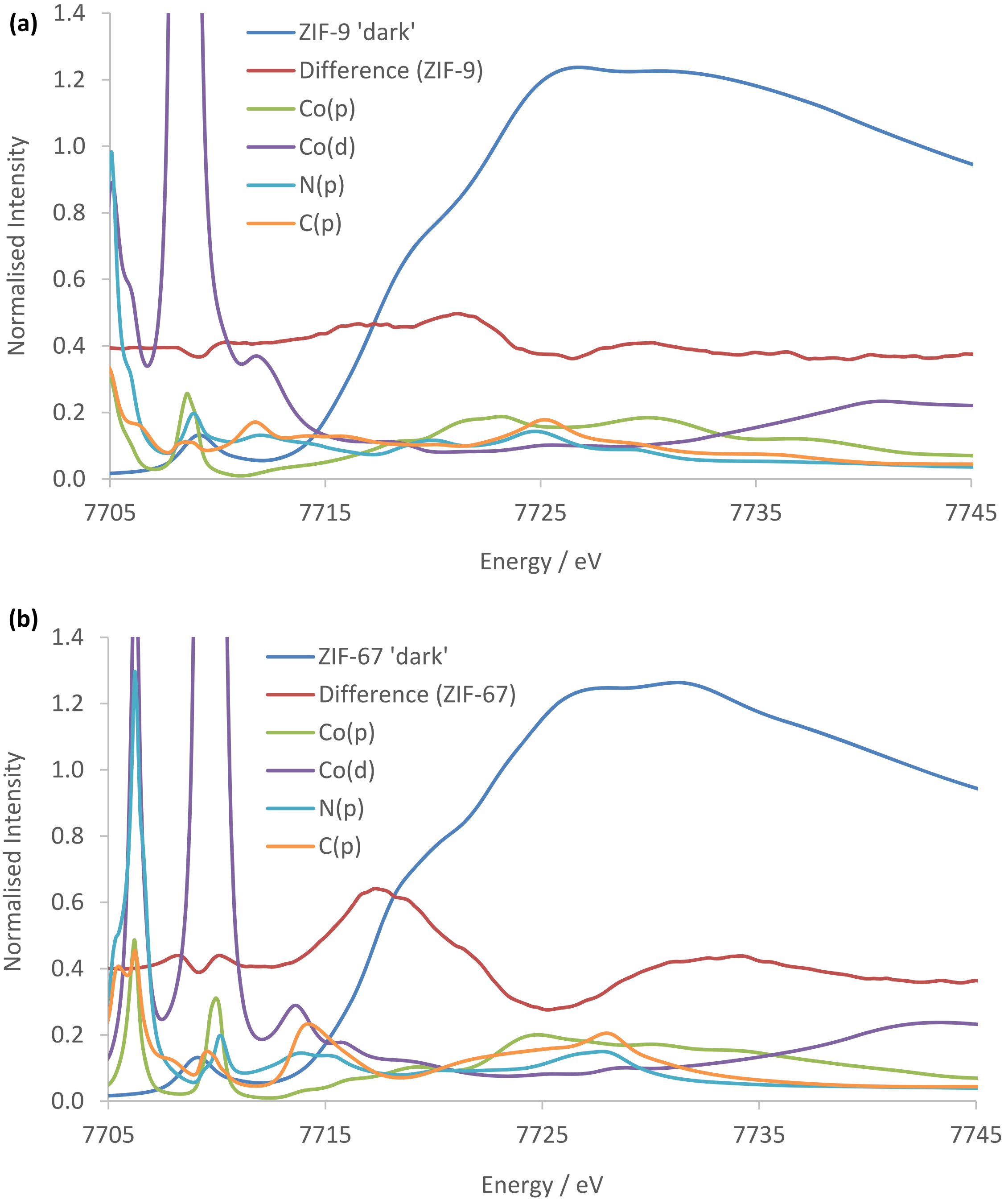

Figure 26: DoS simulation results from the crystallographic structures for (a) ZIF-9 and (b) ZIF-67. The contributions for each orbital set are displayed, the difference spectra are scaled by a factor of 20, and incremented by 0.4 for ease of observation.

The pre-edge is attributed to the Co(1s)→Co(4p) continuum with electron shakedown (7718 eV), terminating at 7727 eV, as Co(p) character occurs in this region. The features at 7727 and 7731 eV are shown to have some C(p), N(p) and Co(p) character, thus the nature of the surrounding ligands influences these features. Subtracting the "dark" from the "hv" spectra allowed for a more critical consideration of the influence of the light source, the difference spectra are overlain in Figure 27.

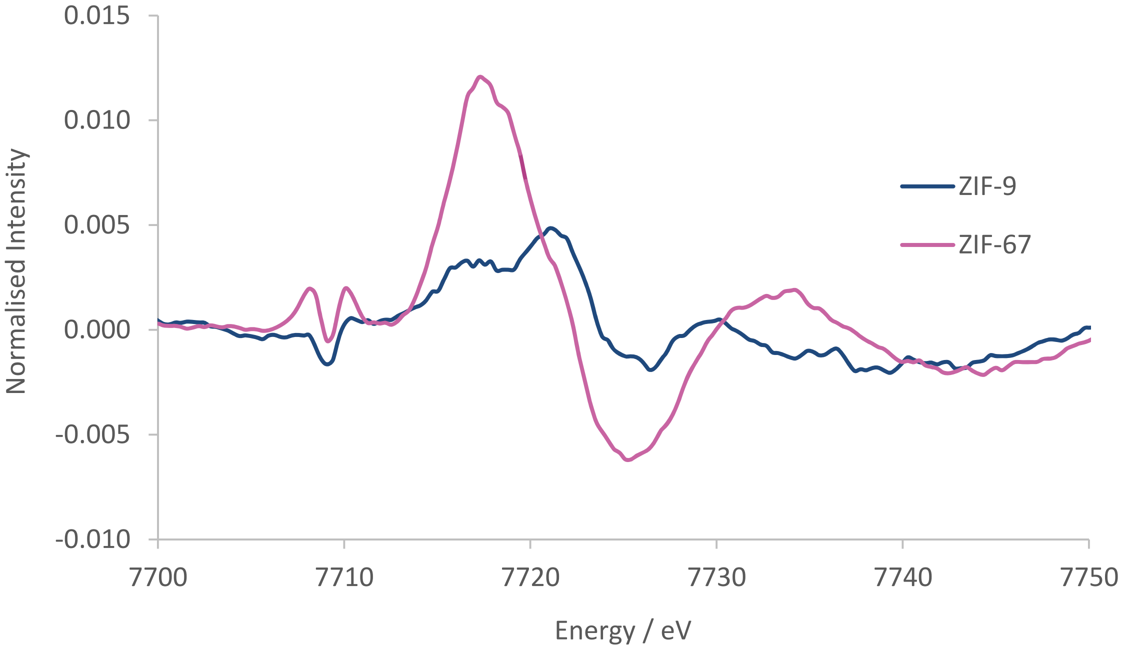

Figure 27: Difference spectra observed in the XAS of ZIF-9 and ZIF-67.

Under "hv" conditions the pre-edge of ZIF-67 shifts to a lower energy value, indicative of an increase in electron density, and partial reduction of Co(II), with electrons logically originating from the methyl-imidazole linker *via* a ligand-to-metal charge transfer (LMCT).[69] This is in agreement with the DoS findings in Figure 26, as the maxima of the difference spectra coincides with the Co(p) system, suggesting increased electron density in these orbitals. A minima coincides with the N(p), suggesting decreased electron density in these orbitals. Although this has previously been linked to an elongation of the Co-N bonds, it was not seen in the EXAFS model. Displayed in Table 7 are the modelling results for the cobalt in both ZIFs occupying a tetrahedral environment, with a first coordination sphere of four nitrogen atoms, which the EXAFS data revealed as a distance of 2.00 (± 0.01) Å from both the "dark" and "hv" spectra.

Table 7: IFEFFIT modelling results for ZIF-9 and ZIF-67.

ZIF-9 Dark

Abs Sc	N	R / Å	$2\sigma^2$ / Å^2	E_f / eV	R_{Factor}
Co-N	4	2.00(1)	0.005(1)	4.18(77)	0.023
Co-C1	4	2.98(3)	0.009(8)		
Co-C2	3	3.04(14)	0.036(46)		

ZIF-9 hv

Abs Sc	N	R / Å	$2\sigma^2$ / Å^2	E_f / eV	R_{Factor}
Co-N	4	2.00(1)	0.005(1)	4.16(73)	0.024
Co-C1	4	2.99(3)	0.010(8)		
Co-C2	3	3.03(17)	0.040(53)		

ZIF-67 Dark

Abs Sc	N	R / Å	$2\sigma^2$ / Å^2	E_f / eV	R_{Factor}
Co-N	4	2.00(1)	0.005(1)	4.50(89)	0.030
Co-C	8	3.00(2)	0.013(4)		
Co-C-N	16	3.12(10)	0.070(42)		

ZIF-67 hv

Abs Sc	N	R / Å	$2\sigma^2$ / Å^2	E_f / eV	R_{Factor}
Co-N	4	2.00(1)	0.006(1)	4.36(86)	0.028
Co-C	8	3.00(2)	0.015(5)		
Co-C-N	16	3.12(10)	0.075(44)		

Fitting parameters: $S_0^2 = 0.77$, as deduced by Co(0) foil. Fit range: $2.6 < k < 12.0$, $1.0 < R < 2.8$, number of independent points: 10.6. Fitted in k^1, k^2 and k^3 spaces simultaneously.

The EXAFS data and models for both Co-ZIFs, including Figure 28 and the figures in Appendix A, are in excellent agreement with the crystallographic data and previous XAS work on these species.[69,93,94] All changes in the EXAFS region were within the errors generated. As with the XANES region, due to the similarities clearly displayed in Figure 28, the “dark” and “hv” appear superimposed on the scale employed.

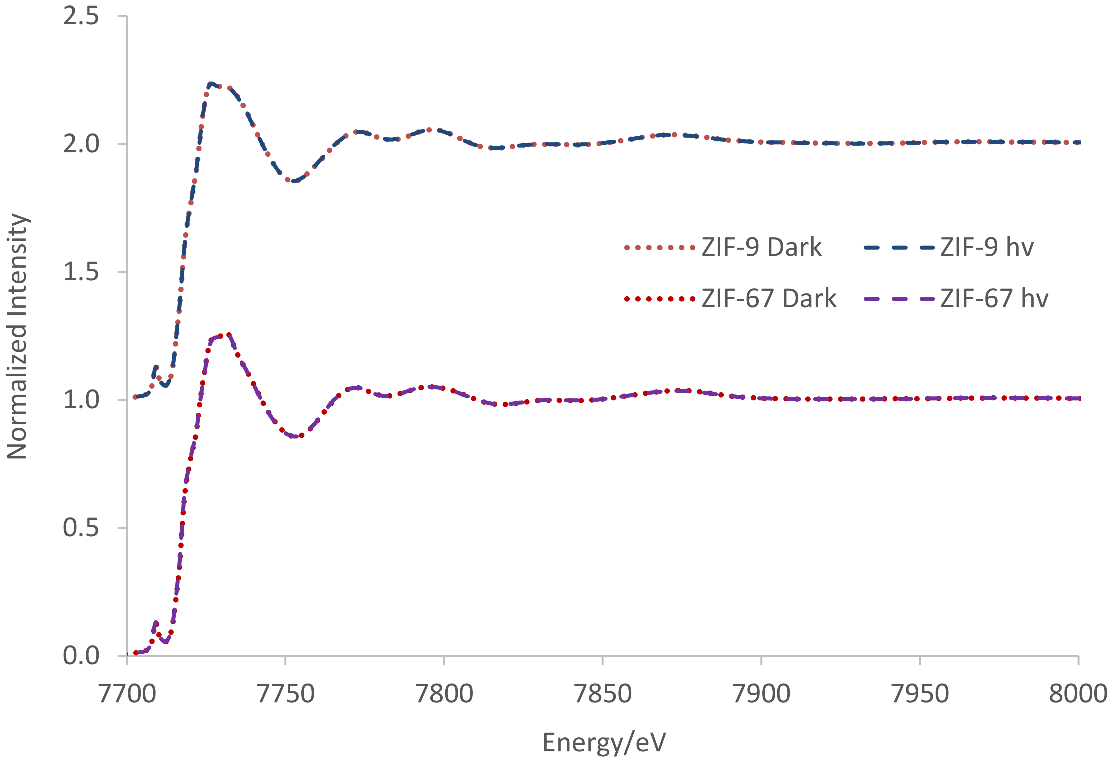

Figure 28: Normalised EXAFS spectra for ZIF-9 and ZIF-67. Both ZIF-9 spectra have been increased by an intensity of 1.0 for ease of comparison.

ZIF-9 does not show as significant a change in the pre-edge energy (Figure 27), thus retains the Co^{2+} character on exposure to the light source, suggesting the LMCT does not occur to the same extent. In contrast, ZIF-67 sustains a more significant change on exposure to light in the XANES region. This is likely due to the extended resonance structure of the aromatic ring of benzimidazole, and the bulkier framework, limiting the motion of the electrons and atoms. However, the positive inductive effect of the methyl group in ZIF-67 has a greater capacity for pushing electrons onto the cobalt atom upon photocatalytic excitation, leading to a greater shift in the XANES.

The photocatalytic tests revealed the choice of photocatalyst has a strong influence on the reaction efficacy. The pivotal step of the proposed mechanism is likely part of the photocatalytic cycle of the cobalt species (Scheme 16), the full mechanism is displayed in Scheme 15 (3.1.3 Mechanistic Insights).

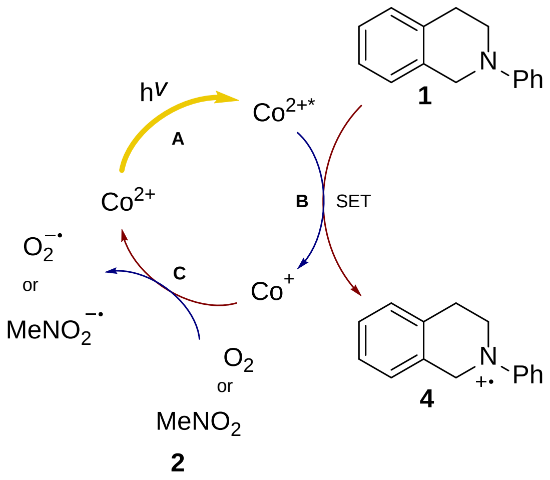

Scheme 16: The proposed photocatalytic cycle for the Co-ZIFs in the aza-Henry reaction.

The cobalt is primarily implicated in three reaction steps: (A) The photocatalytic excitation of Co(II) into a higher energy Co(II)* state; (B) The single electron transfer of Co(II)* to Co(I), generating an amine cationic radical from PhTHIQ in the process; and (C) the oxidation of Co(I) to Co(II) by either oxygen or nitromethane to close the photocatalytic cycle. Though the transition between Co(II) and Co(III) is more common, the photocatalytic reduction of Co(II) to the much less stable Co(I) has been reported. The work of Pattengale et al. used their XAS analysis for ZIF-67 to propose the edge of the Co centre shifting to a lower energy indicates the reduction of the Co centre following photoexcitation.[69] Lazarides et al. detailed a series of photochemical steps using Eosin Y as a photosensitiser with a homogeneous Co-complex.[77] They proposed that hydrogen production occurred through protonation of a Co(I) species to give a Co(III) hydride, which in turn reacts further by reduction and protolysis to give Co(II) and molecular hydrogen.

The XANES analysis suggested that, when excited photochemically, an LMCT occurs, more noticeably in ZIF-67 (Figure 27), increasing the electron density of cobalt and prompting worse photochemical reactivity compared to ZIF-9. It is unlikely that the reduction (C) is rate limiting, as an LMCT would make the transition to divalent cobalt less energy intensive. However, increased electron density and lowering the charge on the Co will weaken interaction with other electrons, hindering the already challenging reduction to Co(I), justifying the slower performance of ZIF-67 over ZIF-9. UV/Vis spectroscopy provided an insight into step (A), where a greater range of visible light wavelengths that ZIF-9 can absorb, relative to ZIF-67, offers more opportunities to form the excited state. However, the broadening of ZIF-9 was only minor, and is unlikely to have a drastic influence on the catalysis when employing the solar simulator. As step (B) is likely the rate determining step in this cycle, it should be the main consideration for intelligent design of future visible light heterogeneous catalysts for this reaction.

Through a combination of UV/Vis and XAS spectroscopy, and theoretical simulations, the range of light adsorbed to activate the cobalt site, and the Co(II)* to Co(I) SET has been shown to play a pivotal role in this reaction. This can be controlled and enhanced through astute selection of the imidazole linker, with benzimidazole (ZIF-9) preventing the LMCT to the same extent as seen with 2-methylimidazole (ZIF-67), resulting in ZIF-9 being a superior photocatalyst in the aza-Henry reaction. This finding opens up possibilities for a wider range of functionalized imidazole linkers to be experimentally, and computationally, screened for this reaction, towards developing an optimised photocatalytic species.

3.3.5 Removal of Residual DMF from ZIF-9

To help determine whether the presence of guest molecules within the ZIF-9 pore was detrimental to catalytic activity, attempts were made to remove the DMF to test the ZIF-9 framework alone. In order to remove the trapped solvent from within the ZIF-9 pores, a sample was heated to 200 ^{o}C under vacuum for 4 hours. The resulting material was characterised to determine whether the DMF had been fully removed whilst keeping the framework intact. The TGA trace in Figure 23 displayed a plateau after loss of DMF, suggesting the framework would be stable without the presence of any guest molecules. Figure 29 reveals the pXRD pattern after drying under vacuum, showing that the material has undergone a significant change. New peaks can be observed at 8 and 9 ^{o}, whilst the peaks that have remained are much weaker. This spectrum can be attributed to ZIF-9-II, a narrow pore phase transition previously reported with the isomorphous ZIF-7. Upon the loss of guest molecules from the as-synthesised ZIF-9-I, the framework shifts in a gate opening/closing manner, as illustrated in Figure 14 (3.1.2.2 Zeolitic-Imidazolate Frameworks (ZIFs)).[63,96] The flexible nature of ZIFs results in a structural transformation from large to narrow pores. It was further supported by the BET, TGA and IR results, which show that despite loss of DMF, the surface area and deemed porosity does not increase dramatically as seen with other ZIFs such as ZIF-67.

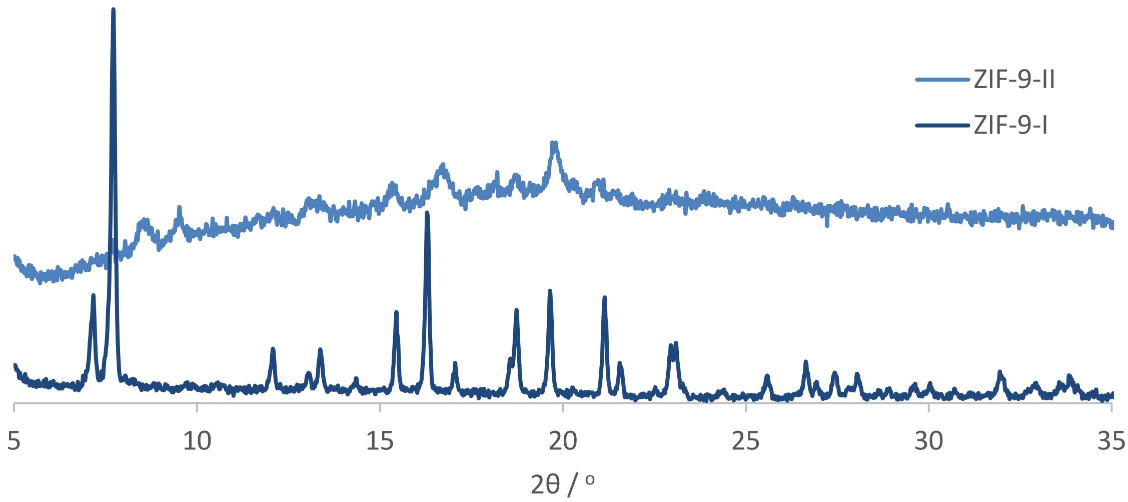

Figure 29: pXRD pattern of ZIF-9 before and after attempting to remove residual DMF.

In Figure 30, ZIF-9-II also reveals a Type III isotherm, indicative of weak adsorbate-adsorbent interactions, as with ZIF-9-I. The surface area of 2 m^2g^{-1} was lower than the as-synthesised ZIF-9. Thus even with the removal of trapped solvent molecules, the material is still not displaying any significant porosity, as a result of the constricted pores.

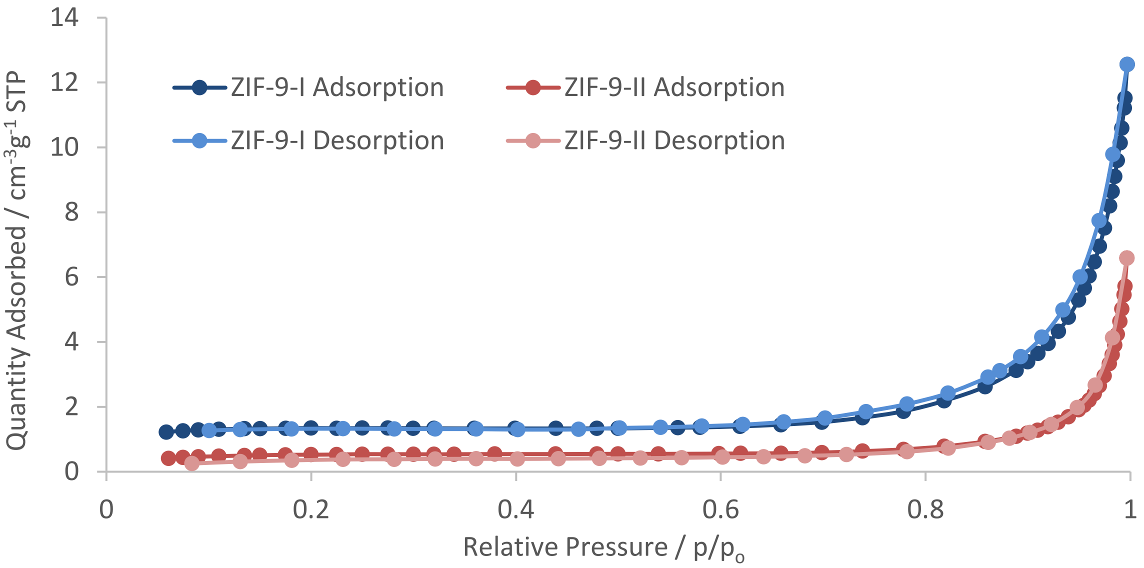

Figure 30: Nitrogen adsorption-desorption isotherm for ZIF-9 after attempting to remove residual DMF.

The TGA in Figure 31 would indicate that the removal of DMF was largely successful, with only a slight drop that points toward the presence of trapped DMF, followed by breakdown of the framework and loss of organics above 310 °C. The more gradual degradation of ZIF-9-I is indicative of varying levels of crystallinity, while the steeper slope of ZIF-9-II is in agreement with the observation from the XRD spectra that there has been a loss of crystallinity. The calculated cobalt content has increased to 20.8 % compared to 18.2 %, closer to the expected value of 20.1 %.

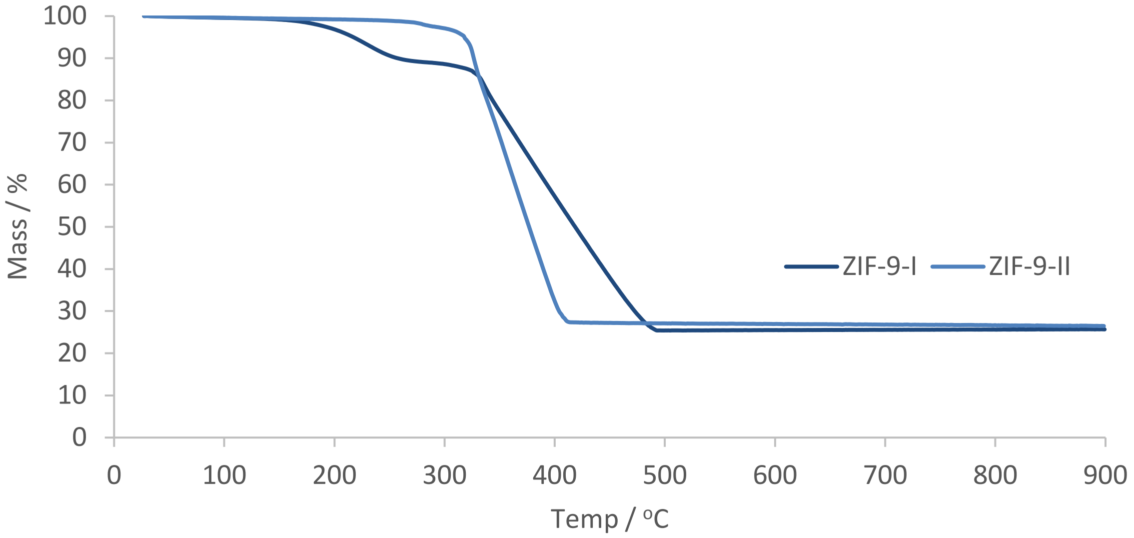

Figure 31: TGA curves of ZIF-9 before and after attempting to remove residual DMF.

The IR spectrum in Figure 32 is also in agreement, with the disappearance of peaks representing DMF whilst the peaks expected for ZIF-9 remain.

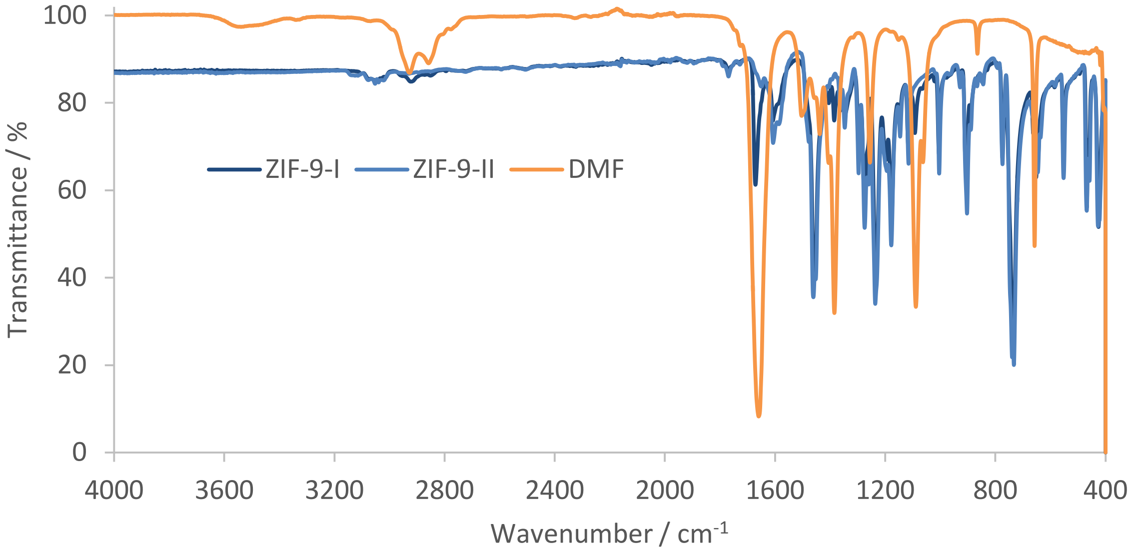

Figure 32: IR spectra for ZIF-9 before and after attempting to remove residual DMF.

The final method of analysis for the dried sample was UV-Vis which yields information on the oxidation and coordination state of the cobalt centre. The strong adsorption in Figure 33, resulting from the LMCT and d-d ligand field transitions discussed in 3.3.3 Rationalising Co-ZIF Activity, suggests the cobalt remains in the same tetrahedral environment. The sample itself also retained its dark blue/purple colour.

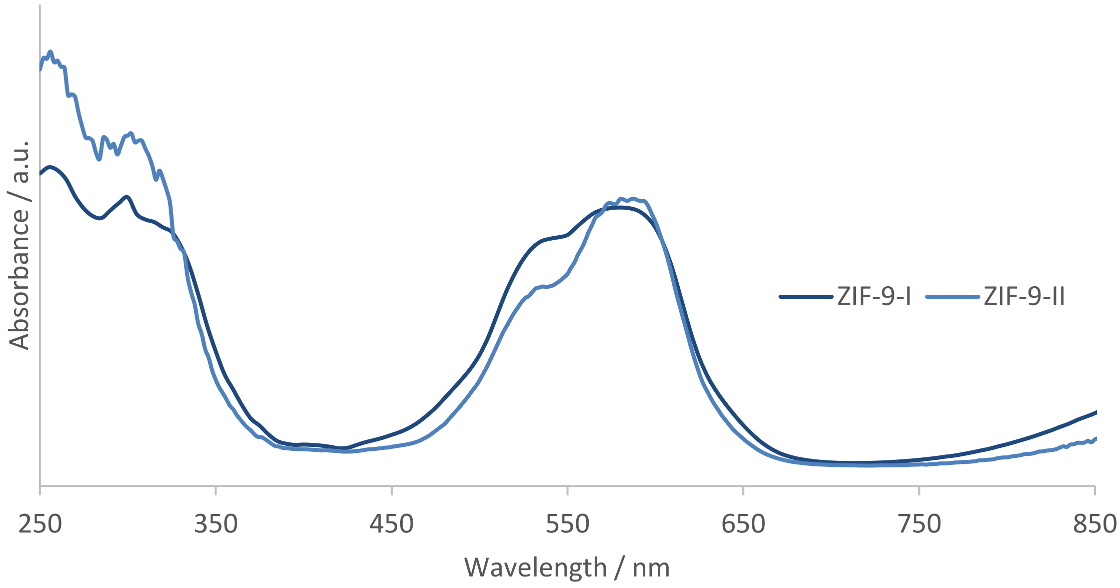

Figure 33: (DR) UV-Vis of ZIF-9 before and after attempting to remove residual DMF.

Using this characterisation data, the attempts to remove the residual DMF by heating under vacuum to 200 ^{o}C can be considered largely successful. Whilst retaining the same coordination motif of ZIF-9-I, the loss of guest molecules lead to an altered structure termed ZIF-9-II, mediated by the tilting of tetrahedral units observed with classic sodalites.[97] The highly-distorted and locally-strained nature of this phase results in poor crystallinity, as observed in the XRD pattern in Figure 29. Following the loss of DMF, catalytic tests with the sample obtained a lower yield of 75 % after 6 hours. As such, due to the applications investigated here not requiring access within the pores, or appearing to suffer any detrimental effect from the presence of trapped DMF, the as-synthesised ZIF-9 is more than satisfactory to continue studying, without the need to process further. If it was of interest further on, then a solvent transfer with DCM before vacuum drying could potentially be a better method to trial.[60] Alternatively, the aza-Henry reaction is also likely to lead to solvent exchange of DMF with the more volatile nitromethane, which could then be removed more easily.

3.3.6 Recyclability

3.3.6.1 Stability Under Illumination

To investigate stability of the Co-ZIFs in reaction conditions, the materials were analysed after exposure to the solar simulator for 6 hours whilst being suspended in nitromethane. Figure 34 shows the XRD patterns for the as-synthesised and post-exposure samples. Whilst there has been some loss in definition and intensity, the patterns remain clear, indicating the structural integrity was retained even if there has been a loss of crystallinity. Notably, the peaks still correspond to

ZIF-9-I in (b), rather than ZIF-9-II. There are two possible reasons for this, either the nitromethane has not displaced the DMF, or any nitromethane within the pores is still present and holding the framework in place.

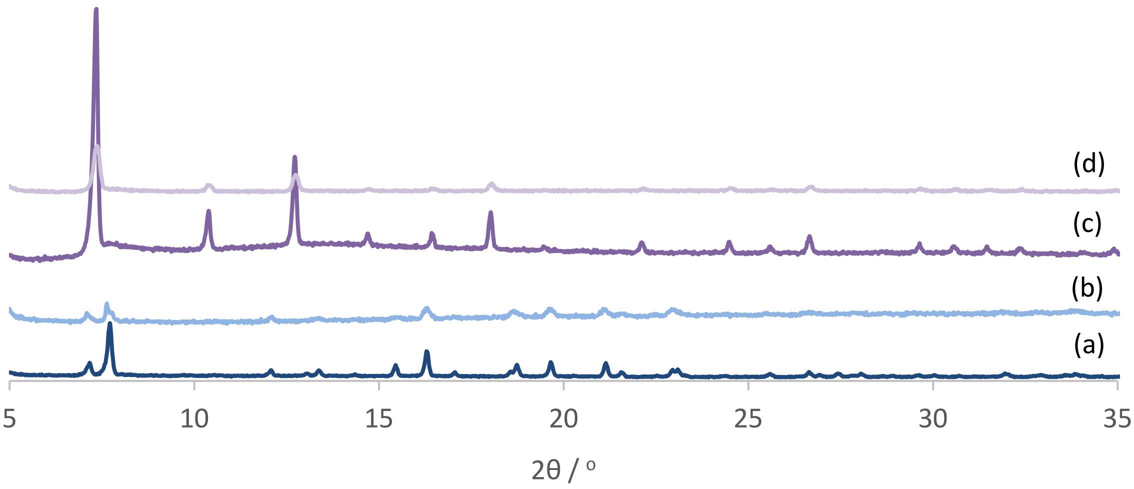

Figure 34: pXRD patterns of: ZIF-9 (a) as synthesised and (b) post exposure, ZIF-67 (c) as synthesised and (d) post exposure.

BET surface area measurements were collected for ZIF-67 post exposure, at 1177 m^2g^{-1} there is a notable drop from the as-synthesised 1303 m^2g^{-1}. This is a sign of amorphisation, alongside the loss of intensity in the XRD pattern. The pores would be expected to become more enclosed as a rigid structure and long-range order is lost. The isotherm plots are compared in Figure 35.

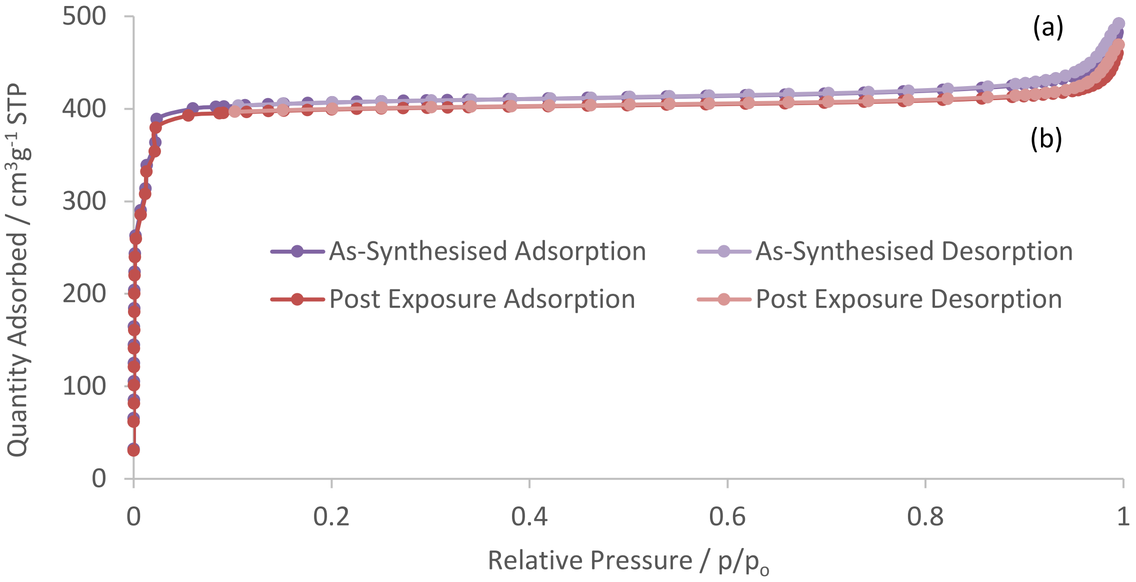

Figure 35: Nitrogen adsorption-desorption isotherm for ZIF-67 after exposure to light with (a) as-synthesised, (b) post exposure.

The UV-Vis spectra seen in Figure 36 retain the same features of the as-synthesised samples, including the LMCT in the UV range, and strong absorbance of visible light for the d-d ligand field transitions. ZIF-9's broad absorbance from 500-625 nm also appears slightly narrowed.

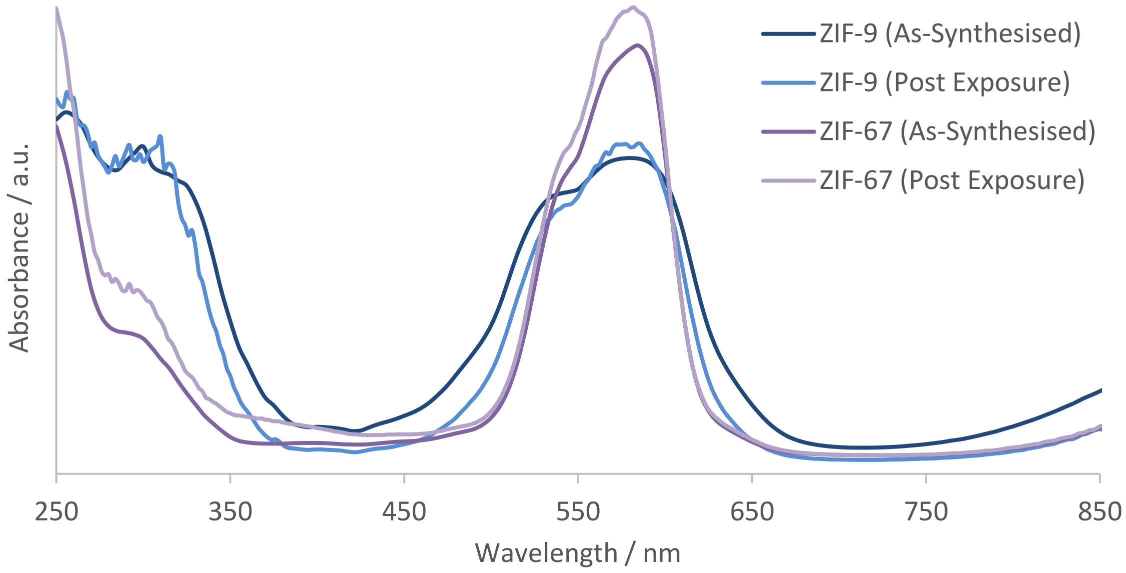

Figure 36: (DR) UV-Vis of Co-ZIFs before and after exposure to light.

3.3.6.2 Reusability Through Multiple Cycles

As heterogeneous catalysts, one of the main attractions to using Co-ZIFs is the potential to reuse the sample through multiple cycles. The Co-ZIFs were recovered from the aza-Henry reaction, washed with nitromethane and tested under the same conditions through a total of five cycles, the results are displayed in Figure 37. For ZIF-9, a slight drop in activity is observed in the second cycle, but high yields are still achieved after five cycles. In contrast, a rise in yield is observed with ZIF-67 after each cycle, which by the 5th is higher than ZIF-9 reached in any of its own five cycles.

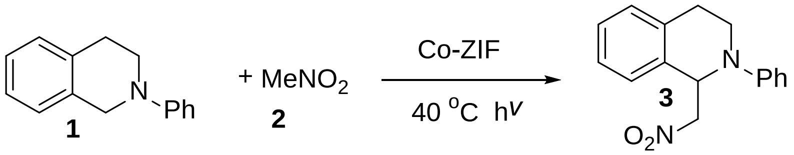

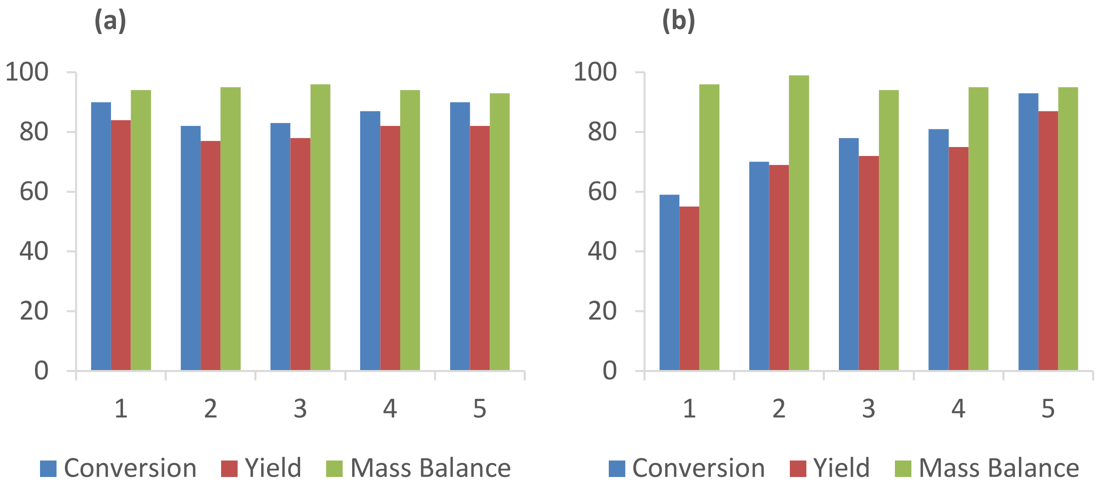

Figure 37: Recyclability tests through five cycles of the aza-Henry reaction with (a) ZIF-9 or (b) ZIF-67.

In order to understand why the ZIFs behaved as they did, both samples of Co-ZIF were washed and dried after the 5th cycle and analysed by pXRD. The 5th cycle ZIF-9 in Figure 38a neither resembles the original sample, nor the desolvated phase ZIF-9-II (Figure 29). It was expected that the high stability of these structures would mean the Co-ZIFs retained the crystalline structure. Or, in the case of ZIF-9, solvent substitution might occur, and upon drying reveal ZIF-9-II.[63] However, the pattern displays new peaks that to the author's knowledge have not been reported in relation to the ZIF materials before. It is unclear what changes have led to this, or the ramifications. Figure 38b also displays a significant change, with no peaks present, suggesting the solid sample is now completely amorphous, this change in nature has coincided with an increase in activity.

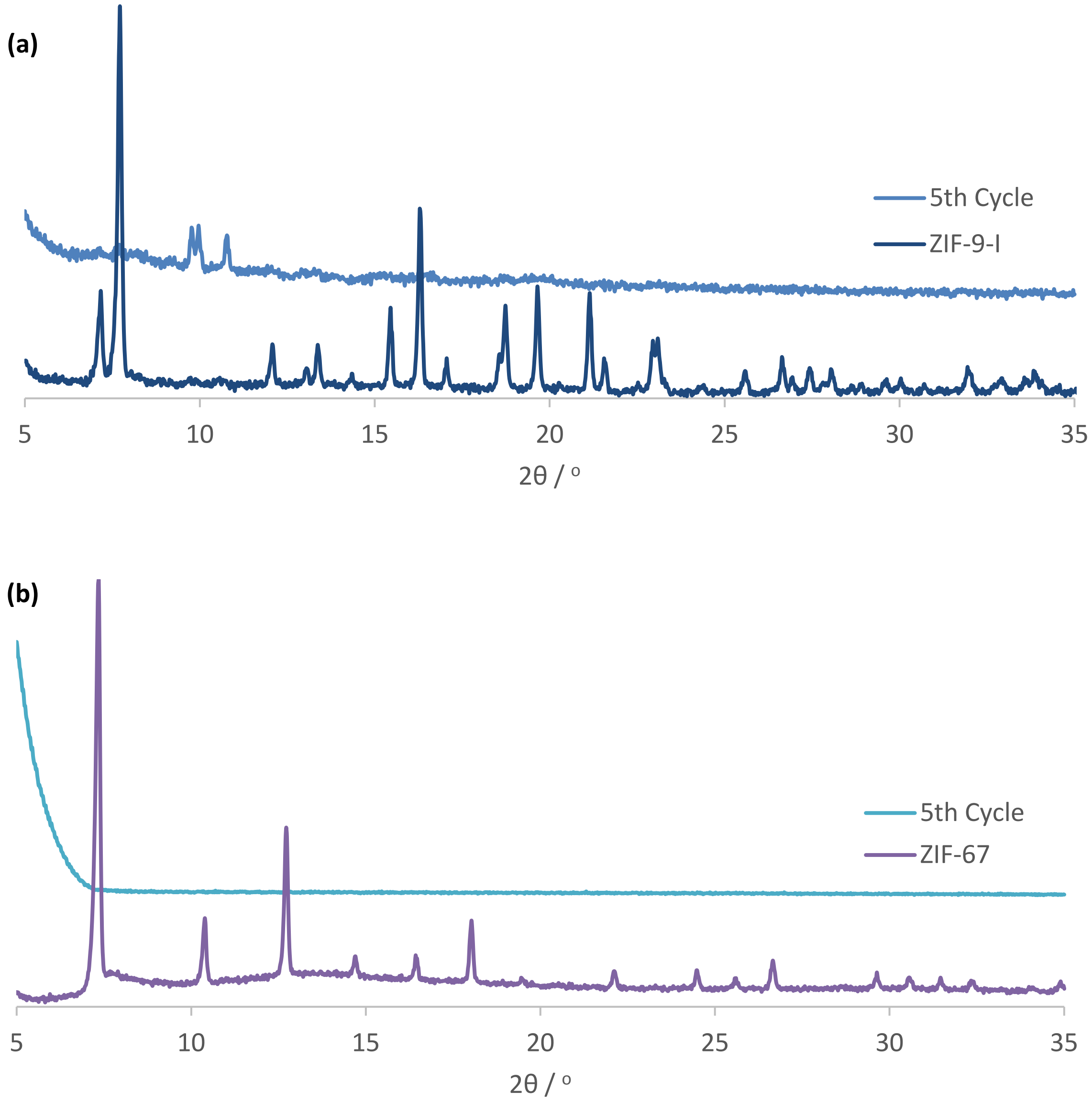

Figure 38: pXRD patterns, before use and after the 5th cycle, for (a) ZIF-9 and (b) ZIF-67.

The amorphisation of MOFs, in particular ZIFs, has been reported as the loss of long-range order while the network itself remains in place.[98] This can occur during synthesis or post-synthetic treatment. It would not be surprising if under these conditions the ZIFs have been amorphised. Considering the continued high performance of the material over five cycles, the retention of peaks in Figure 34, and the minimal loss of solid through each cycle, it is proposed that the network of metal nodes and linkers has remained largely intact but lost their long-range order. More characterisation would need to be collected in order to confirm this is the case, preferably after each cycle to observe how quickly the decline takes place. This would include BET analysis for ZIF-67 to determine the changes in surface area and porosity. The surface area dropped slightly after stirring in nitromethane under light, as revealed in Figure 35, as expected from a sample becoming more amorphous. UV-Vis would also help to reveal the nature of the cobalt environment and whether it has remained tetrahedral, while TGA could show how the thermal stability of a remaining framework has been affected.

3.3.7 Modifying the Synthesis of Co-ZIFs

3.3.7.1 Initial Trials of Modification Methods

Following the high activity of the Co-ZIFs in the aza-Henry, the next step was to investigate ways in which the synthesis could be modified to improve catalytic activity further. Initially this was to tailor the material to cater for a surface reaction, involving various ways to decrease particle size or prevent the agglomeration of particles. Doing so would increase the outer surface area, increasing the number of available active sites, which in turn should increase the rate of reaction, although it has been noted that ZIF-67 has much smaller particles than ZIF-9, but shows lower performance under the solar simulator.

Focusing on ZIF-9, a variety of methods were used for these comparisons. By solvating the cobalt in DMF first, rather than simultaneously with the benzimidazole, it is believed a solvation shell can be established before interacting with the linker, increasing the number of nucleation points.[78] This became evident when the addition of benzimidazole did not cause the solution to become as blue as the general procedure before placing in the oven, implying there was less initial coordination of the cobalt with the linker. Another method was to decrease the concentration of the reaction mixture, which has previously been found to reduce particle size with other MOF syntheses.[99] However, diluting with more DMF also increased the amount of cobalt formate by-product. Conversely, using an excess of the bridging ligand increased the yield of ZIF-9 whilst also effecting particle growth.[80] The use of 1-methylimidazole as a competitive inhibitor for benzimidazole, should slow further growth of the particles when coordinated, but is unlikely to remain a part of the final framework without the ability to deprotonate and obtain a formal charge.[80] Whereas, *tert*-butylamine should behave as a capping agent, slowing particle growth as a competitive inhibitor for benzimidazole, and limiting particle growth as a monodentate ligand.

XRD and SEM were used to analyse whether these modifications were successful. BET would have also been a useful characterisation technique if it weren’t for the strong physisorption of DMF molecules in the pores. Figure 39 shows that three of the procedures formed phase-pure ZIF-9-I. The new peaks observed in (e) and (f) can be attributed to a different phase of ZIF-9 termed ZIF-9-III.[63,100] Unlike the other two phases previously identified, there is no known transition observed from this much denser phase, illustrated in Figure 14 (3.1.2.2 Zeolitic-Imidazolate Frameworks (ZIFs)). The more thermodynamically stable, planar phase is believed to have increased stability in extreme environments such as high pressures, although not applicable with the catalytic tests in this project. The small peaks for ZIF-9-I observed in (e) and (f) suggest the procedure may simply need adjustment, for example using different molar ratios of the substrates. The remaining spectra do contain less intense peaks, indicating the syntheses have affected particle size and/or crystallinity.

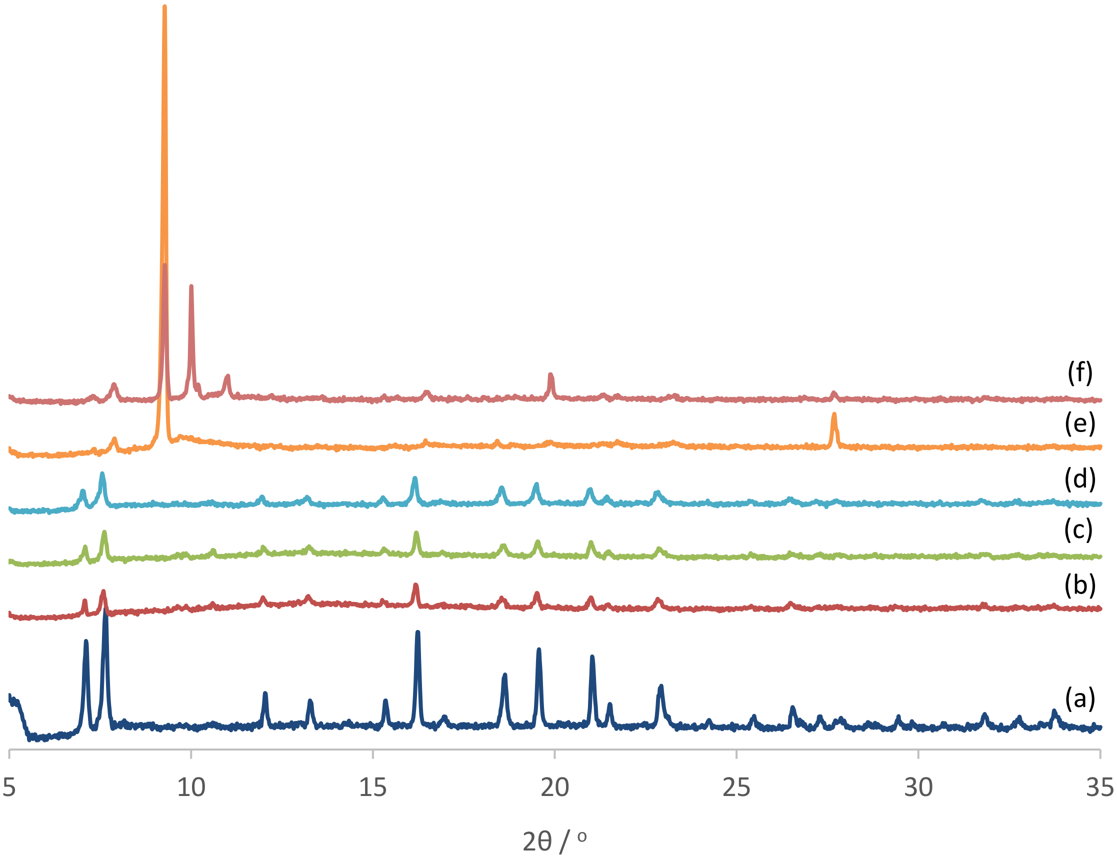

Figure 39: pXRD patterns of each ZIF-9 prep (a) ZIF-9, (b) solvated cobalt, (c) dilution, (d) excess PhIm, (e) 1-MIm (f) *tert*-butylamine.

The spectra in Figure 39a-d were analysed using the Rietveld method and Scherrer equation to generate more quantitative data for the samples. The lattice parameters in Table 8 have all increased slightly, suggesting a more disordered system. Meanwhile crystallite size, which would ideally have decreased, has only managed to do so for the sample using excess linker. Although the calculation of these values is not without flaws, the XRD spectra they are derived from are of low intensity, they do represent a good indication that the excess linker is likely to be worth more investigation rather than the solvation or dilution methods.

Table 8: Crystal structures for ZIF-9 following the initial changes to the synthesis.

	Crystal System	Lattice Parameters / Å	Unit Cell Volume / Å^3	Crystallite Size / Å
ZIF-9	Hexagonal	a = 22.935(17) b = 22.926(14) c = 15.783(10)	7198(8)	528(10)
Solvated	Hexagonal	a = 23.114(9) b = 22.991(10) c = 15.884(10)	7348(6)	543(28)
Diluted	Hexagonal	a = b = 23.145 c = 15.791	7326	573(43)
Excess PhIm	Hexagonal	a = 23.018(17) b = 22.937(2) c = 15.773(5)	7227(2)	478(19)

The SEM images in Figure 40 show the phase pure samples have no consistency in particle size or any definitive morphology. Considering the crystallite sizes determined in Table 8 are much smaller than many of the particles which can be seen in Figure 40, this data suggests the samples are aggregates of microcrystalline particles. An advantage to using MOFs is how easy it is to modify the synthesis in order to change the material's textural properties. Crystallinity was not the focus of these procedures, but rather the particle size and surface area, and as previously mentioned crystallinity is not mandatory to achieving an efficient photocatalyst.[46] So if these approaches were to be investigated further, methods to improving crystallinity could also be developed in conjunction.

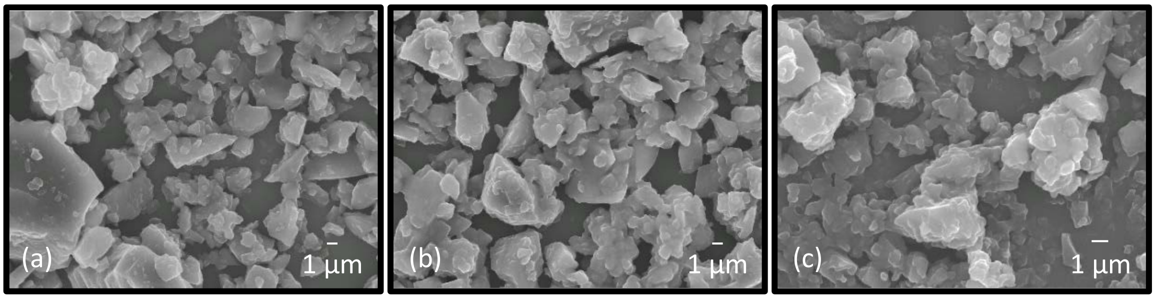

Figure 40: SEM images of (a) solvated cobalt, (b) dilution, (c) excess PhIm.

The three phase pure samples lacked consistency, the solvation of cobalt first had no notable effect, whilst dilution of the reaction mixture resulted in increased cobalt formate by-product forming. An excess of benzimidazole did appear to decrease the quantity of cobalt formate, and it was believed a similar effect could be achieved with the methylated imidazole in lower quantities.

3.3.7.2 Utilising Methylated Imidazoles during Synthesis

The use of methylated imidazole agents would increase the number of ligands the metal centre could coordinate with while building the framework, slowing down formation of particles without surface altering incorporation. Different quantities of 1-methylimidazole (1-MIm) were used in the synthesis of ZIF-9.

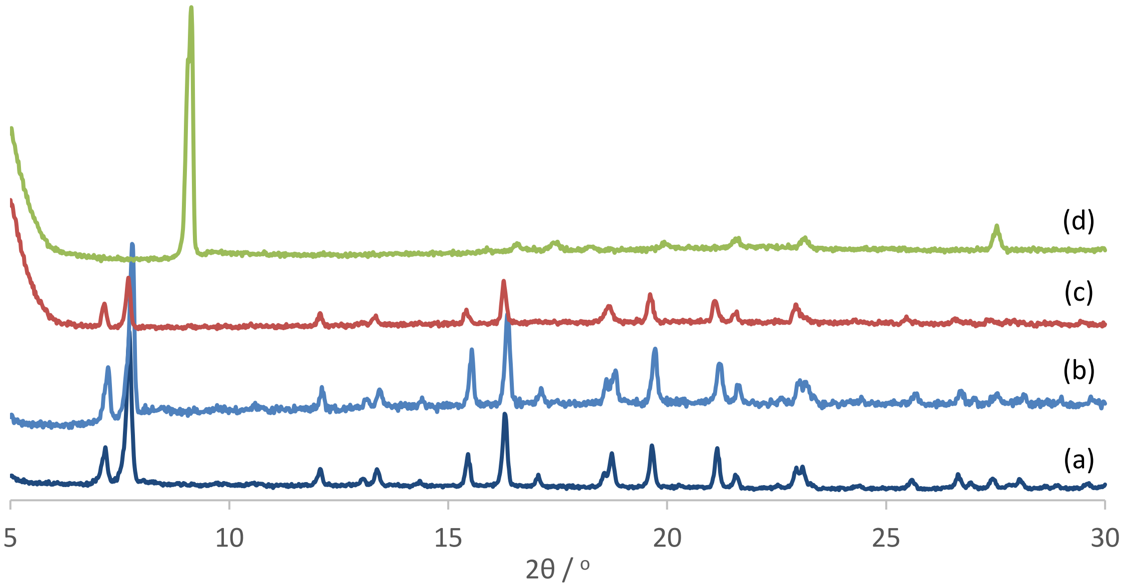

Figure 41: pXRD patterns of each ZIF-9 prep (a) ZIF-9, (b) 1-MIm 0.5 eq., (c) 1-MIm 1 eq., (d) 1-MIm 10 eq..

Figure 41 shows how the XRD pattern of ZIF-9 changes upon increasing amounts of 1-MIm. Addition of 20 eq. w.r.t. benzimidazole was also trialled, however no solid had formed after 48 hours. Clearly visible is that 10 eq. does not produce phase pure ZIF-9-I and is reminiscent of Figure 39e and ZIF-9-III. Table 9 reveals that addition of one equivalent of the methylated imidazole may have reduced the lattice parameters and crystallite size. Although the values are within error, it is likely that a more saturated system may decrease the quantity of DMF trapped within the pores. This would help to reduce the level of disorder in the sample and thus the size of the unit cell.

Table 9: Crystal structures for the synthesis of ZIF-9 with methylated imidazole.

	Crystal System	Lattice Parameters / Å	Unit Cell Volume / Å^3	Crystallite Size / Å
ZIF-9	Hexagonal	a = 22.935(17) b = 22.926(14) c = 15.783(10)	7198(8)	528(10)
0.5 eq.	Hexagonal	a = 22.942(5) b = 22.969(4) c = 15.871(19)	7271(2)	589(20)
1 eq.	Hexagonal	a = 22.966(9) b = 22.915(14) c = 15.745(8)	7194(6)	521(12)

The modified ZIFs were further analysed with SEM (Figure 42) to see whether the particles were visibly smaller. SEM revealed little difference between 0.5 and 1 eq. although aggregates of microcrystalline particles once again appear favoured over the larger crystals observed previously in Figure 24. The 10 eq. sample displayed similar crystals as seen in Figure 42b, with the addition of larger cubic crystals shown in (c). These particles, of approximately 14 µm, have been attributed to ZIF-9-III and compare well with the reported crystals for the isomorphous ZIF-7-III.[101]

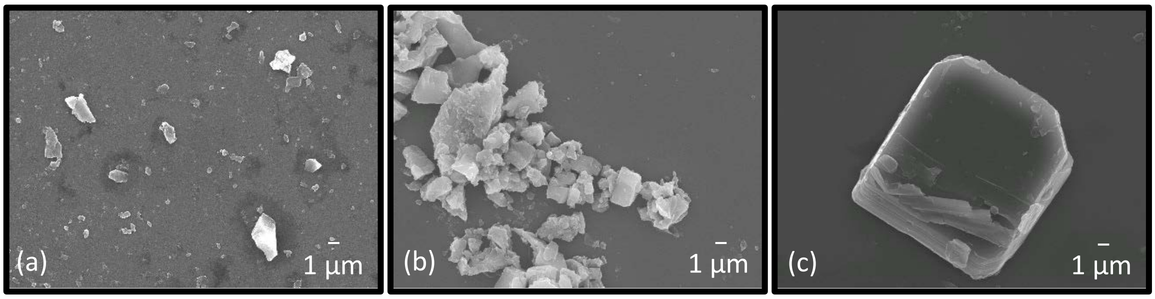

Figure 42: SEM images of (a) ZIF-9-I 1-MIm 0.5 eq., (b) ZIF-9-I 1-MIm 1 eq., (c) ZIF-9-III.

^{1}H NMR was also used to determine whether any of the capping agent remained bonded or coordinated with the framework. When dissolving the solid in DCl, the solution became a bright blue, indicating the breakdown of the framework with the changing environment of cobalt. The organic components were easily observed using NMR, and revealed no methylated imidazole. As such the methylated imidazole can be understood as inhibiting the growth of the framework, but without the ability to deprotonate a nitrogen and produce a charged species, it simply cannot bond strongly enough to the metal centre to remain attached.

Following the characterisation of the materials, the next step was to observe if the methylated imidazoles had affected catalytic activity. In Table 10, a trend can be observed where the more methylated imidazole was used during synthesis, the lower conversion/yield achieved. As discussed in 3.1.4 Potential Developments to Optimise MOFs towards Catalysis, even if the material remains the same, subtle differences to the surface chemistry can affect the outcome of the reaction.[82,83] There appears to be no advantage to employing modulating agents such as 1-MIm at this stage.

Table 10: Control experiments for modified ZIF-9 in the aza-Henry reaction.

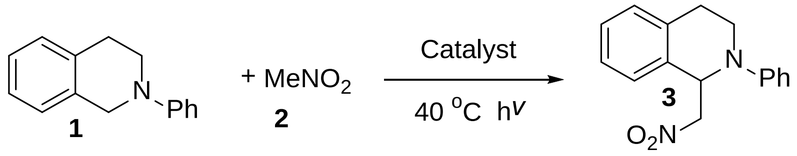

	Conversion / %	Yield / %	Mass Balance / %
Blank	20	20	100
ZIF-9-I	89	84	95
ZIF-9-I (1-MIm 0.5 eq.)	74	71	97
ZIF-9-I (1-MIm 1 eq.)	60	56	96
ZIF-9-III (1-MIm 10 eq.)	50	49	99

Reaction conditions: *N*-phenyl-tetrahydroisoquinoline (0.11 mmol) and catalyst (9 wt%) stirring in nitromethane (1 mL) for 6 h at 40 °C under white LED illumination. Conversion/yield determined by ^{1}H NMR of reaction mixture using mesitylene as an internal standard.

3.3.7.3 Investigating the Ratio of Metal to Ligand During Synthesis

Whilst the addition of methylated imidazole to the ZIF-9 synthesis did not reveal any significant advantages, using a large excess of the linker continues to show promise. Thus the quantity of benzimidazole (PhIm) was increased by multiple values in a series of experiments, the XRD spectra for each are plotted in Figure 43. It became clear that as the ratio of cobalt and PhIm shifts, the quantity of cobalt formate decreases, the peak at 9.5 ° is not present in the procedures using three times or more PhIm. However, the introduction of ZIF-9-III can be seen in Figure 43c, the 2.5x prep, where all three components are observed in the XRD pattern, demonstrating that there is not a ratio which produces the desired pure ZIF-9-I.

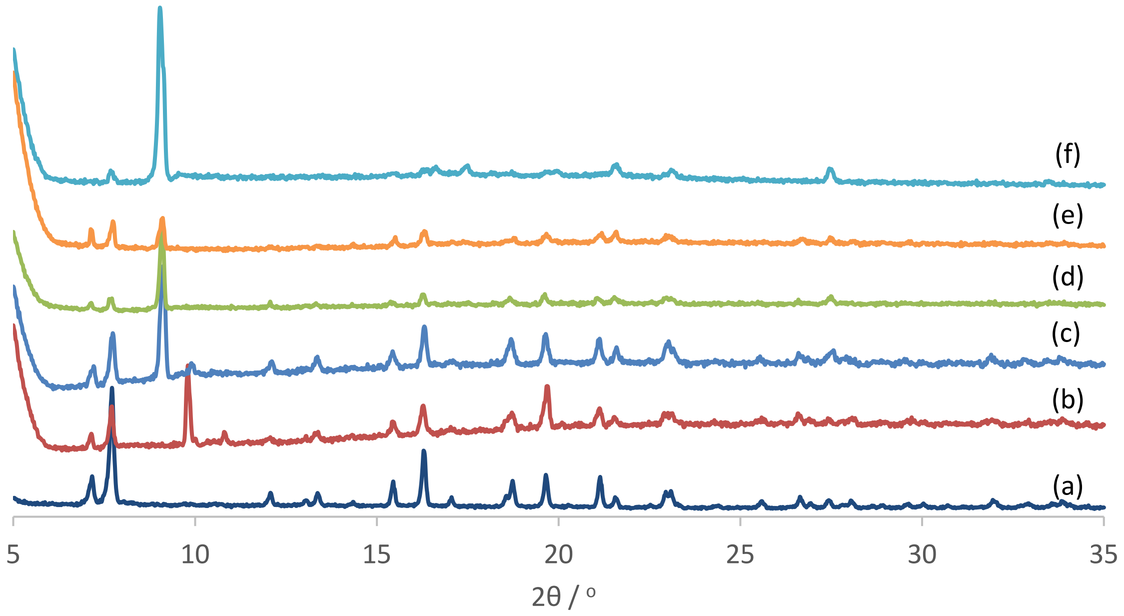

Figure 43: pXRD patterns of each ZIF-9 prep (a) ZIF-9-I, increased PhIm by a scale of (b) 2x, (c) 2.5x, (d) 3x, (e) 4x, (f) 6x.

Displayed in Table 11 are the crystal structures for a select number of samples which used excess PhIm. A trend can be identified: where there is more PhIm in the synthesis, the smaller the crystallite size becomes. The accuracy is of concern, especially considering the large error in the 4x sample, but this does indicate the study is heading in the right direction.

Table 11: Crystal structures for the synthesis of ZIF-9 with excess PhIm.

	Crystal System	Lattice Parameters / Å	Unit Cell Volume / Å^3	Crystallite Size / Å
ZIF-9	Hexagonal	a = 22.935(17) b = 22.926(14) c = 15.783(10)	7198(8)	528(10)
2x	Hexagonal	a = 23.018(17) b = 22.937(2) c = 15.773(5)	7227(2)	478(19)
2.5x	Hexagonal	a = 23.04(2) b = 22.98(2) c = 15.789(10)	7254(12)	408(29)
4x	Hexagonal	a = b = 22.92(2) c = 15.819	7194	104(49)

SEM images were collected for three of the samples in Figure 43 to observe how the particles compare to the capped ZIFs. In Figure 44, images for the 2x, 4x and 6x samples show how, upon increased excess of PhIm, the inconsistent crystals of ZIF-9 are gradually replaced with the cubic crystals of ZIF-9-III. Particle size for ZIF-9-III varied depending on how large the excess of PhIm was, measuring approximately 17 µm and 23 µm for the 4x and 6x prep respectively.

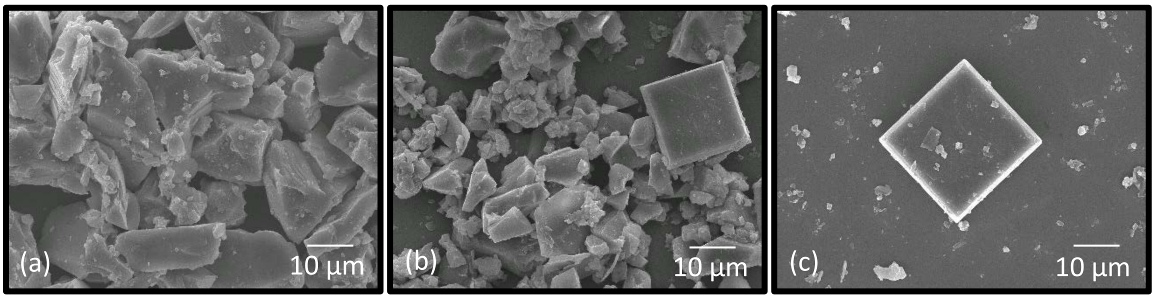

Figure 44: SEM images of ZIF-9 preps with increased PhIm (a) 2x, (b) 4x and (c) 6x.

BET, TGA and UV-Vis were employed to further understand ZIF-9-III. The isotherm plot in Figure 45 displays Type III characteristics, with BET surface area measurements of 3 m^2g^{-1}. As expected, and along with previous ZIF-9 studies, ZIF-9-III displays non-porous behaviour typical of its much denser characteristics.

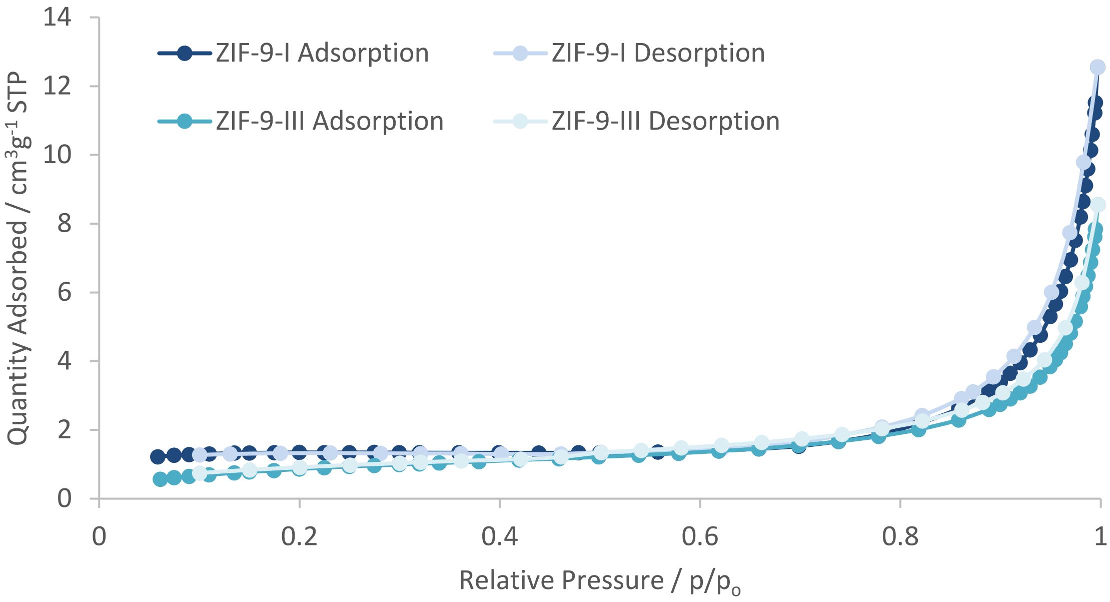

Figure 45: Nitrogen adsorption-desorption isotherm plot for ZIF-9-III.

The UV-Vis spectra displayed in Figure 46 show that ZIF-9-III maintains the same features as ZIF-9-I, including strong absorbance between 500-630 nm. The spectra suggests that the framework still consists of tetrahedral Co^{2+} metal centres.

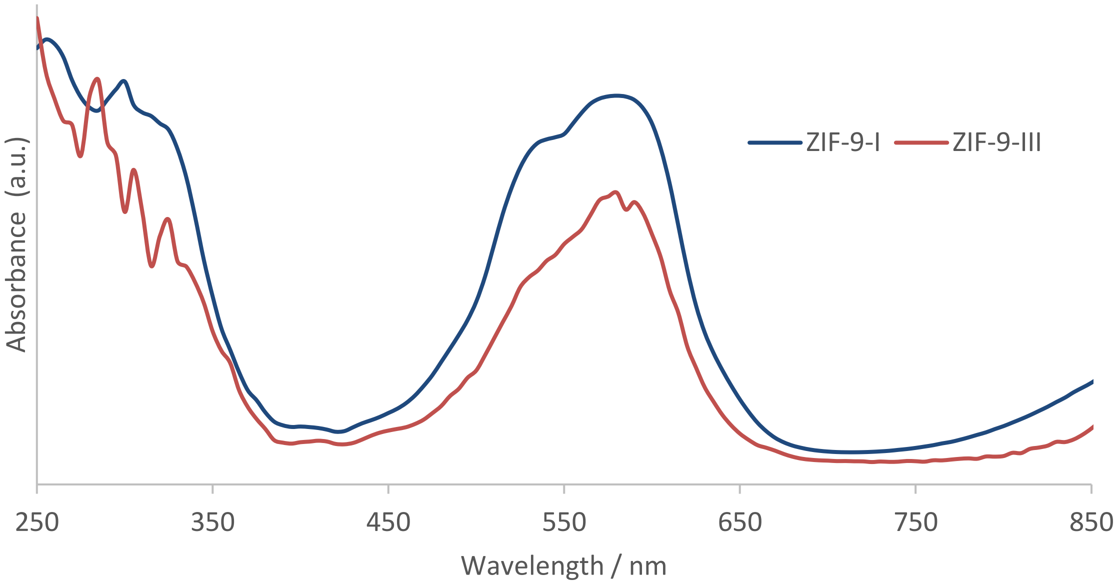

Figure 46: (DR) UV-Vis of ZIF-9-I and ZIF-9-III.

TGA revealed that, unlike ZIF-9-I, there does not appear to be any trapped solvent within the pores, which is likely a result of the much denser arrangement not permitting guest molecules. Framework breakdown begins to occur at a slightly higher temperature, approximately 350 °C. Calculations using the mass loss profile were also concurrent with the same molecular formula of [Co(PhIm)$_2$].

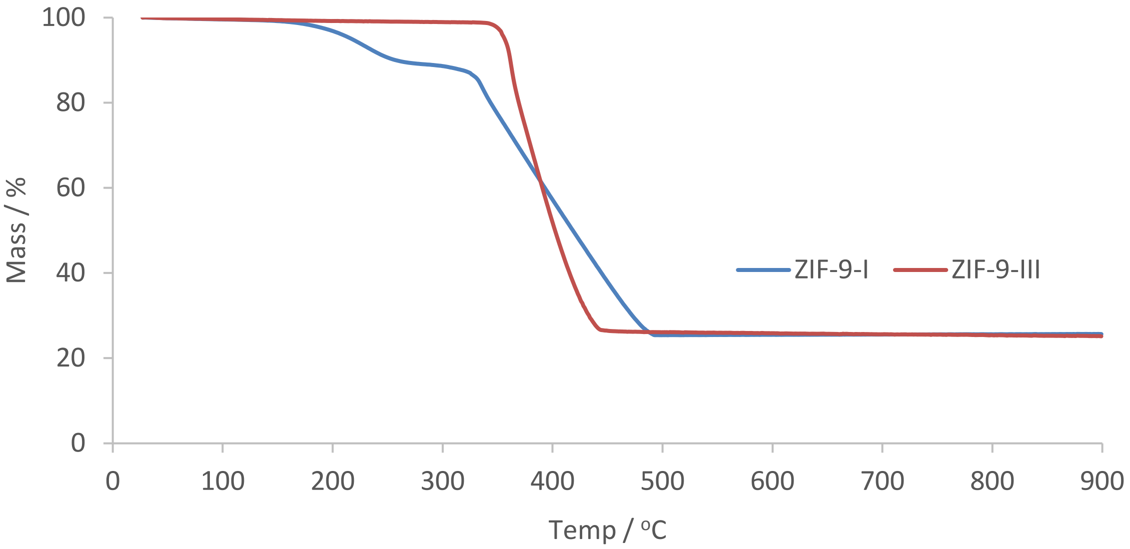

Figure 47: TGA curves for ZIF-9-I and ZIF-9-III.

Table 12 shows that the much denser ZIF-9-III resulted in reduced activity for the aza-Henry reaction, which could be attributed to less accessible cobalt sites. However, it is not clear why the 2x prep resulted in a similar drop in activity. This is suggestive that altering the ratio of metal to linker in the synthesis can have a notable effect on the application of the ZIF, even though no significant differences were observed in the characterisation.

Table 12: Control experiments for modified ZIF-9 in the aza-Henry reaction.

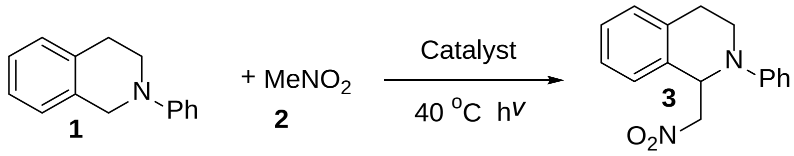

	Conversion / %	Yield / %	Mass Balance / %
Blank	20	20	100
ZIF-9-I	89	84	95
ZIF-9-I (2x PhIm)	52	51	99
ZIF-9-III	50	49	99

Reaction conditions: *N*-phenyl-tetrahydroisoquinoline (0.11 mmol) and catalyst (9 wt%) stirring in nitromethane (1 mL) for 6 h at 40 °C under white LED illumination. Conversion/yield determined by ^{1}H NMR of reaction mixture using mesitylene as an internal standard.

3.3.8 Substrate Scope

With Co-ZIFs confirmed as displaying high activity in the aza-Henry reaction, the effects of using different THIQs was examined. Up till now 9 wt% of catalyst had been employed as it is unclear how many active sites are actually accessible to the substrates. The quantity of catalyst was to be kept in line with previous studies by using a comparative molar amount of cobalt. Thus 6 mol% w.r.t. cobalt, as determined by ICP (18.6 wt%) and TGA (18.2 wt%), of the ZIFs were employed. The substrate scope was limited to varying the aromatic group on the tertiary amine site.[1] A more electron rich aromatic group will help to stabilise the positively charged intermediate formed after photoexcitation. This results in the higher yields observed for products 3b and 3c in Table 13. Whereas, the less electron rich aryl groups lead to the significantly lower yields observed for products 3e and 3f. Some variability is expected as the literature is inconsistent with how the different aromatic groups ultimately effect the yield, with many reporting a decrease for all additional substrates.[18,19,102,103]

---

[1] Starting materials 1b-f were kindly synthesised by Luke Shirley.

Table 13: Control experiments for the aza-Henry reaction with varying aryl-substituents.

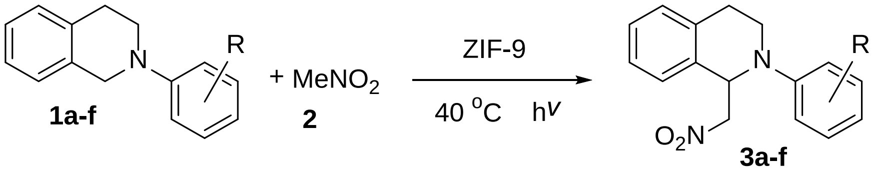

SM	Prod	R	Conversion / %	Yield / %	Mass Balance / %
1a	3a	H	90	84	94
1b	3b	4-Me	91	91	99
1c	3c	4-OMe	98	92	94
1d	3d	4-Cl	64	64	100
1e	3e	4-CF_3	57	47	90
1f	3f	2-F	42	39	97

Reaction conditions: *N*-aryl-tetrahydroisoquinoline (0.11 mmol) and ZIF-9 (6 mol%) stirring in nitromethane (1 mL) for 6 h at 40 °C under a solar simulator with 515 nm filter. Conversion/yield determined by ^{1}H NMR of reaction mixture using mesitylene as an internal standard.

3.3.9 Summary of Characterisation

Below is a summary of what was learned from each characterisation method employed:

XRD	Confirmation of a successful synthesis and phase purity of the samples Identifying which phase of ZIF-9 has formed Identifying impurities such as cobalt formate or ZIF-9-III An indication of crystallinity, comparing lattice parameters and crystallite sizes Questioning the role of crystallinity in the activity of ZIF-9 - Recycled ZIFs appear amorphous but retain excellent yields - Modified syntheses reduced crystallinity and yields
BET	Further confirmation of a successful synthesis Measured surface area at 4 and 1303 cm^2g^{-1} for ZIF-9 and ZIF-67 respectively
SEM	Observing particle shape and size, ZIF-9 at 4.3 µm, and ZIF-67 at 315 nm Compared the effects of procedures wishing to modulate particle sizes, noting that ZIF-9 appears to adopt aggregates of microcrystalline particles

TGA	Thermal stability of ZIFs, both breaking down at higher temperatures than typical MOFs at 300 and 400 ^{o}C for ZIF-9 and ZIF-67 respectively Observing presence of guest molecules in ZIF-9 Calculation of elemental composition of cobalt at 18.2 and 26.7 % Indication of crystallinity by the gradient of breakdown
ICP	Calculation of elemental composition of cobalt at 18.6 and 26.2 % Comparative to theoretical and TGA calculations
UV-Vis	Observing which wavelengths of light may illicit a photoresponse Noting the tetrahedral character of the Co^{2+} sites - LMCT in the UV-range - d-d ligand field transitions with peaks at 540, 570 and 590 nm
IR	Further confirmation of a successful synthesis Compares well to the literature and free imidazoles Identifies the presence of DMF by a carbonyl peak at 1657 cm^{-1}
XAS	Studying the photoresponse of Co-ZIFs Noted a shift in the pre-edge feature for both Co-ZIFs to a lower energy Indication of a LMCT occurring as a result of exposure to light, more prominent with ZIF-67 Greater understanding of the proposed mechanism and the challenging reduction of Co(II) Justified the higher yield for ZIF-9 over ZIF-67 Established a direction for further study of Co-ZIFs as photocatalysts

3.4 Conclusion

Two Co-ZIFs have been identified as active photocatalysts in the aza-Henry reaction, utilising visible light. Both frameworks offer a straight forward synthesis, with cheap materials. ZIF-67 has additional benefits of forming at room temperature, using an aqueous system. Whilst previous reports of CDCs which use heterogeneous photocatalysts tend to incorporate more expensive metals, here a cheaper cobalt material was demonstrated to achieve excellent yields of up to 91 % in 6 hours. As a solid catalyst, the Co-ZIFs were easily recovered from the reaction and retained their high activity through five cycles.

Characterisation of the Co-ZIFs was carried out to rationalise why, despite the two materials being very similar in nature, changing the organic linker had such a significant effect on photocatalytic activity. Through a combination of UV-Vis and XAS spectroscopy, as well as theoretical simulations, it was shown that the range of light adsorbed to activate the cobalt site and the Co(II)* to Co(I) single electron transfer, play a pivotal role in this reaction. This can be controlled and enhanced through astute selection of the imidazole linker, with benzimidazole (ZIF-9) preventing the LMCT seen with 2-methylimidazole (ZIF-67), leading to ZIF-9 performing better as a photocatalyst. This finding opens up possibilities for a wider range of functionalised imidazole linkers to be experimentally, and computationally, screened for this reaction, towards developing an optimised photocatalytic species. Installing cobalt in the precise coordination environment of the ZIF-9 framework grants the benefits of a recyclable heterogeneous photocatalyst for future sustainable organic transformations.

The synthesis was modified to investigate whether subtle changes to the established protocol for ZIF-9 would improve the catalytic activity further. This focused on methods which could produce smaller particle sizes, which would in theory increase the external surface area and thus the number of available active sites. Structural changes were observed in the XRD and SEM results, a loss of crystallinity, introduction of the denser phase ZIF-9-III, and noticeable aggregation. These changes to the framework were detrimental to catalytic activity. Efforts could instead be moved towards discouraging aggregation of particles which should aid catalytic activity by further increasing the external surface area.

Following the analysis of the Co-ZIFs with UV-Vis and XAS spectroscopy, thereby elucidating the nature of the photoexcitation and mechanism, the role of the linker was recognised as crucial to the catalyst's activity. Trialling a range of functionalised imidazoles, experimentally and computationally, could help to identify a Co-ZIF that further limits the LMCT which occurs under illumination, resulting in an even greater capacity for photocatalytic behaviour. Subsequently, work on this project could focus on broadening the substrate scope, varying the tetrahydroisoquinoline to determine how different functional groups on the aromatic rings can affect the activity. Studying different nucleophiles such as nitroethane, malonates, indole, phenylacetylene, and 2-naphthol, all common substrates tested with CDCs, would help to further demonstrate how well the Co-ZIFs compare with other reported systems.

Additional optimisation of the process may reveal that a lower quantity of catalyst might improve yields, due to the loss of transparency with the suspension of the Co-ZIFs in solution. Decreasing the quantity of any chemical would appeal from a Green Chemistry standpoint, but especially one that incorporates a metal such as cobalt. To help gain a better perspective of the decline in crystallinity, and strengthen the argument for their use despite this, a more in-depth characterisation of the recycled materials is required. This would include but is not limited to BET, UV-Vis, and TGA, which would ideally reveal a decline in crystallinity by showing lower surface areas and a drop in thermal stability, but indicate the coordination of the cobalt with the linker remains the same. Establishing the stability of these materials is essential to approving their usage on a larger scale, including whether cobalt leaches from the framework. Elemental analysis of the reaction mixture following removal of the catalyst would ideally find no cobalt present. This is of particular importance considering such contamination is a stumbling block for transition-metal catalysed operations, in applications such as the synthesis of pharmaceuticals.

3.5 Experimental

3.5.1 Control Experiments

3.5.1.1 *N*-Phenyl-1,2,3,4-tetrahydroisoquinoline (1a)

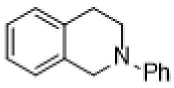

The procedure[10] for the starting material used throughout the project was as follows: Copper (I) iodide, (476 mg, 2.50 mmol) and potassium phosphate (10.119 g, 47.7 mmol) were placed under an inert atmosphere before adding 2-propanol (23.8 mL), ethylene glycol (2.6 mL, 47.6 mmol), 1,2,3,4-tetrahydroisoquinoline (4.8 mL, 35.7 mmol) and iodobenzene (2.7 mL, 23.8 mmol). The reaction mixture was then heated to 90 °C and left stirring for 24 hours. Afterwards, it was left to cool to room temperature before adding diethyl ether (50 mL) and water (50 mL). The organic layer was extracted by diethyl ether (2 x 50 mL) before washing the combined organic phases with brine (50 mL) and drying over magnesium sulphate. The solvent was removed by rotary evaporation, the dark brown oil was purified by column chromatography on silica gel (hexane/ethyl acetate 19:1). The yield was recorded at 3.238 g, 65 %. A peach solid with R_f of 0.25 in the eluent mentioned. NMR was in good agreement with the literature:[10] ^{1}H NMR (400 MHz, $CDCl_3$): δ 7.32-7.27 (2H, m), 7.21-7.14 (4H, m), 6.99 (2H, d, J = 8.0 Hz), 6.83 (1H, t, J = 7.3 Hz), 4.42 (2H, s), 3.57 (2H, t, J = 5.9 Hz), 3.00 (2H, t, J = 5.8 Hz). ^{13}C NMR (101 MHz, $CDCl_3$): δ 150.71, 135.03, 134.63, 129.34, 128.66, 126.67, 126.47, 126.16, 118.80, 115.29, 50.89, 46.67, 29.27.

3.5.1.2 1-(Nitromethyl)-*N*-phenyl-1,2,3,4-tetrahydroisoquinoline (3a)

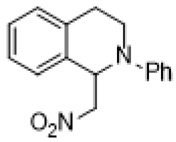

A typical reaction[21] involved adding **1a** (23 mg, 0.11 mmol), and a catalyst (2 mg, 9 wt%) to nitromethane **2** (1 mL) in a small glass vial. Mesitylene (13 µL) was added as an internal standard, before leaving the mixture to stir for 6 hours at 40 °C. ^{1}H NMR of the crude reaction mixture was used to calculate conversions/selectivities, a representative spectra is included in the Appendix. Additional conditions used: wrapping the vial in foil to exclude light, under white LEDs, using *tert*-butyl hydroperoxide (40 %, 14 mg, 0.15 mmol) as an oxidant, or with the solar simulator. The raised temperature was as a result of the light sources emitting heat, and the conditions were replicated for the control experiments in the dark. NMR was in good agreement with the literature:[21] ^{1}H NMR (400 MHz, $CDCl_3$): δ 7.27-7.16 (5H, m), 7.14 (1H, d, J = 7.3 Hz), 6.98 (2H, d, J = 8.2 Hz), 6.85 (1H, t, J = 7.3 Hz), 5.55 (1H, t, J = 7.2 Hz), 4.88 (1H, dd, J = 12.1, 7.8 Hz), 4.57 (1H, dd, J = 11.7, 6.7 Hz), 3.71-3.58 (2H, m), 3.09 (1H, ddd, J = 16.3, 8.7, 5.8 Hz), 2.80 (1H, dt, J = 16.3, 5.0 Hz). ^{13}C NMR (101 MHz, $CDCl_3$): δ 148.57, 135.42, 133.08, 129.65, 129.34, 128.27, 127.15, 126.85, 119.59, 115.26, 78.94, 58.34, 42.24, 26.62

3.5.1.3 Substrate Scope (3b-f)

The isoquinoline **1** (0.11 mmol) and ZIF-9 (2 mg, 6 mol%) were suspended in nitromethane (1 mL), with mesitylene (13 µL), in a small glass vial. The mixture was set stirring under the solar simulator with the 515 nm filter for 6 hours, temperature monitored at 40 °C. ^{1}H NMR of the crude reaction mixture was used to calculate conversions/selectivities. NMR spectra were in good agreement with the literature.

1-(Nitromethyl)-2-(p-tolyl)-1,2,3,4-tetrahydroisoquinoline (**3b**)[28]

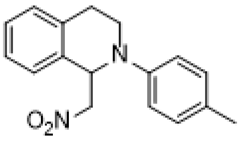

^{1}H NMR (400 MHz, CDCl$_3$): δ 7.25-7.13 (4H, m), 7.06 (2H, d, J = 8.34 Hz), 6.88 (2H, d, J = 8.54 Hz), 5.49 (1H, dd, J = 7.88, 6.78 Hz), 4.87 (1H, dd, J = 11.92, 8.39 Hz), 4.60 (1H, dd, J = 11.97, 6.16 Hz), 3.70-3.55 (2H, m), 3.10-3.01 (1H, m), 2.75 (1H, dt, J = 16.69, 4.40 Hz), 2.25 (3H, s)

2-(4-Methoxyphenyl)-1-(nitromethyl)-1,2,3,4-tetrahydroisoquinoline (**3c**)[28]

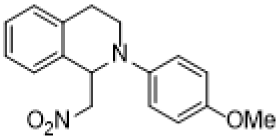

^{1}H NMR (400 MHz, CDCl$_3$): δ 7.26-7.13 (4H, m), 6.92 (2H, d, J = 8.84 Hz), 6.81 (2H, d, J = 8.55 Hz), 5.39 (1H, dd, J = 8.29, 6.04 Hz), 4.85 (1H, dd, J = 11.90, 8.90 Hz), 4.60 (1H, dd, J = 11.96, 5.64 Hz), 3.75 (3H, s), 3.62-3.55 (2H, m), 3.06-2.95 (1H, m), 2.70 (1H, dt, J = 16.44, 3.58 Hz)

2-(4-Chlorophenyl)-1-(nitromethyl)-1,2,3,4-tetrahydroisoquinoline (**3d**)[28]

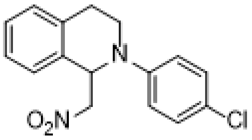

^{1}H NMR (400 MHz, CDCl$_3$): δ 7.27-7.14 (6H, m), 6.93-6.87 (2H, m), 5.50 (1H, dd, J = 7.68, 6.52 Hz), 4.87 (1H, dd, J = 11.94, 8.20 Hz), 4.61 (1H, dd, J = 11.97, 6.23 Hz), 3.69-3.57 (2H, m), 3.12-3.02 (1H, m), 2.79 (1H, dt, J = 16.61, 4.68 Hz)

1-(Nitromethyl)-2-(4-(trifluoromethyl)phenyl)-1,2,3,4-tetrahydroisoquinoline (**3e**)[104]

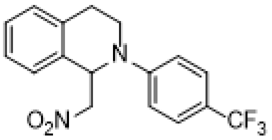

^{1}H NMR (400 MHz, CDCl$_3$): δ 7.29-7.14 (4H, m), 7.03 (2H, d, J = 8.73 Hz), 6.96 (2H, d, J = 8.73 Hz), 5.63 (1H, t, J = 7.16 Hz), 4.9 (1H, dd, J = 11.89, 7.96 Hz), 4.64 (1H, dd, J = 12.02, 6.68 Hz), 3.77-3.67 (2H, m), 3.18-3.08 (1H, m), 2.89 (1H, dt, J = 16.57, 5.36 Hz)

2-(2-Fluorophenyl)-1-(nitromethyl)-1,2,3,4-tetrahydroisoquinoline (**3f**)[105]

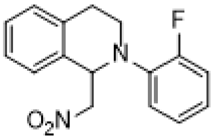

^{1}H NMR (400 MHz, CDCl$_3$): δ 7.29-6.85 (8H, m), 5.35 (1H, dd, J = 9.75, 4.59 Hz), 4.87 (1H, dd, J = 12.27, 9.56 Hz), 4.62 (1H, dd, J = 12.37, 4.72 Hz), 3.65-3.52 (2H, m), 2.95-2.85 (1H, m), 2.68 (1H, dt, J = 16.68, 3.04 Hz)

3.5.2 Catalysts

3.5.2.1 ZIF-9

The procedure followed the work of Li & Kim.[106] Cobalt (II) nitrate hexahydrate (1.11 g, 3.8 mmol) and benzimidazole (0.33 g, 2.8 mmol) were dissolved in DMF (50 mL) before heating to 130 °C for 48 hours. Once at room temperature the solution was filtered and washed with DMF (3 x 10 mL). Red and blue crystals were collected and left in a drying oven. The solid was ground before centrifuging in chloroform (3 x 10 mL). The supernatant was decanted each time before removing the solvent *in vacuo*. The blue/purple solid was dried under vacuum at 100 ^{o}C for 6 hours. Analysed by pXRD to confirm phase purity.

The procedure was altered in various ways to modulate particle size. Initially this included: dissolving the cobalt and leaving to stir for 15 mins before adding benzimidazole, using twice the amount of DMF, using twice the amount of benzimidazole, and adding 1-methylimidazole (4.6 g, 56 mmol) or *tert*-butylamine (4.1 g, 56 mmol) to the reaction mixture. Addition of 1-methylimidazole occurred prior to benzimidazole.

Table 14: Gel compositions for ZIF-9 syntheses.

	Gel Composition Co/PhIm/1-MIm/DMF	Quantity of PhIm / g	Quantity of 1-Mim / g
ZIF-9	1 : 0.737 : 0 : 646	0.33	-
ZIF-9 (1-Mim 0.5 eq.)	1 : 0.737 : 0.368 : 646	0.33	0.115
ZIF-9 (1-Mim 1 eq.)	1 : 0.737 : 0.737 : 646	0.33	0.229
ZIF-9 (1-Mim 10 eq.)	1 : 0.737 : 7.37 : 646	0.33	2.29
ZIF-9 (1-Mim 20 eq.)	1 : 0.737 : 14.7 : 646	0.33	4.58
ZIF-9 (2x PhIm)	1 : 1.47 : 0 : 646	0.66	-
ZIF-9 (2.5x PhIm)	1 : 1.84 : 0 : 646	0.825	-
ZIF-9 (3x PhIm)	1 : 2.21 : 0 : 646	0.99	-
ZIF-9 (4x PhIm)	1 : 2.95 : 0 : 646	1.32	-
ZIF-9 (6x PhIm)	1 : 4.42 : 0 : 646	1.98	-

3.5.2.2 ZIF-67

Typical procedure[91] used a gel composition of 1 : 44.7 : 1280 (Co/2-Mim/H_2O). 2-methylimidazole (5.5 g, 67 mmol) was dissolved in water (20 mL), before adding $Co(NO_3)_2.6H_2O$ (0.45 g, 1.5 mmol) in water (3 mL) and stirring the mixture for 6 hours. The purple precipitate was collected by centrifugation, washing with water (2 x 10 mL) and methanol (2 x 10 mL). The solid was dried at 100 ^oC for 6 hours under vacuum. Analysed by pXRD to confirm phase purity.

3.6 References

1 C.-J. Li and B. M. Trost, *Proc. Natl. Acad. Sci. U. S. A.*, 2008, **105**, 13197–13202.

2 B. M. Trost, *Science (80-.).*, 1991, **254**, 1471–1477.

3 B. A. Arndtsen, R. G. Bergman, T. A. Mobley and T. H. Peterson, *Acc. Chem. Res.*, 1995, **28**, 154–162.

4 S. a. Girard, T. Knauber and C. J. Li, *Angew. Chemie - Int. Ed.*, 2014, **53**, 74–100.

5 F. Roudesly, J. Oble and G. Poli, *J. Mol. Catal. A Chem.*, 2017, **426**, 275–296.

6 C. Li, *Acc. Chem. Res.*, 2009, **42**, 335–344.

7 P. Anastas and J. Warner, *Green Chemistry: Theory and Practice*, Oxford University Press, 1998.

8 U. Rinner, H. L. Hillebrenner, D. R. Adams, T. Hudlicky and G. R. Pettit, *Bioorg. Med. Chem. Lett.*, 2004, **14**, 2911–2915.

9 D. Lucet, T. Le Gall and C. Mioskowski, *Angew. Chemie - Int. Ed.*, 1998, **37**, 2580–2627.

10 Z. Li, D. S. Bohle and C.-J. Li, *Proc. Natl. Acad. Sci. U. S. A.*, 2006, **103**, 8928–8933.

11 N. Chatani, T. Asaumi, S. Yorimitsu, T. Ikeda, F. Kakiuchi and S. Murai, *J. Am. Chem. Soc.*, 2001, **123**, 10935–10941.

12 K. Alagiri, G. S. R. Kumara and K. R. Prabhu, *Chem. Commun.*, 2011, **47**, 11787.

13 M. Ghobrial, K. Harhammer, M. D. Mihovilovic, M. Schnuerch and M. Schnürch, *Chem. Commun.*, 2010, **46**, 8836–8.

14 T. Sugiishi and H. Nakamura, *J. Am. Chem. Soc.*, 2012, **134**, 2504–2507.

15 M. Z. Wang, C. Y. Zhou, M. K. Wong and C. M. Che, *Chem. - A Eur. J.*, 2010, **16**, 5723–5735.

16 H. Mo and W. Bao, *Adv. Synth. Catal.*, 2009, **351**, 2845–2849.

17 W.-J. J. Yoo and S. Kobayashi, *Green Chem.*, 2014, **16**, 2438.

18 L. D. Shirley, V. Ceban, M. Meazza and R. Rios, *ChemistrySelect*, 2016, **1**, 13–15.

19 M. Rueping, J. Zoller, D. C. Fabry, K. Poscharny, R. M. Koenigs, T. E. Weirich and J. Mayer, *Chem. - A Eur. J.*, 2012, **18**, 3478–3481.

20 T. Zeng, G. Song, A. Moores and C. J. Li, *Synlett*, 2010, **13**, 2002–2008.

21 S.-L. Zhu, S. Ou, M. Zhao, H. Shen and C.-D. Wu, *Dalt. Trans.*, 2015, **44**, 2038–2041.

22 X.-L. Yang, C. Zou, Y. He, M. Zhao, B. Chen, S. Xiang, M. O'Keeffe and C.-D. Wu, *Chem. - A Eur. J.*, 2014, **20**, 1447–1452.

23 W.-Q. Zhang, Q.-Y. Li, Q. Zhang, Y. Lu, H. Lu, W. Wang, X. Zhao and X.-J. Wang, *Inorg. Chem.*, 2016, **55**, 1005–1007.

24 C. Wang, Z. Xie, K. E. DeKrafft and W. Lin, *J. Am. Chem. Soc.*, 2011, **133**, 13445–13454.

25 C. J. Wu, J. J. Zhong, Q. Y. Meng, T. Lei, X. W. Gao, C. H. Tung and L. Z. Wu, *Org. Lett.*, 2015, **17**, 884–887.

26 J. Herrmann, *Catal. Today*, 1999, **53**, 115–129.

27 B. Wang, D. P. Shelar, X. Z. Han, T. T. Li, X. Guan, W. Lu, K. Liu, Y. Chen, W. F. Fu and C. M. Che, *Chem. - A Eur. J.*, 2015, **21**, 1184–1190.

28 W. P. To, Y. Liu, T. C. Lau and C. M. Che, *Chem. - A Eur. J.*, 2013, **19**, 5654–5664.

29 L. Huang and J. Zhao, *RSC Adv.*, 2013, **3**, 23377–23388.

30 R. Neumann and M. Dahan, *Nature*, 1997, **388**, 353–355.

31 C. Döbler, G. Mehltretter and M. Beller, *Angew. Chemie - Int. Ed.*, 1999, **38**, 3026–3028.

32 L. Bernardi, B. F. Bonini, E. Capito, G. Dessole, M. Comes-Franchini, M. Fochi and A. Ricci, *J. Org. Chem.*, 2004, **69**, 8168–8171.

33 H. Adams, J. C. Anderson, S. Peace and A. M. K. Pennell, *J. Org. Chem.*, 1998, **63**, 9932–9934.

34 H. Bartling, A. Eisenhofer, B. Konig and R. M. Gschwind, *J. Am. Chem. Soc.*, 2016, **138**, 11860–11871.

35 V. Ramamurthy, *Photochemistry in Confined Spaces*, VCH, New York, 1991.

36 A. Corma and H. Garcia, *Chem. Commun.*, 2004, **13**, 1443–1459.

37 D. Farrusseng, *Metal-Organic Frameworks: Applications from Catalysis to Gas Storage*, John Wiley & Sons, 2011.

38 A. Corma, H. García and F. X. Llabrés i Xamena, *Chem. Rev.*, 2010, **110**, 4606–4655.

39 J. Lee, O. K. Farha, J. Roberts, K. a Scheidt, S. T. Nguyen and J. T. Hupp, *Chem. Soc. Rev.*, 2009, **38**, 1450–1459.

40 M. Jacoby, *Chem. Eng. News*, 2013, **91**, 34–35.

41 C. C. Wang, J. R. Li, X. L. Lv, Y. Q. Zhang and G. S. Guo, *Energy Environ. Sci.*, 2014, **7**, 2831–2867.

42 S. Wang and X. Wang, *Small*, 2015, **11**, 3097–3112.

43 K. Meyer, M. Ranocchiari and J. A. van Bokhoven, *Energy Environ. Sci.*, 2015, **8**, 1923–1937.

44 S. S. Y. Chui, S. M. F. Lo, J. P. H. Charmant, a G. Orpen and I. D. Williams, *Science (80-.).*, 1999, **283**, 1148–1150.

45 M. a. Nasalevich, M. van der Veen, F. Kapteijn and J. Gascon, *CrystEngComm*, 2014, **16**, 4919.

46 K. G. M. Laurier, F. Vermoortele, R. Ameloot, D. E. De Vos, J. Hofkens and M. B. J. Roeffaers, *J. Am. Chem. Soc.*, 2013, **135**, 14488–14491.

47 T. Zhang and W. Lin, *Chem. Soc. Rev.*, 2014, **43**, 5982–5993.

48 A. Dhakshinamoorthy, A. M. Asiri and H. García, *Angew. Chemie - Int. Ed.*, 2016, **55**, 5414–5445.

49 A. Dhakshinamoorthy, M. Alvaro and H. Garcia, *ACS Catal.*, 2011, **1**, 48–53.

50 S. Mosleh, M. R. Rahimi, M. Ghaedi, K. Dashtian and S. Hajati, *RSC Adv.*, 2016, **6**, 17204–17214.

51 K. S. Park, Z. Ni, A. P. Cote, J. Y. Choi, R. Huang, F. J. Uribe-Romo, H. K. Chae, M. O’Keeffe and O. M. Yaghi, *Proc. Natl. Acad. Sci.*, 2006, **103**, 10186–10191.

52 A. Phan, C. J. Doonan, F. J. Uribe-Romo, C. B. Knobler, M. Okeeffe and O. M. Yaghi, *Acc. Chem. Res.*, 2010, **43**, 58–67.

53 S. R. Venna and M. A. Carreon, *J. Am. Chem. Soc.*, 2010, **132**, 76–78.

54 A. F. Gross, E. Sherman and J. J. Vajo, *Dalt. Trans.*, 2012, **41**, 5458–5460.

55 C. Chizallet, S. Lazare, D. Bazer-Bachi, F. Bonnier, V. Lecocq, E. Soyer, A. A. Quoineaud and N. Bats, *J. Am. Chem. Soc.*, 2010, **132**, 12365–12377.

56 U. P. N. Tran, K. K. A. Le and N. T. S. Phan, *ACS Catal.*, 2011, **1**, 120–127.

57 M. Zhu, D. Srinivas, S. Bhogeswararao, P. Ratnasamy and M. A. Carreon, *Catal. Commun.*, 2013, **32**, 36–40.

58 Y. Li, F. Liang, H. Bux, W. Yang and J. Caro, *J. Memb. Sci.*, 2010, **354**, 48–54.

59 J. Zakzeski, A. Dbczak, P. C. a Bruijnincx and B. M. Weckhuysen, *Appl. Catal. A Gen.*, 2011, **394**, 79–85.

60 L. T. L. Nguyen, K. K. a. Le, H. X. Truong and N. T. S. Phan, *Catal. Sci. Technol.*, 2012, **2**, 521–528.

61 S. Wang, W. Yao, J. Lin, Z. Ding and X. Wang, *Angew. Chemie - Int. Ed.*, 2014, **53**, 1034–1038.

62 S. Wang and X. Wang, *Appl. Catal. B Environ.*, 2015, **162**, 494–500.

63 P. Zhao, G. I. Lampronti, G. O. Lloyd, M. T. Wharmby, S. Facq, A. K. Cheetham and S. A. T. Redfern, *Chem. Mater.*, 2014, **26**, 1767–1769.

64 Y. Sun, Y. Li and J. Tan, *ACS Appl. Mater. Interfaces*, 2018, **10**, 41831–41838.

65 H. Bux, F. Liang, Y. Li, J. Cravillon and M. Wiebcke, *J. Am. Chem. Soc.*, 2009, **131**, 16000–16001.

66 T. Truong, T. M. Hoang, C. K. Nguyen, Q. T. N. Huynh and N. T. S. Phan, *RSC Adv.*, 2015, **5**, 24769–24776.

67 K. Y. A. Lin and H. A. Chang, *J. Taiwan Inst. Chem. Eng.*, 2015, **53**, 40–45.

68 H. Yang, X.-W. He, F. Wang, Y. Kang and J. Zhang, *J. Mater. Chem.*, 2012, **22**, 21849.

69 B. Pattengale, S. Yang, J. Ludwig, Z. Huang, X. Zhang and J. Huang, *J. Am. Chem. Soc.*, 2016, **138**, 8072–8075.

70 W. Zhan, Q. Kuang, J. Zhou, X. Kong, Z. Xie and L. Zheng, *J. Am. Chem. Soc.*, 2012, **135**, 1926–1933.

71 T. T. Isimjan, H. Kazemian, S. Rohani and A. K. Ray, *J. Mater. Chem.*, 2010, **20**, 10241.

72 C. Dey and R. Banerjee, *Chem. Commun.*, 2013, **49**, 6617.

73 D. Buso, K. M. Nairn, M. Gimona, A. J. Hill and P. Falcaro, *Chem. Mater.*, 2011, **23**, 929–934.

74 G. Lu, S. Li, Z. Guo, O. K. Farha, B. G. Hauser, X. Qi, Y. Wang, X. Wang, S. Han, X. Liu, J. S. DuChene, H. Zhang, Q. Zhang, X. Chen, J. Ma, S. C. J. Loo, W. D. Wei, Y. Yang, J. T. Hupp and F. Huo, *Nat. Chem.*, 2012, **4**, 310–316.

75 P. Falcaro, A. J. Hill, K. M. Nairn, J. Jasieniak, J. I. Mardel, T. J. Bastow, S. C. Mayo, M. Gimona, D. Gomez, H. J. Whitfield, R. Riccò, A. Patelli, B. Marmiroli, H. Amenitsch, T. Colson, L. Villanova and D. Buso, *Nat. Commun.*, 2011, **2**, 237–245.

76 J. A. Johnson, J. Luo, X. Zhang, Y. S. Chen, M. D. Morton, E. Echeverría, F. E. Torres and J. Zhang, *ACS Catal.*, 2015, **5**, 5283–5291.

77 T. Lazarides, T. McCormick, P. Du, G. Luo, B. Lindley and R. Eisenberg, *J. Am. Chem. Soc.*, 2009, **131**, 9192–9194.

78 N. L. Torad, M. Hu, Y. Kamachi, K. Takai, M. Imura, M. Naito, Y. Yamauchi, E. S. Material, C. C. This and T. R. Society, *Chem. Commun.*, 2013, **49**, 2521–2523.

79 N. A. Khan, I. J. Kang, H. Y. Seok and S. H. Jhung, *Chem. Eng. J.*, 2011, **166**, 1152–1157.

80 J. Cravillon, R. Nayuk, S. Springer, A. Feldhoff, K. Huber and M. Wiebcke, *Chem. Mater.*, 2011, **23**, 2130–2141.

81 G. A. Somorjai and Y. Li, *Introduction to Surface Chemistry and Catalysis*, John Wiley & Sons, 2nd edn., 2010.

82 K. M. Bratlie, H. Lee, K. Komvopoulos, P. Yang and G. A. Somorjai, *Nano Lett.*, 2007, **7**, 3097–3101.

83 V. Komanicky, H. Iddir, K.-C. Chang, A. Menzel, G. Karapetrov, D. Hennessy, P. Zapol and H. You, *J. Am. Chem. Soc.*, 2009, **131**, 5732–5733.

84 J. Cravillon, C. A. Schröder, R. Nayuk, J. Gummel, K. Huber and M. Wiebcke, *Angew. Chemie - Int. Ed.*, 2011, **50**, 8067–8071.

85 J. A. Widegren and R. G. Finke, *J. Mol. Catal. A Chem.*, 2003, **198**, 317–341.

86 K. V. Yumashev, I. A. Denisov, N. N. Posnov, N. V. Kuleshov and R. Moncorge, *J. Alloys Compd.*, 2002, **341**, 366–370.

87 R. Trujillano, F. Villain, C. Louis and J. F. Lambert, *J. Phys. Chem. C*, 2007, **111**, 7152–7164.

88 R. Banerjee, A. Phan, B. Wang, C. Knobler, H. Furukawa, M. O'Keeffe and O. M. Yaghi, *Science (80-.).*, 2008, **319**, 939–944.

89 Z. Öztürk, J. P. Hofmann, M. Lutz, M. Mazaj, N. Z. Logar and B. M. Weckhuysen, *Eur. J. Inorg. Chem.*, 2015, **2015**, 1625–1630.

90 G. Férey, *Chem. Soc. Rev.*, 2008, **37**, 191–214.

91 J. Qian, F. Sun and L. Qin, *Mater. Lett.*, 2012, **82**, 220–223.

92 Y.-S. Li, F.-Y. Liang, H. Bux, A. Feldhoff, W.-S. Yang and J. Caro, *Angew. Chemie Int. Ed.*, 2010, **49**, 548–551.

93 F. Hillman, J. M. Zimmerman, S. Paek, M. R. A. Hamid, W. T. Lim and H. Jeong, *J. Mater. Chem. A*, 2017, **5**, 6090–6099.

94 A. Moen, D. G. Nicholson, B. S. Clausen, P. L. Hansen, A. Molenbroek and G. Steffensen, *Chem. Mater.*, 1997, **9**, 1241–1247.

95 R. Sarangi, J. Cho, W. Nam and E. I. Solomon, *Inorg. Chem.*, 2011, **50**, 614–620.

96 S. Aguado, G. Bergeret, M. P. Titus, V. Moizan, C. Nieto-Draghi, N. Bats and D. Farrusseng, *New J. Chem.*, 2011, **35**, 546–550.

97 E. Bonaccorsi and S. Merlino, *Rev. Mineral. Geochemistry*, 2005, **57**.

98 T. D. Bennett and A. K. Cheetham, *Acc. Chem. Res.*, 2014, **47**, 1555–1562.

99 D. M. Jiang, A. D. Burrows and K. J. Edler, *CrystEngComm*, 2011, **13**, 6916–6919.

100 Q.-F. Yang, X.-B. Cui, J.-H. Yu, J. Lu, X.-Y. Yu, X. Zhang, J.-Q. Xu, Q. Hou and T.-G. Wang, *Cryst. Eng. Comm.*, 2008, **10**, 1534–1541.

101 B. Reif, F. Fabisch, M. Hovestadt, M. Hartmann and W. Schwieger, *Microporous Mesoporous Mater.*, 2017, **243**, 65–68.

102 Q. Liu, Y. N. Li, H. H. Zhang, B. Chen, C. H. Tung and L. Z. Wu, *Chem. - A Eur. J.*, 2012, **18**, 620–627.

103 Z. Li and C. J. Li, *J. Am. Chem. Soc.*, 2005, **127**, 3672–3673.

104 H. Li, Y. Yang, C. He, L. Zeng and C. Duan, *ACS Catal.*, 2019, **9**, 422–430.

105 M. Brzozowski, J. A. Forni, G. P. Savage and A. Polyzos, *Chem. Commun.*, 2015, **51**, 334.

106 Q. Li and H. Kim, *Fuel Process. Technol.*, 2012, **100**, 43–48.

Chapter 4: Functionalisation of Benzoxazoles

4.1 Introduction

4.1.1 Functionalisation of Benzoxazoles

After the success of Co-ZIFs in the aza-Henry reaction, different CDCs were investigated to find another one with the potential for these materials to offer an exciting alternative to the current reported systems. As with C-C bond forming CDCs, those forming new C−N bonds have proven to be of significant importance in Organic Chemistry because they mitigate the need to prefunctionalise the C−H or N−H bonds of the starting materials, and formally, hydrogen is the only by-product.[1–3] The amination of benzoxazole to afford 2-aminobenzoxazoles has attracted much attention, in part because of the ease with which they can be formed using a CDC protocol and their ubiquity as substructures in many therapeutically important molecules. A few examples are shown in Figure 48, these compounds have been explored in the treatment of insomnia (a),[4] central nervous system disorders (b),[5] and Alzheimer's (c).[6]

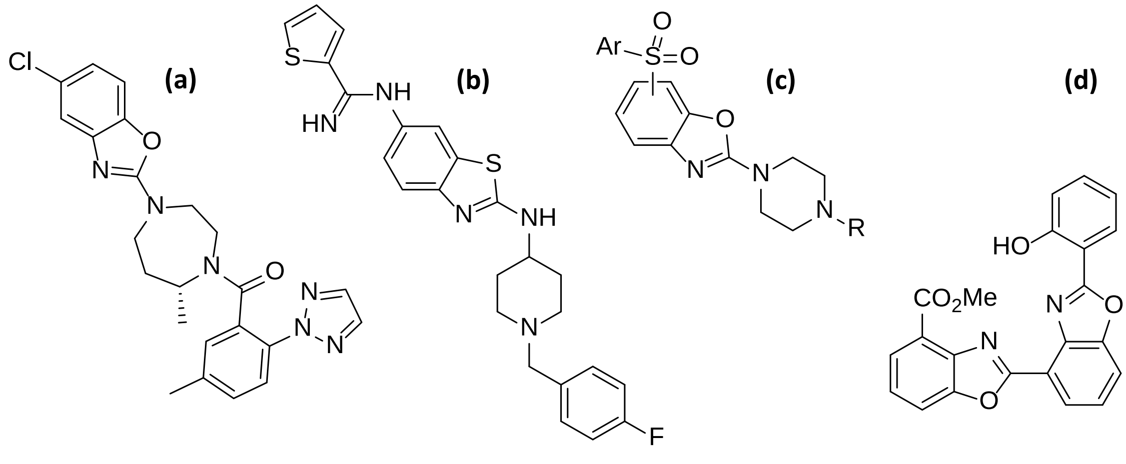

Figure 48: Literature examples of functionalised azoles.

In general, heteroarylamines are ubiquitous in pharmaceuticals and functional materials.[7–10] The benzoxazole motif is a constituent of a wide range of biologically active natural products, and often incorporated in drug design. As important scaffolds, an increasing number of 2-substituted benzoxazoles have been extensively studied for their biological and therapeutic activities from 1990 until today. These include the treatment of autoimmune diseases,[11] as an anticancer agent,[12,13] and their antibacterial or antifungal activities.[14–16] One such example is UK-1 (Figure 48d) which displays a wide spectrum of potent anticancer activity against leukaemia, lymphoma, and certain solid tumour-derived cell lines.[17,18] Given the importance of the azole motif in medicinal and material chemistry, significant efforts have been focused on the development of new synthetic procedures for the generation of these heterocyclic compounds.

Buchwald-Hartwig-type amination reactions and those mediated by copper are the most powerful and reliable methods available for N-arylation.[19–23] However, since these procedures employ aryl halides as the starting material, the direct amination of a C-H bond in heteroaromatics would avoid additional halogenation steps and the creation of halogenated waste. Among the many types of C-H functionalisation of azoles documented is direct C-H amination. It provides a rapid and straightforward route to the heteroarylamines, pioneered by Mori,[24,25] Schreiber,[26] Chang,[27,28] and Miura.[9,29] Although C-N bond formation takes place regioselectively at the 2-position of azoles, the reaction conditions employed were rather harsh (120-140 °C), or involved undesirable precursors such as chloroamines. The transition metal catalysed C-amination,[30–32] and in particular the direct C-H functionalisation of azole rings,[2,33–37] is a powerful and efficient approach in organic synthesis. These methods are typically mediated by a copper species under basic conditions and an oxygen atmosphere, with organocopper species proposed as intermediates (Scheme 17, pathway A).[38] Otherwise, a variety of catalytic systems have been employed under acidic conditions, with an isolatable intermediate (Scheme 17, pathway B). The reactions tend to show an advantage in atom efficiency compared to related cross-coupling with organometallic compounds.[39]

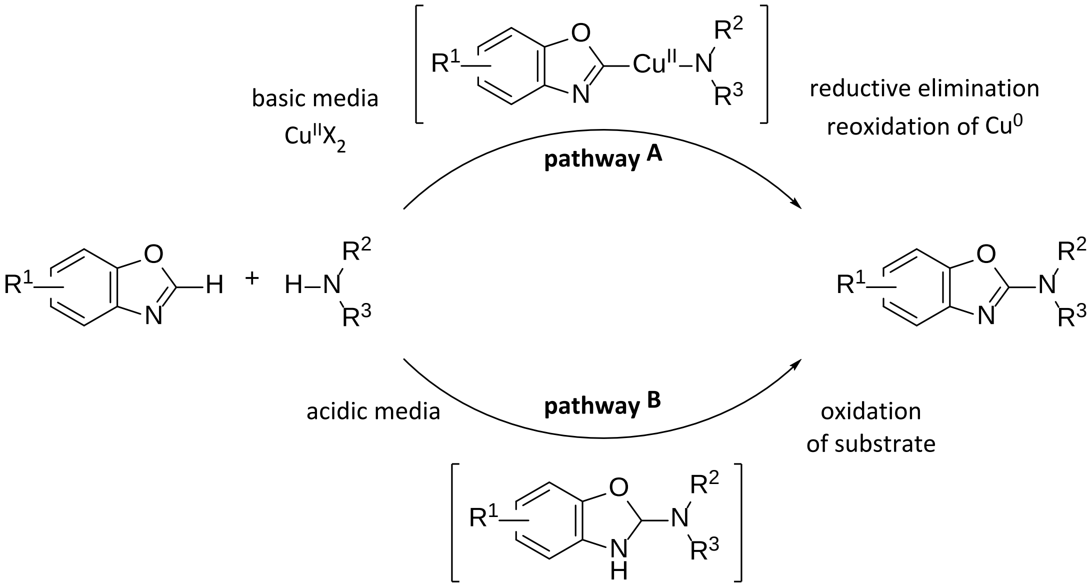

Scheme 17: Typical methods for the direct amination of benzoxazoles.

Alternatively, rather than functionalising a benzoxazole directly, more complex substrates can be used during synthesis of the scaffold itself to achieve the desired substituted product. Classical methods for the synthesis of benzoxazoles involve two approaches. One is the copper-catalysed intra-molecular orthoarylation of *o*-haloanilides, or the intermolecular domino annulations of *o*-arylhalides with acyl-amides.[40–42] The second approach is the condensation of 2-aminophenol with carboxylic acid derivatives under strong acid/high temperature conditions,[43] or as represented in Scheme 18, aldehydes with subsequent oxidation of the phenolic imine using strong oxidants such as DDQ,[44] $PhI(OAc)_2$,[45] or PCC.[46]

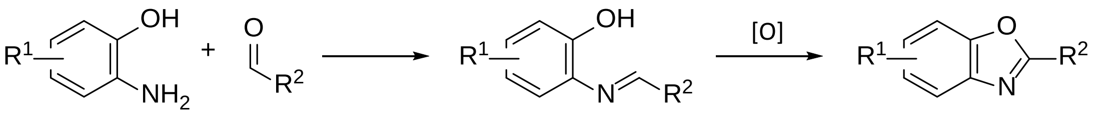

Scheme 18: Representation for the formation of functionalised benzoxazoles under oxidative conditions.

Catalytic oxidative reactions using oxygen as the terminal oxidant have recently received more attention because of their green chemistry and atom economy aspects. So far, the aerobic catalytic synthesis of benzoxazoles has been reported with iron(III) chloride,[47] palladium(II) acetate,[48] alum,[49] 4-methoxy-TEMPO,[50] copper nanoclusters,[51] and activated carbon.[52] However, in most cases, relatively high catalyst loading/reaction temperatures are required for the preparation of these 5-membered heterocycles. New catalytic methodologies to prepare these compounds under mild conditions are highly desirable.

Although amidines are a prevalent structural motif in medicinal chemistry, displaying high bioactivities,[53–55] their use as a synthon for the formation of various amine-containing compounds has been less widespread. This is especially notable upon considering that, although imines exhibit a variety of reactivity through addition, reduction, or cycloaddition reactions, the structurally analogous amidines have not been frequently utilised except in limited cyclisation sequences.[56,57]

Among the various approaches to the amino-substituted structures, direct C–H amination has been focused on for its atom economy, leading to inspiring progress in the past decade.[24,26,27,29] Whilst at this stage, 2-substituted benzoxazoles are generally synthesised by the oxidative cyclisation of phenolic amidines/imines, mediated by strong oxidants working in concert with transition metal catalysts.[51,58–60]

Considering the significance of such motifs, and seeing the potential that Co-ZIFs had following their success with the aza-Henry, these reactions seemed ideal for exploring Co-ZIF catalysis.

4.1.1.1 Amination of Benzoxazoles

To determine how the Co-ZIFs would compare with the current literature, a table has been included in the Appendix detailing some reports for the amination of (5-methyl)benzoxazole with piperidine (Scheme 19). The key examples are expanded on here.

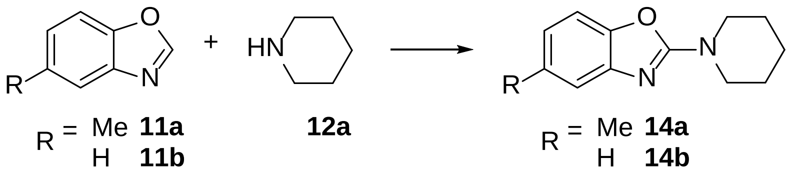

Scheme 19: Amination of (5-methyl)benzoxazole with piperidine.

Metal-free systems primarily focus on halogenating agents which promote the rearomatisation of the ring.[28,61,62] Although employing stoichiometric amounts of undesirable reagents such as (diacetoxyiodo)benzene/NBS/IBX, excellent yields of over 90 % can be achieved in as little as 5 minutes from the isolated intermediate. More innovative examples include the electrochemical oxidation of the intermediate with catalytic quantities of tetrabutylammonium iodide.[63] This method garnered mixed success depending on the substrates tested, ranging from excellent yields of over 95 %, to disappointing ones nearer 30 %. Haemoglobin VHb was found to form the radical intermediates arising from TBHP, which go on to oxidise the substrate under mild conditions.[64] There are also reports utilising light, whether by inducing the formation of radicals from tetrabromomethane,[65] or promoting a SET with a ruthenium complex.[66] Most frequently, homogeneous transition metal complexes have been employed, including iron,[59,67] copper,[68,69] and nickel.[70] The metals have been proposed to induce radical formation from oxidants such as TBHP, or to help draw the two substrates together to facilitate a reaction. A main drawback to these catalytic systems is their homogeneous nature, since difficult separation from reaction mixtures means that the catalyst can rarely be reused. As established previously, heterogeneous catalysts tend to have a much easier and cheaper recovery, and often benefit from increased stability. In an effort to reduce waste and improve efficiency, thus adhering to the principles of green chemistry,[71] it is unsurprising that more and more research is going into discovering heterogeneous systems which can replace their conventional homogeneous counterparts. By incorporating the active transition metal in a framework, there is the opportunity to retain the high catalytic activity, and reuse the material after the reaction has finished. This presents another opportunity for MOFs to be explored as catalysts, taking advantage of their hybrid nature permitting a range of synthetic modifications to tune catalytic performance.[72–74] Examples of heterogeneous catalysis are limited for the amination of benzoxazoles. Recent reports include copper encapsulated in TiO$_2$,[75] although moderate yields simply declined over the course of four cycles. Porous γ-MnO$_2$ on the other hand maintained high yields through a few cycles before starting to deteriorate.[76]

The report which inspired the exploration of Co-ZIFs was that of the homogeneous complex Co(OAc)$_2$ with TBHP.[77] High yields of up to 84 % were reported after 6 hours, with a wide scope of azoles and amines. The aim was to achieve the same high yields with Co-ZIFs, utilising their heterogeneous nature to recycle the catalyst and replicate these results over multiple cycles, an aim somewhat achieved by Chen et al. in a publication from 2018.[78] They discovered that an interpenetrated mixed-ligand cobalt MOF synthesised under hydrothermal conditions, and exhibiting good chemical stabilities, could achieve yields of 26-96 % in 12 hours in conjunction with acetic acid and TBHP, with minimal loss of activity across five cycles.

Whilst the overall reaction is the formation of a new C-N bond, many of the catalysts were only involved in the rearomatisation of the ring *via* the oxidative formation of a C-O bond from a C-H and O-H bond. There are similarities between this rearomatisation and the aza-Henry reaction, such as the C_{sp2}-H being adjacent to a tertiary amine and a conjugated group in both reactions. Both the homogeneous and heterogeneous reports of cobalt catalysis suggest that the cobalt centre triggers radical formation from the TBHP, which goes on to rearomatise the ring and form the desired product.[78,79] This can be seen in the partial mechanism in Scheme 20 for the amination of 5-methylbenzoxazole with piperidine, where the intermediate **13a** can be isolated after formation, with or without acetic acid. It seems safe to assume that the Co-ZIFs would behave in a similar fashion, which could be supported by radical-trapping experiments. For example, Guo et al. found that adding TEMPO as a radical scavenger to their reaction using ZIF-67 and TBHP significantly reduced the yield achieved.[80]

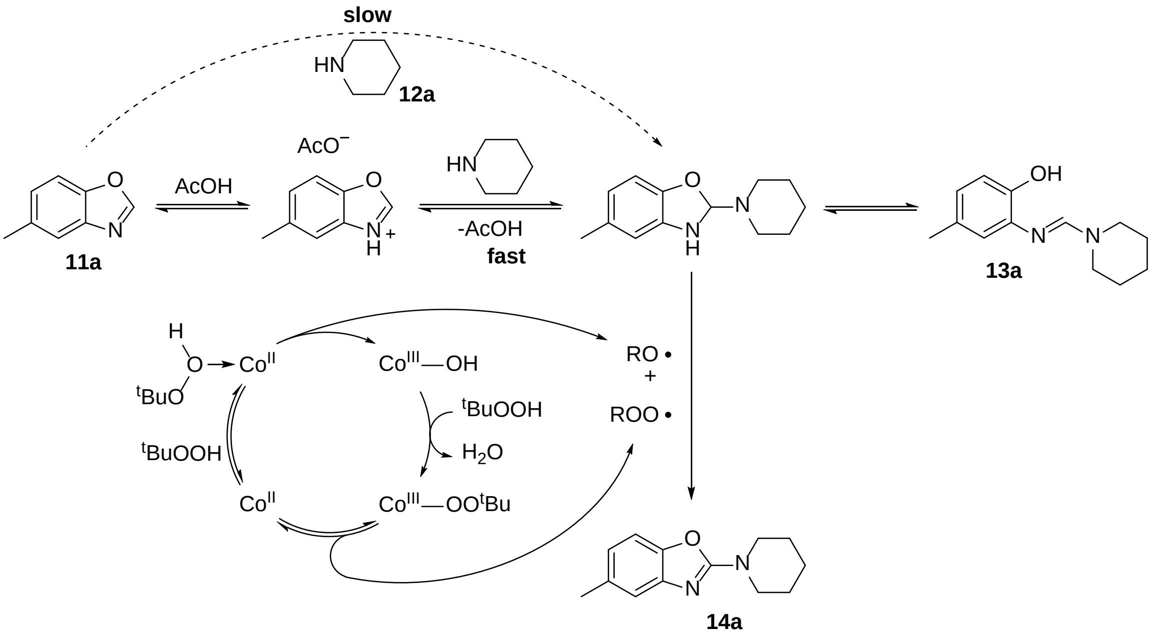

Scheme 20: Proposed reaction mechanism for the amination of 5-methylbenzoxazole with piperidine, using cobalt catalysis.

As cobalt catalysis has already been reported with this reaction, including the use of a heterogeneous MOF, the aim for employing Co-ZIFs in this reaction is to achieve comparable if not higher yields across the substrate scope, ideally in less time, and over multiple cycles. The chance to remove an additive from the reaction, whether it is the acetic acid or TBHP, would also be beneficial.

4.1.1.2 Formation of 2-Substituted Benzoxazole

Similarly to Table 34 collected for the amination of (5-methyl)benzoxazole with piperidine, Table 35 has been included in the Appendix to detail several reports for the formation of benzoxazole from 2-aminophenol and benzaldehyde (Scheme 21).

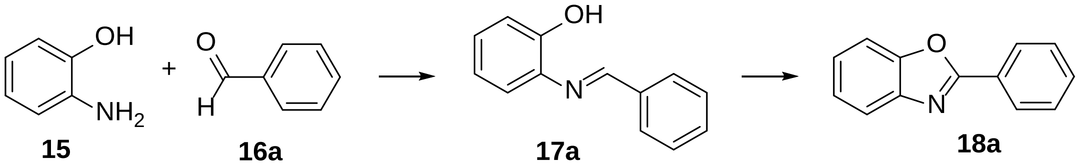

Scheme 21: Formation of 2-phenylbenzoxazole from 2-aminophenol and benzaldehyde.

Over the past few years, homogeneous examples for this reaction have become less common, with high performing examples involving the use of a basic additive such as KCN[81,82] or a strong oxidant.[44] High temperatures of 120-140 °C are frequently involved in both homogeneous and heterogeneous examples: 4-methoxy-TEMPO achieved 90 % in 5 hours,[50] while recyclable materials such as an ionic liquid grafted onto silica,[83] and a superacid Hf(IV)-based MOF[84] were able to achieve yields of 98 and 95 % respectively, with only a slight loss over five cycles. There are also multiple examples that run at room temperature; they can involve heavy metals such as europium[85] and bismuth,[86] or the more environmentally friendly zinc.[87]

One report utilised a recyclable heterogeneous cobalt catalyst.[88] By adsorbing nitrogen-ligated cobalt(II) acetate complexes on SiO_2, followed by pyrolysis at 800 °C, they were able to synthesise a Co-based nanocomposite catalyst. It was successful in promoting the aerobic oxidation of the Schiff bases with reported yields of 86-99 % in 24 hours, and no loss of activity over five cycles. The Co-ZIFs would ideally achieve comparative yields in less time, while benefitting from a less intensive synthetic procedure to form the catalyst itself.

There is no clear consensus on how the catalysts typically promote the reaction. Often they are reported to aid the formation of the imine intermediate, while the second step is a simple oxidation, although some reports do propose their metal catalysts play a role in the oxidation step.[85,89] A common theme was the use of oxygen as an oxidant, whether from the air, or a more saturated system. Thus it would be desirable if the Co-ZIFs could also work under these conditions, and/or utilise light. This would help them to stand out from the current literature, where it is common for a recyclable heterogeneous catalyst to achieve yields of over 90 %.

Considering the similarities of the intermediate for the amination product, and that of the aryl product, the partial mechanism in Scheme 22 illustrates how the reaction could undergo *via* the same radical formation from TBHP, initiated by the cobalt centres. Once again, this proposal could be supported by radical-trapping experiments.

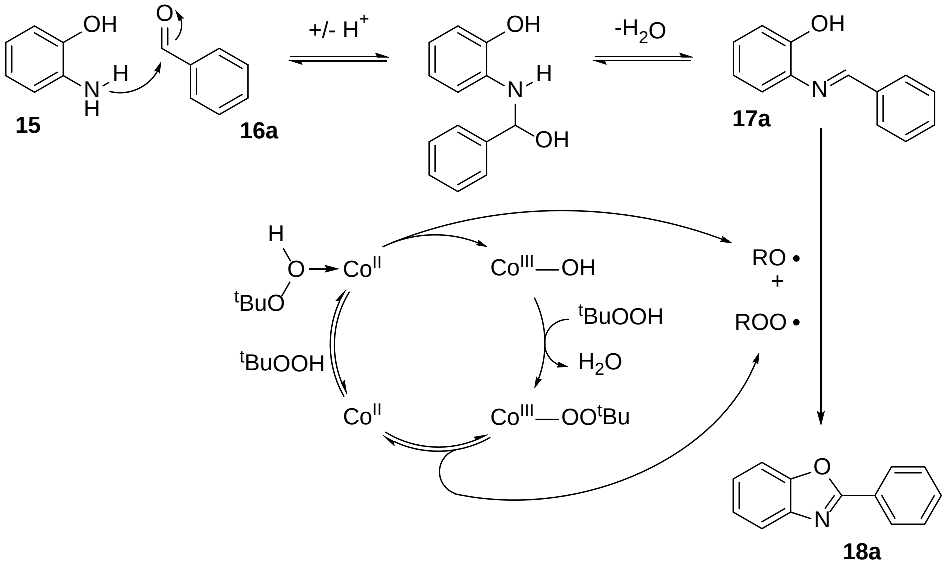

Scheme 22: Proposed reaction mechanism for the formation of a 2-substituted benzoxazole with 2-aminophenol and benzaldehyde, using cobalt catalysis.

4.1.2 Stability of Co-ZIFs

Although significant progress has been made in the use of MOFs as catalysts, many challenges remain. Due to their nature, such as the hydrophilic metal nodes, many reported MOF catalysts are sensitive to air, moisture and different organic solvents, which have limited the practicality of MOFs in certain transformations. Examination of a framework's stability, and their resistance to different solvents and conditions, is essential to studying their applications.[72,90–92]

In contrast, ZIFs have displayed exceptional chemical and thermal stability, surpassing that of most MOFs,[93] as demonstrated in Chapter 3, where the Co-ZIFs displayed high thermal stability, even after the removal of guest molecules. Whilst the hydrophobic pore and surface structures reduce the effectiveness of these materials as catalysts in aqueous media, it also contributes to their high hydrothermal stability. The higher basicity of the imidazolate linker compared to other linkers typically used in MOF synthesis, such as carboxylates, result in stronger metal-ligand bonds and enhanced stability towards water.[94] ZIF-67, among other ZIFs, have expressed stability in a variety of boiling solvents, including methanol and toluene. [95–97]

However, they are not without weakness, ZIF-8 was reported to degrade with ammonia and hydrogen sulphide.[92] Significantly, while many reports note strength under basic conditions, enduring boiling concentrated solutions of sodium hydroxide for example, they tend to avoid mention of their stability in acidic media. To become established as a catalyst in a range of applications, the frameworks should also be stable under oxidizing conditions, although there are limited publications which have investigated this aspect of ZIF nature.

Leus et al. conducted systematic and long-term stability tests on ZIF-8, which due to the isostructural nature and established similarities to ZIF-9 and ZIF-67, can be used to further our understanding of what conditions these materials may endure.[98] The paper confirmed ZIF-8 can withstand hydrothermal treatment with no changes observed to the crystal structure and only a minor decrease in surface area measurements. However, storage in water over the course of two months led to the appearance of new diffraction peaks, attributed to the chemical reaction of the framework with CO_2 in the presence of moisture.[99] ZIF-8 retained good crystallinity after 3 days at pH = 4, but significant degradation had occurred after 2 months, with new diffraction peaks observed which could signify the carbonates noted after long-term storage in water. The framework immediately dissolved in a solution of pH = 0. ZIF-8 displayed good stability in basic media, no changes being observed to the crystal structure and only a minor decrease in surface area measurements after 3 days, but once again the appearance of peaks relating to carbonates appeared after long-term exposure. Finally Leus et al. trialled the exposure to the commonly used oxidant H_2O_2. Only the surface area measurements had been slightly affected after 3 days but they discovered the material was almost fully amorphised after 2 months.

In Chapter 3, the Co-ZIFs were characterised after stirring in nitromethane, under illumination, for 6 hours. pXRD revealed both samples retained their structural integrity, but the reduced intensity suggested a loss of crystallinity, whilst surface area measurements for ZIF-67 showed a drop from 1303 m^2g^{-1} to 1177 m^2g^{-1}. The catalyst was recovered after five cycles and displayed significant changes. The pXRD revealed loss of all peaks representing ZIF-9, with new ones which could signify the formation of complex carbonates such as those seen with ZIF-8 or ZIF-67, but to the author's knowledge this has not been investigated for ZIF-9 or the isostructural ZIF-7. Regardless, any changes which did occur to the ZIF-9 framework had minimal effect on the catalytic activity. ZIF-67 was completely amorphised, which appeared to aid catalytic activity, as yields continued to increase over the five cycles. Linking these results with that of ZIF-8 in the literature, it can be ascertained that the catalysts are transformed under redox conditions, but this does not necessarily equate to framework breakdown or a drop in catalytic activity. Applying this knowledge to the conditions employed with other cobalt catalysts in the benzoxazole functionalisation reactions, the Co-ZIFs can be assumed to retain their integrity under weakly acidic conditions, but leaching and eventual breakdown may occur. Any accessible Co^{II} in ZIF-9/67 is also likely to be converted to Co^{III} in the presence of TBHP, but it remains unclear to what extent structural changes will occur, and what this would mean for the framework and any wider applications.

4.1.3 Microwave Chemistry

Optimisation is a known bottleneck in the drug discovery process, hence the desire for technologies which allow for more rapid synthesis. In the interest of green and sustainable chemistry, there is a great desire to find more efficient modes of stimulating chemical reactions than conventional heating. This includes photochemistry, as discussed in Chapter 3, but also ultrasonic and high-pressure systems. Microwaves are a more efficient form of heating than conventional means such as oil baths, reaching higher temperatures quickly. They heat the system internally by direct coupling of microwave energy with polar molecules, be they solvents, reagents, or catalysts.[100] This efficiency leads to a dramatic reduction in residence times from days or hours to minutes or seconds. A drawback of heterogeneous catalysis is longer reaction times, which can be combatted with microwave chemistry. This would allow many reaction parameters such as time, temperature, solvents, concentration, and catalysts, to be evaluated in a fraction of the time they would otherwise. Compound libraries can then be rapidly synthesised in either a parallel or sequential automated format.

In the electromagnetic spectrum, microwave radiation is located between IR and radio with a frequency range of 300 MHz to 300 GHz. While ultraviolet and visible radiation initiates reactions *via* valence electrons (photochemistry), and IR excites *via* vibrations, microwaves excite molecular rotations. Lab systems generally work at a wavelength of 12.24 cm (2.45 GHz), corresponding to an energy of 0.00001 eV, which is not sufficient to even break a H-bond (0.04-0.44 eV). Therefore, it cannot induce chemical reactions, as no bond breaking can occur.

If a non-polar solvent is used, then selective heating of the catalyst and substrates can be achieved. A polar catalyst can absorb extra energy and heat to a higher temperature than the overall reaction temperature, thus making the process more energy efficient. The temperature distribution is also unique to microwave irradiation and can enhance adsorption and desorption of the substrate on the catalyst surface.[101] Catalytic processes with short reaction times lower residence time at high temperature, and safeguard the catalyst from deactivation and decomposition, consequently increasing the overall efficiency of the catalyst and entire protocol.[102]

Microwave chemistry is known to reduce side reactions, increase yields, and improve reproducibility. [103] With conventional heating, the temperature of the reaction vessel is higher than that of the mixture. In contrast, microwave irradiation produces homogenous internal heating, and reaction vessels are usually made out of materials that can be considered microwave transparent, such as borosilicate glass or quartz. This minimises wall effects, which may lead to specific microwave effects such as diminished catalyst deactivation. In the majority of cases the reason for the observed rate enhancements is a purely thermal/kinetic effect that is a consequence of the high reaction temperatures that can be rapidly attained.

Heating occurs *via* two main mechanisms: dipolar polarisation and ionic conduction. Charged particles in a sample, are affected by ionic conduction. When irradiated, the dipoles or ions align in the applied electric field. As the field oscillates, the dipole or ion attempts to realign itself with the alternating electric field. In the process, energy is lost in the form of heat through molecular friction and dielectric loss.[103,104] Since microwave reactions are typically performed at a carefully optimised reaction temperature for the desired pathway, this can lead to cleaner transformations, and fewer by-products.[105] Combined with rapid heating, cooling and the minimisation of wall effects, yields can increase dramatically.[103,104,106] The ease with which reactions can be carried out at higher temperatures often changes selectivity, if that higher temperature favours a different product, which would ideally be the desired one.[107] However, if it is not the desired product, then a higher temperature will speed up the reaction, but will reduce selectivity, thus microwave chemistry cannot be considered a solution for every synthetic problem.[108]

Despite microwaves being renowned for their more even heating, there was one report that observed some of the aluminium catalyst support underwent a phase change which could only occur at a temperature notably higher than the average recorded for the reaction. [109] This suggested there were hotspots forming, which resulted in rate enhancements and a shift in the equilibrium constant. It was difficult to determine the true nature of these effects, but it is a factor to consider for how the Co-ZIFs might respond as hot spots can be bad for yields and ideally would be suppressed.

One problem that concerns the use of solid metal-containing catalysts in microwaves is the arcing phenomenon which can be particularly hazardous with flammable solvents. However, it is characteristically linked to large metal particles, the small ZIF particles would be considered safe.[110]

Microwaves have a promising future in the selective synthesis of high added value chemicals, natural products, and/or intermediates that find many applications in medicine, fragrances and pharmaceuticals. Since there is very little in the literature for MOF catalysis in microwave chemistry,[111] and to the author's knowledge no publications have explored Co-ZIFs in this manner, microwave chemistry represents a novel field of study.

4.2 Aims and Objectives

Following on from the successful application of ZIF-9 and ZIF-67 in the photocatalytic aza-Henry reaction, it was decided to trial the two Co-ZIFs in two functionalising benzoxazole reactions. Firstly investigating the amination of benzoxazoles with secondary amines, under oxidative conditions, extending the scope of ZIFs in cross-dehydrogenative couplings. In this example, forming a bond between a carbon atom and a heteroatom. Ideally, this would demonstrate the expedient nature of ZIFs as catalysts by removing superfluous additives and/or utilising photocatalysis.

Other objectives were to:

i. probe the recyclability through multiple cycles, stability under conditions not present in the aza-Henry, and substrate scope with various amines and benzoxazoles;

ii. utilise characterisation of the pristine and used materials to make assertions towards the strengths and weaknesses of these Co-ZIFs;

iii. explore the novel use of Co-ZIFs as catalysts in microwave chemistry, observing their response and exploiting the benefits to this aspect of sustainable chemistry, which enables shorter reaction times;

iv. trial similar reactions, including the formation of 2-functionalised benzoxazoles, and compare how the Co-ZIFs behave with the similar intermediates to help infer how the reaction progresses and propose a mechanism; and

v. gain a better understanding of the role that Co-ZIFs play in redox catalysis, using the catalytic data and characterisation collected throughout the work conducted here, thereby evaluating the suitability of Co-ZIFs for such transformations by drawing comparisons with previous studies during this work, and in the wider literature.

4.3 Results and Discussion

4.3.1 Initial Findings for Amination of Benzoxazole

4.3.1.1 Employing Acetic Acid

Having identified benzoxazole aminations as the next class of reaction to investigate with the Co-ZIFs, the first step was to run some initial experiments to evaluate the potential. Following the report of Kim et al,[79] the first experiment was run at room temperature with ZIF-9, acetic acid and TBHP. Entry 1 of Table 15 reveals low conversion of the benzoxazole and a yield of just 39 %, highlighting the need for further optimisation when heterogenising active metals.

Table 15: Initial control experiments for the optimisation of the benzoxazole amination.

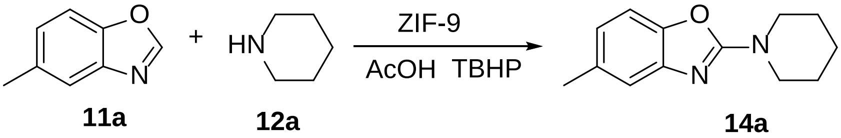

Entry	Solvent	Temp. / °C	Amine / eq.	Cat. / mg	Cat.	Acid / eq.	Conv. / %	Yield / %	Mass Balance / %
1	$CHCl_3$	23	1.2	2	ZIF-9	1.2	50	39	89
2	DCM	23	1.2	2	ZIF-9	1.2	43	30	86
3	Toluene	23	1.2	2	ZIF-9	1.2	55	30	75
4	MeCN	23	1.2	2	ZIF-9	1.2	41	35	94
5	MeCN	50	1.2	2	ZIF-9	1.2	62	50	89
6	MeCN	50	3	2	ZIF-9	1.2	>99	81	82
7	MeCN	50	3	1	ZIF-9	1.2	>99	78	78
8	MeCN	40	3	1	ZIF-9	1.2	>99	83	84
9	MeCN	40	3	1	ZIF-67	1.2	96	78	83
10	MeCN	40	3	1	ZIF-67	2.5	>99	88	89
11	MeCN	40	3	1	ZIF-67	3.0	96	81	85

5-methylbenzoxazole (0.1 mmol), piperidine, AcOH, TBHP (1.2 eq.), and Co-ZIF in solvent (1 mL) for 6 h. Yield calculated by ^1H NMR, using mesitylene as an internal standard.

Different solvents were screened, focusing on the polar aprotic examples that had been trialled in previous reports with similar catalysts.[78,79] Despite the slightly lower yield, acetonitrile appeals as a non-halogenated solvent. Near full conversion and a yield of 83 % was achieved in entry 8 by increasing the temperature to 40 °C, and the quantity of amine, overcoming a slight drop when reducing the quantity of catalyst used. ZIF-67 was tested whilst varying the quantity of acid, achieving the highest yield so far of 88 % in entry 10. Despite the clear differences early on during the aza-Henry process, ZIF-67 performs comparably well with ZIF-9.

In Table 16, the results for different oxidants are shown. Copper acetate and silver nitrate were able to catalyse the reaction without the need for ZIF-9, similar to other metal-free reports which only utilise stoichiometric quantities of oxidant.[28,62] However, the highest yield was maintained by TBHP, in conjunction with ZIF-9.

Table 16: Optimisation of oxidant used in the benzoxazole amination.

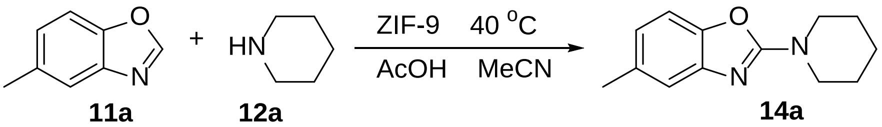

Entry	Oxidant	Conv. / %	Yield / %	Mass Balance / %
1	TBHP	>99	88	88
2	$PhI(OAc)_2$	30	17	95
3	1-Fluoro-2,4,6-trimethylpyridinium -trifluoromethanesulfonate	4	0	99
4	Cerium ammonium nitrate	11	0	89
5	$Cu(OAc)_2$	100	48	56
6	Silver nitrite	61	52	91

5-methylbenzoxazole (0.1 mmol), piperidine (3 eq.), AcOH (2.5 eq.), oxidant (1.2 eq.), ZIF-9 (1 mg) in acetonitrile (1 mL) at 40 °C for 6 h. Conversion of 11a and yield of 14a were calculated by ^{1}H NMR, using mesitylene as an internal standard.

Table 17 shows confirmation of how each component is essential. The results show the reaction does not occur under exposure to light, with atmospheric oxygen, in contrast to the aza-Henry, thus the cobalt is being promoted under a different mechanism, in the presence of TBHP. This could also explain why ZIF-67 performs comparably to ZIF-9, whereas before it was hindered by the extent to which an LMCT occurs under illumination. It was believed the acetic acid was simply required to form the intermediate quickly and efficiently, to enable the reaction to reach completion. However, it also appears to have a role in the rearomatisation as a significant quantity of the intermediate was observed, but had been unable to transform to the desired product.

Table 17: Control experiments for the amination of 5-methylbenzoxazole with piperidine, using AcOH and Co-ZIF.

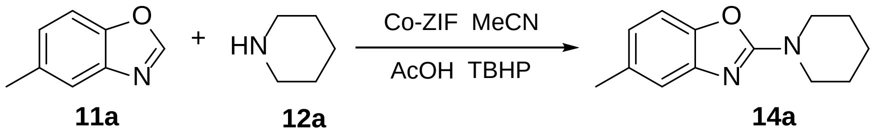

Entry	Catalyst	Acid	Oxidant	Conv. / %	Inter. / %	Yield / %	Mass Balance / %
1	ZIF-9	AcOH	TBHP	>99	0	88	88
2	-	AcOH	TBHP	71	68	*trace*	98
3	ZIF-9	-	TBHP	43	36	3	96
4[a]	ZIF-9	AcOH	atmos. O_2	95	93	0	93
5	ZIF-67	AcOH	TBHP	>99	0	88	89

5-methylbenzoxazole (0.1 mmol), piperidine (3 eq.), acetic acid (2.5 eq.), TBHP in decane (5.5 M, 1.2 eq.) and Co-ZIF (1 mg) stirring in acetonitrile (1 mL) for 6 hours at 40 °C. Yield calculated by ^{1}H NMR, using mesitylene as an internal standard. [a] Illuminated with white LEDs.

4.3.1.2 Recyclability

During initial recyclability tests for ZIF-67, only a tiny quantity of white solid could be retrieved from the first cycle, revealing the framework was unstable under the conditions employed. Whilst solid could be recovered in the ZIF-9 experiments, the quantity of the catalyst reduced after each cycle, such that more than 3 cycles could not be achieved. The results are displayed in Figure 49, and show a steady drop for the amount of intermediate transformed into product.

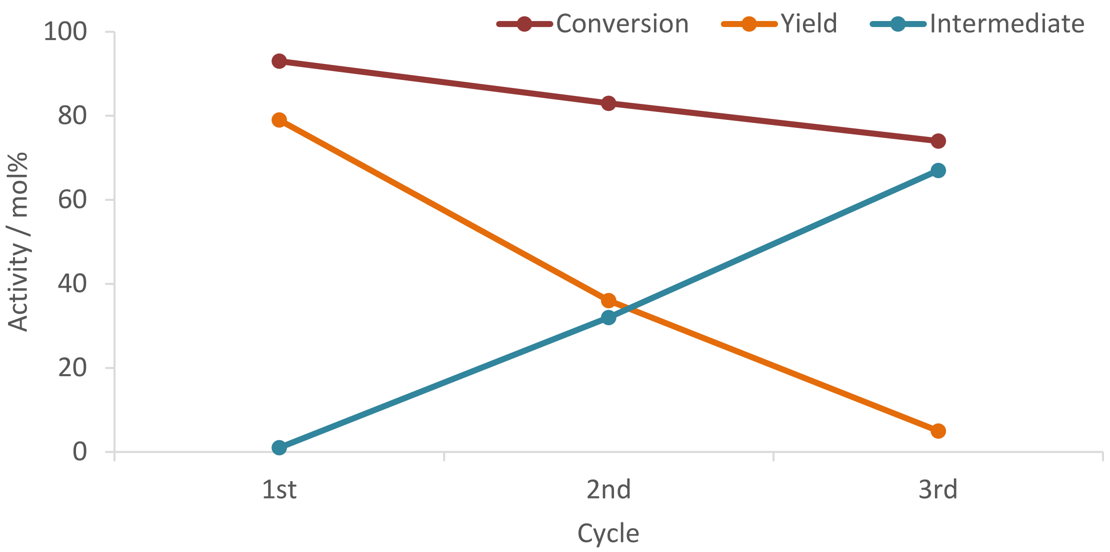

Figure 49: Recyclability experiments for the benzoxazole amination with ZIF-9. Performed at r.t., analysed after 16 h.

Bearing in mind the study of Leus et al.,[112] whilst the use of TBHP is assumed to have some effect on the framework, the swift destruction of the structure is likely due to the acid employed. It is known that CoAlPOs – a zeolite formed from aluminium and phosphorus tetrahedra with small quantities of cobalt incorporated – in the presence of acetic acid, can leach cobalt into the solution.[113] Homogeneous cobalt is likely more effective at catalysing the reaction than when within a rigid framework. Therefore, the acetic acid is observed breaking down the ZIFs, leaching cobalt into solution, leading to the high yields observed. The next step was to confirm whether cobalt within the ZIF could behave as a successful heterogeneous catalyst in this reaction.

4.3.2 Two-Step Process for the Amination of Benzoxazole

4.3.2.1 Optimisation

In order to circumvent the use of any acid, the reaction was to be split into two steps, which has been demonstrated previously in other reports.[28,61,62,64–67] The intermediate can be quickly and efficiently formed by stirring the benzoxazole in piperidine, with no additional solvent or acid additive, and then removing any excess amine *in vacuo* once full conversion is achieved. The substrate would then be used directly in the second step with the catalyst and oxidant. Having altered the process by splitting the reaction in this way, further optimisation needed to occur to ensure the right conditions were being used. This was to be expected as in the previous iteration the cobalt was being homogenised, by retaining the cobalt in the rigid framework, the kinetics of the reaction was likely to slow. A mixture of solvents, concentrations, and temperatures were trialled, the results of which are displayed in Table 18. All conditions achieved moderate to high yields with only the r.t. experiment failing to reach full conversion. Samples collected over the course of 24 hours revealed a decrease in rate, such that achieving a yield rivalling that of 78 % did not appear possible. It was clear from these tests that the already established conditions were optimal for the two-step process, thus settling on 24 hours at 40 °C in 1 mL of solvent. It is notable that increasing the temperature further led to full conversion being reached sooner, but ultimately to the detriment of the mass balance, with unidentified by-products forming in greater number.

Table 18: Optimisation for the second step of the benzoxazole amination with ZIF-67.

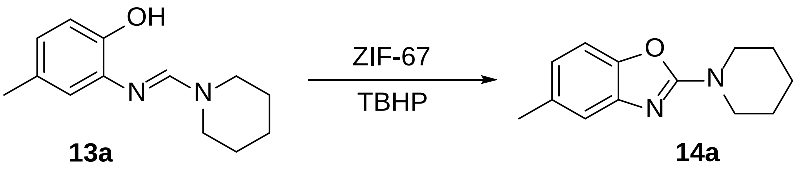

Entry	Solvent	Solvent Qty / mL	Temp. / °C	Time / h	Conv. / %	Yield / %	Mass Balance / %
1	Acetonitrile	1	40	24	100	78	78
2	Toluene	1	40	24	100	73	73
3	Chloroform	1	40	15	100	68	68
4	Water[a]	1	40	24	100	72	72
5	Acetonitrile	0.5	40	21	100	71	71
6	Acetonitrile	0.5	50	9	100	71	71
7	Acetonitrile	1	23 (r.t.)	24	84	62	79
8	Acetonitrile	1	50	21	100	76	76

5-methylbenzoxazole (0.1 mmol), TBHP in decane (~5.5 M, 1.5 eq.) and ZIF-67 (2 mg), stirring in acetonitrile (1 mL) for 24 hours. Yield calculated by ^{1}H NMR, using mesitylene as an internal standard. [a] Water/acetonitrile (95:5).

Figure 50 shows the Co-ZIFs achieving similar yields under the optimised conditions, and no product forming without the catalyst present.

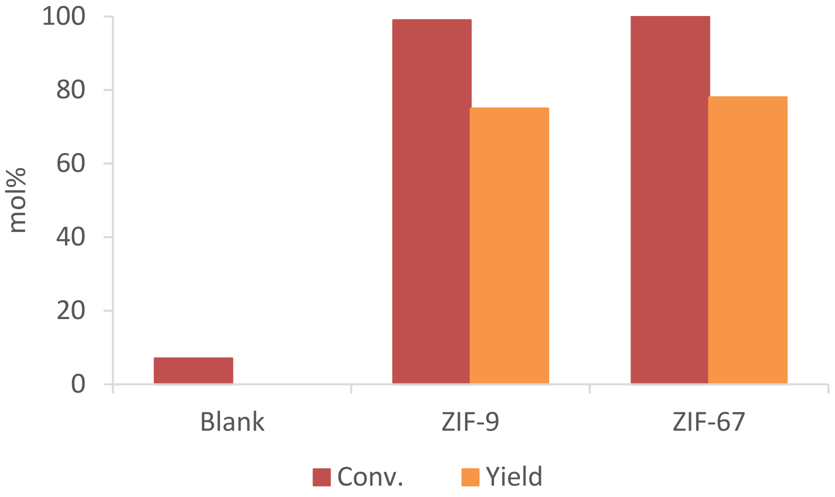

Figure 50: Results for the amination of 5-methylbenzoxazole with piperidine, using Co-ZIFs.

Rate plots were collected to better understand the kinetics of the reaction, the yield that could be achieved, and in what time. In Figure 51 it is clear the majority of product is formed in the first 6 hours, with >99 % conversion reached after 24 hours.

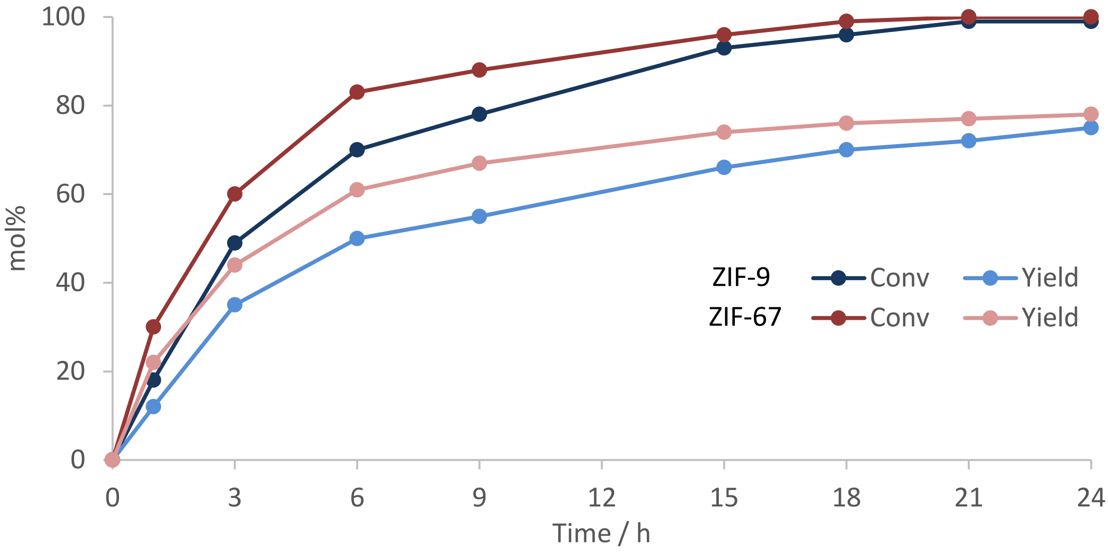

Figure 51: Rate plots for the amination of 5-methylbenzoxazole with piperidine, using Co-ZIFs.

4.3.2.2 Recyclability

After the removal of acetic acid, it was essential to demonstrate the ZIFs were now recyclable in the benzoxazole amination. In Figure 52, although a steady drop in yield is observed for both Co-ZIFs, the selectivity/mass balance actually remains fairly constant, or even improves for ZIF-9. The conditions may need to be altered through each cycle to maintain full conversion and higher yields, for example by increasing the temperature slightly each time.

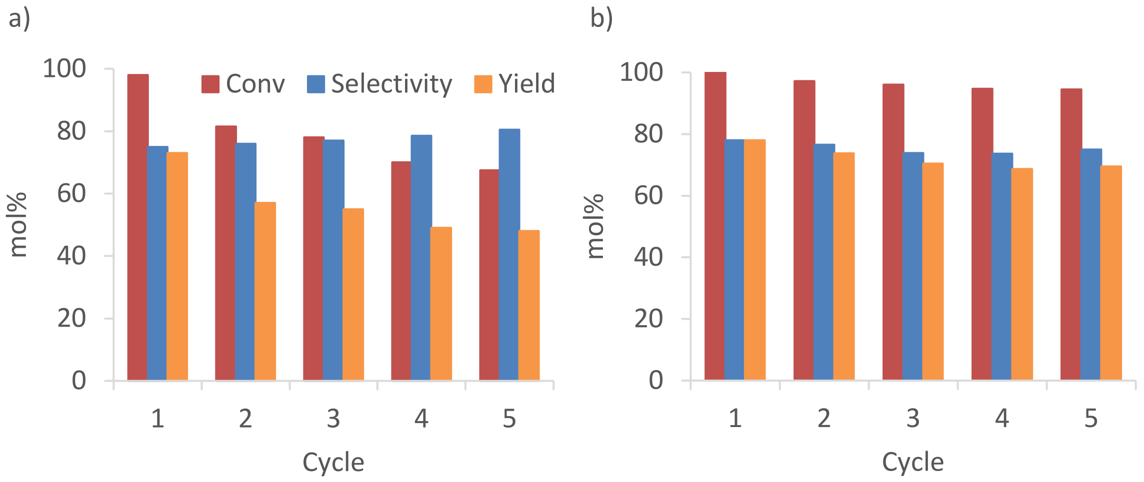

Figure 52: Recyclability in the amination of 5-methylbenzoxazole with piperidine using a) ZIF-9 and b) ZIF-67.

Following the superior recyclability tests for ZIF-67, with a drop in conversion no more than 5 % over five cycles, the process was repeated on a larger scale to gain further understanding. Despite full conversion not being achieved in 24 hours, the same trend of the smaller scale trials can be observed in Figure 53, with similar selectivity.

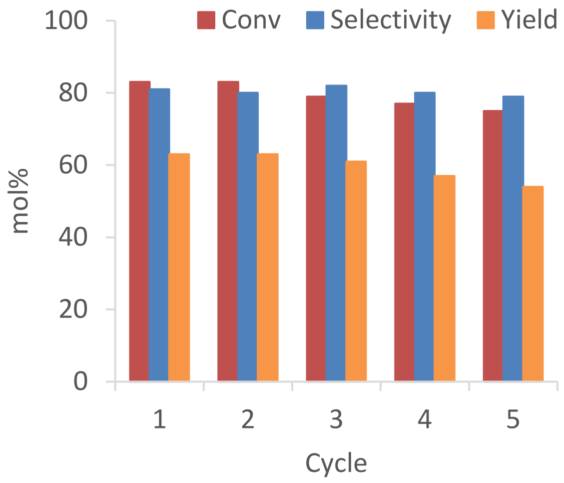

Figure 53: Larger scale recyclability of the amination of 5-methylbenzoxazole with piperidine, using ZIF-67.

The Co-ZIFs were recovered from a series of experiments under different conditions, then characterised by pXRD. Although the peaks in Figure 54b are less intense than 54a, the pattern does reveal that acetic acid has not completely destroyed the framework. A new peak appears in Figure 54c which might correspond to the denser ZIF-9-III, but it is unclear whether the other peaks are present for this conformation. Analysis from the two-step process in Figure 54d-e shows a new unknown peak arising at 10 °, and through the five cycles the material loses all peaks related to that of ZIF-9-I, coinciding with a drop in yield achieved. The new peaks may also correspond to complex carbonates which have been reported to form when ZIF-8 or ZIF-67 are exposed to moisture and carbon dioxide. To the author's knowledge, this has not been investigated with ZIF-9 or the isostructural ZIF-7, but a peak would be expected in that region if this was the case.[99] The peak does not match those seen after the recyclability tests in the aza-Henry in Chapter 3. Solid state NMR would elucidate the nature of the ligands environment, and may provide some clarity on how the sample has been affected. Overall, the results suggest ZIF-9 has been amorphised to an extent, and unlike ZIF-67 in the aza-Henry reaction, this has a detrimental effect on the catalytic activity. The amorphisation may have occurred as a result of the oxidant, the work of Leus et al. found ZIF-8 was eventually amorphised in the presence of hydrogen peroxide.[98]

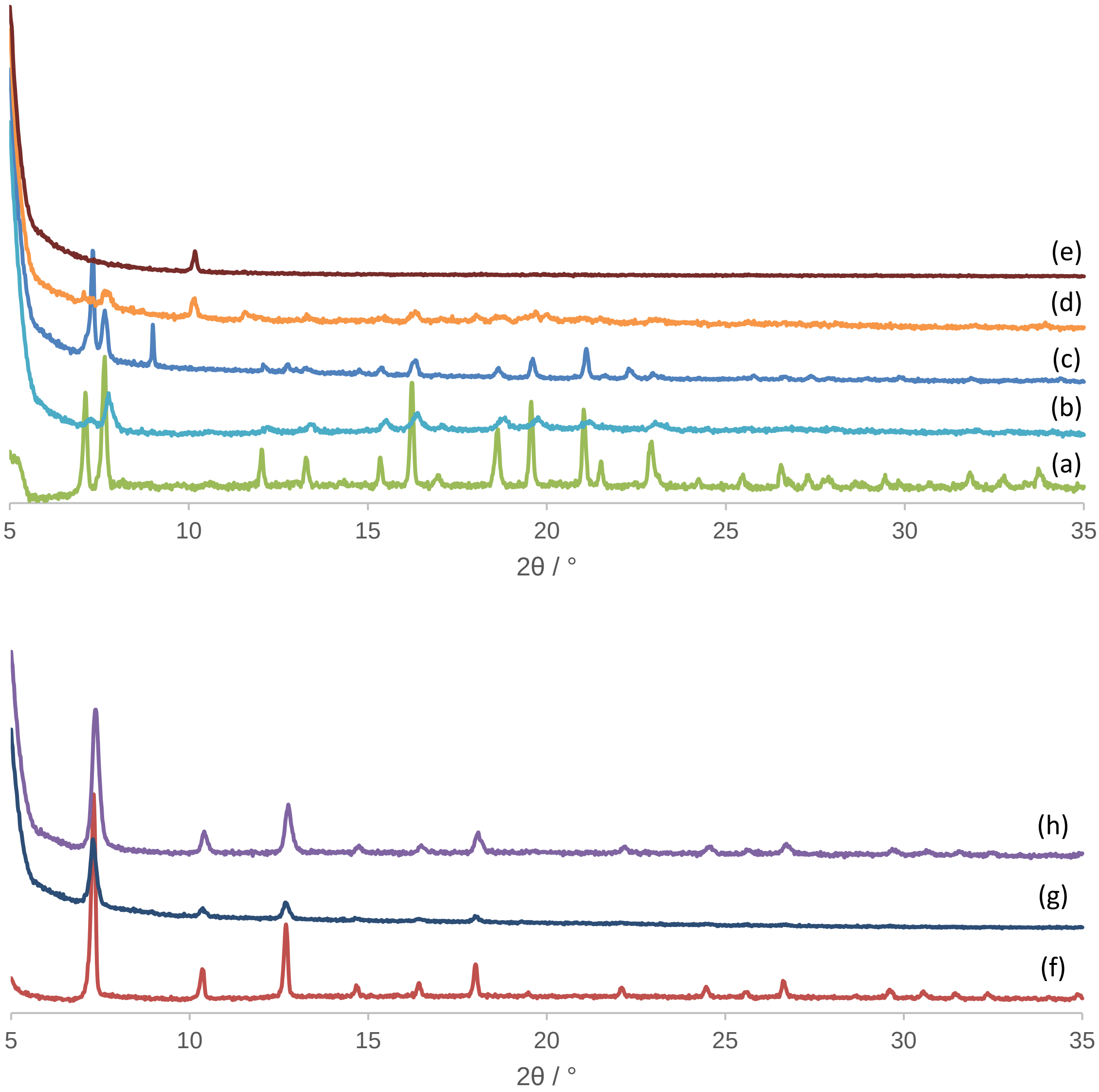

Figure 54: pXRD spectra of ZIF-9 (a) fresh, (b) with AcOH and TBHP, (c) with AcOH and no TBHP, (d) 1st cycle, (e) 5th cycle; and ZIF-67 (f) fresh, (g) 1st cycle, (h) 5th cycle.

In contrast, Figure 54g-h reveals ZIF-67 retains its crystalline structure through 5 cycles, despite complete breakdown in the presence of acetic acid. The results from the two-step process are suggestive of the strong and stable framework expected from these zeolitic materials.

The IR spectra in Figure 55 are for the fresh and 5th cycle samples, which match well for both Co-ZIFs. This supports the argument that ZIF-9 may have become amorphous, but its coordination remains intact. There is also a significant reduction in the intensity of the carbonyl peak observed from DMF in the 5th cycle sample. This is to be expected, as the act of stirring the material in acetonitrile is likely to displace the DMF molecules with the less bulky and more volatile solvent.

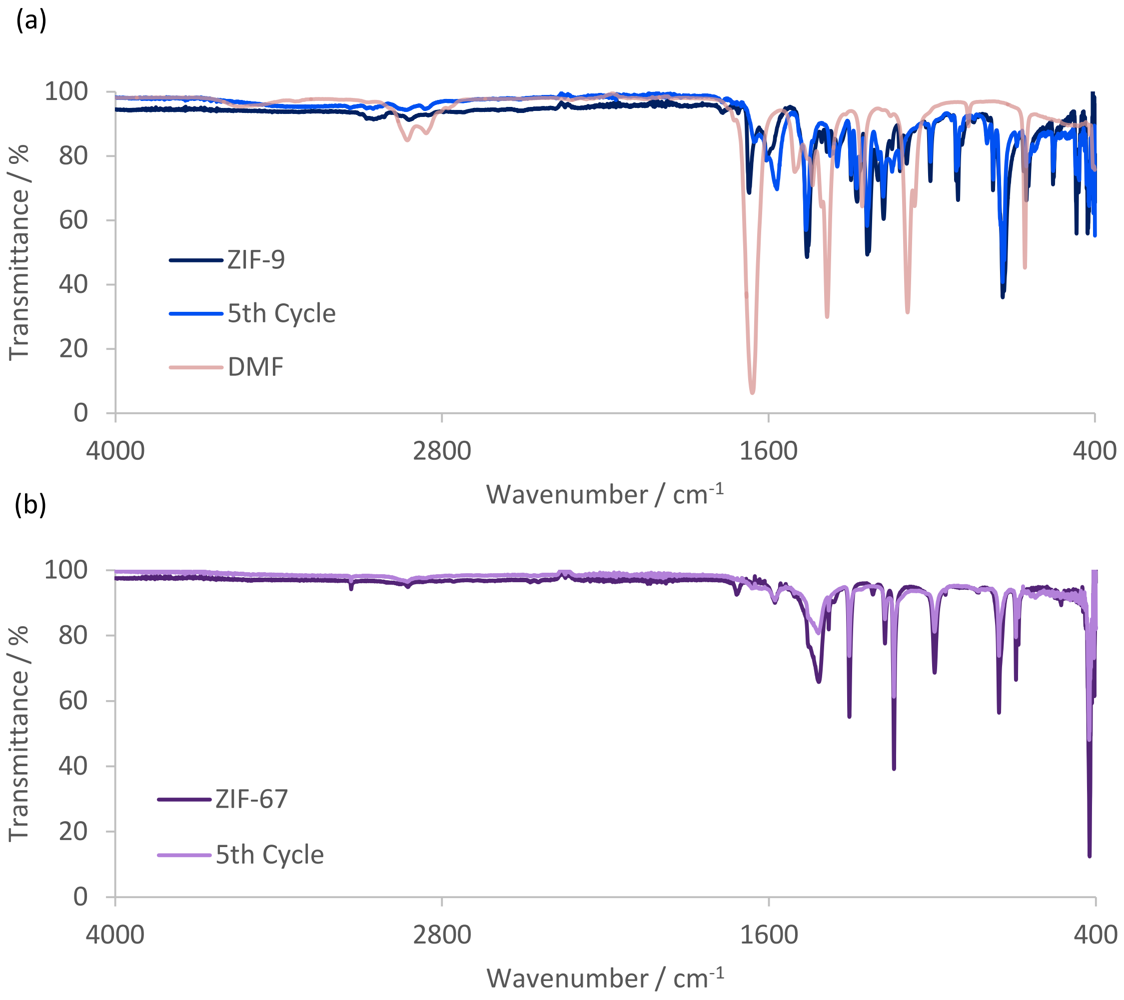

Figure 55: IR spectra for as synthesized and recycled samples of a) ZIF-9 and b) ZIF-67.

4.3.2.3 Substrate Scope

Having established the ZIFs capability within the amination of 5-methylbenzoxazole with piperidine, and confirming ZIF-67 is recyclable, the next step was to vary the substrates. In total three benzoxazoles and various amines were trialled, Table 19 details the mixed success.

Table 19: Substrate scope in the benzoxazole amination with ZIF-67.

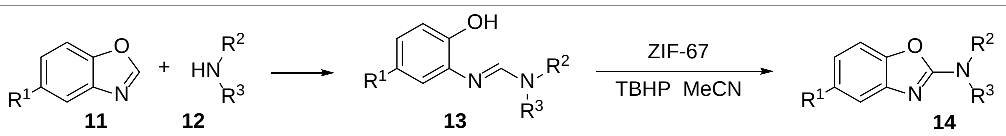

Entry	**11** R^1	**12** Amine	**13** Intermediate	Temp. / °C	**14** Product	Conv. / %	Yield / %
1	Me	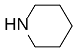	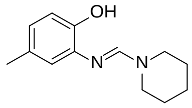	40	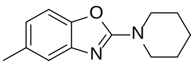	100	78
2[a]	Cl	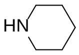	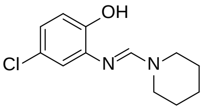	40	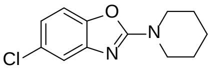	100	33
3[a]	H	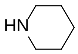	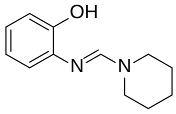	50	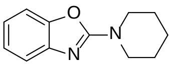	100	28
4	Me	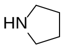	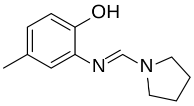	40	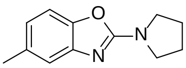	100	68
5[a, b]	Me	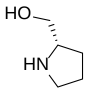	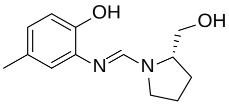	40	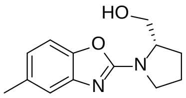	100	61
6	Me	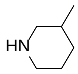	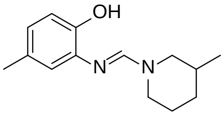	40	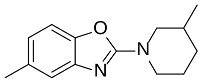	100	78
7	Me	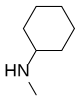	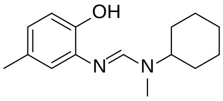	40	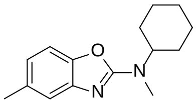	100	76
8	Me	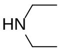	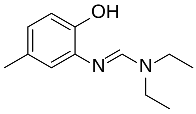	50	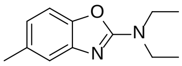	100	92
9	Me	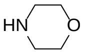	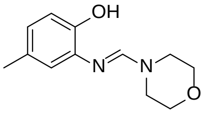	40	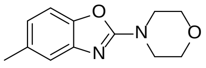	100	73
10	Me	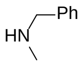	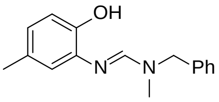	40	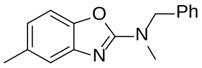	100	69
11	Me	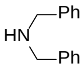	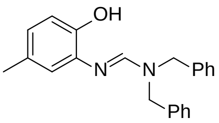	60	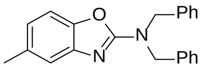	100	81
12	Me	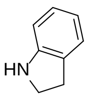	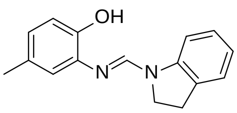	40-70	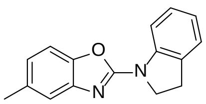	55	0

3 (0.1 mmol), TBHP (1.2 eq.), ZIF-67 (2 mg) stirring in MeCN (1 mL) for 24 h. Activity calculated by ^{1}H NMR, with mesitylene as an internal standard. [a] TBHP (2 eq.) [b] Reaction ran for 6 h.

When comparing these results to literature examples from Table 34 in the Appendix, it is clear that the yields achieved with Co-ZIFs are lower than the average result from the homogeneous systems, using 5-methylbenzoxazole and piperidine. However, of the three heterogeneous examples, only the interpenetrated cobalt MOF gave a higher yield of 93 %.[78] Despite the notable difference of 15 %, ZIF-67 does compare well across the substrate scope. Some results remain considerably higher for the Co-MOF, 96 and 77 % respectively for the morpholine and benzylmethylamine experiments. Others perform far poorer, 53, 26 and 64 % respectively for pyrrolidine, diethylamine and dibenzylamine. Both retain high activity over five cycles, and have an aqueous synthesis, although ZIF-67 forms in less time and at room temperature. The reaction conditions are not dissimilar, the Co-MOF runs for 12 hours at room temperature, employing TBHP and using acetonitrile, but also with the addition of acetic acid. In contrast to the Co-ZIFs, the interpenetrated MOF appears resistant to the acetic acid. Overall, where the Co-MOF may excel with certain substrates, ZIF-67 offers a suitable alternative, which does not require an acid additive.

Other amines trialled were pyrrole, diisopropylamine and cyclohexylamine, none of which were successful in forming a stable intermediate, believed to be a result of their reduced nucleophilicity. The lone pair in pyrrole is crucial to the aromaticity of the ring, and while addition of a strong base would deprotonate the nitrogen centre, increasing its nucleophilicity, the formation of the intermediate is known to favour acidic conditions.[63,78,79] This is why acetic acid was added after difficulty with diisopropylamine was observed, but the intermediate did not appear stable and could not be isolated. Although the intermediate with cyclohexylamine was observed by ^{1}H NMR, it appeared to quickly deteriorate, and the literature suggests the final product would not form anyway.[63,79]

4.3.2.4 Amine Deactivation

When isolating the intermediate, it was discovered residual amine from the first step can adversely affect yield in the second step. This was first observed when attempting to combine the two steps, as instead of removing the excess piperidine (approximately 1 eq.) under vacuum, the solution of intermediate was used directly in the second step, achieving only 30 % yield. This contrasts with the previous one-step procedure, where a larger excess of amine improved the yield.

This effect was further exemplified during the substrate scope. Initially the experiments with morpholine achieved 62 % yield, where the quantity of residual amine was higher because significant decay of the unstable intermediate would occur if the sample was left to dry for too long. However, upon repeating the amination and ensuring the utmost care was taken to lower the quantity of residual morpholine, the yield was increased to 73 % (entry 9 Table 23). The experiments of benzylmethylamine experienced a similar increase, from 48 to 69 % (entry 10 Table 23) when due care was taken.

In addition, the control experiments with Co-ZIFs for the one-step process without acetic acid were still forming the intermediate, typically in large quantities. However, the rearomatisation was not occurring. The key difference is that without the acid leaching cobalt into the solution, the metal remains in the rigid framework, and is more prone to deactivation. If the excess piperidine was interacting strongly with the available active sites, it would hinder the essential step with the intermediate and/or oxidant which led to formation of the desired product.

Co^{2+} is considered a borderline Lewis Acid (LA), and Co^{3+} a hard LA. Secondary amines are typically stronger bases than ammonia, which itself is a known hard Lewis base. Therefore the excess amines would have strong interactions with a hard LA, such as the cobalt centres present on the surface of the ZIF, which due to surface defects may present as incomplete shells. The basicity of each amine will also differ, varying the ability to poison the surface cobalt. Although the results suggest that any excess amine present could have a detrimental effect on the activity of the catalyst, as they block the active sites. Additionally, if the Co-ZIFs are to be employed, the starting material may also need to be clear of amine sites with an available lone pair. This presents a much more pressing issue, as the work demonstrated here is to illustrate the potential of Co-ZIFs to perform this class of reaction, which could occur as part of a multi-step synthesis of a larger molecule. Biologically active compounds, such as those shown in Figure 48 (page 97), typically have multiple amine functional groups, thus the poisoning of cobalt sites becomes a serious drawback.

A literature search on the deactivation of cobalt sites with amines found the adsorption of larger molecules onto cobalt sites would lead to steric hindrance or multiple-site adsorption, which could hamper further adsorption of the desired substrates.[114] The interaction of secondary amines with cobalt sites has not been studied extensively. However, it can be inferred that in all likelihood the amine interacts strongly with the cobalt surface, thus blocking active sites which could react with the desired substrates, whether it is the benzoxazole substrate or the oxidant.

To learn more about this process, and how it may limit the use of Co-ZIFs, characterisation of the poisoned catalyst would be useful. Using IR, a shift in the peak for the N-H bond of the secondary amine may occur as it behaves as a LB. Diethylamine may be small enough to fit within the pores, exaggerating this effect for easier observation. However, care should be taken not to overpower the desired peaks with excess diethylamine, or leave the sample to dry and remove too much diethylamine. Efforts to remove the solvent from a sample taken directly from the reaction would likely remove the excess amine in the process and inevitably change how the amine interacts with the catalyst.

4.3.2.5 Proposed Mechanism

Overall, the reaction is forming of a new C-N bond, but it is believed that the catalyst is only involved in the rearomatisation of the ring, *via* the oxidative formation of a C-O bond from a C-H and an O-H bond. Both the homogeneous and heterogeneous reports of cobalt catalysis suggest the cobalt centre triggers radical formation from TBHP, which goes on to oxidise the substrate and form the desired product.[78,79] To support this assumption, TEMPO was added to the reaction of the amidine with TBHP. In the literature, this radical scavenger experiment has both prevented a high yield being achieved, or been of no consequence.[67,76] With ZIF-67, the added TEMPO had minimal effect on the yield, achieving 75 %, signifying that radical formation does not occur as part of the mechanism. This is in contrast to the work of Guo et al. which discovered a significant drop in yield for their reaction using ZIF-67 and TBHP, when a radical scavenger was added.[80]

CDCs between a C_{sp2}-H and O-H have not been studied as extensively as the C-C bond formations, hence details of a mechanism are hard to come by. In Chapter 3, the mode of action for ZIFs, as investigated by Chizallet et al.,[115] included Lewis acid sites on the surface where the cobalt centres would only have three ligands. Taking into account this Lewis acidic nature, the double bond present, and the use of TBHP seemingly without radical formation, a Katsuki-Sharpless epoxidation was considered.[116] The proposed mechanism is illustrated in Scheme 23 where it is believed that the cobalt acts as a Lewis acid, drawing the TBHP and substrate closer together. This initiates an epoxidation of the C=N bond, eliminating *tert*-butanol in the process. Intramolecular attack of the three-membered ring would swiftly follow to form the hydroxylamine and close the desired five-membered ring. Finally, rearomatisation occurs by eliminating water.

Using this mechanism, the variation of the substrate scope between the interpenetrated Co-MOF and ZIF-67 could be a result of the different approaches to oxidation. The radicals may favour certain substrates, while the epoxidation with cobalt may prefer others. Notably, the work in Chapter 3 found that in a redox reaction with a Co(II)-Co(I) transition, ZIF-9 was more suitable due to the nature of the ligands and the lower extent to which a LMCT occurred, as observed with the XAS data. In contrast, for the amination of benzoxazole, a redox reaction with more Co(II)-Co(III) character is proposed, and the results favour the use of ZIF-67. The reason may once again lie in the inductive effects of the linker substituents. The methyl groups in ZIF-67 would push more electronegativity onto the Co centre, whereas the aromatic rings in ZIF-9 are inductively withdrawing, therefore offering less stabilisation for the 3+ transition state.

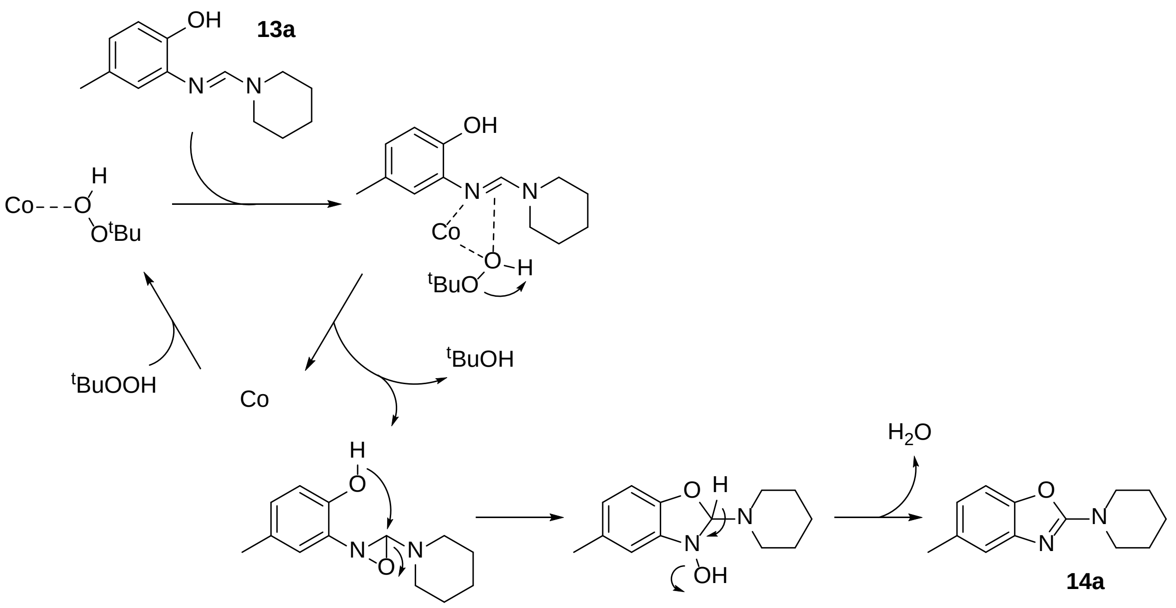

Scheme 23: Proposed reaction mechanism for the amination of 5-methylbenzoxazole with piperidine, using Co-ZIFs and TBHP.

4.3.2.6 Microwave

As discussed in 4.1.3, utilising microwave synthesis is an effective way of facilitating a reaction, often significantly reducing the time taken to achieve the product, as well as more efficient heating. To the author’s knowledge, Co-ZIFs have not been tested catalytically using microwave chemistry. The reaction with 5-methylbenzoxazole and piperidine was trialled, the results of which are shown in Table 20. Although acetonitrile is a low microwave absorbing solvent, that does not preclude it from being applied, because the substrates will be polar, and the overall dielectric properties of the reaction medium do in most cases allow sufficient heating by microwaves. Initially high temperatures were used but it was swiftly determined that this was unnecessary. When the solvent was varied, it was discovered that chloroform did not result in an adequate suspension of the catalyst, thus a mixed system was employed, which ultimately lead to a higher yield of 72 % in entry 7. The results still fell short of the 78 % reached with the conventional isothermal procedure.

Table 20: Optimisation for the amination of 5-methylbenzoxazole with piperidine, using microwave synthesis.

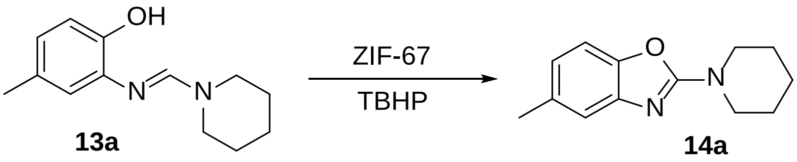

Entry	Temp / °C	MeCN / mL	$CHCl_3$ / mL	Conv / %	Yield / %	Mass Balance / %
1	80	1	-	100	59	62
2	60	1	-	100	62	66
3	40	1	-	27	14	89
4	60	0.5	-	100	63	67
5	50	0.5	-	100	64	67
6	45	0.5	-	83	54	74
7	50	0.25	0.25	**100**	**72**	**76**
8	45	0.25	0.25	96	65	73
9[a]	40	-	-	100	61	62

3 (0.1 mmol), TBHP (1.5 eq.) and ZIF-67 (2 mg) was set stirring in the solvent to achieve a good suspension, before placing in the microwave reactor for 1 hour. Activity calculated by ^{1}H NMR, using mesitylene as an internal standard. [a] DCM (0.5 mL).

Due to the disappointing yields observed during the benzoxazole scope, the reactions with benzoxazole and 5-chlorobenzoxazole were also run in the microwave in the hopes that a higher yield could be achieved. However, the data shown in Table 21 reveals that even the highest yields achieved could not match those of the previous procedure, a reduction from 33 to 25 % and 28 to 24 % respectively, with >99 % conversion.

Table 21: Trial experiments for the amination of benzoxazoles with piperidine, using ZIF-67.

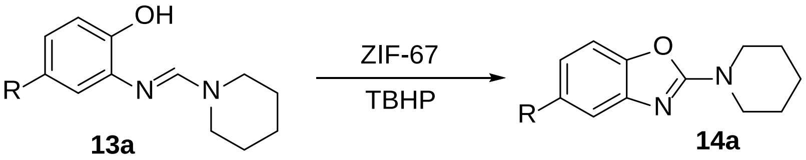

Entry	R	Temp / °C	Time / h	Conv / %	Yield / %	Mass Balance / %
1	H	70	0.5	100	25	25
2	Cl	60	1	>99	24	25

3 (0.1 mmol), TBHP (1.5 eq.) and ZIF-67 (2 mg) was set stirring in acetonitrile (0.25 mL) and chloroform (0.25 mL) to achieve a good suspension, before placing in the microwave reactor for 1 hour. Activity calculated by ^{1}H NMR, using mesitylene as an internal standard.

Although it was not possible during this brief investigation to reach or better the yields from the conventional batch results, it was interesting to note that comparative yields could at least be achieved in as a little as one hour. The ZIFs have potential in microwave synthesis, which will appeal to those who may want to trial the catalyst through an optimisation process for another reaction. However, this is a preliminary study, more experimental work needs to be undertaken to fully exploit this novel field of study. This would include further optimisation, such as testing different solvent systems; as well as analysing the catalyst after the reaction and testing its recyclability, to ensure the framework remains stable under these conditions.

4.3.3 Formation of 2-Substituted Benzoxazoles

4.3.3.1 Catalysis

Having successfully functionalised benzoxazole in the 2-position with a variety of amines, the next stage was to utilise a similar intermediate in the formation of the benzoxazole ring from 2-aminophenol and an aldehyde. The first step is aided by the reactivity of the aldehyde group, and at 100 °C full conversion to the intermediate was achieved in 15 minutes. However, the reversible nature of the reaction made isolation of the intermediate difficult. Rather than mimic the separated two-step process of the amination, the solution of intermediate was cooled slightly before diluting with acetonitrile, then adding the catalyst and TBHP. Optimisation of this second step is displayed in Table 22, where the time, temperature, solvent, and quantity of oxidant has been explored. The highest yield achieved was 76 % after 30 minutes. ZIF-9 required more time to reach full conversion and a moderate yield of 67 %, while no reaction occurred without Co-ZIF.

Table 22: Optimisation of the ring closure to form a 2-substituted benzoxazole with Co-ZIFs.

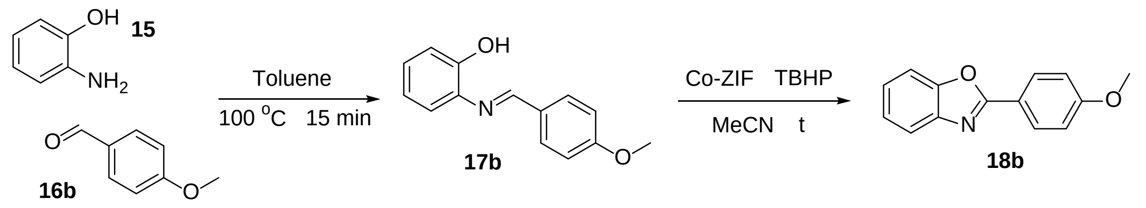

Entry	Temp. / °C	t / min	TBHP / eq.	Catalyst	Conv. / %	Yield / %	Mass Balance / %
1	50	120	1.5	ZIF-67	85	36	52
2	60	180	1.5	ZIF-67	100	73	73
3[a]	60	120	1.5	ZIF-67	100	49	49
4	70	30	1.5	ZIF-67	**100**	**76**	**76**
5	70	15	2	ZIF-67	100	64	64
6	70	30	1	ZIF-67	100	68	68
7	70	60	1.5	ZIF-9	100	67	67
8	70	15	1.5	Blank	0	0	100

2-Aminophenol (0.1 mmol) and 4-methoxybenzaldehyde (1.1 eq.) was dissolved in toluene (0.12 mL) and heated to 100 °C for 15 min. Solution cooled to 70 °C before diluting with acetonitrile (0.75 mL), then adding Co-ZIF (2 mg) and TBHP. Activity calculated by ^{1}H NMR, using mesitylene as an internal standard. [a] Chloroform used instead of acetonitrile.

Having achieved a high yield with ZIF-67 in just 45 minutes, the aldehyde was varied to determine the scope of the reaction. The results in Table 23 indicate that changing the substituent on the phenyl ring has little effect. In the literature review attached in the Appendix for the formation of benzoxazole using 2-aminophenol and benzaldehyde, all but one entry achieved yields of 90 % or more. Many of these systems not only reached higher yields than the 75 % obtained with ZIF-67, but they were often quicker and at lower temperatures. Most of the heterogeneous examples utilised a transition metal, including one which was a cobalt-based nanocomposite. After 24 hours, the nanocomposite obtained yields approximately 20 % higher than ZIF-67 across the substrate scope, utilising oxygen instead of a peroxide as the oxidant.[88] ZIF-67 excels in its synthesis, which is less intensive, forming quickly at room temperature in aqueous solvent.

However, that 20 % difference in yield is significant, and in order to make a solid case for ZIF-67, efforts should be made to identify by-products and improve the mass balance.

Table 23: Substrate scope for the formation of 2-functionalised benzoxazoles, using ZIF-67.

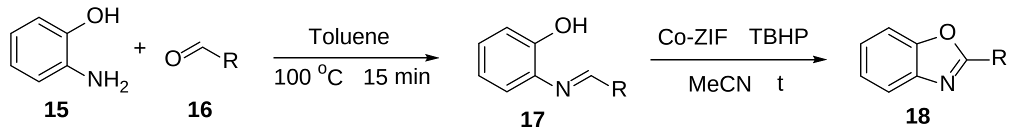

Entry	Aldehyde	t / min	Conv. / %	Yield / %	Mass Balance / %
1	4-OMe	30	100	76	76
2	4-Cl	30	100	79	79
3	H	30	100	75	75
4	4-Me	30	100	79	79

2-Aminophenol (0.1 mmol) and aldehyde (1.1 eq.) was dissolved in toluene (0.12 mL) and heated to 100 °C for 15 min. Solution cooled to 70 °C before diluting with solvent (0.75 mL), then adding ZIF-67 (2 mg) and TBHP (1.5 eq.). Activity calculated by ^{1}H NMR, using mesitylene as an internal standard.

This brief study has demonstrated that the Co-ZIFs have the ability to enable oxidations like this. The yield could likely be improved with further optimisation, for example by tuning the catalyst or investigating different solvent systems.

4.3.3.2 Proposed Mechanism

Papers reporting the formation of 2-substituted benzoxazoles do not go into depth on the proposed mechanism, when starting with an aminophenol and an aldehyde. However, considering the similarity of the intermediate and that of the amination reaction, the mechanism proposed earlier of the Katsuki-Sharpless style epoxidation utilising the Lewis acidic nature of Co-ZIFs can be applied, and is illustrated in Scheme 24.

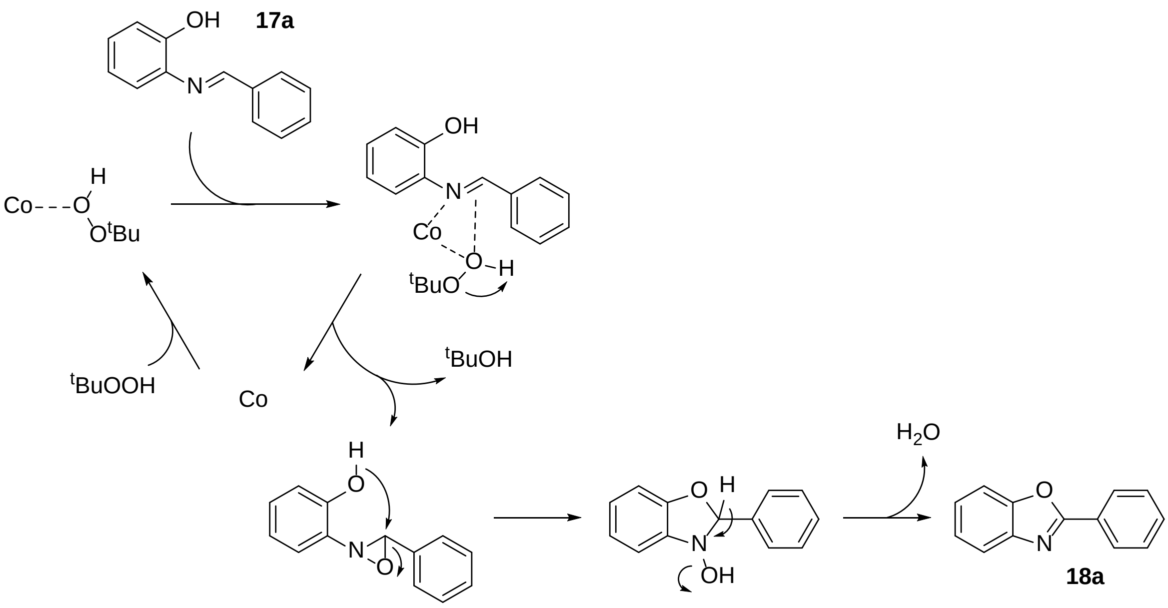

Scheme 24: Proposed reaction mechanism for the formation of a 2-substituted benzoxazole from 2-aminophenol and benzaldehyde, using Co-ZIF and TBHP.

Similarly to the amination procedure, it is believed that the cobalt acts as a Lewis acid, drawing the TBHP and substrate closer together. This initiates an epoxidation of the C=N bond, eliminating *tert*-butanol in the process. Intramolecular attack of the three-membered ring would swiftly follow to form the hydroxylamine and close the desired five-membered ring. Finally, rearomatisation occurs by eliminating water.

In contrast to the amination, which required 24 hours to reach a yield over 75 %, the reaction in Scheme 24 occurs in just 30 minutes to achieve a similar yield. This can be attributed to the greater conjugation observed in the final product, and thus increased stability and the draw of its formation.

4.3.4 Critical Comparison of Co-ZIFs and their Modes of Action

In Chapter 3, the work with Co-ZIFs focused on their photoactive nature in the aza-Henry reaction. Using advanced spectroscopic techniques, it was rationalised that despite the two materials being very similar in nature, changing the organic linker had a significant effect on photocatalytic activity. Through a combination of UV-Vis and XAS spectroscopy, as well as theoretical simulations, it was shown that the range of light adsorbed to activate the cobalt site, and the Co(II)* to Co(I) single electron transfer, plays a pivotal role in this reaction. This can be controlled and enhanced through astute selection of the imidazole linker, with benzimidazole (ZIF-9) preventing the LMCT occurring to the same extent seen with 2-methylimidazole (ZIF-67). Thus leading to ZIF-9's superior performance as a photocatalyst, concluding that it is more tailored towards the photo-induced Co(II)-Co(I) transition believed to occur for the activation of tetrahydroisoquinolines towards nucleophilic attack.

In contrast, it is the Lewis acidic nature of Co-ZIFs that is proposed to enable the formation of the benzoxazole motif. The cobalt centre draws the peroxide and substrate close together, with more likelihood of a Co(II)-Co(III) transition (Scheme 23 and Scheme 24). The catalytic data revealed marginally higher yields with ZIF-67, reaching 78 and 76 % compared to the 75 and 67 % with ZIF-9, for the amination and arylation respectively. During recyclability tests, the mass balance for both catalysts remained fairly consistent, but there was a drop in activity, more notably with ZIF-9. pXRD for the used catalysts suggest amorphisation of ZIF-9 occurs over the course of five cycles (Figure 54), whereas ZIF-67 remains crystalline. The resilience of the ZIF-67 framework results in a significantly higher yield for the fifth cycle. Therefore, it appears the once disadvantageous nature of the 2-methylimidazole ligands, may now aid the suitability for the framework to catalyse these CDCs.

As these are emerging materials, there are limited examples for the catalytic applications of Co-ZIFs. However, of those published, a common theme is a Co(II)-Co(III) transition during an oxidation reaction, with the majority using ZIF-67.[80,117–119] This is likely a result of the more practicable synthesis, and potentially having reached the same conclusion that the framework is more suitable to the Co(II)-Co(III) transition than ZIF-9, due to the inductive effects of the linker substituents. In these reactions, the catalyst has been reported to generate radicals from oxidising agents, in contrast to the mechanism proposed in this work. ZIF-67 has also been reported to enable a cascade redox condensation without the need for an additional redox agent.[120] There are reports of Co-ZIFs being used solely for their Lewis acidic properties to achieve organic transformations.[121,122] A photo-induced Co(II)-Co(I) transition for ZIF-67 was reported during an XAS study of the material,[123] which is supported by further XAS studies and catalytic data in this work with the aza-Henry reaction. It has now been demonstrated in a number of reactions that the catalytic applications for Co-ZIFs rely on the ligands that have been used to build the framework. This further highlights the potential of experimentally and computationally screening a wider range of functionalised imidazole linkers, towards developing an optimised catalytic species, for a variety of redox reactions.

4.4 Conclusion

Two Co-ZIFs have been identified as catalysts in the formation of 2-functionalised benzoxazoles. Both demonstrated recyclability in the amination, although the proposed amorphisation of ZIF-9 appeared to have a significant impact on activity, unlike ZIF-67 which retained its crystallinity, and only suffered a slight drop in activity across five cycles. The substrate scope revealed strengths and weaknesses to different amines and benzoxazoles, contrasting those reported for a different Co-MOF, and highlighting the effects potentially caused by their two different mechanisms.[78] Although the yields in the preliminary study for microwave chemistry could not quite surpass those with conventional heating, the novel use of Co-ZIFs in this manner has highlighted a potential area where these materials could excel. Yields remained consistent in the formation of benzoxazole from 2-aminophenol and various benzaldehydes, despite comparing poorly with the literature. Demonstrating that while the Co-ZIFs ability to catalyse these reactions has been confirmed, optimisation is still required to strengthen the argument for their application. Likewise with the study of Co-ZIFs in the aza-Henry reaction, it has been shown that the ligands chosen to build the ZIF are integral to activity displayed. ZIF-9 appears to present a stronger argument for photocatalytic Co(II)-Co(I) transitions, whereas ZIF-67 appears more inclined towards Co(II)-Co(III) transitions, as it retains its crystallinity and high activity throughout multiple cycles of the benzoxazole amination.

To advance this work, focus would be best placed on how to increase the yields for these functionalisation reactions. In particular, investigating the mechanism, with a more detailed look at which side-reactions are occurring. This is essential considering the results from the substrate scope revealed the variability of the catalyst in achieving high yields. Ideally, the majority of yields in the substrate scope would be brought in line with literature values of more than 90 %. Any optimisation process could be undertaken using the microwave, which would increase the rate at which different conditions can be tested. The brief tests already conducted with the microwave could be bolstered by trialling different solvents. Non-polar solvents are transparent to microwave heating, although it is unclear whether this would benefit or hinder the reaction. For instance, microwave energy used to heat a reaction in toluene would be focused on the substrates and catalyst. Additional optimisation would also need to account for recyclability. The yield for ZIF-67 dropped from 78 to 70 % over the course of five cycles, despite characterisation showing the framework retained crystallinity, unlike ZIF-9. By performing the reaction on a larger scale, BET analysis could be collected for the used catalyst to help further elucidate what changes may have occurred. Once these issues have been addressed, a broader substrate scope can be carried out, hopefully addressing the significant issues surrounding the use of different benzoxazoles in the amination. Finally, one of the advantages of heterogeneous catalysis is the application under flow. If the recyclability and mass balance issues have been addressed, then demonstrating these materials perform well under flow would support the argument that they could be applied to a more industrial scale.

4.5 Experimental

4.5.1 Synthesis of Intermediates 13a-l (Table 19, page 117)

***13a**: 4-Methyl-2-((piperidin-1-ylmethylene)amino)phenol*

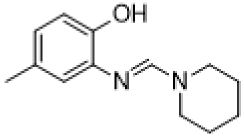

5-Methylbenzoxazole (1 mmol) was dissolved in piperidine (2 mmol) and left stirring at 40 °C. After 30 minutes a cream solid had formed and was dried *in vacuo*. NMR was in good agreement with the literature.[28] ^{1}H NMR (400 MHz, $CDCl_3$): δ 7.69 (1H, s), 6.8-6.76 (1H, m) 6.73-6.69 (2H, m), 3.54 (2H, br), 3.32 (2H, br), 2.25 (3H, s) 1.75-1.66 (2H, m), 1.66-1.58 (4H, m). ^{13}C NMR (100 MHz, $CDCl_3$): δ 151.65, 148.00, 137.17, 128.97, 123.85, 116.37, 112.97, 47.21, 26.87, 24.83, 21.03.

***13b**: 4-Chloro-2-((piperidin-1-ylmethylene)amino)phenol*

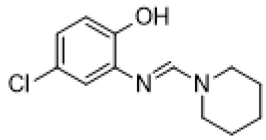

5-Chlorobenzoxazole (1 mmol) was dissolved in piperidine (2 mmol) and left stirring at room temperature. After 1 hour a cream solid had formed and was dried *in vacuo*. ^{1}H NMR (400 MHz, $CDCl_3$): δ 7.68 (1H, s), 6.88 (1H, d, J = 2.32), 6.85 (1H, dd, J = 8.38, 2.35), 6.79 (1H, d, J = 8.38), 3.64 (2H, br), 3.36 (2H, br), 1.70-1.60 (2H, m), 1.60-1.49 (4H, m). ^{13}C NMR (100 MHz, $CDCl_3$): δ 150.76, 147.75, 137.37, 123.18, 121.67, 114.40, 112.87, 49.78, 23.78, 23.54. IR (thin film): 3100 cm^{-1} (w, br, O-H), 2937 cm^{-1} (w, sp^2 C-H), 2826 cm^{-1} (s, sp^3 C-H), 1630 cm^{-1} (m, C=N), 1592 cm^{-1} (m, benzene C=C), 1447 cm^{-1} (m, C-H), 1267 cm^{-1} (m, C=N). ESI-MS: m/z 239.

***13c**: 2-((Piperidin-1-ylmethylene)amino)phenol*

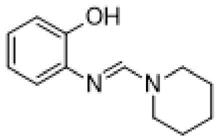

Benzoxazole (1 mmol) was dissolved in piperidine (2 mmol) and left stirring at room temperature. After 1 hour a cream solid had formed and was dried *in vacuo*. NMR was in good agreement with the literature.[38] ^{1}H NMR (400 MHz, $CDCl_3$): δ 7.71 (1H, s), 6.95-6.87 (3H, m), 6.80-6.74 (1H, m), 3.55 (2H, br), 3.29 (2H, br), 1.75-1.54 (6H, m). ^{13}C NMR (100 MHz, $CDCl_3$): δ 151.76, 150.26, 137.50, 123.56, 119.87, 115.48, 113.34, 46.79, 26.36, 24.79.

***13d**: 4-Methyl-2-((pyrrolidine-1-ylmethylene)amino)phenol*

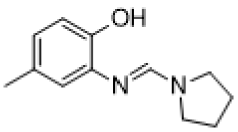

5-Methylbenzoxazole (1 mmol) was dissolved in pyrrolidine (2 mmol) and left stirring at room temperature. After 1 hour a cream solid had formed and was dried *in vacuo*. NMR was in good agreement with the literature.[28] ^{1}H NMR (400 MHz, $CDCl_3$): δ 7.98 (1H, s), 6.78 (1H, d, J = 7.86), 6.75-6.68 (2H, m), 3.57-3.49 (4H, m), 2.25 (3H, s), 2.01-1.92 (4H, br). ^{13}C NMR (100 MHz, CDCl$_3$): δ 149.28, 148.03, 137.32, 128.86, 123.76, 116.24, 112.93, 48.99, 45.50, 25.29, 24.84, 21.02.

***13f**: 4-Methyl-2-(((3-methylpiperidin-1-yl)methylene)amino)phenol*

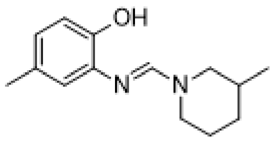

5-Methylbenzoxazole (1 mmol) was dissolved in 3-methylpiperidine (2 mmol) and left stirring at room temperature. After 1 hour a cream solid had formed and was dried *in vacuo*. ^{1}H NMR (400 MHz, CDCl$_3$): δ 7.70 (1H, s), 6.81-6.77 (1H, m), 6.74-6.69 (2H, m), 4.37 (1H, br), 3.46 (1H, br), 3.25-2.38 (2H, m), 2.25 (3H, s), 1.93-1.84 (1H, m), 1.79-1.70 (1H, m), 1.70-1.60 (1H, m), 1.60-1.46 (1H, m), 1.26-1.14 (1H, m), 0.95 (3H, d, J = 6.61). ^{13}C NMR (100 MHz, CDCl$_3$): δ 151.57, 147.95, 137.16, 128.94, 123.79, 116.37, 112.93, 57.29, 50.02, 33.27, 30.50, 24.13, 21.00, 19.04. IR (thin film): 3100 cm^{-1} (w, br, O-H), 2946 cm^{-1} (w, sp^2 C-H), 2866 cm^{-1} (s, sp^3 C-H), 1628 cm^{-1} (m, C=N), 1600 cm^{-1} (m, benzene C=C), 1444 cm^{-1} (m, C-H), 1261 cm^{-1} (m, C=N). ESI-MS: m/z 233.

***13g**: N-Cyclohexyl-N'-(2-hydroxy-5-methylphenyl)-N-methylformimidamide*

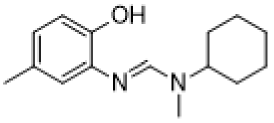

5-Methylbenzoxazole (1 mmol) was dissolved in *N*-cyclohexylmethylamine (2 mmol) and left stirring for 16 hours at 75 °C. The solution was dried *in vacuo* where a cream solid formed. NMR was in good agreement with the literature.[28] ^{1}H NMR (400 MHz, CDCl$_3$): δ 7.86 (0.85H, s), 7.69 (0.15H, br), 6.83-6.79 (1H, m), 6.76-6.68 (2H, m), 4.35 (0.15H, br), 3.30-3.10 (0.85H, m), 2.97 (3H, s), 2.25 (3H, s), 1.95-1.80 (4H, m), 1.77-1.66 (1H, m), 1.64-1.46 (2H, m), 1.46-1.28 (2H, m), 1.16 (1H, qt, J = 12.90, 3.52). ^{13}C NMR (100 MHz, CDCl$_3$): δ 151.84, 147.97, 137.40, 128.86, 123.63, 116.32, 112.86, 62.19, 58.62, 33.60, 33.21, 31.82, 29.83, 26.28, 25.82, 25.44, 25.10, 20.99.

***13h**: N,N-Diethyl-N'-(2-hydroxy-5-methylphenyl)formimidamide*

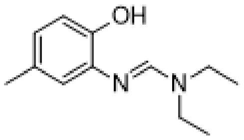

5-Methylbenzoxazole (1 mmol) was dissolved in diethylamine (2 mmol) and left stirring for 72 hours at 40 °C. The solution was dried *in vacuo* where a cream solid formed. NMR was in good agreement with the literature.[124] ^{1}H NMR (400 MHz, CDCl$_3$): δ 7.66 (1H, s), 6.73-6.69 (1H, m), 6.67-6.61 (2H, m), 3.44 (2H, br), 3.26 (2H, br), 2.18 (3H, s), 1.14 (6H, t, J = 7.13). ^{13}C NMR (100 MHz, CDCl$_3$): δ 151.37, 147.99, 137.30, 128.94, 123.70, 116.20, 112.91, 45.83, 20.90, 12.26.

***13i**: 4-Methyl-2-((morpholinomethylene)amino)phenol*

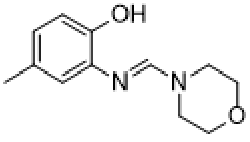

5-Methylbenzoxazole (1 mmol) was dissolved in morpholine (1 mmol) and acetonitrile (100 µL), the solution was left stirring for 2 hours at 40 °C. The solution was dried *in vacuo*, forming a brown oil. NMR was in good agreement with the literature.[28] ^{1}H NMR (400 MHz, $CDCl_3$): δ 7.65 (1H, s), 6.74-6.70 (1H, m), 6.70-6.65 (2H, m), 3.7-3.65 (4H, m), 3.49 (4H, br), 2.25 (3H, s). ^{13}C NMR (100 MHz, $CDCl_3$): δ 151.21, 147.84, 136.23, 129.00, 124.46, 116.45, 113.18, 66.58, 49.18, 46.46, 20.86.

***13j**: N-Benzyl-N'-(2-hydroxy-5-methylphenyl)-N-methylformimidamide*

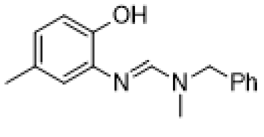

5-Methylbenzoxazole (1 mmol) was dissolved in *N*-benzylmethylamine (2 mmol) and left stirring for 5 hours at 40 °C. The solution was dried *in vacuo*, forming a yellow oil. ^{1}H NMR (400 MHz, $CDCl_3$): δ 7.91 (0.6H, s), 7.79 (0.4H, s), 7.34-7.12 (5H, m), 6.77-6.64 (3H, m), 4.64 (0.8H, s), 4.39 (1.2H, s), 2.90 (3H, s), 2.19 (3H, s). ^{13}C NMR (100 MHz, $CDCl_3$): δ 152.71, 152.41, 148.27, 148.02, 136.75, 136.71, 128.96, 128.83, 128.50, 128.31, 128.02, 127.87, 127.36, 127.13, 126.83, 124.15, 120.44, 116.51, 113.12, 110.38, 57.29, 55.99, 50.64, 38.24, 35.90, 32.83, 20.97. IR (thin film): 3379 cm^{-1} (w, br, O-H), 3029 cm^{-1} (w, sp^2 C-H), 2915 cm^{-1} (s, sp^3 C-H), 1632 cm^{-1} (m, C=N), 1605 cm^{-1} (m, benzene C=C), 1242 cm^{-1} (m, C=N). ESI-MS: m/z 255.

***13k**: N,N-Dibenzyl-N'-(2-hydroxy-5-methylphenyl)formimidamide*

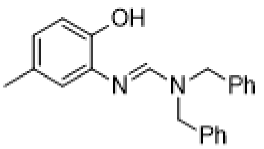

5-Methylbenzoxazole (1 mmol) was dissolved in dibenzylamine (1 mmol) and left stirring for 48 hours at 80 °C. The solution was purified using column chromatography, an orange oil was formed after drying the product *in vacuo*. NMR was in good agreement with the literature.[28] ^{1}H NMR (400 MHz, $CDCl_3$): δ 7.99 (1H, s), 7.34-7.06 (10H, m), 6.76-6.63 (3H, m), 6.56 (1H, br), 4.54 (2H, s), 4.30 (2H, s), 2.18 (3H, s). ^{13}C NMR (100 MHz, $CDCl_3$): δ 152.36, 148.03, 136.73, 136.45, 129.01, 128.76, 128.06, 127.67, 127.54, 124.39, 116.50, 113.23, 54.44, 47.98, 20.95.

***13l**: 2-((Indolin-1-ylmethylene)amino)-4-methylphenol*

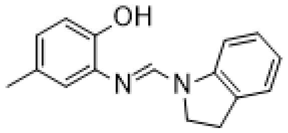

5-Methylbenzoxazole (1 mmol) was dissolved in indoline (1 mmol) and acetonitrile (50 µL), the solution was left stirring at 50 °C. After 5 hours the solution was dried *in vacuo*, forming a beige solid. ^{1}H NMR (400 MHz, $CDCl_3$): δ 8.41 (1H, s), 7.15-7.06 (2H, m), 7.00 (1H, br), 6.88 (1H, td, J = 7.45, 0.83), 6.78-6.70 (3H, m), 4.10-4.03 (2H, m), 3.11 (2H, t, J = 8.59), 2.21 (3H, s). ^{13}C NMR (100 MHz, $CDCl_3$): δ 152.63, 148.25, 143.07, 136.02, 131.54, 129.12, 127.65, 125.78, 125.26, 122.73, 116.54, 113.52, 110.30, 47.32, 27.40, 20.89. IR (thin film): 3337 cm^{-1} (m, O-H), 2953cm^{-1} (w, sp^2 C-H), 2907 cm^{-1} (s, sp^3 C-H), 1629 cm^{-1} (m, C=N), 1589 cm^{-1} (m, benzene C=C), 1494 cm^{-1} (m, benzene C=C), 1235 cm^{-1} (m, C=N). ESI-MS: m/z 253.

4.5.2 Control Experiments 14a-k

Initial experiments dissolved 5-Methylbenzoxazole **11a** (13.3 mg, 0.1 mmol) in acetonitrile (1 mL). Co-ZIF (1 mg, 4 mol%), piperidine **12a** (29.8 µL, 0.3 mmol), acetic acid (14.4 µL, 0.25 mmol) and TBHP (5.5 M in decane, 21 µL, 0.12 mmol) were then added. The reaction was left stirring at 40 ^{o}C and monitored by ^{1}H NMR using mesitylene as an internal standard to calculate catalytic activity.

Typical synthesis for the second step of the amination started by dissolving the *o*-hydroxybenzamidine **13** (21.8 mg, 0.1 mmol) in acetonitrile (1 mL) before adding TBHP (5.5 M in decane, 21 µL, 0.12 mmol) and ZIF-67 (2 mg). The reaction was left stirring at 40 ^{o}C and monitored by ^{1}H NMR using mesitylene as an internal standard to calculate catalytic activity. When isolating the product **14**, the reaction mixture was directly purified using column chromatography with an eluent of hexane/ethyl acetate (9:1), the product was dried *in vacuo*.

***14a**: 5-Methyl-2-(piperidin-1-yl)benzoxazole*

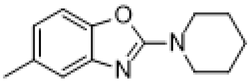

Isolated yield of 69 %. NMR for the cream solid was in good agreement with the literature.[77] ^{1}H NMR (400 MHz, CDCl$_3$): δ 7.14 (1H, dq, J = 0.97, 0.68), 7.09 (1H, d, J = 8.08), 6.79 (1H, ddq, J = 8.08, 1.64, 0.64), 3.67-3.61 (4H, m), 2.38 (3H, s), 1.70-1.64 (6H, m). ^{13}C NMR (100 MHz, CDCl$_3$): δ 162.80, 147.00, 143.65, 133.55, 121.02, 116.56, 108.01, 46.74, 25.38, 24.23, 21.66.

***14b**: 5-Chloro-2-(piperidin-1-yl)benzoxazole*

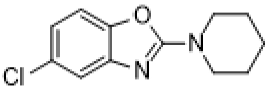

NMR for the yellow/cream solid was in good agreement with the literature.[38] ^{1}H NMR (400 MHz, CDCl$_3$): δ 7.21 (1H, d, J = 2.05), 7.04 (1H, d, J = 8.41), 6.87 (1H, dd, J = 8.41, 2.10), 3.61-3.55 (4H, m), 1.65-1.58 (6H, m). ^{13}C NMR (100 MHz, CDCl$_3$): δ 162.11, 146.28, 143.80, 128.11, 119.00, 115.01, 107.98, 45.54, 24.20, 22.96.

***14c**: 2-(Piperidin-1-yl)benzoxazole*

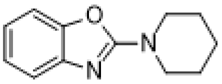

NMR for the cream solid was in good agreement with the literature.[65] ^{1}H NMR (400 MHz, CDCl$_3$): δ 7.27 (1H, dd, J = 7.78, 0.47), 7.16 (1H, dd, J = 7.92, 0.42), 7.07 (1H, td, J = 7.66, 0.73), 6.92 (1H, td, J = 7.73, 0.94), 3.62-3.56 (4H, m), 1.65-1.58 (6H, m). ^{13}C NMR (100 MHz, CDCl$_3$): δ 161.44, 147.67, 142.36, 122.80, 119.24, 114.97, 107.53, 45.59, 24.23, 23.06.

***14d**: 5-Methyl-2-(pyrrolidin-1-yl)benzoxazole*

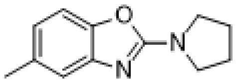

NMR for the cream solid was in good agreement with the literature.[28] ^{1}H NMR (400 MHz, CDCl$_3$): δ 7.08 (1H, s), 7.04 (1H, d, J = 8.07), 6.71 (1H, d, J = 8.05), 3.61-3.51 (4H, m), 2.31 (3H, s), 2.01-1.90 (4H, m). ^{13}C NMR (100 MHz, CDCl$_3$): δ 160.17, 146.14, 142.75, 132.38, 119.62, 115.36, 106.87, 46.35, 24.58, 20.53.

***14e**: (1-(5-Methylbenzoxazol-2-yl)pyrrolidin-2-yl)methanol*

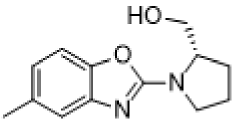

5-Methylbenzoxazole (1 mmol) was dissolved in prolinol (1 mmol) and acetonitrile (50 µL), left stirring for 7 hours at room temperature. The red/brown solid was dried *in vacuo*, purity calculated through ^{1}H NMR, before directly dissolving in acetonitrile (1 mL) with TBHP (2 eq.) and ZIF-67 (2 mg). Reaction halted after 6 hours and directly purified by column chromatography. ^{1}H NMR (400 MHz, CDCl$_3$): δ 7.04 (1H, d, J = 7.74), 7.04 (1H, dq, J = 0.87, 0.58), 6.73 (1H, ddq, J = 8.21, 1.50, 0.58), 5.91 (1H, br), 4.05 (1H, qd, J = 7.21, 2.65), 3.77-3.65 (3H, m), 3.58 (1H, dt, J = 10.31, 7.29), 2.30 (3H, s), 2.15-2.06 (1H, m), 2.01-1.80 (2H, m), 1.67 (1H, ddd, J = 12.56, 8.10, 7.24). ^{13}C NMR (100 MHz, CDCl$_3$): δ 162.09, 146.94, 142.33, 133.76, 121.19, 116.38, 108.12, 66.58, 62.95, 48.58, 29.51, 24.22, 21.49. IR (thin film): 3284 cm^{-1} (w, O-H), 2954 cm^{-1} (w, sp^2 C-H), 2877 cm^{-1} (s, sp^3 C-H), 1642 cm^{-1} (m, C=N), 1587 cm^{-1} (m, benzene C=C), 1258 cm^{-1} (m, C=N). ESI-MS: m/z 233.

***14f**: 5-Methyl-2-(3-methylpiperidin-1-yl)benzoxazole*

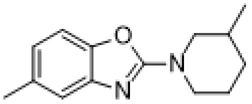

NMR for the cream solid was in good agreement with the literature.[125] ^{1}H NMR (400 MHz, CDCl$_3$): δ 7.06 (1H, dq, J = 0.95, 0.66), 7.02 (1H, d, J = 8.07), 6.72 (1H, ddq, J = 8.07, 1.64, 0.65), 4.15-4.05 (2H, m), 2.94 (1H, ddd, J = 12.96, 12.05, 3.15), 2.62 (1H, dd, J = 12.95, 10.76), 2.31 (3H, s), 1.83-1.74 (1H, m), 1.74-1.48 (4H, m), 1.14-1.02 (1H, m), 0.89 (3H, d, J = 6.63). ^{13}C NMR (100 MHz, CDCl$_3$): δ 161.55, 145.79, 142.46, 132.43, 119.86, 115.37, 106.85, 51.98, 45.00, 31.65, 29.62, 23.76, 20.52, 17.91.

***14g**: N-Cyclohexyl-N,5-dimethylbenzoxazol-2-amine*

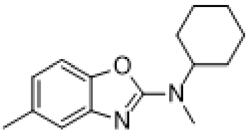

NMR for the cream solid was in good agreement with the literature.[28] ^{1}H NMR (400 MHz, CDCl$_3$): δ 7.07 (1H, dq, J = 0.78, 0.66), 7.03 (1H, d, J = 8.02), 6.70 (1H, ddq, J = 8.06, 1.56, 0.58), 4.04 (1H, tt, J = 11.53, 3.61), 2.98 (3H, s), 2.31 (3H, s), 1.83-1.72 (4H, m), 1.67-1.61 (1H, m), 1.51-1.31 (4H, m), 1.13-0.99 (1H, m). ^{13}C NMR (100 MHz, CDCl$_3$): δ 162.97, 146.82, 143.64, 133.36, 120.54, 116.23, 107.79, 56.68, 30.01, 29.51, 25.64, 25.50, 21.55.

***14h**: N,N-Diethyl-5-methylbenzoxazol-2-amine*

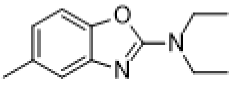

NMR for the cream solid was in good agreement with the literature.[125] ^{1}H NMR (400 MHz, $CDCl_3$): δ 7.07 (1H, dq, J = 0.61), 7.03 (1H, d, J = 8.07), 6.70 (1H, ddq, J = 8.06, 0.95), 3.50 (4H, q, J = 7.14), 2.31 (3H, s), 1.20 (6H, t, J = 7.13). ^{13}C NMR (100 MHz, $CDCl_3$): δ 161.37, 145.94, 142.74, 132.34, 119.49, 115.20, 106.80, 41.87, 20.52, 12.47.

***14i**: 5-Methyl-2-morpholinobenzoxazole*

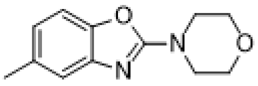

NMR for the cream solid was in good agreement with the literature.[28] ^{1}H NMR (400 MHz, $CDCl_3$): δ 7.10 (1H, dq, J = 0.91, 0.65), 7.06 (1H, d, J = 8.13), 6.77 (1H, ddq, J = 8.13, 1.59, 0.58), 3.76-3.72 (4H, m), 3.63-3.58 (4H, m), 2.32 (3H, s). ^{13}C NMR (100 MHz, $CDCl_3$): δ 162.28, 146.90, 142.94, 133.77, 121.62, 116.87, 108.18, 66.22, 45.73, 21.53.

***14j**: N-Benzyl-N,5-dimethylbenzoxazol-2-amine*

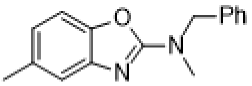

NMR for the cream solid was in good agreement with the literature.[125] ^{1}H NMR (400 MHz, $CDCl_3$): δ 7.30-7.19 (5H, m), 7.11 (1H, s), 7.06 (1H, d, J = 8.09), 6.75 (1H, d, J = 8.09), 4.67 (2H, s), 3.04 (3H, s), 2.32 (3H, s). ^{13}C NMR (100 MHz, $CDCl_3$): δ 162.15, 146.11, 142.62, 135.48, 132.59, 127.71, 126.64, 119.98, 115.53, 107.04, 52.80, 34.14, 20.52.

***14k**: N,N-Dibenzyl-5-methylbenzoxazol-2-amine*

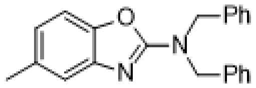

NMR for the cream solid was in good agreement with the literature.[28] ^{1}H NMR (400 MHz, $CDCl_3$): δ 7.29-7.16 (10H, m), 7.14 (1H, s), 7.07 (1H, d, J = 8.09), 6.77 (1H, d, J = 8.09), 4.62 (4H, s), 2.34 (3H, s). ^{13}C NMR (100 MHz, $CDCl_3$): δ 162.31, 146.03, 142.58, 135.38, 132.72, 127.69, 126.91, 126.67, 120.14, 115.65, 107.17, 49.29, 20.53.

4.5.3 Control Experiments 18a-d

Typical synthesis involved dissolving 2-aminophenol **15** (10.9 mg, 0.1 mmol) in toluene (120 µL) with the benzaldehyde **6** (0.11 mmol). The solution was left stirring for 15 minutes at 100 °C, monitoring by ^{1}H NMR using mesitylene as an internal standard showed full conversion to the intermediate **17**. The solution was removed from the heat source, ZIF-67 (2 mg, 9 mol%), TBHP (5.5 M in decane, 21 µL, 0.12 mmol) and acetonitrile (0.8 mL) was added before leaving at 70 °C until full conversion of the intermediate had occurred. When isolating the product **18**, the reaction mixture was directly purified using column chromatography with an eluent of hexane/ethyl acetate (9:1), the product was dried *in vacuo*.

***18a**: 2-(4-Methoxyphenyl)benzoxazole*

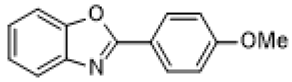

NMR for the white solid was in good agreement with the literature.[126] ^{1}H NMR (400 MHz, CDCl$_3$): δ 8.16-8.11 (2H, m), 7.69-7.64 (1H, m), 7.51-7.46 (1H, m), 7.29-7.22 (2H, m), 6.98-6.93 (2H, m), 3.83 (3H, s). ^{13}C NMR (100 MHz, CDCl$_3$): δ 163.20, 162.34, 150.69, 142.29, 129.40, 124.61, 124.43, 119.72, 119.63, 114.38, 110.39, 55.47.

***18b**: 2-(4-Chlorophenyl)benzoxazole*

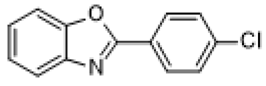

NMR for the orange solid was in good agreement with the literature.[127] ^{1}H NMR (400 MHz, CDCl$_3$): δ 8.13-8.09 (2H, m), 7.72-7.67 (1H, m), 7.53-7.47 (1H, m), 7.45-7.40 (2H, m), 7.32-7.26 (2H, m). ^{13}C NMR (100 MHz, CDCl$_3$): δ 162.07, 150.75, 142.00, 137.77, 129.28, 128.85, 125.66, 125.35, 124.75, 120.09, 110.63.

***18c**: 2-Phenylbenzoxazole*

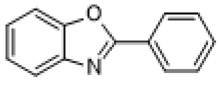

NMR for the white solid was in good agreement with the literature.[126] ^{1}H NMR (400 MHz, CDCl$_3$): δ 8.21-8.15 (2H, m), 7.72-7.66 (1H, m), 7.53-7.47 (1H, m), 7.47-7.41 (3H, m), 7.30-7.24 (2H, m). ^{13}C NMR (100 MHz, CDCl$_3$): δ 163.04, 150.77, 142.11, 131.52, 128.91, 127.63, 127.18, 125.11, 124.58, 120.02, 110.60.

***18d**: 2-(p-Tolyl)benzoxazole*

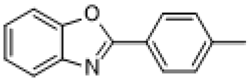

NMR for the white solid was in good agreement with the literature.[128] ^{1}H NMR (400 MHz, CDCl$_3$): δ 8.08-8.03 (2H, m), 7.70-7.65 (1H, m), 7.50-7.45 (1H, m), 7.28-7.21 (4H, m), 2.34 (3H, s). ^{13}C NMR (100 MHz, CDCl$_3$): δ 163.30, 150.68, 142.17, 142.06, 129.64, 127.59, 124.87, 124.48, 124.39, 119.84, 110.49, 21.65.

4.5.4 Catalysts

4.5.4.1 ZIF-9

The procedure followed the work of Li & Kim.[129] Cobalt (II) nitrate hexahydrate (1.11 g, 3.8 mmol) and benzimidazole (0.33 g, 2.8 mmol) were dissolved in DMF (50 mL) before heating to 130 °C for 48 hours. Once at room temperature the solution was filtered and washed with DMF (3 x 10 mL). Red and blue crystals were collected and left in a drying oven. The solid was ground before centrifuging in chloroform (3 x 10 mL). The supernatant was decanted each time before removing the solvent *in vacuo*. The blue solid was dried under vacuum at 100 ^{o}C for 6 hours.

4.5.4.2 ZIF-67

This procedure followed the work of Qian *et al*.[95] Typical procedure involved dissolving 2-methylimidazole (5.5 g, 67 mmol) in water (20 mL). Cobalt (II) nitrate hexahydrate (0.45 g, 1.5 mmol) in water (3 mL) was added and the mixture left stirring for 6 hours. The purple precipitate was collected by centrifugation, washing with water (3 x 10 mL) and methanol (3 x 10 mL). The solid was dried at 100 ^{o}C for 6 hours under vacuum.

4.6 References

1 C. S. Yeung and V. M. Dong, *Chem. Rev.*, 2011, **111**, 1215–1292.

2 S. H. Cho, J. Y. Kim, J. Kwak and S. Chang, *Chem. Soc. Rev.*, 2011, **40**, 5068–5083.

3 Y. Park, Y. Kim and S. Chang, *Chem. Rev.*, 2017, **117**, 9247–9301.

4 C. D. Cox, M. J. Breslin, D. B. Whitman, J. D. Schreier, G. B. Mcgaughey, M. J. Bogusky, A. J. Roecker, S. P. Mercer, R. A. Bednar, W. Lemaire, J. G. Bruno, D. R. Reiss, C. M. Harrell, K. L. Murphy, S. L. Garson, S. M. Doran, T. Prueksaritanont, W. B. Anderson, C. Tang, S. Roller, T. D. Cabalu, D. Cui, G. D. Hartman, S. D. Young, K. S. Koblan, C. J. Winrow, J. J. Renger and P. J. Coleman, *J. Med. Chem.*, 2010, **53**, 5320–5332.

5 S. C. Annedi, J. Ramnauth, S. P. Maddaford, P. Renton, S. Rakhit, G. Mladenova, P. Dove, S. Silverman, J. S. Andrews, M. D. Felice and F. Porreca, *J. Med. Chem.*, 2012, **55**, 943–955.

6 K. G. Liu, J. R. Lo, T. A. Comery, G. Ming, J. Y. Zhang, D. M. Kowal, D. L. Smith, L. Di, E. H. Kerns, L. E. Schechter and A. J. Robichaud, *Bioorg. Med. Chem. Lett.*, 2009, **19**, 1115–1117.

7 R. Hili and A. Yudin, *Nat. Chem. Biol.*, 2006, **2**, 284–287.

8 P. S. Taylor, P. Ghalsasi and P. M. Lahti, *Tetrahedron Lett.*, 2004, **45**, 6295–6298.

9 N. Matsuda, K. Hirano, T. Satoh and M. Miura, *Org. Lett.*, 2011, **13**, 2860–2863.

10 A. F. Pozharskii, A. T. Soldatenkov and A. R. Katritzky, *Heterocycles in Life and Society*, John Wiley & Sons, 2nd edn., 2011.

11 D. C. Tully, H. Liu, P. B. Alper, A. K. Chatterjee, R. Epple, M. J. Roberts, J. A. Williams, K. T. Nguyen, D. H. Woodmansee, C. Tumanut, J. Li, G. Spraggon, J. Chang, T. Tuntland, J. L. Harris and D. S. Karanewsky, *Bioorg. Med. Chem. Lett.*, 2006, **16**, 1975–1980.

12 S. M. Courtney, P. A. Hay, R. T. Buck, C. S. Colville, D. W. Porter, D. I. C. Scopes, F. C. Pollard, M. J. Page, J. M. Bennett, M. L. Hircock, E. A. Mckenzie, C. R. Stubberfield and P. R. Turner, *Bioorg. Med. Chem. Lett.*, 2004, **14**, 3269–3273.

13 J. Easmon, G. Pu, K. Thies, G. Heinisch and J. Hofmann, *J. Med. Chem.*, 2006, **49**, 6343–6350.

14 K. Wolfart, A. Molnar, M. Kawae, N. Motohashi and J. Molnar, *Biol. Pharm. Bull.*, 2004, **27**, 1462–1464.

15 I. Yildiz-Oren, I. Yalcin, E. Aki-Sener and N. Ucarturk, *Eur. J. Med. Chem.*, 2004, **39**, 291–298.

16 C. Ramalingan, S. Balasubramanian, S. Kabilan and M. Vasudevan, *Eur. J. Med. Chem.*, 2004, **39**, 527–533.

17 M. R. Deluca and S. M. Kerwin, *Tetrahedron Lett.*, 1997, **38**, 199–202.

18 M. Ukei, K. Ueno, S. Miyadoh, K. Abe, K. Shibata, M. Taniguchi and S. Oi, *J. Antibiot. (Tokyo).*, 1993, **46**, 1089–1094.

19 D. S. Surry and S. L. Buchwald, *Angew. Chemie Int. Ed.*, 2008, **47**, 6338–6361.

20 J. F. Hartwig, *Acc. Chem. Res.*, 2008, **41**, 1534–1544.

21 H. Rao, H. Fu, Y. Jiang and Y. Zhao, *Angew. Chemie Int. Ed.*, 2009, **48**, 1114–1116.

22 J. Kim and S. Chang, *Chem. Commun.*, 2008, 3052–3054.

23 J. Kim, S. Y. Lee, J. Lee, Y. Do and S. Chang, *J. Org. Chem.*, 2008, **73**, 9454–9457.

24 D. Monguchi, T. Fujiwara, H. Furukawa and A. Mori, *Org. Lett.*, 2009, **11**, 1607–1610.

25 D. Monguchi, A. Yamamura, T. Fujiwara, T. Somete and A. Mori, *Tetrahedron Lett.*, 2010, **51**, 850–852.

26 Q. Wang and S. L. Schreiber, *Org. Lett.*, 2009, **11**, 5178–5180.

27 S. H. Cho, J. Y. Kim, S. Y. Lee and S. Chang, *Angew. Chemie Int. Ed.*, 2009, **48**, 9127–9130.

28 J. Joseph, J. Y. Kim and S. Chang, *Chem. - A Eur. J.*, 2011, **17**, 8294–8298.

29 T. Kawano, K. Hirano, T. Satoh and M. Miura, *J. Am. Chem. Soc.*, 2010, **132**, 6900–6901.

30 J. F. Hartwig, *Nature*, 2008, **455**, 314–322.

31 M. M. Diaz-Requejo and P. J. Perez, *Chem. Rev.*, 2008, **108**, 3379–3394.

32 C. Liang, F. Collet, F. Robert-Peillard, P. Muller, R. H. Dodd and P. Dauban, *J. Am. Chem. Soc.*, 2008, **130**, 343–350.

33 H. Do and O. Daugulis, *J. Am. Chem. Soc.*, 2007, **129**, 12404–12405.

34 L. Ackermann, A. Althammer and S. Fenner, *Angew. Chemie - Int. Ed.*, 2009, **48**, 201–204.

35 J. Huang, J. Chan, Y. Chen, C. J. Borths, K. D. Baucom, R. D. Larsen and M. M. Faul, *J. Am. Chem. Soc.*, 2010, **132**, 3674–3675.

36 H. Hachiya, K. Hirano, T. Satoh and M. Miura, *Angew. Chemie Int. Ed.*, 2010, **49**, 2202–2205.

37 Y. Nakao, N. Kashihara, K. S. Kanyiva and T. Hiyama, *Angew. Chemie Int. Ed.*, 2010, **49**, 4451–4454.

38 S. Wertz, S. Kodama and A. Studer, *Angew. Chemie Int. Ed.*, 2011, **50**, 11511–11515.

39 G. Dyker, *Angew. Chemie Int. Ed.*, 1999, **38**, 1698–1712.

40 R. D. Viirre, G. Evindar and R. A. Batey, *J. Org. Chem.*, 2008, **73**, 3452–3459.

41 G. Evindar and R. A. Batey, *J. Org. Chem.*, 2006, **71**, 1802–1808.

42 G. Altenhoff and F. Glorius, *Adv. Synth. Catal.*, 2004, **346**, 1661–1664.

43 M. Terashima, M. Ishii and Y. Kanaoka, *Synthesis (Stuttg).*, 1982, **1982**, 484–485.

44 J. Chang, K. Zhao and S. Pan, *Tetrahedron Lett.*, 2002, **43**, 951–954.

45 R. S. Varma, R. K. Saini and O. Prakasht, *Tetrahedron Lett.*, 1997, **38**, 2621–2622.

46 C. Praveen, K. H. Kumar, D. Muralidharan and P. T. Perumal, *Tetrahedron Lett.*, 2008, **64**, 2369–2374.

47 C. Ke, T. YongQiang and Z. FuMin, *Sci. China Chem.*, 2010, **53**, 130–134.

48 W. Chen and Y. Pang, *Tetrahedron Lett.*, 2009, **50**, 6680–6683.

49 S. S. Pawar, D. V Dekhane, M. S. Shingare and S. N. Thore, *Aust. J. Chem.*, 2008, **61**, 905–909.

50 Y.-X. Chen, L.-F. Qian, W. Zhang and B. Han, *Angew. Chemie Int. Ed.*, 2008, **47**, 9330–9333.

51 M. Kidwai, V. Bansal, A. Saxena, A. Swati and S. Mozumdar, *Tetrahedron Lett.*, 2006, **47**, 8049–8053.

52 Y. Kawashita, N. Nakamichi, H. Kawabata and M. Hayashi, *Org. Lett.*, 2003, **5**, 3713–3715.

53 D. D. Diaz and M. G. Finn, *Chem. Commun.*, 2004, **2004**, 2514–2516.

54 A. Porcheddu, G. Giacomelli and I. Piredda, *J. Comb. Chem.*, 2009, **11**, 126–130.

55 L. Cai, Y. Han, S. Ren and L. Huang, *Tetrahedron*, 2000, **56**, 8253–8262.

56 L. M. Naumova, V. N. Charushin, O. N. Chupakhin and G. G. Izmailova, *Chem. Heterocycl.*

Compd., 1985, **21**, 326–331.

57 A. G. Mikhailovskii and M. I. Bakrin, *Chem. Heterocycl. Compd.*, 1991, **27**, 1091–1094.

58 J. Xu, J. Li, Z. Wei, Q. Zhang and D. Shi, *RSC Adv.*, 2013, **3**, 9622–9624.

59 J. Wang, J. Hou, J. Wen, J. Zhang and X. Yu, *Chem. Commun.*, 2011, **47**, 3652–3654.

60 W.-J. Yoo, H. Yuan, H. Miyamura and S. Kobayashi, *Adv. Synth. Catal.*, 2011, **353**, 3085–3089.

61 X. Wang, D. Xu, C. Miao, Q. Zhang and W. Sun, *Org. Biomol. Chem.*, 2014, **12**, 3108–3113.

62 Y. S. Wagh, N. J. Tiwari and B. M. Bhanage, *Tetrahedron Lett.*, 2013, **54**, 1290–1293.

63 W. Gao, W. Li, C. Zeng, H. Tian, L. Hu and R. D. Little, *J. Org. Chem.*, 2014, **79**, 9613–9618.

64 F. Li, Z. Li, X. Tang, X. Cao, C. Wang and J. Li, *ChemCatChem*, 2019, **11**, 1192–1195.

65 T. Keshari, V. P. Srivastava and L. D. S. Yadav, *RSC Adv.*, 2014, **4**, 5815–5818.

66 V. P. Srivastava and L. D. S. Yadav, *Synlett*, 2013, **24**, 2758–2762.

67 D. Xu, W. Wang, C. Miao, Q. Zhang, C. Xia and W. Sun, *Green Chem.*, 2013, **15**, 2975–2980.

68 Y. Li, Y. Xie, R. Zhang, K. Jin, X. Wang and C. Duan, *J. Org. Chem.*, 2011, **76**, 5444–5449.

69 K. Cao, J. Wang, L. Wang, Y. Li and X. Yu, *Synth. Commun.*, 2014, **44**, 2848–2853.

70 Y. Li, J. Liu, Y. Xie, R. Zhang, K. Jin, X. Wang and C. Duan, *Org. Biomol. Chem.*, 2012, **10**, 3715–3720.

71 P. Anastas and J. Warner, *Green Chemistry: Theory and Practice*, Oxford University Press, 1998.

72 J. Lee, O. K. Farha, J. Roberts, K. a Scheidt, S. T. Nguyen and J. T. Hupp, *Chem. Soc. Rev.*, 2009, **38**, 1450–1459.

73 A. Corma, H. García and F. X. Llabrés i Xamena, *Chem. Rev.*, 2010, **110**, 4606–4655.

74 S. Ou and C.-D. Wu, *Inorg. Chem. Front.*, 2014, **1**, 721–734.

75 P. K. Dutta, S. Sen, D. Saha and B. Dhar, *European J. Org. Chem.*, 2018, 657–665.

76 P. Pal, A. K. Giri, H. Singh, S. C. Ghosh and A. B. Panda, *Chem. - An Asian J.*, 2014, **9**, 2392–2396.

77 J. Y. Kim, S. H. Cho, J. Joseph and S. Chang, *Angew. Chemie Int. Ed.*, 2010, **49**, 9899–9903.

78 S. C. Chen, N. Li, F. Tian, N. N. Chai, M. Y. He and Q. Chen, *Mol. Catal.*, 2018, **450**, 104–111.

79 J. Y. Kim, S. H. Cho, J. Joseph and S. Chang, *Angew. Chemie - Int. Ed.*, 2010, **49**, 9899–9903.

80 C. Guo, Y. Zhang, X. Nan, C. Feng, Y. Guo and J. Wang, *Mol. Catal.*, 2017, **440**, 168–174.

81 H. Naeimi and S. Rahmatinejad, *Synth. React. Inorganic, Met. Nano-Metal Chem.*, 2016, **46**, 471–476.

82 H. Naeimi and S. Rahmatinejad, *Polycycl. Aromat. Compd.*, 2016, **36**, 773–788.

83 T. T. Nguyen, X.-T. T. Nguyen, T.-L. H. Nguyen and P. H. Tran, *ACS Omega*, 2019, **4**, 368–373.

84 L. H. T. Nguyen, T. T. Nguyen, H. L. Nguyen, T. L. H. Doan and P. H. Tran, *Catal. Sci. Technol.*, 2017, **7**, 4346–4350.

85 A. Ziarati, A. Sobhani-Nasab, M. Rahimi-Nasrabadi, M. R. Ganjali and A. Badiei, *J. Rare Earths*, 2017, **35**, 374–381.

86 Z. Benzekri, S. Sibous, H. Serrar, A. Ouasri, S. Boukhris, A. Rhandour and A. Souizi, *J. Iran. Chem. Soc.*, 2018, **15**, 2781–2787.

87 S. Banerjee, S. Payra, A. Saha and G. Sereda, *Tetrahedron Lett.*, 2014, **55**, 5515–5520.

88 J. He, F. Lin, X. Yang, D. Wang, X. Tan and S. Zhang, *Org. Process Res. Dev.*, 2016, **20**, 1093–1096.

89 F. M. Moghaddam, V. Saberi, S. Kalhor and N. Veisi, *Appl. Organomet. Chem.*, 2018, **32**, 4240.

90 N. Li, J. Xu, R. Feng, T.-L. Hu and X.-H. Bu, *Chem. Commun.*, 2016, **52**, 8501–8513.

91 P. Horcajada, R. Gref, T. Baati, P. K. Allan, G. Maurin, P. Couvreur, G. Férey, R. E. Morris and C. Serre, *Chem. Rev.*, 2012, **112**, 1232–1268.

92 A. J. Howarth, Y. Liu, P. Li, Z. Li, T. C. Wang, J. T. Hupp and O. K. Farha, *Nat. Rev. Mater.*, 2016, **1**, 1–15.

93 G. Férey, *Chem. Soc. Rev.*, 2008, **37**, 191–214.

94 K. S. Park, Z. Ni, A. P. Cote, J. Y. Choi, R. Huang, F. J. Uribe-Romo, H. K. Chae, M. O'Keeffe

and O. M. Yaghi, *Proc. Natl. Acad. Sci.*, 2006, **103**, 10186–10191.

95 J. Qian, F. Sun and L. Qin, *Mater. Lett.*, 2012, **82**, 220–223.

96 R. Banerjee, A. Phan, B. Wang, C. Knobler, H. Furukawa, M. O'Keeffe and O. M. Yaghi, *Science (80-.).*, 2008, **319**, 939–944.

97 K. Zhou, B. Mousavi, Z. Luo, S. Phatanasri, S. Chaemchuen and F. Verpoort, *J. Mater. Chem. A*, 2017, **5**, 952–957.

98 K. Leus, T. Bogaerts, J. De Decker, H. Depauw, K. Hendrickx, H. Vrielinck, V. Van Speybroeck and P. Van Der Voort, *Microporous Mesoporous Mater.*, 2016, **226**, 110–116.

99 C. Mottillo and T. Friščić, *Angew. Chemie Int. Ed.*, 2014, **53**, 7471–7474.

100 C. O. Kappe and D. Dallinger, *Nat. Rev. Drug Discov.*, 2006, 5, 51–63.

101 S. Horikoshi and N. Serpone, *Catal. Sci. Technol.*, 2014, 4, 1197–1210.

102 V. Polshettiwar and R. S. Varma, *Green Chem.*, 2010, **12**, 743–754.

103 C. O. Kappe, *Angew. Chemie Int. Ed.*, 2004, **43**, 6250–6284.

104 A. de la Hoz and A. Loupy, Eds., *Microwaves in Organic Synthesis*, Wiley-VCH Verlag GmbH & Co. KGaA, Weinheim, Germany, Third., 2012.

105 D. M. P. Mingos, *Microwave Assisted Organic Synthesis*, Blackwell Publishing, Oxford, 2005.

106 C. O. Kappe, D. Dallinger and S. S. Murphree, Eds., *Practical Microwave Synthesis for Organic Chemists—Strategies, Instruments, and Protocols*, Wiley-VCH, Weinheim, 2008.

107 V. A. Chebanov, V. E. Saraev, S. M. Desenko, V. N. Chernenko, S. V Shishkina, O. V Shishkin, K. M. Kobzar and C. O. Kappe, *Org. Lett.*, 2007, **9**, 1691–1694.

108 T. N. Glasnov, W. Stadlbauer and C. O. Kappe, *J. Org. Chem.*, 2005, **70**, 3864–3870.

109 X. Zhang, D. O. Hayward, D. Michael and P. Mingos, *Catal. Letters*, 2003, **88**, 33–38.

110 A. Datan, A. Kulkarni and B. Török, *Green Chem.*, 2012, 14, 17–37.

111 T. L. H. Doan, T. Q. Dao, H. N. Tran, P. H. Tran and T. N. Le, *Dalt. Trans.*, 2016, **45**, 7875–7880.

112 K. Leus, T. Bogaerts, J. De Decker, H. Depauw, K. Hendrickx, H. Vrielinck, V. Van Speybroeck and P. Van Der Voort, *Microporous Mesoporous Mater.*, 2016, **226**, 110–116.

113 G. Sankar, R. Raja and J. M. Thomas, *Catal. Letters*, 1998, **55**, 15–23.

114 J. Ibáñez, M. Araque-Marin, S. Paul and M. Pera-Titus, *Chem. Eng. J.*, 2019, **358**, 1620–1630.

115 C. Chizallet, S. Lazare, D. Bazer-Bachi, F. Bonnier, V. Lecocq, E. Soyer, A. A. Quoineaud and N. Bats, *J. Am. Chem. Soc.*, 2010, **132**, 12365–12377.

116 T. Katsuki and K. B. Sharpless, *J. Am. Chem. Soc.*, 1980, **102**, 5974–5976.

117 K. Y. A. Lin and H. A. Chang, *J. Taiwan Inst. Chem. Eng.*, 2015, **53**, 40–45.

118 T. Truong, T. M. Hoang, C. K. Nguyen, Q. T. N. Huynh and N. T. S. Phan, *RSC Adv.*, 2015, **5**, 24769–24776.

119 J. Zakzeski, A. Dbczak, P. C. a Bruijnincx and B. M. Weckhuysen, *Appl. Catal. A Gen.*, 2011, **394**, 79–85.

120 V. D. Nguyen, C. K. Nguyen, K. N. Tran, T. N. Tu, T. T. Nguyen, H. V. Dang, T. Truong and N. T. S. Phan, *Appl. Catal. A Gen.*, 2018, **555**, 20–26.

121 L. T. L. Nguyen, K. K. a. Le, H. X. Truong and N. T. S. Phan, *Catal. Sci. Technol.*, 2012, **2**, 521–528.

122 L. Yang, L. Yu, M. Sun and C. Gao, *Catal. Commun.*, 2014, **54**, 86–90.

123 B. Pattengale, S. Yang, J. Ludwig, Z. Huang, X. Zhang and J. Huang, *J. Am. Chem. Soc.*, 2016, **138**, 8072–8075.

124 D. Yu, S. Lee, N. Sum and Y. Zhang, *Adv. Synth. Catal.*, 2012, **354**, 1672–1678.

125 Y. Qiu, J. Struwe, T. H. Meyer, J. C. A. Oliveira and L. Ackermann, *Chem. - A Eur. J.*, 2018, **24**, 12784–12789.

126 S. P. Marsden, A. E. McGonagle and B. McKeever-Abbas, *Org. Lett.*, 2008, **10**, 2589–2591.

127 Z. Luo, H. Wu, Y. Li, Y. Chen, J. Nie, S. Lu, Y. Zhu and Z. Zeng, *Adv. Synth. Catal.*, 2019, **361**, 4117–4125.

128 A. S. Singh, M. Singh, N. Mishra, S. Mishra, A. K. Agrahari and V. K. Tiwari, *ChemistrySelect*, 2017, **2**, 154–159.

129 Q. Li and H. Kim, *Fuel Process. Technol.*, 2012, **100**, 43–48.

Chapter 5: Mesoporous Silicas as Scaffolds for Organocatalysts

5.1 Introduction

5.1.1 Basis for Immobilising Organocatalysts

As discussed in Chapter 1, organocatalysis has emerged as a powerful tool in asymmetric reactions. One arc of exploration has been the immobilisation of organocatalysts onto an insoluble support, to solve one of the greatest challenges associated with these compounds. The use of organocatalysts in larger-scale chemical processes is limited by their homogeneous nature resulting in lower stability, agglomeration/aggregation of active sites, as well as a difficult and expensive recovery from the reaction mixture. Although anchoring the organic entity requires additional steps, it is believed to be worthwhile as the design of a heterogeneous organocatalyst could improve activity and selectivity, before being recovered easily for reuse. This change in activity/selectivity is accredited to the steric effect the support and linker may offer, as well as the increased stability of the catalyst, and thus the likely increased stability of any transition state involved.

To date, there are a limited number of reports of immobilised organocatalysts capable of achieving the high activity/selectivity that has been established with their homogeneous counterparts.[1] This highlights the need to develop the supports, methods and catalysts chosen for immobilisation to realise the full potential of this approach.

5.1.2 Choice of Supports

There are a number of support types available, and as the active site will be in close proximity to its surface, careful consideration should be taken when selecting which support to use. It is desirable to be able to tailor the properties of the support such as its hydrophobicity, functionality, topology and thermal stability, as each factor could prevent the desired reaction from taking place. It is an additional bonus if there are synergistic interactions with the support, which could boost the material’s potential applications. Solubility factors and solvent versatility play an important role when choosing the support as they are vital to achieving optimum reaction conditions. The organic entity must also be considered to ensure that the active site remains free after the anchoring process. For example, an amino acid would be attached *via* a side chain, so that the amine remains free to interact with the substrates.

5.1.2.1 Method of Bonding

There are two general concepts for the immobilisation of a catalyst, through covalent or non-covalent bonding. Non-covalent anchoring uses entrapment or electrostatic interactions to produce a strong hold on the organic molecule.[2] This method is typically quick and cheap with minimal modification to the parent catalyst. However, it is also believed to be more prone to leaching than a covalent equivalent. An example of this method is the anchoring of an *L*-proline derivative within β-cyclodextrin. The molecule is held fast by taking advantage of the hydrophobic interactions of the phenyl ring with the inner surface of the cyclodextrin, and the ability to form H-bonds between the substrate and the hydroxyl groups around the opening.[3] It is easily prepared by heating the two components in ethanol and water, before removing the solvent. The catalyst achieved high yields and enantioselectivities in aldol reactions such as the one illustrated in Scheme 25.

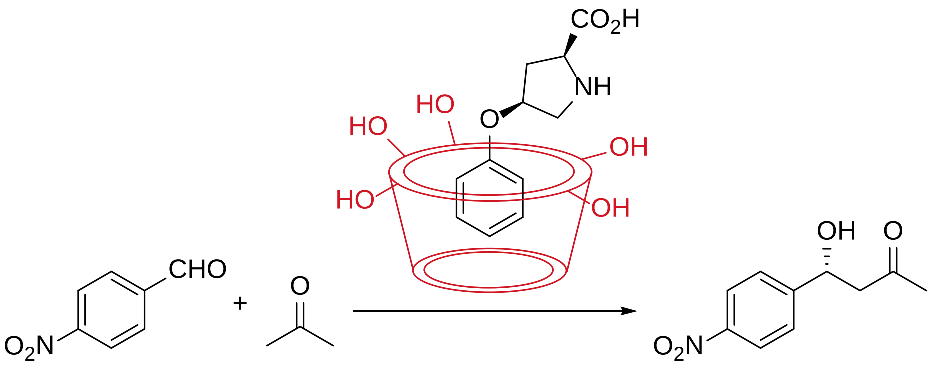

Scheme 25: Asymmetric aldol reaction of a benzaldehyde with acetone, catalysed by *L*-proline immobilised in β-cyclodextrin.

Although forming a covalent linkage can be synthetically more demanding, the strong complex-support binding and retention of the ligand is well worth the effort in order to minimise leaching and exploit the benefits of heterogenisation. This should come hand-in-hand with improved reusability too. Tethering tends to require modifying the parent catalyst to add an appropriate handle on which to anchor the support. Options available include dendrimers[4] and PEG supports[5,6] which are soluble in polar solvents – a homogeneous trait which could be beneficial. However, they tend to suffer from poor recyclability due to decreasing activity, and the need for treatment steps. Polystyrenes have arisen as one of the most popular choice of supports, and can be recovered by a simple filtration. This was demonstrated by functionalising *L*-proline derivatives with unsaturated side-chains which can be immobilised onto pre-functionalised polystyrenes (Scheme 26).[7,8] Whilst successful in catalysing their reported reactions, and performing similarly if not better than their monomeric counterparts, the anchored prolines still struggle to compare with their simpler parent catalyst.

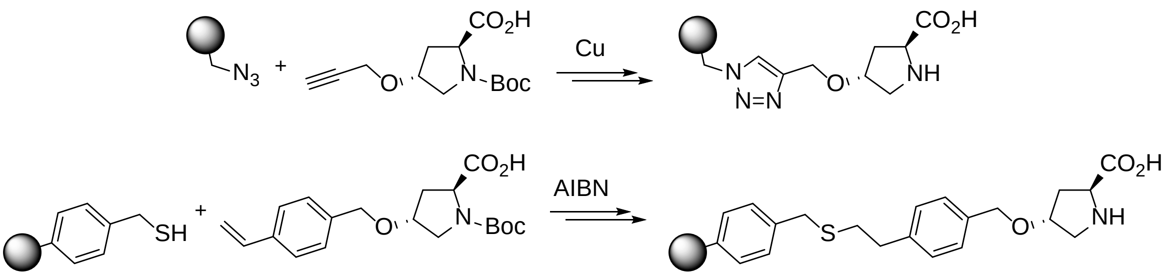

Scheme 26: Amino acid immobilisation on polystyrene supports.

5.1.2.2 Mesoporous Silicas

In the past two decades, the development of silicas as supports has generated more attention.[9,10] Silylation has emerged as the most reliable method to prepare organic-inorganic hybrids. Catalytic sites can be added and hydrophobicity easily manipulated by exploiting silanol groups on the surface, and employing simple "click" chemistry.[9] There are a wide range of silicas to choose from with varied surface areas and porosities, many of which are commercially available. Silica itself is a general term for the different forms of SiO_2, composed of a disordered manner of SiO_4 tetrahedra with shared vertices. More ordered silicas can be synthesised under hydrothermal conditions, using structure-directing agents to promote various morphologies, although amorphous silica is frequently used instead because of its availability. These are split into three classes:[11]

1. Silica gels are formed by polymerising primary silicates. They can be modulated by altering the duration of gel aging or drying conditions. Drying under heat promotes the partial collapse of the pore system, resulting in lower surface areas and pore volume. Whilst more mild conditions form aerogels with high porosity and surface areas. Current processes also allow for the preparation of narrow pore size distributions, from microporous to macroporous, with a range of 5-2000 Å to choose from.

2. Precipitated silica on the other hand uses conditions to prevent the formation of gels, obtaining larger particles with wider pore size distributions. Fumed silicas are prepared from aerosols at high temperatures, resulting in higher purities. Although non-porous, their small particle size offers low to moderate surface areas. The surface holds many silanols of different natures, isolated, vicinal, and even double/triple hydroxyls on a single silica atom.

3. Non-porous supports allow for easy accessibility to the active site. While studies have revealed the concave surfaces within the channels of porous silicas can have a beneficial effect on stereoselectivity over convex surfaces seen with the likes of cabosil.[12,13] Where the concave surface is less accessible, it is dependent on the pore size and if there is

enough space for transport of substrates to and from the active site. The restrictions a concave surface would have on the approach and evacuation of key substrates is illustrated in Figure 56.

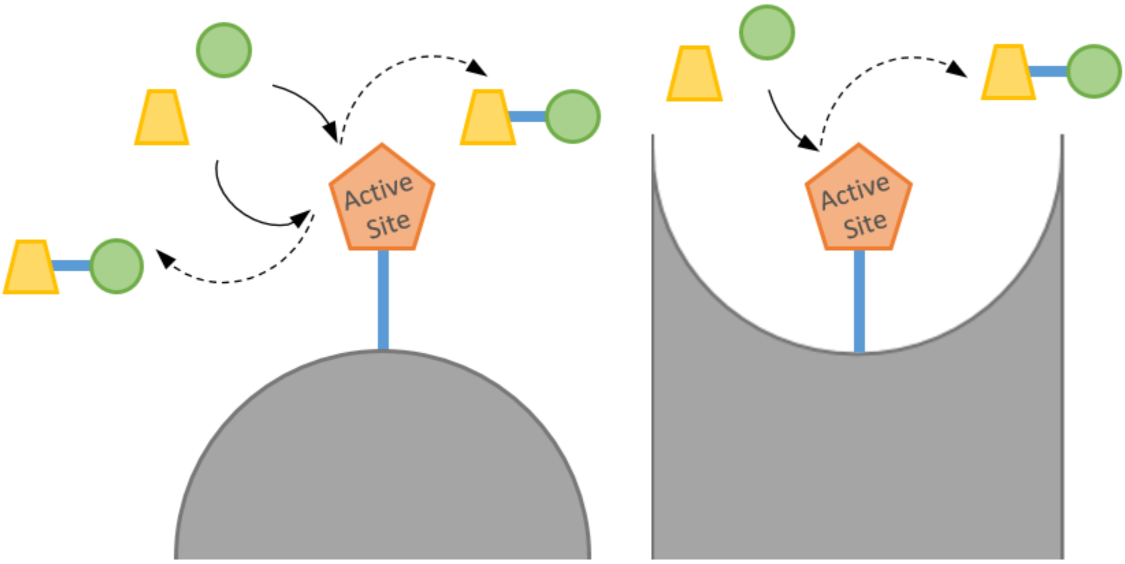

Figure 56: Constraints of an active site on convex and concave surfaces.

Constrained environments can manipulate the substrate's orientation to favour a desired stereoisomer.[13] The different properties of silicas will also have a significant effect on catalyst loading and diffusion, which in turn is likely to effect the selectivity and activity of the anchored catalyst.

Crystalline architectures such as MCM-41 and SBA-15 can be synthesised, offering long range order of mesopores. However, as the pore walls consist of amorphous silica, there is no short range order, thus sharing traits with zeolites and amorphous silicas. This partial crystallinity is useful for anchoring organic molecules, and tailoring pore size with the use of SDAs. MCM-41 is a hexagonal structure with straight channels typically 30 Å in diameter, but can be modified between 15-200 Å.[14] SBA-15 is also a hexagonal structure with curved mesopores and thick microporous walls, resulting in high thermal stability.[15] Pore sizes are typically larger than MCM-41 at 80 Å, although the procedure can be modified to achieve mesopores between 40-140 Å.

5.1.2.3 Grafting onto Silica

Forming a covalent linkage has become the most frequently employed method for immobilising homogeneous catalysts. In order for this to occur with silicas, the support and ligand must be functionalised in a way to enable immobilisation. Pendant silanol groups work well with this methodology, which could include reacting directly with a siloxane functionalised catalyst.

Alternatively, a wide variety of functional groups can be attached to the surface of inorganic supports, there are many commercial examples of siloxanes with cyano-, thiol-, amine- and halide-groups on differing tether lengths. These groups can then react with suitably functionalised ligands to form a new covalent bond, anchoring the organic motif to the support. One such example uses AIBN as a radical initiator in the reaction of vinyl-functionalised ligands with thiol-functionalised silica, as displayed in Scheme 27.[16] However, when using this approach, it is important to consider how the remaining silanol groups may interact with the catalyst intended to be anchored. There are mixed reports of the role silanols can play, one report proposed they can help orientate access trajectory,[17] while another found the facile protection of silanols with trimethylsilyl groups led to an increase in hydrophobicity and improved enantioselectivities.[18]

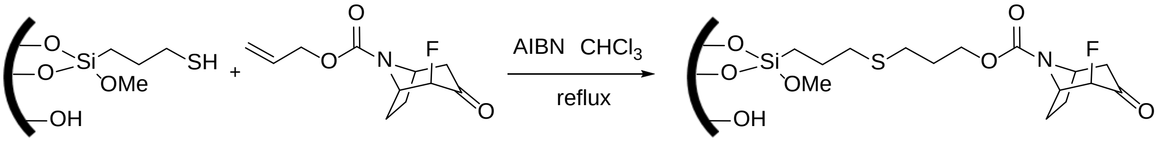

Scheme 27: Preparation of silica-bound α-fluorotropinones.

Using this information, the subsequent material should adhere to the following characteristics:

- Minimal modification to the parent catalyst
- Robust linkage
- Accessible and isolated active site

5.1.3 Characterisation

Having selected to work with mesoporous silicas, and the bulk of the material being a silica support, characterising the organic matter now presents several difficulties. With no metal present, analytical methods previously used to gain structural understanding (such as UV-Vis) offer very little useful information, whilst XRD can simply confirm the structural integrity of ordered silicas before and after immobilisation. The most common organocatalysts contain nitrogen, therefore a simple elemental analysis is often the first technique employed. By avoiding the use of nitrogen containing solvents during the immobilisation process, this can be a reliable method to quantify how much active catalyst is present. Evidence for a covalent anchor can be gained by studying the BET adsorption isotherms, as it would limit the area available for gaseous molecules to adsorb, thus reducing the specific surface area observed. A decrease in pore volume will also indicate the catalyst being anchored within the channels and not only on the outer surface. ^{13}C MAS NMR has become a strong technique to analyse the presence of immobilised catalyst, by comparing the peaks observed with those of the parent catalyst in the solution phase. However, it can be difficult to discern intricacies due to the low content of the ^{13}C isotope, within an already low content of carbon in the sample, generating weak spectra. ^{29}Si NMR is more likely to provide details on covalent anchoring, with the appearance of peaks downfield to the bulk material corresponding to the silicon at the base of the tether. IR spectra are also likely to be complicated by the support masking absorbance in the active site. Peaks would be expected for C-H, N-H and O-H bonds, as well as new peaks around 1000 cm^{-1} for the Si-O environments in the tether, which would further support a covalent anchor. Whilst each of these methods struggle to be as definitive as methods used for the parent catalyst, collectively they may elucidate the nature of the immobilised material.

5.1.4 Choice of Catalyst

Due to their chirality, high functionality, and flexibility for anchoring options, amino acids have been ahead of the pack as the most popular class of organocatalysts to immobilise. As mentioned in Chapter 1, there is a long-standing goal towards identifying a general organocatalyst that can promote a large number of enantioselective reactions, through multiple modes of activation, with good substrate tolerance. The Jørgensen-Hayashi (J-H) series of *L*-proline derivatives have shown great promise in this respect. The bulky diarylprolinol silyl ethers have shown exceptional stereochemical control, applied to a diverse range of asymmetric organic transformations,[19–21] most notably with stereoselective Michael additions.[22] A few examples of possible reactions pathways are highlighted in Figure 57.

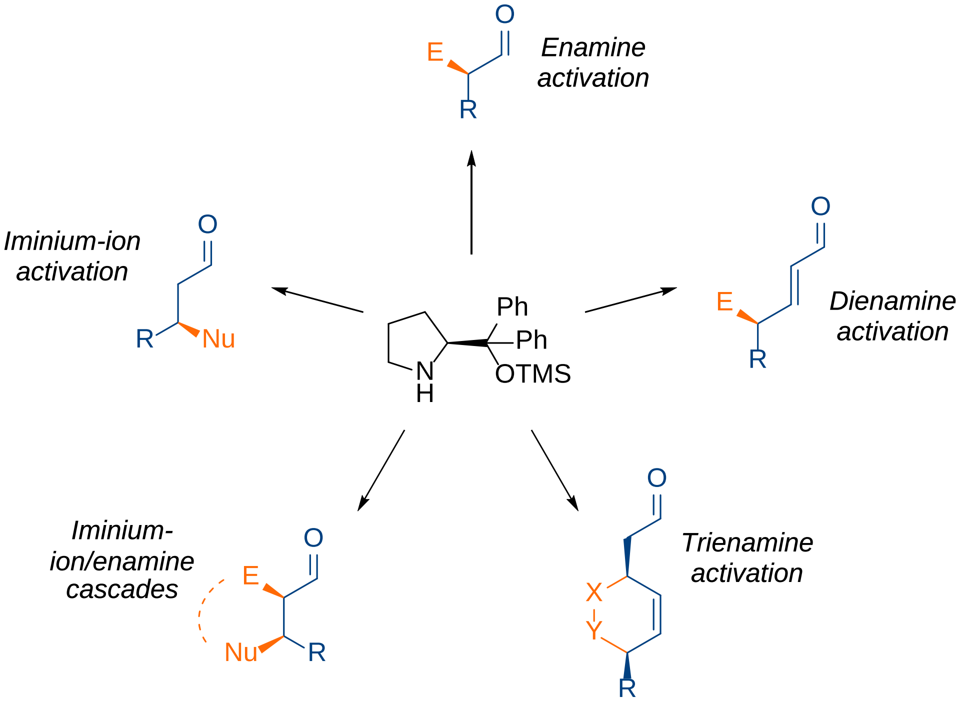

Figure 57: Possible reaction pathways for diarylprolinol silyl ether catalysis.

Some examples of immobilised proline derivatives on various heterogeneous supports have been collected in Table 36, attached in the Appendix. One report chose to graft a J-H catalyst onto SBA-15. The catalyst achieved high yields of 73-82 % and excellent enantioselectivities of 94-96 % in three Michael additions, one of which is displayed in Scheme 28.

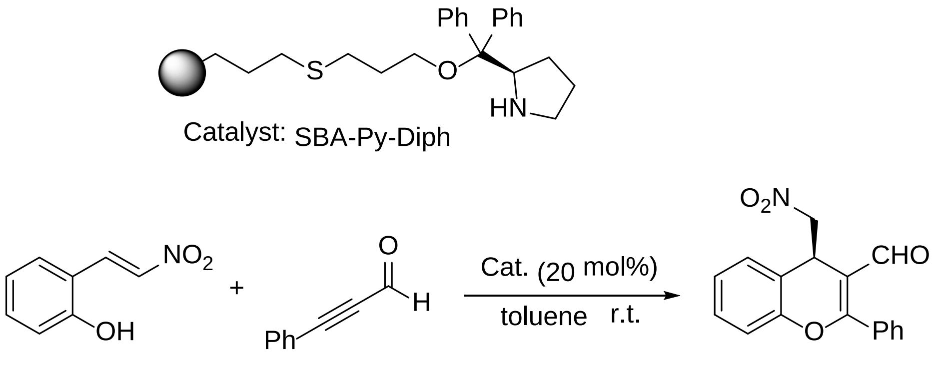

Scheme 28: Oxa-Michael-Michael cascade reaction with an immobilised proline catalyst.

5.1.5 Immobilising the Chosen Catalyst onto the Chosen Support

Thiol-functionalisation of the silica surface, before reacting with a vinyl-functionalised catalyst to form a covalent tether, has proven successful in immobilising the organic motif and utilising it to catalyse organic transformations. Another example is shown in Scheme 29 with the J-H catalyst performing a Henry-Michael reaction *via* an enamine intermediate.[23] The aim for the work detailed here is to imitate the procedure for immobilisation, then apply it to iminium catalysis.

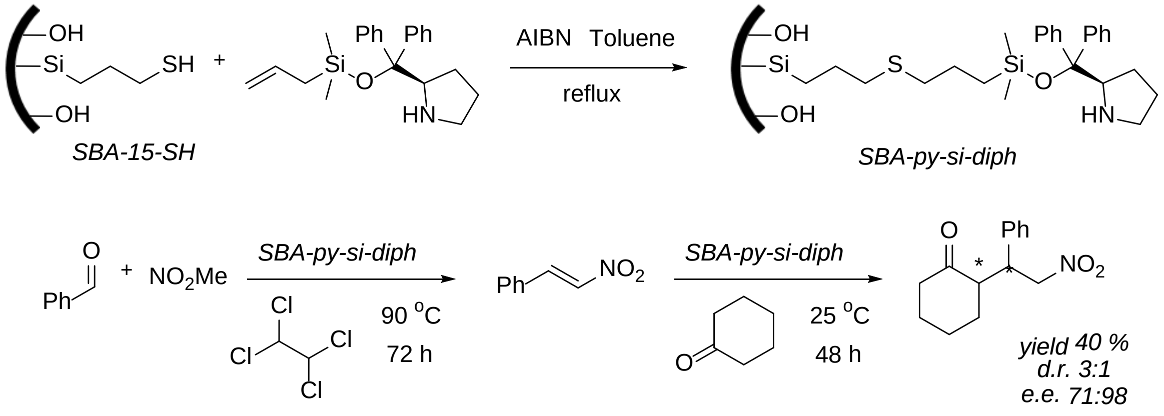

Scheme 29: Grafting of pyrrolidine catalyst followed by catalysis of a Henry-Michael reaction.

In selecting the J-H catalyst, the branched chain was thought to be the best choice to use for immobilisation, rather than functionalising at the 4-position on the ring which can prove more expensive.[24] Displayed in Scheme 30 is a method used to covalently immobilise the J-H catalyst. The relatively cheap diphenylprolinol can undergo a facile substitution to form a strong Si-O bond, adding an alkene group to the motif. Pendant silanols are used to attach thiol groups to the support surface with more Si-O bonds. The tethering silica atom varies in coordination depending on the number of ethoxy-groups remaining, which will generate three peaks in the ^{29}Si NMR. Finally, a radical addition immobilises the catalyst with a thiol ether. Each step is performed in nitrogen free solvents, such that elemental analysis can provide a reliable method to quantifying the loading achieved.

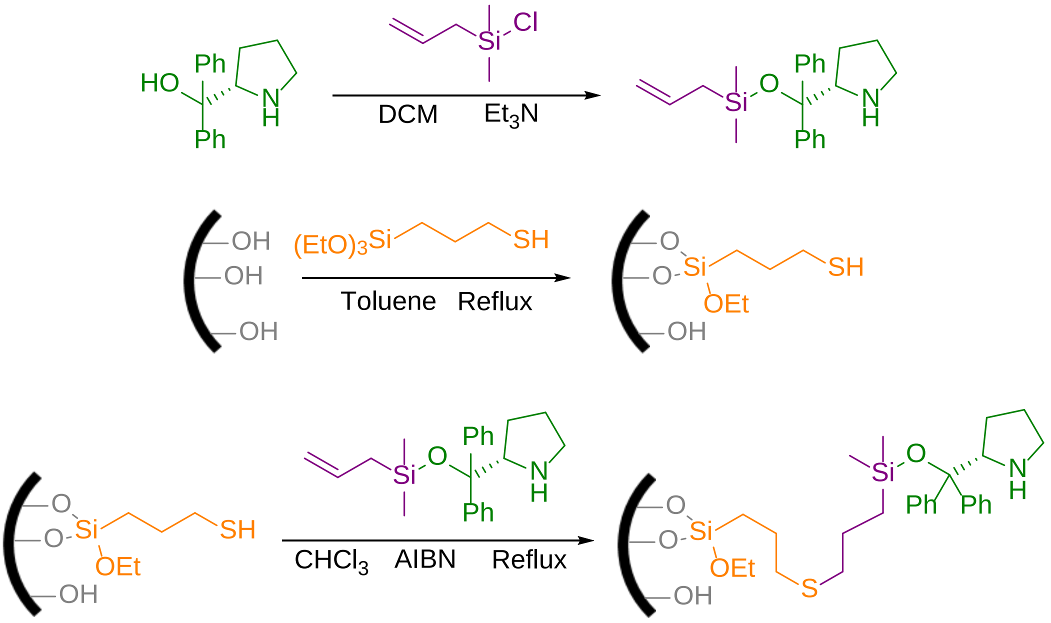

Scheme 30: Method for the immobilisation of a diarylprolinol on silica supports.

It has been noted tether length is able to influence the reaction. Using a long tether such as the one in Scheme 30 can lift the catalyst further from the surface, maintaining the catalyst's more homogeneous behaviour. Beneficial effects have been observed as a result, including improved enantioselectivity and lower levels of leaching.[18,25] However, longer tethers also risk increased steric hindrance if within constricting pore channels. It is believed pore volume is significant to any organic transformation trialled as a smaller constricted space will mean that the active site is still close to the surface of the silica, reducing its homogeneous traits. It would be of interest to investigate whether there is a "goldilocks" pore size, one that is wide enough to not decrease the effectiveness of the catalyst and transport to and from, but one that may also be constricted enough to promote selectivity towards the desired product. The aim of this approach is to be able to trial the catalyst in batch reactions to gain assurance of its activity and potential, before ultimately finding a method to utilise flow chemistry.[26,27]

5.1.6 Cyclopropanation

Sequential iminium-enamine catalysis was discussed in Chapter 1, a limitation was that the electrophile and nucleophile must be simultaneously present while not reacting with each other.

An alternative is to use a nucleophile with a leaving group, such that after initial addition of the nucleophile to the iminium ion, intramolecular attack could occur to remove the leaving group and form a cyclic product. An example of this is the work of Kunz and MacMillan, the reaction shown in Scheme 31 achieved high yields and stereoselectivity.[28]

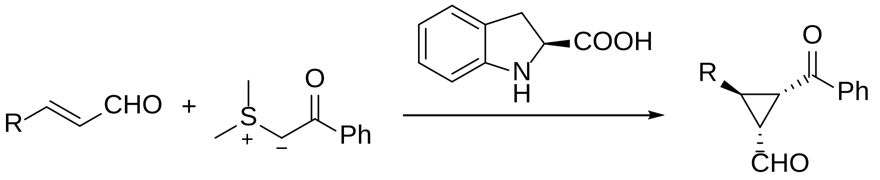

Scheme 31: Cyclopropanation of α,β-unsaturated aldehydes with a β-oxosulfonium ylide.

The cyclopropane structure can be found in a variety of compound classes such as terpenes, pheromones, fatty acid metabolites and unnatural amino acids.[29] Whilst derivatives have shown a wide range of biological activities, including insecticidal, antibiotic, antifungal, antitumor, and antiviral.[30] The motif is well known as being a versatile intermediate for a variety of synthetically useful ring-opening reactions.[31] Understandably, the unusual structural properties and abundance of cyclopropanes in natural products and pharmaceuticals has attracted organic chemists. In particular, the enantioselective synthesis of substituted cyclopropanes with desirable chirality, for which novel and more efficient methods are still developing.[32]

The Simmons-Smith cyclopropanation discovered that alkenes reacting with diiodomethane in the presence of activated zinc could give high yields of cyclopropanes.[33,34] It was advantageous due to the scope of substrates that could be used, tolerance to various functional groups, and stereospecificity. Since then, multiple methodologies have been reported investigating the scope of enantioselectivity. With the advent of organocatalysis as a powerful alternative for asymmetric catalysis, the interest in synthesising cyclopropanes has not been exempt from this. The majority of these reports utilise a Michael-initiated ring-closing (MIRC) of pre-enolised or readily enolisable nucleophilic species.[28,35–39] More recently, derivatives of aryl methanes have been reported as sufficient nucleophiles. Particularly with nitro groups in the *ortho*- and/or *para*-positions of the aryl group, as this results in strong inductive and resonance effects, increasing the molecule's nucleophilicity.

In the past year, our research group has published the first enantioselective cyclopropanation of enals using benzyl chlorides.[40] In Scheme 32 is one example of the homogeneous catalyst (S)-α,α-diphenylprolinol trimethylsilyl ether, a chiral secondary amine that gives high yields and selectivities in the formation of formyl cyclopropanes. One aim for the work presented here is to reproduce these results with an immobilised variation.

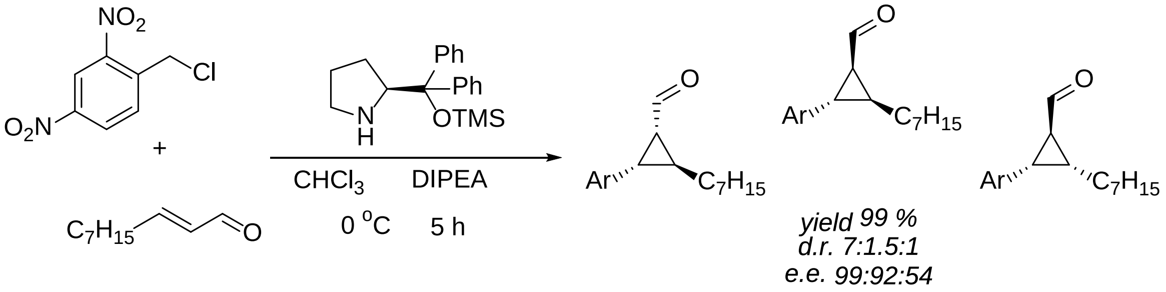

Scheme 32: Cyclopropanation of 2,4-dinitrobenzyl chloride and *trans*-decenal.

The mechanism displayed in Scheme 33 illustrates how this asymmetric Michael addition-α-alkylation cascade proceeds. Activation of the α,β-unsaturated aldehyde (**22**) with the aminocatalyst **23** forms an iminium intermediate, the *trans*-stereoisomer is favoured to reduce steric clash from the side chain. Deprotonation of the benzyl halide **21** at the α-position, stabilised by strong mesomeric effects of the nitro-groups, leads to *in situ* generation of a carbanion. The resulting nucleophilic attack of the unsaturated chain is directed to the *Re*-face, away from the bulky silyl ether on the pyrrolidine ring. An organocascade reaction is further initiated through the enamine intermediate in an irreversible intramolecular α-alkylation towards the now electrophilic centre on the benzyl halide. A 3-exo-trig cyclisation then occurs, leading to the cyclopropane product, and regeneration of the catalyst. Michael additions tend to be reversible to some degree, which makes them less than ideal when testing new catalytic systems. The Michael addition here is paired with an organocascade resulting in an irreversible process, allowing for a better understanding of the catalyst's potential.

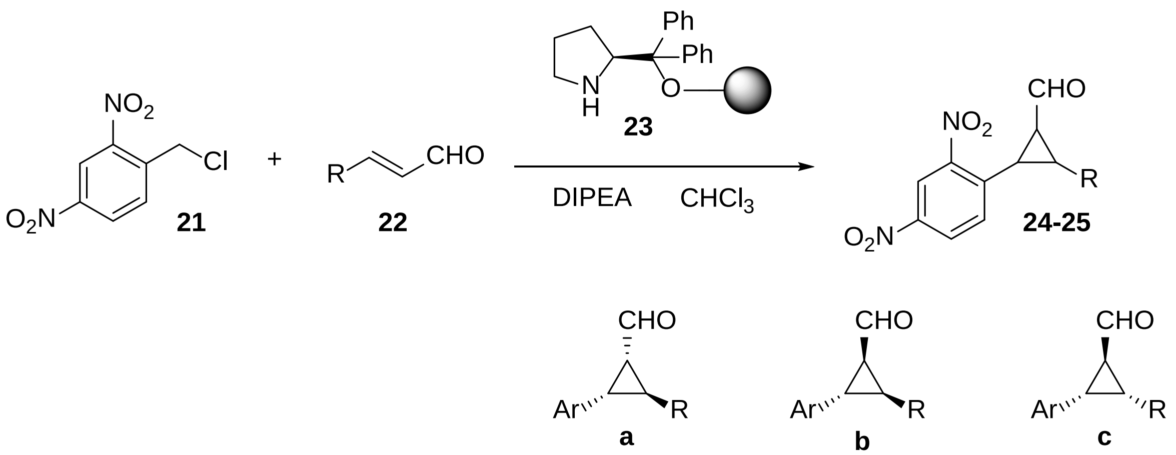

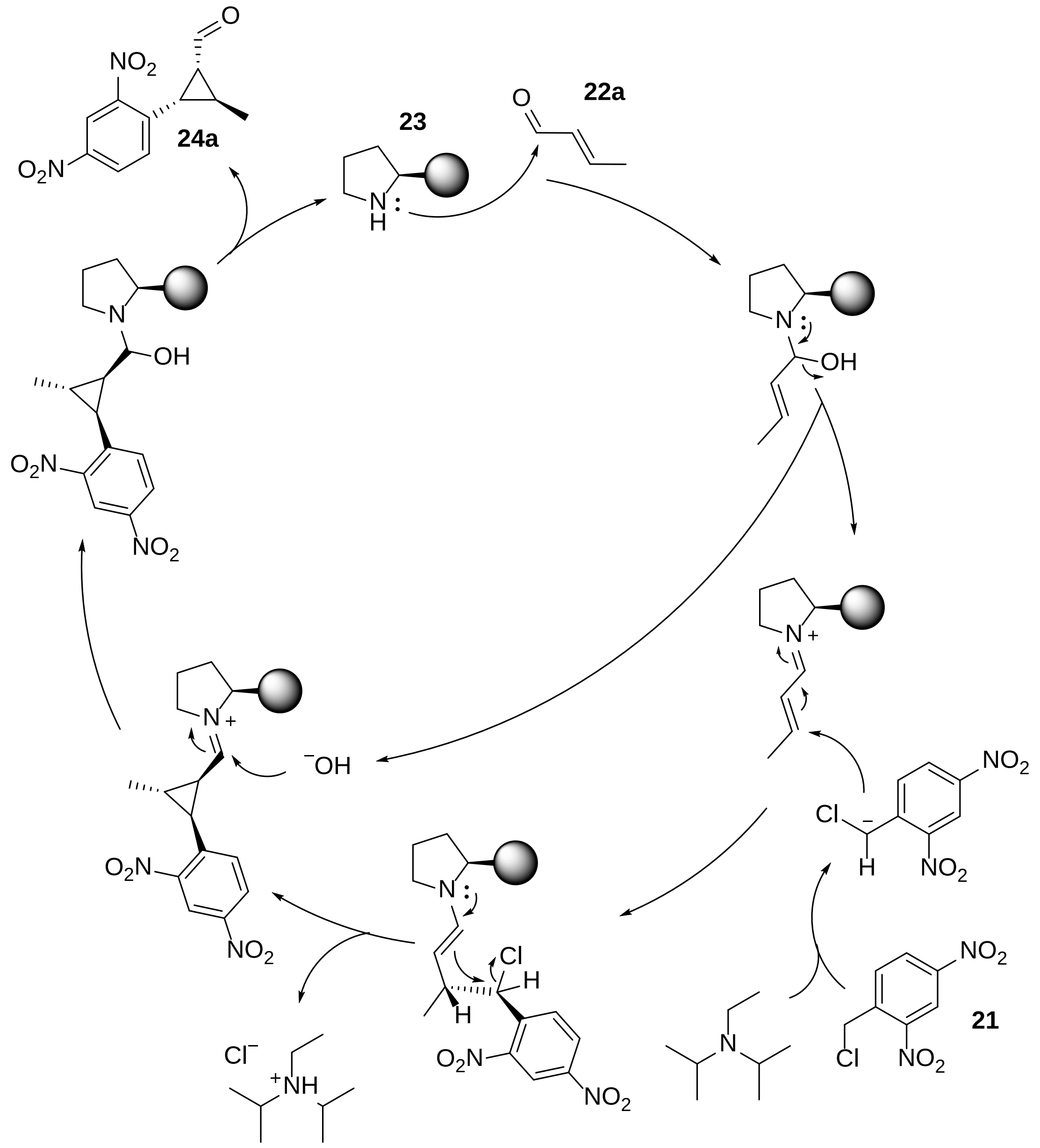

Scheme 33: Proposed mechanism for the cyclopropanation of 2,4-dinitrobenzyl chloride and *trans*-crotonaldehyde using a chiral secondary amine catalyst.

5.2 Aims and Objectives

The following scheme will be explored:

i. Using click chemistry, immobilise a Jørgensen-Hayashi catalyst onto a variety of mesoporous silicas, including disordered and ordered examples with a range of pore sizes from 30-250 Å;

ii. Confirm the immobilisation of the organic motif using characterisation techniques including NMR, IR, and BET;

iii. Test each material in the cyclopropanation reaction of 2,4-dinitrobenzylchloride and an α,β-unsaturated aldehyde, rationalising the yields and selectivities with the characterisation to make structure-property correlations;

iv. Use the data to infer the distribution of active sites, the effect of pore size, and whether an optimum diameter is identifiable;

v. Decide which support has the most promise and investigate how it may be manipulated to best improve the catalytic results, such as viewing the ways in which hydrophobicity can be altered to monitor the effect the surface has on catalysis;

vi. And exploit the benefits of heterogeneous catalysis by collecting, characterising and recycling the catalyst through a number of cycles, using the characterisation to determine how the catalyst has been affected, and the scope for reusability.

5.3 Results and Discussion

5.3.1 Immobilisation on Silica Supports

The first step was to anchor the chosen catalyst onto a range of mesoporous silicas, including four disordered samples with pore sizes from 30-250 Å, and two ordered silicas MCM-41 and SBA-15. The immobilisation was initially confirmed by elemental analysis. By avoiding the use of nitrogen containing solvents, the nitrogen content of the sample could be reliably used to determine the loading of the catalyst, as displayed in Table 24. The supports were each exposed to the same quantity of thiol linker and catalyst precursor per gram during the synthesis. Therefore, the loading is dependent on the accessibility of the surface sites.

Table 24: Nitrogen content and loading of catalyst onto silica supports.

	Support	Nitrogen Content / %	Loading / mmolg^{-1}
23a	Silica 30 Å	0.59	0.42
23b	Silica 60 Å	0.64	0.45
23c	Silica 150 Å	0.75	0.53
23d	Silica 250 Å	0.87	0.62
23e	MCM-41	0.68	0.48
23f	SBA-15	0.94	0.67

Whilst these results quantify catalyst loading, further characterisation was conducted to help confirm the immobilisation. In processing the ^{13}C and ^{29}Si solid state NMR spectra, the peaks relating to the organic entity can be identified, as well as the different silica environments that have been newly incorporated. The carbon spectra are stacked together with that of the catalyst precursor in Figure 58. As expected, due to the bulk of the porous framework and low quantity of organics, visualising the peaks becomes difficult. However, clear similarities can be observed, with peaks around 127 ppm relating to the phenyl rings, 26 ppm for the alkyl chain, and 0 ppm arising from the methyl groups on the silica atom. Emerging peaks at 16 and 11 ppm can be attributed to terminal silyl fragments, expected at the base of the tether.

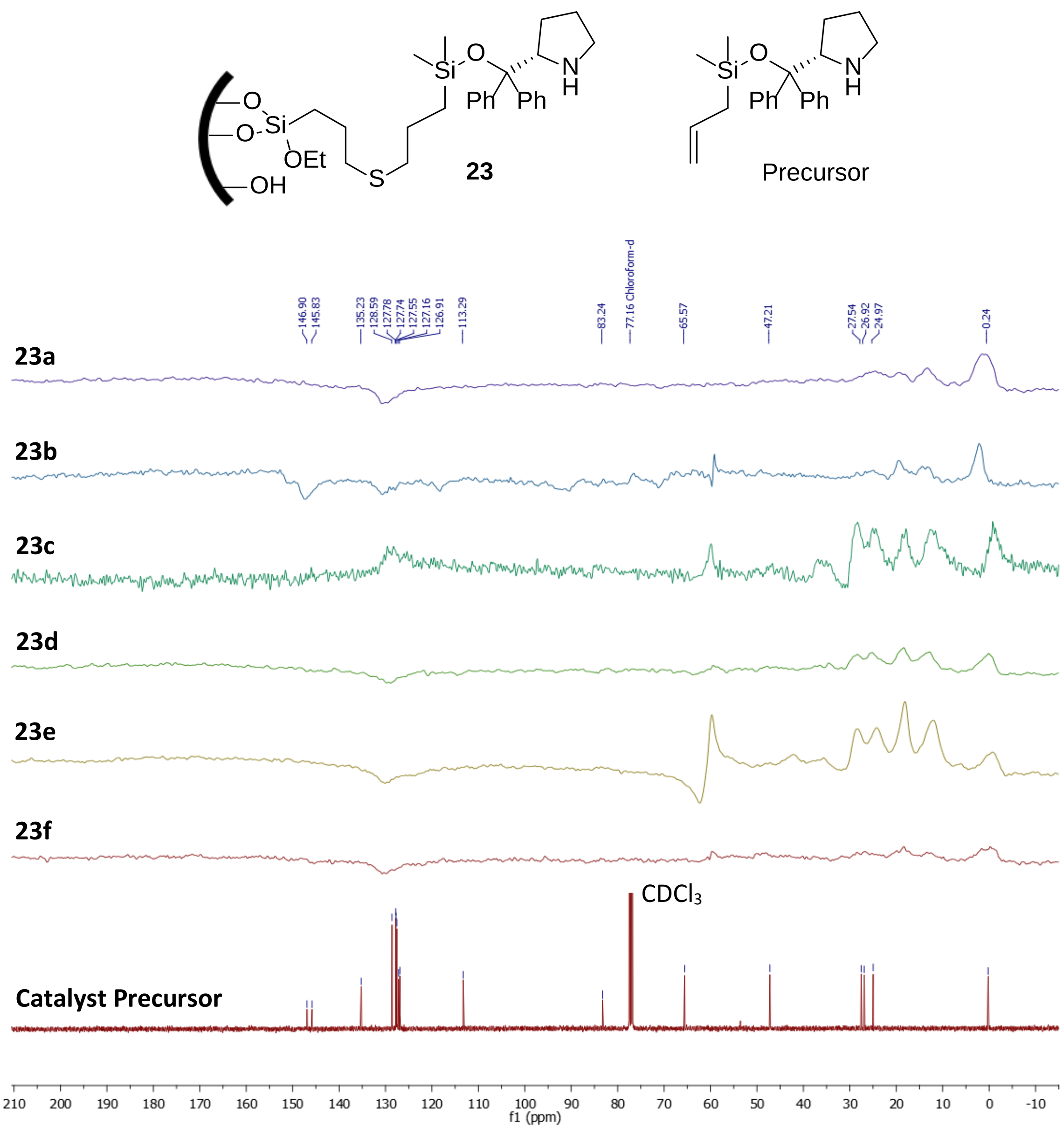

Figure 58: ^{13}C NMR for immobilised catalysts and the catalyst precursor, solution spectrum in CDCl$_3$.

When comparing the ^{13}C NMR spectra of the thiol-functionalised silica with the anchored material, represented in Figure 59 with MCM-41, it can be deduced that the peaks in the aromatic region and near 0 ppm have arisen as a result of the catalyst precursor. The matching of peaks surrounding 20 ppm can be assigned to the short carbon chain from the thiol functionalisation, but may also mask additional carbon environments in the full tether.

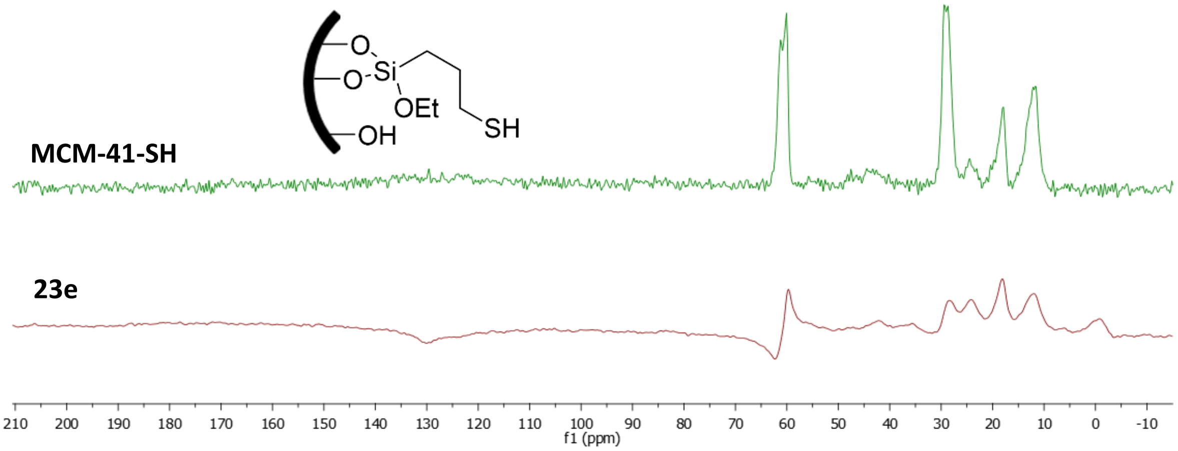

Figure 59: ^{13}C NMR of MCM-41 thiol-functionalised and with immobilised prolinol.

The ^{29}Si NMR spectra in Figure 60 reveals a large peak at -110 ppm for the bulk of the material. Three peaks, between -55 and -70 ppm, can be assigned to the silicon atom at the base of the tether. Each of these peaks correspond to the different coordination environments on the surface, whether there are one, two or no ethoxy groups. The peak of low intensity at 10 ppm relates to the silicon atom within the tether.

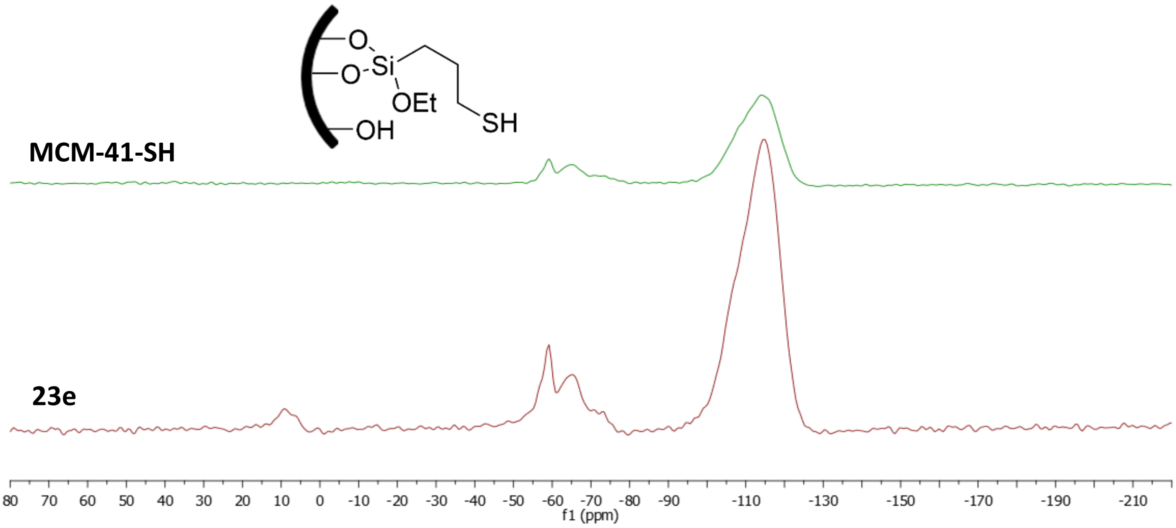

Figure 60: ^{29}Si NMR for MCM-41 thiol-functionalised and with immobilised prolinol.

IR spectra were collected for each sample. The whole spectrum is displayed for the alkene functionalised catalyst precursor, the thiol linker MPTES, and **23e** as a representative anchored material. Peaks that would be of interest for **23e** are dwarfed by the intense peaks arising from the bulk material. With the organics hidden within the pores, it is hard to visualise where the relevant peaks may be appearing.

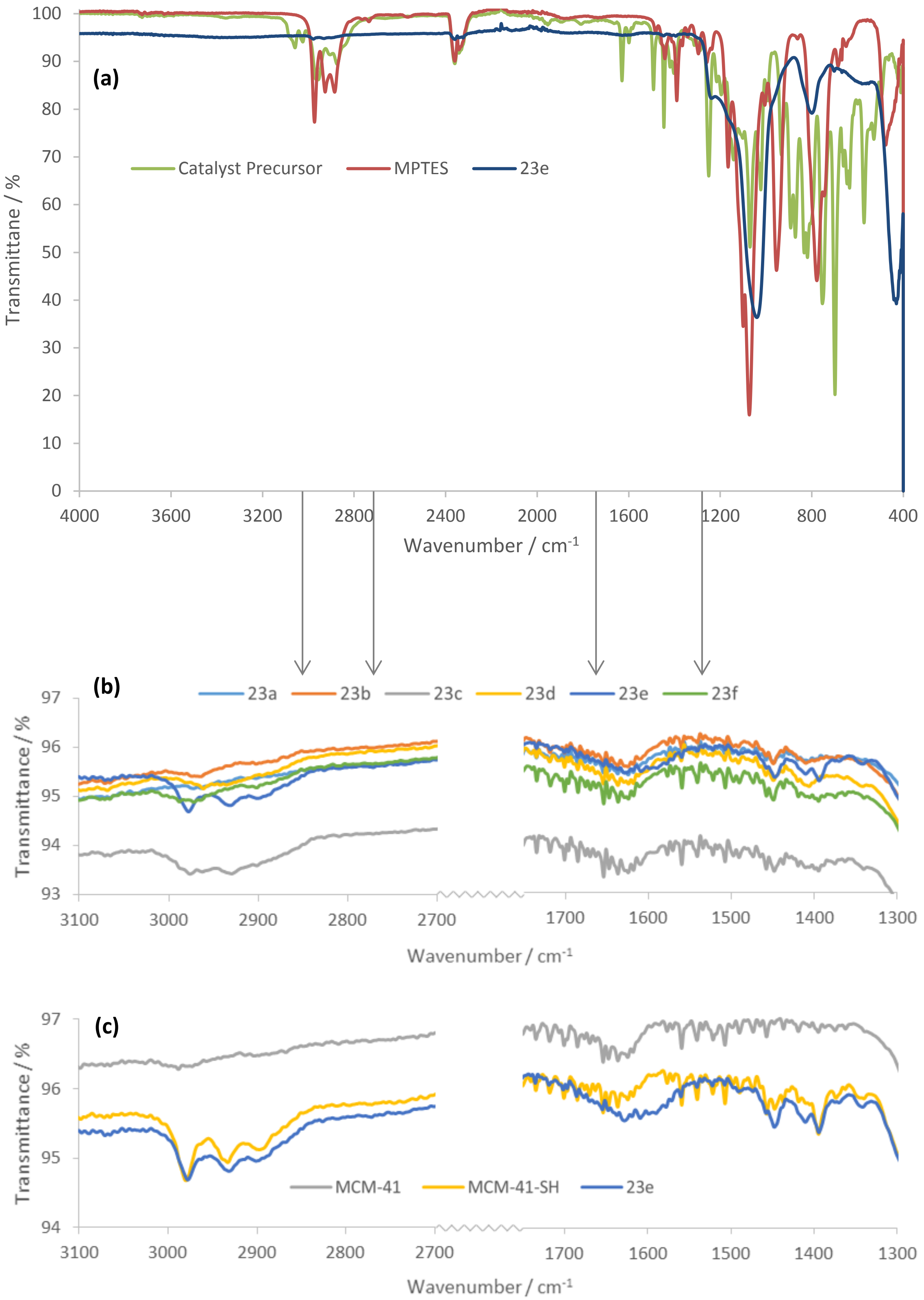

Figure 61: IR spectra for (a) organic moieties and **23e**, (b) magnified sections for immobilised catalysts **23a-f**, (c) magnified sections for MCM-41 variants.

By zooming in on two regions, 3100-2700 cm^{-1} and 1750-1300 cm^{-1}, the peaks assigned to C-H and C=C bonds become more clear. The disappearance of peaks between 3100-3010 cm^{-1}, corresponding to the alkene C-H stretch in the catalyst precursor, help to confirm that this functional group was used to anchor the compound. Between 3000-2800 cm^{-1} there are undulations observed in all anchored species, relating to the alkane C-H stretching. This is shown more closely with MCM-41, where these appear upon addition of MPTES but could also relate to the catalyst precursor. The aromatic C=C stretching that is seen with the catalyst precursor accounts for a new peak at 1450 cm^{-1} and is also likely to correspond to the widening of the peak at 1600 cm^{-1}. Finally the peak at 1400 cm^{-1} is thought to originate from alkane C-H bending.

The TGA traces in Figure 62 were used to observe thermal stability. As expected, breakdown begins to occur between 150-200 ^{o}C, which demonstrates higher thermal stability than the homogeneous catalyst with a TMS group. This suggests that the support lends some extra stability to the catalyst. However, considering enantioselectivity is heavily impacted by a rise in temperature, this does not necessarily suggest that reactions could or should be held at higher temperatures, but rather offers an indication of the beneficial effects of heterogenisation to the stability of the catalyst.

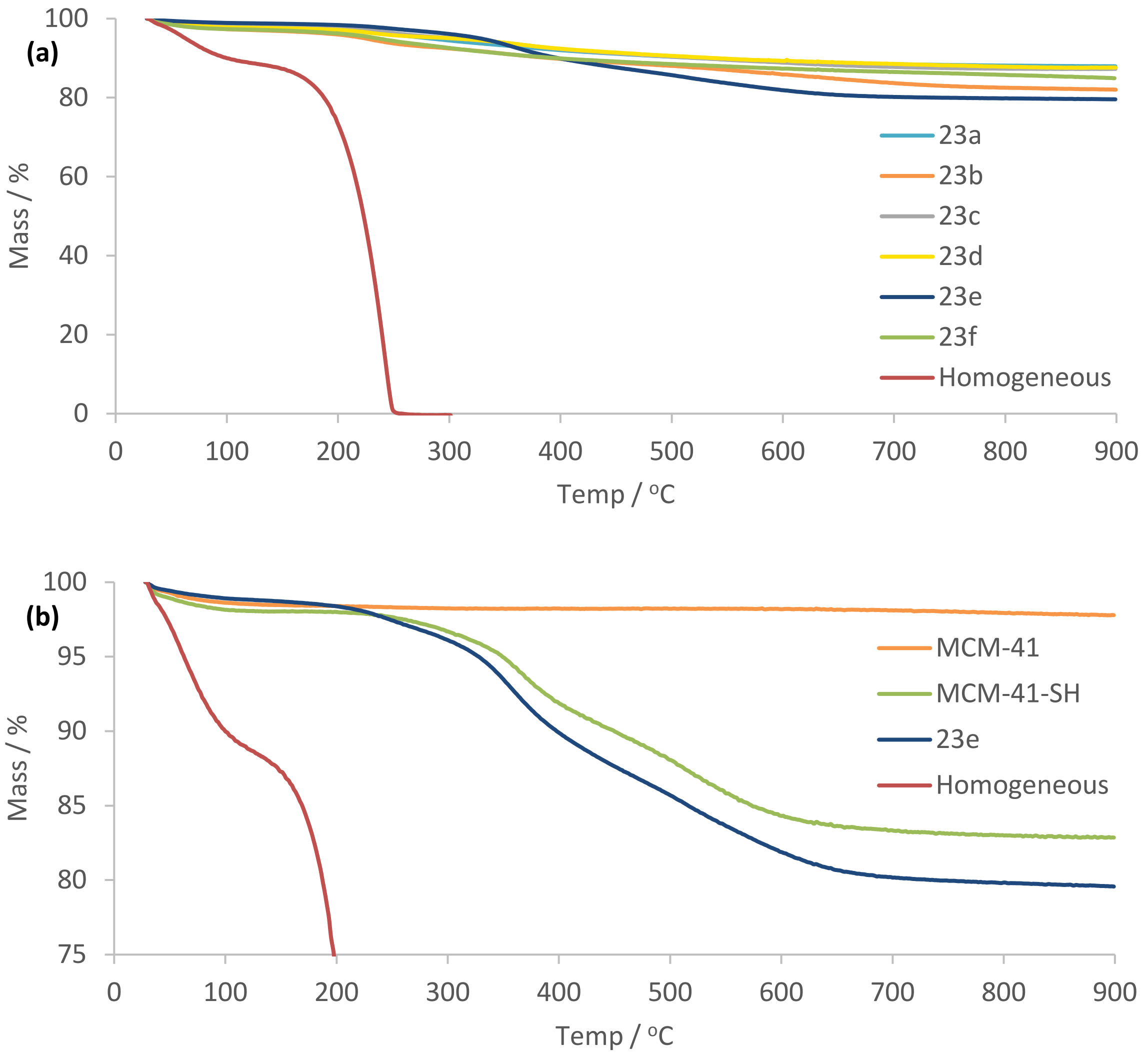

Figure 62: TGA curves of (a) immobilised catalysts and parent catalyst, (b) a closer look at the representative MCM-41 samples, and parent catalyst.

Nitrogen-adsorption studies were used to compare the empty frameworks with the anchored supports. BET offers a way of substantiating a covalent anchor by comparing the specific surface area before and after immobilisation. Covalent attachment should reduce the surface area observed as some of the surface sites previously available for adsorption of gas molecules are now occupied by the immobilised catalyst.

In Table 25, upon functionalisation of the surface silanols in each sample, there is a decrease in surface area, pore volume, and pore diameter. Data was also collected for the thiol-functionalised 60 Å and MCM-41 frameworks. In the case of MCM-41, it shows intermediary steps for each value, unlike the 60 Å samples which are comparable after addition of the catalyst. An interesting point to note is that whilst MCM-41 has the highest surface area, its porosity, especially its pore volume, appears drastically reduced once organics are anchored. This is as a result of its structural configuration, where the smaller dimensions of its pores leave it susceptible to being filled up with the organic structure. Therefore surface area is not indicated to be of paramount importance when anchoring, but rather the accessibility of the surface. Hence MCM-41 achieves one of the lowest loadings and lowest density of catalyst, despite the same quantity per gram being added to each support.

The density of grafted catalyst gives an indication of how isolated the active sites are. In theory, the higher the density, the more crowded the surface. However, using MCM-41 as an example, the reason the density is so low could be a result of its constricted pores. The organics could be grouped together around the pore apertures, and not within the bulk, highlighting the inherent flaw of such quantitative analysis. Whilst this data cannot confirm the presence and integrity of the catalyst, it could play a role in explaining why a framework may perform better catalytically, and identifying that “goldilocks” pore size.

The BET isotherm plots for all the mesoporous silicas tabulated can be found in Appendix B. Each plot reveals a hysteresis, as expected for mesoporous samples, corresponding to a type IV isotherm.

Table 25: Nitrogen-adsorption/desorption data for each framework.

Silica	Variant	Loading / mmolg^{-1}	BET Surface Area / m^{2}g^{-1}	Pore Volume / cm^{3}g^{-1}		D-H Pore Diameter / Å (Desorption)	Density / µmolm^{-2}
				Adsorption	Desorption		
30 Å	Empty	-	452	0.41	0.41	30	-
	23a	0.42	265	0.24	0.23	≤22[a]	0.93
60 Å	Empty	-	378	0.89	0.93	72	-
	Thiol	-	336	0.66	0.67	67	-
	23b	0.45	335	0.65	0.67	63	1.20
150 Å	Empty	-	280	1.07	1.11	150	-
	23c	0.53	241	0.86	0.88	140	1.90
250 Å	Empty	-	272	1.56	1.66	215	-
	23d	0.62	238	1.18	1.19	207	2.31
MCM-41	Empty	-	1493	1.16	1.13	27	-
	Thiol	-	971	0.67	0.41	≤22[a]	-
	23e	0.48	791	0.52	0.23	≤25[a]	0.32
SBA-15	Empty	-	729	0.91	0.87	67	-
	23f	0.67	423	0.68	0.65	63	0.92

[a] The model used is unreliable when determining microporous values.

The characterisation detailed here has been used to support the conclusion that the catalyst was successfully anchored as proposed in the introduction. Elemental analysis allowed for the loading of the catalyst to be calculated, and saw an increase parallel to pore size. Gas adsorption experiments could not categorically determine whether there were any active sites immobilised within the pores, but rather suggested that the supports with smaller pores may only have active sites around the pore aperture. Although both ^{13}C and ^{29}Si NMR displayed the expected peaks, intricacies were hard to identify due to the nature of the material. Similarly to the IR spectra which further supported the proposed immobilisation, despite the silica bulk decreasing the intensity of more relevant peaks. TGA demonstrated an increase in thermal stability, a benefit to heterogenising an organocatalyst. The characterisation displayed subtle differences in the likes of the NMR and IR, whereas the gas adsorption data is likely to provide more understanding of any differences in catalysis which may occur.

5.3.2 Testing Immobilised Catalysts in a Cyclopropanation

In order to select the conditions to test each immobilised catalyst in the cyclopropanation, initial trials were run with **23c**. Two α,β-unsaturated aldehydes were chosen which had previously given excellent enantioselectivity with the parent catalyst. The less sterically hindered crotonaldehyde (**22a**) enables a faster reaction, useful for a heterogeneous system that is expected to slow the rate of reaction. The extra bulk of the longer carbon chain in decenal (**22b**) promotes higher selectivity, but lowers the rate of reaction. Whilst these effects were not obvious with the parent catalyst in a homogeneous system, it does appear to play a role during this study. In order to achieve a high enough yield to compare each system, whilst minimising the background reaction, the reaction was left for 24 or 72 hours depending on the temperature. 20 mol% of catalyst was used to mimick the homogeneous examples our research group has successfully investigated,[40] and was calculated using the nitrogen content from elemental analysis.

The results in Table 26 reveal lower yields and enantioselectivity compared to the parent catalyst. Cooling the reaction to 0 °C was very effective at increasing enantioselectivity for the homogeneous catalyst. However, cooling the reaction with **23c** significantly increased reaction time to achieve lower yields, yet it could not exceed an e.e. greater than 90 %. There's a Catch-22 that in order to improve the yield by decreasing the influence of the background reaction, and thus increasing enantioselectivity, a higher temperature is desirable. But in doing so the higher temperature also decreases the selectivity of the reaction. This highlights the importance of rigorous optimisation when adjusting catalysis from a homogeneous to a heterogeneous system. Because **22b** resulted in higher enantioselectivity and a lower blank compared to **22a**, to test how the other frameworks compared, **22b** was used at room temperature for 24 hours in subsequent experiments.

Table 26: Investigation of conditions to use for further trials.

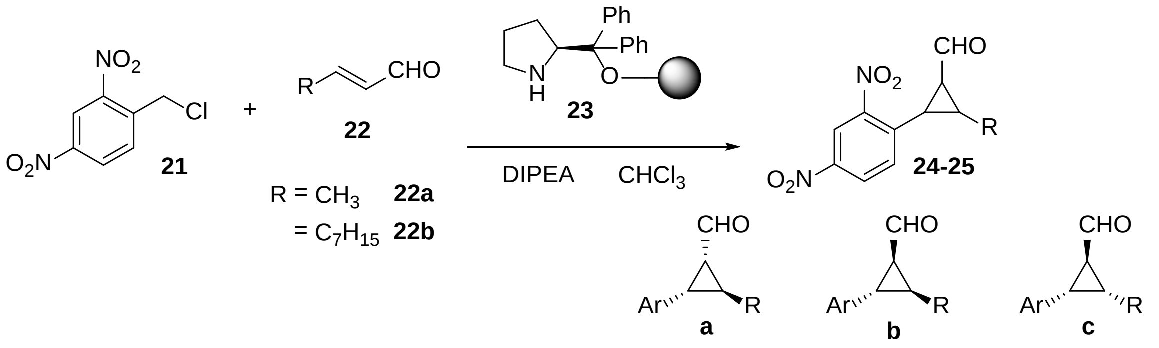

R	Catalyst	Temp.	Time / h	Yield / %	d.r. (a : b : c)	e.e. (a : b : c)
Me **22a**	Homogeneous[a]	0 °C	3-5	61	8 : 3 : 1	98 : 73 : 60
	Blank	r.t.	24	28	1 : 1 : 1	-
		0 °C	72	8	1.3 : 1.7 : 1	-
	Silica 150 Å	r.t.	24	43	1.1 : 1.4 : 1	-
		0 °C	72	26	1.2 : 1.6 : 1	-
	23c	r.t.	24	80	1.5 : 1.5 : 1	52 : 22 : 50
		0 °C	72	48	2.6 : 3.1 : 1	80 : 21 : 82
n-C$_7$H$_{15}$ **22b**	Homogeneous[a]	0 °C	3-5	99	7 : 1.5 : 1	99: 92 : 54
	Blank	r.t.	24	11	1.8 : 1.6 : 1	-
		0 °C	72	2	-	-
	Silica 150 Å	r.t.	24	22	2.2 : 2.1 : 1	-
		0 °C	72	8	1.3 : 1.3 : 1	-
	23c	r.t.	24	40	4.8 : 1.6 : 1	72 : 47 : 30
		0 °C	72	28	5.6 : 1.6 : 1	85 : 71 : 55

Reaction conditions: 2,4-dinitrobenzyl chloride (0.46 mmol), α,β-unsaturated aldehyde (0.92 mmol), DIPEA (0.51 mmol), catalyst (20 mol%), in CHCl$_3$ (1 mL). Yield and d.r. determined by ^{1}H NMR of reaction mixture using mesitylene as an internal standard. e.e. determined by HPLC analysis with a chiral column. [a] (S)-α,α-diphenylprolinol trimethylsilyl ether.[40]

Table 27 has some complex results. The enantioselectivity is unexpectedly high when considering the blank reaction (entry 1) and the unmodified supports of entries 3 and 4 appear to make up a significant portion of the organocatalysed yield with **23b**. However, the addition of SBA-15 hinders the production of product (entry 10). By assigning a quarter of product from the reaction with **23f** (entry 11) as occurring from a background reaction, and therefore racemic, the high enantioselectivity of 74 % can be justified, despite the yield being less than double that of the blank. Functionalising the framework with thiol groups did decrease the yield for Silica 60 Å (entries 3 and 4), suggesting that the lower concentration of pendant silanols may discourage the background reaction from occurring. Replacing the silanol sites that might induce a reaction with the desired chiral active sites, results in a higher than expected increase in enantioselectivity. Ultimately, the conditions employed do not yield satisfactory results with the catalyst as pathways for a racemic reaction hold too much prominence.

It can be argued that 150 Å serves as a “goldilocks” pore size, one that is wide enough to promote the homogeneous effectivity of the catalyst, whilst constricted enough to promote higher selectivity. However, whilst the intermediary pore size of **23c** did achieve the highest yield, with no gradual increase/decrease either side, the result appears as more of an anomaly. The silicas tested here are all commercially available, ideally more silicas with pore sizes between 60 and 250 Å would be trialled to better visualise any trends. There has been work on altering the surfactant used in the synthesis of SBA-15 to change the porosity observed. This would be an interesting direction of study in order to better understand these results, with potential pore sizes ranging from 50-300 Å.[41]

Another hurdle to cross is the much lower activity compared to the parent catalyst. The length of the tether was questioned because there is enough flexibility that the amine may be able to interact with the surface of the support. Considering the results in Table 27 show the support itself directly effects the reaction, the surface chemistry is called into question.

Table 27: Results for the cyclopropanation using the anchored catalyst on different supports.

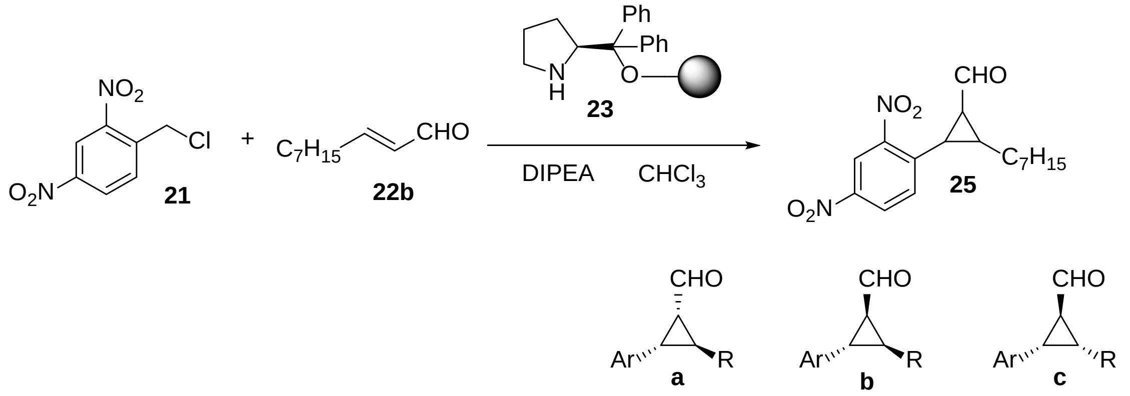

Entry	Catalyst	Yield / %	d.r. (a : b : c)	e.e. (a : b : c)
1	Blank	11	1.8 : 1.6 : 1	-
2	**23a** (30 Å)	19	2.8 : 1.4 : 1	70 : 40 : 42
3	Silica 60 Å	19	1.9 : 1.9 : 1	-
4	Silica 60 Å-SH	14	2.3 : 2.3 : 1	-
5	**23b** (60 Å)	20	2.3 : 1.3 : 1	65 : 34 : 32
6	Silica 150 Å	22	2.2 : 2.1 : 1	-
7	**23c** (150 Å)	40	4.8 : 1.6 : 1	72 : 47 : 30
8	**23d** (250 Å)	17	2.7 : 1.7 : 1	52 : 16 :12
9	**23e** (MCM-41)	12	3 : 2.1 : 1	47 : 15 : 15
10	SBA-15	4	3 : 2 : 1	-
11	**23f** (SBA-15)	19	2.6 : 1.4 : 1	74 : 44 : 48

Reaction conditions: 2,4-dinitrobenzyl chloride (0.46 mmol), α,β-unsaturated aldehyde (0.92 mmol), DIPEA (0.51 mmol), catalyst (20 mol%), in chloroform (1 mL) at r.t. for 24 h. Yield and d.r. determined by ^{1}H NMR of reaction mixture, using mesitylene as an internal standard. e.e. determined by HPLC analysis with a chiral column.

5.3.3 Capping the Pendant Silanol Groups

Capping agents such as methyltrimethoxysilane can be used to react with any remaining pendant silanol groups after the initial silylation. This would increase the hydrophobicity of the surface and thus affect the interactions between the immobilised catalyst and the surface, as well as the reaction substrates themselves. This process was applied to the 150 Å silica support to give **23g**, with the aim to decrease the rate at which the background reaction occurs, and consequently increase enantioselectivity. In Table 28, the data for the different variants of Silica 150 Å have been compared. Although the surface area and pore volume remains similar between **23c** and **23g**, there is a drop in the density of grafted catalyst and in pore diameter, as a result of the methyl groups now attached across the surface. The indication of increased bulk suggests the catalyst and methyl groups have been successfully immobilised on the surface of **23g**.

Table 28: Loading and nitrogen adsorption/desorption data for Silica 150 Å with and without immobilised catalyst.

Variant	Loading of catalyst / mmolg^{-1}	BET Surface Area / m^{2}g^{-1}	Pore Volume / cm^{3}g^{-1}		D-H Pore Diameter / Å (Desorption)	Density of grafted catalyst / µmolm^{-2}
			Adsorption	Desorption		
Empty	0	280	1.07	1.11	150	-
23c	0.53	241	0.86	0.88	140	1.90
Capped	0	241	0.95	0.96	121	-
23g	0.45	248	0.91	0.89	125	1.61

The capped silicas were trialled in the cyclopropanation. In Table 29 they have been compared to the previous iterations to observe a clear drop in yield and selectivity. The yield with Capped 150 Å (entry 4) drops 5 % as it does with **23g** (entry 5), suggesting that the background reaction is occurring at a lower rate, but the expected increase in selectivity does not follow.

Table 29: Results for the cyclopropanation comparing the capped catalyst with the previous iteration.

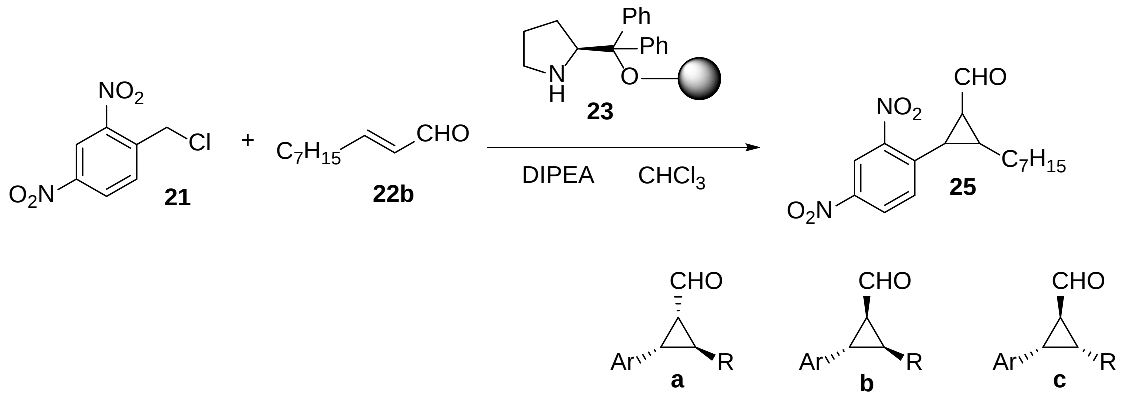

Entry	Catalyst	Yield / %	d.r. (a : b : c)	e.e. (a : b : c)
1	Blank	11	1.8 : 1.6 : 1	-
2	Silica 150 Å	22	2.2 : 2.1 : 1	-
3	**23c**	40	4.8 : 1.6 : 1	72 : 47 : 30
4	Capped 150 Å	17	2.3 : 2.1 : 1	-
5	**23g**	35	4.3 : 1.9 : 1	56 : 32 : 33

Reaction conditions: 2,4-dinitrobenzyl chloride (0.46 mmol), α,β-unsaturated aldehyde (0.92 mmol), DIPEA (0.51 mmol), catalyst (20 mol%), in chloroform (1 mL) at r.t. for 24 h. Yield and d.r. determined by ^{1}H NMR of reaction mixture, using mesitylene as an internal standard. e.e. determined by HPLC analysis with a chiral column.

One hypothesis is that the hydrogen-bonds between the surface silanols and nitro-groups help to hold the substrates within the vicinity of the catalyst, as displayed in Scheme 34. These intermolecular forces draw the substrates closer and position them to achieve the desired enantiomer. This synergistic effect would be unique to the grafted catalyst and desirable if it was not also masked by a lower rate of reaction.

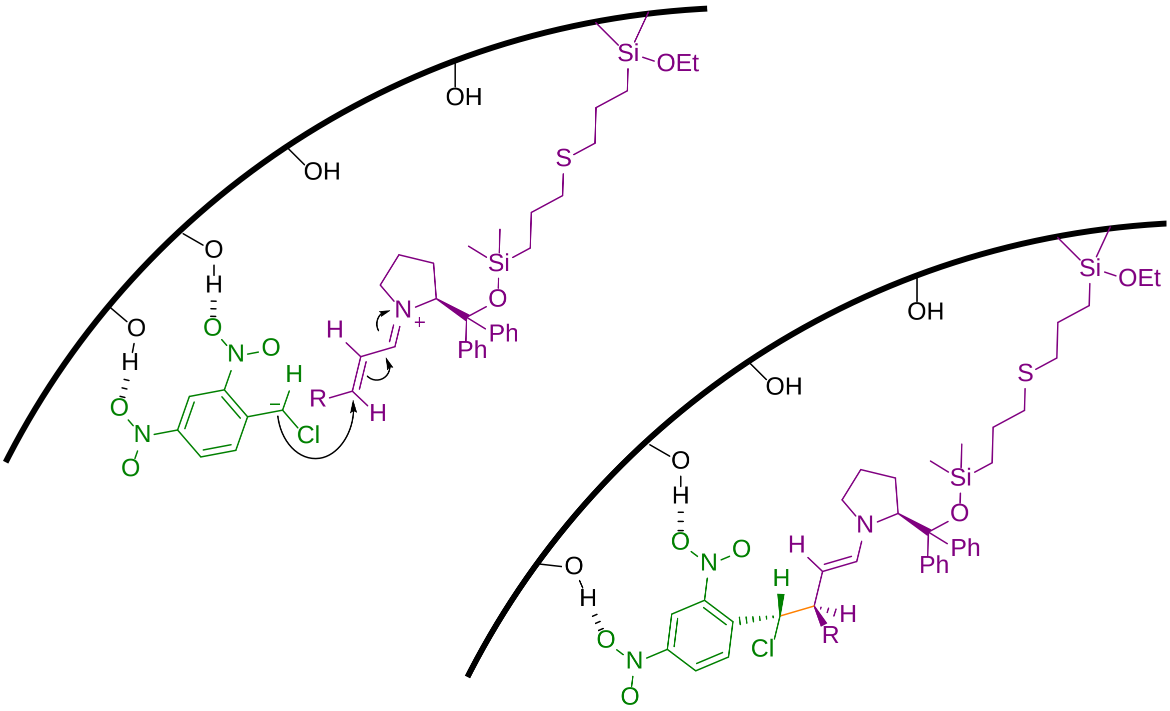

Scheme 34: Proposed directing effects of surface silanols in the cyclopropanation reaction.

These results demonstrate that it would be undesirable to cap the surface silanols, although methods to reduce the background reaction are still paramount. The next step may be to look into the ratio of catalyst sites to surface silanols, and determine whether the composition of the surface could be changed to reduce the effect surface silanols have on aiding the reaction singularly, whilst promoting the synergy between them and the amine as proposed in Scheme 34.

As it stands, whilst an array of characterisation has been collected for the immobilised catalysts, there remains no clear reasoning as to why the catalyst immobilised onto 150 Å silica (**23g**) offers a higher yield compared to the other materials tested.

5.3.4 Recyclability

After the reaction with **23c**, the catalyst was washed thoroughly and characterised with the same techniques to determine what changes may have occurred. The sample was subsequently taken through a further four cycles to observe changes in activity, and analysed once more. The performance of **23c** over the course of five cycles is displayed in Figure 63. There is a significant loss of activity after the first reaction, such that it becomes comparable to the other immobilised materials in Table 27. The yield and diastereoselectivity worsen over the following cycles, but the values do remain higher than the blank (11 %, 1.8:1.6:1).

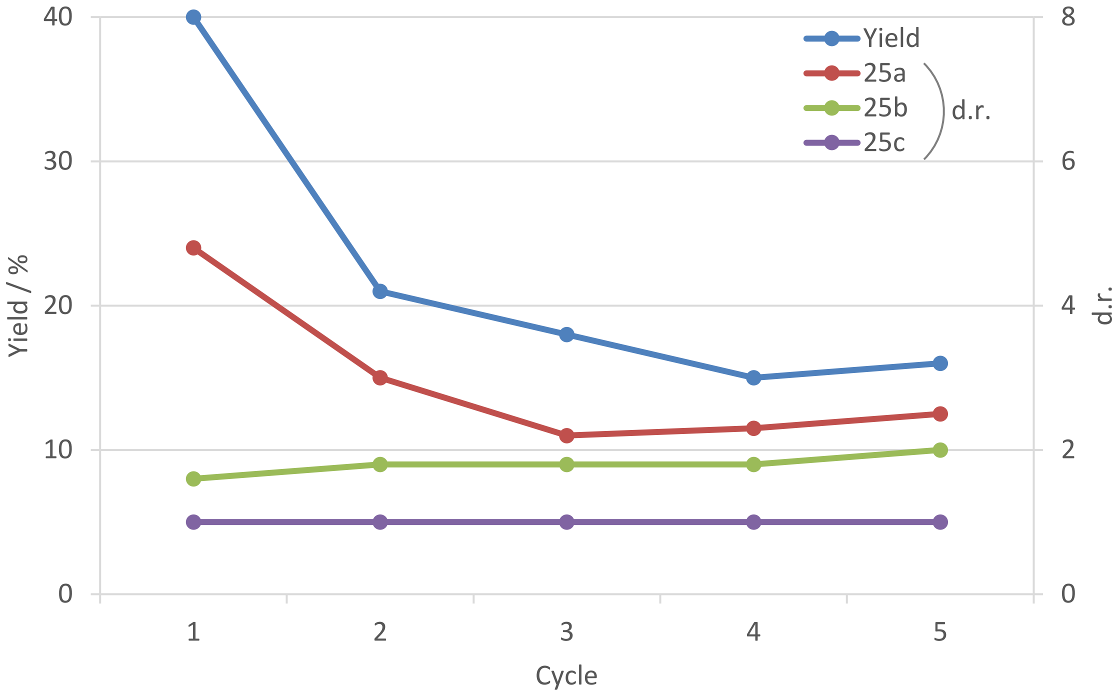

Figure 63: Performance of **23c** over the course of five cycles.

Overall this is a disappointing finding as the foremost reason for anchoring organocatalysts is to be able to collect and reuse them through multiple cycles. Whereas, the results here clearly demonstrate **23c** is unable to achieve the high yield, and selectivity of the homogeneous analogue,[40] and upon further cycles its performance worsens still.

Characterisation of the used catalyst was collected to understand the considerable loss of activity. In Table 30, the BET analysis and loading of the used samples is shown alongside **23c** and the plain silica. The gas adsorption studies showing a slight decrease in certain values, together with a rise in nitrogen content from the 5th cycle, indicates some reaction components may still be present.

Table 30: Nitrogen adsorption data and loading of 23c before and after use.

Framework	BET Surface Area / m^2g^{-1}	Pore Volume / cm^3g^{-1}		D-H Pore Diameter / Å (Desorption)	Loading / $mmolg^{-1}$
		Adsorption	Desorption		
Empty	280	1.07	1.11	150	-
23c	241	0.86	0.88	140	0.53
23c 1st Cycle	233	0.80	0.82	138	0.53
23c 5th Cycle	236	0.80	0.81	130	0.55

As displayed in Figure 64, ^{13}C NMR showed some subtle differences between the two samples. A new peak appears at 32 ppm, further implying organic material was retained within the support.

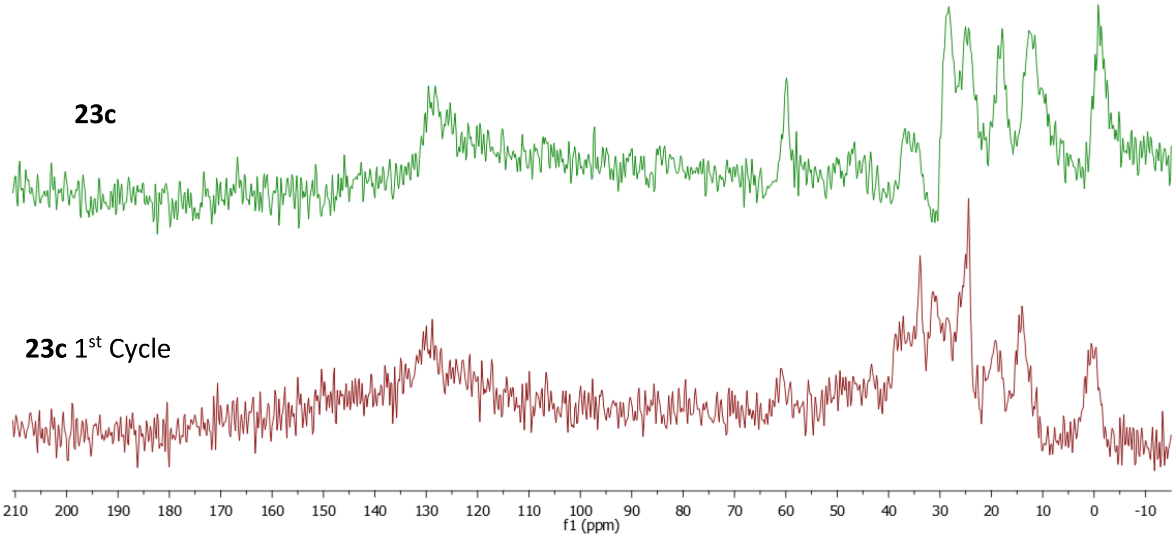

Figure 64: ^{13}C NMR for **23c** before and after use.

The ^{29}Si NMR in Figure 65 does not show any significant differences. The peaks remain at 10 and -65 ppm for the silica atoms attached within and at the end of the tether.

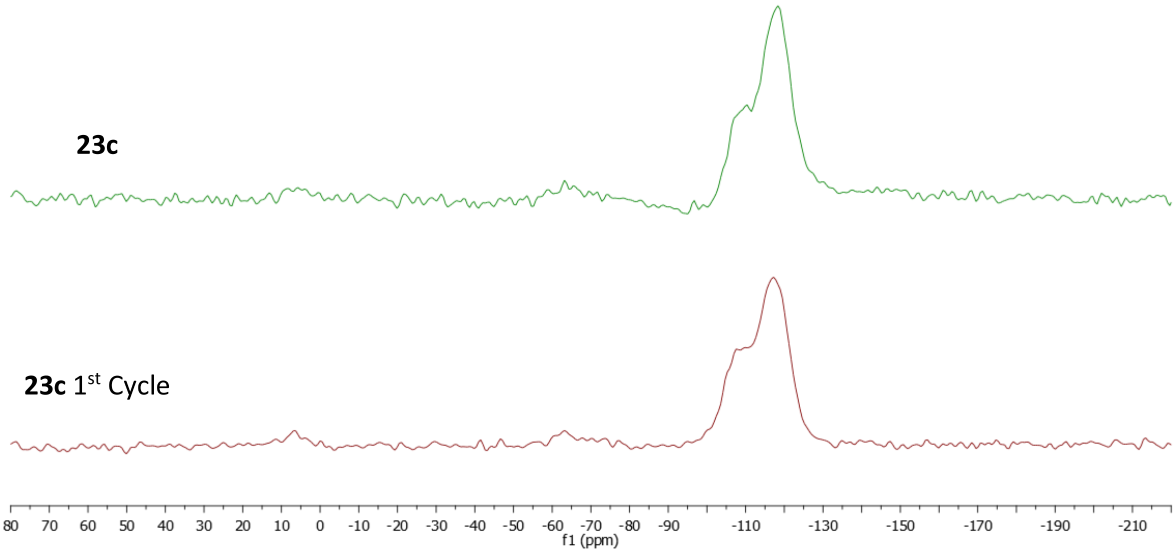

Figure 65: ^{29}Si NMR for **23c** before and after use.

Whilst beneficial to collect, the characterisation of **23c** after use in the cyclopropanation does not clarify much, rather it suggests some substrates from the reaction are still within the pores.

5.3.5 Recognising the Flaws in the Method

The catalyst has been successfully immobilised on a support, and has demonstrated the ability to catalyse a Michael addition to form asymmetric cyclopropanes. However, the results have been disappointing, with the highest yield achieved using decenal at just 40 %, far lower than the 99 % achieved with the parent catalyst. Diastereoselectivity was also poor in comparison, while the enantioselectivity never breached 90 %. Recyclability should have been the redeeming factor, yet a steep decline from the already low activity was observed after just one cycle. This was wholly inadequate because the ability to reuse a heterogeneous catalyst through multiple cycles is the chief reason for spending the time and resources to immobilise an otherwise highly efficient catalyst. Therefore, if work is to continue on this project it should focus on how the support, tether and immobilisation process can be optimised to warrant immobilisation.

One of the obvious routes of investigation is to vary the density of active sites on the support. This is particularly relevant considering the synergistic effect proposed with the acidic silanol sites and the basic amine sites, the ratio of which should be varied to determine the optimal conditions for catalysis. Furthermore, site isolation can be considered, whilst difficult to interpret for small mesopores such as those in MCM-41 (30 Å), the larger pores of **23c** (150 Å) would be more susceptible to achieve greater distances between active sites.

It has been proposed that a lower loading of the organic matter prevents amine aggregation on the support surface. A study on the condensation of aldehydes found higher densities led to a significant drop in yield of nearly 40 %.[42] It was noted that spacing between acid-base groups must be controlled in order to maximise their cooperative action and minimise neutralisation. Very low ligand loading has to be applied to achieve site isolation, so the highest activity tends to be observed with the most voluminous catalyst.[2] This brings into question the validity of deciding that 150 Å silica was the best support from those trialled during this work. In Table 31, the pore size is compared to the loading and density achieved for **23a-d**. A clear trend is observed – more catalyst can be grafted onto supports with larger pores – highlighting a fundamental flaw with the procedure for immobilisation. In the synthesis for each catalyst, the quantity of the thiol-functionalised chain and the catalyst precursor remain the same. However, it is clear that the larger pores enable more organic material to be anchored because more constricted pore sizes would result in the organic being first immobilised around the pore aperture, and then lead to restricted access into the bulk of the material. This indicates that the density values are not truly representative of site isolation either, because the active sites will be grouped close to one another around the pore aperture. With this in mind, it is evident the immobilisation procedure has been designed to maximise the number of active sites on the silica surface, contrary to the advice from previous studies which suggests this will be detrimental to the yield achieved.[2,42]

Table 31: Loading and density of immobilised catalysts.

Catalyst	Pore Size / Å	Loading / mmolg^{-1}	Density / µmolm^{-2}
23a	30	0.42	0.93
23b	60	0.45	1.20
23c	150	0.53	1.90
23d	250	0.62	2.31

The reason for the 150 Å silica generating the best results is likely because the pore apertures were not as constrained and crowded as for **23a-b**, but it managed to avoid the aggregation of active sites which prevented **23d** from excelling. By understanding these factors, a new set of experiments can be proposed which achieves a range of loadings and densities for each support, using a much lower quantity of the ligands. To be able to truly compare the catalytic activity of each support, the loading of catalyst would ideally be the same for all materials. The assumption will be that lower loadings result in higher yields, which would also help suppress the effect of the background reaction, and improve selectivity. The inevitable increase in the quantity of silica used to account for a lower loading may begin to affect stirring and mass distribution in the vessel, in which case a more dilute reaction may be desired.

Sankaranarayanapillai et al. found their sample of immobilised amine with the lowest density of active sites achieved the highest yields.[42] They tested different densities of catalyst, including 0.33, 0.66 and 1 µmolm^{-2}, far lower than the 1.90 µmolm^{-2} of **23d**. These densities represent a good starting point to aim for during any future investigation, and should be easy to achieve by adding in the appropriate quantity of (3-mercaptopropyl)triethoxysilane during synthesis. Assuming every molecule is successfully anchored to the surface, to achieve a density of around 0.33 µmolm^{-2} on 150 Å silica, only 92 µmolg^{-1} of silane would be required. This is markedly lower than the 1660 µmolg^{-1} used during this work, and serves to demonstrate the flaw with the synthesis conducted so far. Once a range of desired loadings have been generated, elemental analysis, nitrogen-adsorption experiments and density calculations can be used to quantify site isolation, before comparing with any catalytic activity. Quantitative data such as this is essential to drawing structure-property correlations, as well as reaching a reliable conclusion on how varying the loading effects catalysis, and how effective immobilisation is for organocatalysis.

5.4 Conclusion

A pyrrolidine silyl ether was successfully anchored onto a variety of mesoporous silicas, with immobilisation confirmed using a range of characterisation. Elemental analysis allowed for the loading of the catalyst to be calculated, and saw an increase parallel to pore size. Although both ^{13}C and ^{29}Si NMR displayed the expected peaks, intricacies were hard to identify due to the nature of the material. Similarly, IR spectra further supported the proposed immobilisation, despite the silica bulk decreasing the intensity of more relevant peaks. Gas adsorption experiments could not categorically determine whether there were any active sites immobilised within the pores, but rather suggested that the supports with smaller pores may only have active sites around the pore aperture. Each material was then trialled in a cyclopropanation reaction with a benzyl halide and an α,β-unsaturated aldehyde. The catalytic tests with decenal revealed that amorphous silica with 150 Å pores was the most effective, achieving the highest yields (40 %) along with high enantioselectivity (72 %). Decreasing the temperature can lead to higher enantioselectivity, although it affords significantly lower yields. Whilst 150 Å silica was identified as the most promising support, the nature of the synthetic procedure means that questions still remain. The other supports should not be discounted without further work taking into account their pore dimensions and site isolation effects. The selected catalyst was also tested through five cycles and displayed a sharp drop in activity after the first reaction, followed by a steady decline to just 16 % yield in the fifth cycle. The used catalyst was characterised to determine how it had been affected but with little clarification to explain the drop in activity. Further testing surrounding recyclability is essential as this would be the major benefit to immobilising an otherwise highly successful catalyst.

The results described in this work, although not excellent from a synthetic point of view, have identified key factors to consider when designing an immobilised catalyst. Anchored catalysts are often less active than their homogeneous counterpart because of its limited mobility. However, what is lost in efficiency can be gained in other practical aspects such as recyclability. Once these problems have been addressed, immobilisation can be viewed as an opportunity to achieve a more sustainable process, rather than an expensive and time-consuming drawback.

5.5 Future Work

5.5.1 Optimisation

An investigation into the density of active sites on the support surface has been identified as the most substantial route to optimising the immobilisation process, but it is by no means the only one.

5.5.1.1 Quantity of Catalyst

In addition to the loading of catalyst on the support, the quantity of catalyst added to the reaction should also be considered. According to the literature, adding more catalyst to the reaction does not tend to affect the enantioselectivity, although this may also be in examples where there is not a significant background reaction occurring.[43,44] The lower rate from heterogenised catalysts suggests that more catalyst should be used, especially if this is not seen to decrease the enantioselectivity.[45] Therefore when utilising an immobilised catalyst, more active sites may be required, offset by the fact that as a heterogeneous catalyst, it should at least be reusable over multiple cycles. However, considering that the cyclopropanation tested during this work used 20 mol% of the homogeneous parent catalyst, any more than that may be considered far too much. Instead, where the immobilised catalysts might really excel could transpire to be in reactions that have been reported with lower quantities of the homogeneous counterpart, to allow for an increase with the supported samples. A leading factor that has driven the immobilisation of these organocatalysts is the high quantity required for them across a multitude of reactions, at least if they are anchored onto a support they could be recycled.

5.5.1.2 Length of Tether

When a parent catalyst is already well established, such as the J-H series, there is a strong desire to replicate its free nature when anchoring it to a support. This is why the use of a long tether was justified, because the increased conformational entropy will decrease the amount of time the active site is held near the surface, resulting in more homogeneous behaviour. However, as discussed in 5.3.3 Capping the Pendant Silanol Groups, a decrease in activity was observed when the surface was modified, suggesting that there were favourable interactions between the catalyst, substrate, and support. This effect was discussed by Wang et al. when they proposed the bifunctional nature of their grafted amine sites with the acidic silanols.[17] There is no clear evidence for exactly how the support interacts with the catalyst/substrates. By altering the length of the tether, a stronger argument can be made when defining this relationship. Indeed the desire for more homogeneous behaviour is brought into question if the bifunctional nature of a supported catalyst can be exploited. The length of the tether is not often a focal point of investigation, but rather the strength of each bond. Reports which have delved into this topic do not reach a clear conclusion, some preferred longer tethers for their higher yields and/or selectivity,[6,46] while others suffered from lower enantioselectivity which negated any increase in yield.[47] Of particular interest is striking a balance between pore size and tether length, as a long tether within a constrained environment is likely to struggle more to achieve efficient mass transfer from the active site.[48] This may not be so relevant for the likes of 150 Å silica, but a shorter tether may improve the results from the smaller pore structures, including the ordered ones such as SBA-15. Ideally, a range of chain lengths would be tested within different pore sizes to identify the optimal design.

A potential pathway to achieve a shorter tether is proposed in Scheme 35, where the amine site is first protected, before utilising the hydroxyl group as a nucleophile. Attempts were made to immobilise the catalyst in this fashion using a Boc protecting group. However, the nucleophilic substitution proved difficult, with the hydroxyl attacking the carbonyl functionality in the protecting group, leading to an intramolecular cyclisation. *p*-Methyoxyphenyl (PMP) or *p*-methoxybenzyl (PMB) do not have a carbonyl group, and as such they would be a more appropriate choice for protection. As with any immobilisation process, care should be taken to ensure the reaction conditions do not harm the integrity of the chiral catalyst.

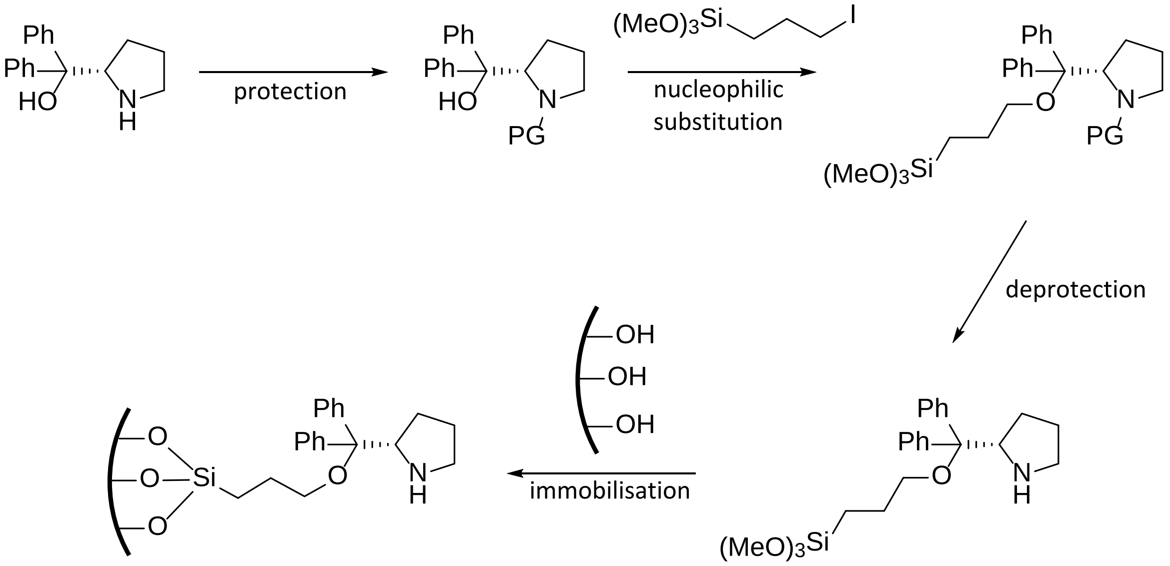

Scheme 35: Possible pathway for the immobilisation of a J-H catalyst on a silica support.

5.5.1.3 Different Supports

Graphene and derivatives have attracted increasing attention as catalysts,[49] in part due to their unique chemical and physical properties.[50–52] The inertness, large surface area, stability, and wide availability of chemically derived graphenes, such as graphene oxide (GO) and reduced graphene oxide (rGO), make them ideal candidates as supports for immobilisation. Their planar nature aids mass transfer, whereas conventional supports often struggle with diffusion effects/mass transfer as a result of their porous nature. Ideally graphene is a single layer material, but two or more layers are also being investigated. 3D frameworks/networks of graphene[53] may be a better choice for their higher surface areas, and high strength endurance for catalyst loading, while also facilitating mass transfer.[54,55] However, high-quality graphene has been shown to be unnecessary for application in heterogeneous catalysis, increasing the economic and technical appeal for these materials.[49] GO can be characterised as a single graphitic monolayer with randomly distributed aromatic regions and oxygenated aliphatic regions containing hydroxyl, epoxy, carbonyl and carboxyl groups. The hydroxyl and epoxy groups lie above and below each layer, whereas carboxylic groups usually exist along the edges. The presence of these functional groups enables easy surface modification, while maintaining the desirable attributes of the support. Reducing the material to form rGO removes most of these defects, strengthening the π-network.

Georgakilas et al. wrote a detailed review on the functionalisation of graphene, including the approaches and applications.[56] When considering the J-H organocatalyst, there appear to be two viable options for immobilisation. The first approach is to utilise the functional groups on GO to form a covalent anchor. Many reports functionalise the surface with amine groups, typically to immobilise metals,[57–59] which is undesirable because elemental analysis of nitrogen is a useful technique to calculate catalyst loading. However, there are multiple routes which can utilise the carboxylic groups along the edge of graphene sheets, leaving the bulk of the material unblemished.[60] The hydroxyl and epoxy groups appear to offer the best opportunity to afford an immobilised organocatalyst. Zhang et al. demonstrated the facile nature of silylanisation by anchoring a catalyst precursor with a silyl linkage, at room temperature.[61] An example of the chain which could be used has already been discussed, following a similar protocol to **23c** where the surface is functionalised with thiol groups before attaching the precursor.

Thus far the supports considered during this work have all relied on a covalent anchor, the second approach looks at this differently. By adding a pyrene tag to the desired catalyst, strong π-π interactions with rGO should immobilise it on the surface. Heavy transition metals have been immobilised in this fashion, although it appears recyclability is not always a guarantee, with one example being significantly less efficient from the fourth cycle onwards.[62] On the other hand, high production of hydrogen gas with iridium was maintained across 10 cycles.[63] Whilst another publication investigating palladium or ruthenium on rGOs conducted hot filtration experiments, revealing the catalysis was heterogeneous in nature and had no detectable leaching or boomerang effect.[64]

Scheme 36 illustrates a potential pathway to form a catalyst precursor which could be immobilised onto a graphene surface. If this direction of study is to be seriously considered, then it is likely that an easier, more efficient process to form a suitable catalyst precursor could be found. The one proposed here is simply to indicate the possibilities of this route, and as a comparative tool by utilising a similar mechanism used for **23c**, forming a tether of a reasonable length. The catalyst precursor can then be stirred in solution with a sample of rGO to immobilise the organocatalyst.

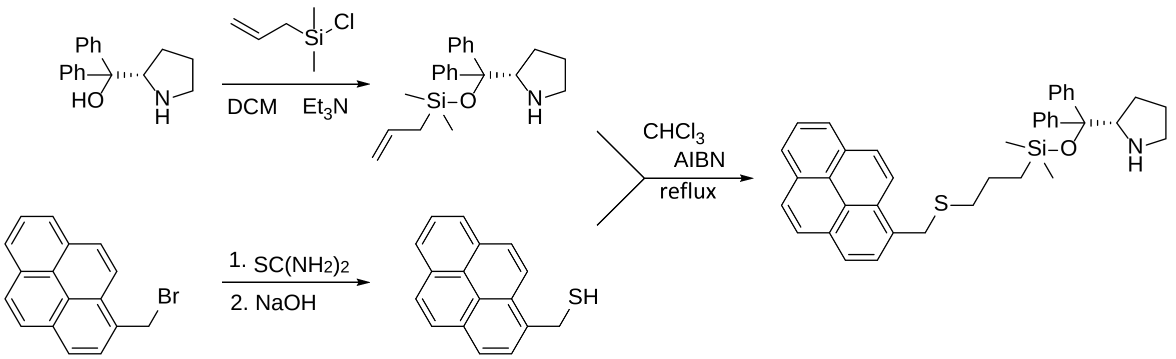

Scheme 36: Potential pathway to form a catalyst precursor for graphene immobilisation.

5.5.1.4 Anchoring at the 4-Position

A major advantage to using proline as a catalyst, or as a precursor to one, is its low cost. On the one hand, this brings into question the necessity of spending more time and resources immobilising it onto a support, especially if the results cannot compare with the parent catalyst. Conversely, it has been suggested supporting such a low-cost catalyst can serve as a model case study for more complex and expensive catalysts.[24] One such example is the same proline catalyst anchored at the 4-position. Although forming 4-hydroxyproline requires extra steps, and thus increases the cost, there are reports which have successfully anchored at this position and achieved promising results.[23,26] One argument for using this position is to create more space around the active site, helping to replicate the parent catalyst's homogeneous behaviour. Hayashi et al. found that more bulky silyl ethers, even just a triethyl group rather than the usual trimethyl, lead to a slower rate of reaction.[19] However, the organic moiety will naturally favour positions which decrease steric clash, therefore the chain would be held out of the way from the active site most of the time. This effect could be one of the many factors which affect the rate and activity of the immobilised catalyst, as such it should be an aspect to investigate when looking to optimise the process.

5.5.1.5 Flow

As part of the drive towards more sustainable chemistry, waste minimisation and catalyst recovery are crucial to any process design. Hence the appeal of heterogeneous catalysts, and their application in a continuous flow system. Applying organocatalysis in flow chemistry has been limited so far by the often short lifespans of the organocatalyst itself. Designing a more stable immobilised organocatalyst would validate this approach, and has become increasingly common as immobilisation of chiral moieties continues to improve.[65–68] One particular example anchored a J-H type catalyst onto polystyrene *via* a 4-hydroxyl group, proving robust over 48 hours in the enantioselective cyclopropanation of α,β-unsaturated aldehydes.[26] High yields and selectivity were achieved despite limitations with the process in batch, as they sought to minimise contact time between the catalyst and the base-sensitive product.

When reviewing a process under flow, it's important to consider the principles of Green Chemistry. For example, ensuring an efficient system that reduces the amount of waste produced and maximises atom economy; or evaluating the choice of solvents used for the flow as well as in the preparation of the catalysts. Whilst the next step for this project would be to optimise the immobilisation process, and determine whether high yield and selectivity can be achieved in the cyclopropanation of 2,4-dinitrobenzylchloride with α,β-unsaturated aldehydes, this work should be done with the aim to apply it to a flow system, and have sustainability in mind.

5.5.2 Reactions

Following further optimisation, some interesting reactions have been identified to test. These involve Michael additions, and the potential to exploit the acid-base nature of the material.

5.5.2.1 Michael-Michael-Aldol

The synthesis of a spiro compound *via* a Michael-Michael-aldol reaction has been afforded in good yields, catalysed with diphenyl prolinol derivatives.[69] The reaction in Scheme 37 could be a good opportunity to showcase the anchored materials due to the excellent diastereoselectivity that is usually observed. Furthermore, the inherent acidity of the support surface may mitigate the need for benzoic acid, or reduce the quantity required.

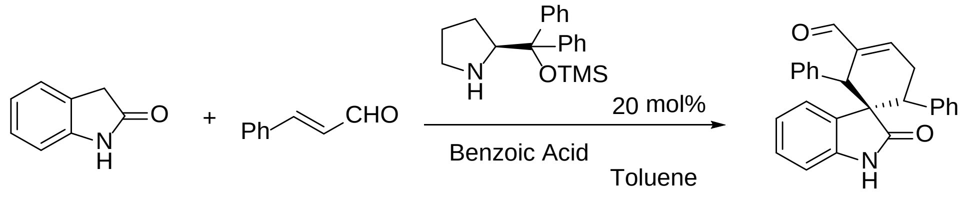

Yield 71 %
d.r. >25:1
e.e. >99 %

Scheme 37: Michael-Michael-aldol reaction with a J-H catalyst.

5.5.2.2 Conjugate Addition

In 2006, the J-H series of catalysts were reported in the conjugate addition of malonates to aromatic α,β-unsaturated aldehydes, as a precursor to chiral lactones and lactams.[70] The reaction illustrated in Scheme 38 is a promising option to test the immobilised catalyst, in an attempt to imitate the good yields and excellent enantioselectivities.

R	Yield / %	e.e. / %
Bn	80	91
Me	85	94

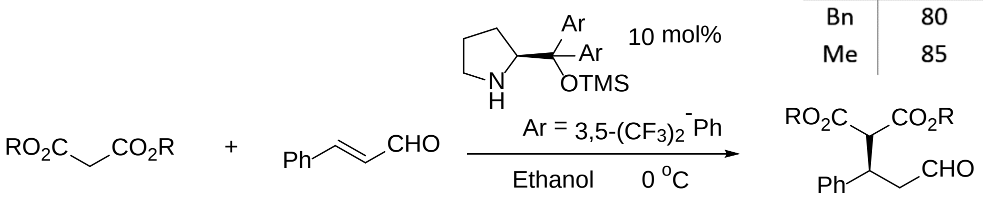

Scheme 38: Conjugate addition of malonates to unsaturated aldehydes with a J-H catalyst.

It was remarked upon in 5.5.1.1 Quantity of Catalyst that increasing the amount added to a reaction is unlikely to have an effect on enantioselectivity, but may increase the rate of reaction, which is particularly useful for heterogenised catalysts. This reaction represents one example where increasing the quantity of catalyst may be forgiven if the material can be recovered and reused successfully.

5.5.2.3 Acid-Base Catalysis

The acidic nature of the surface selected may cause difficulties in reactions where this is not required. However, it may also present a significant strength in acid-base catalysis. Avoiding the mutual deactivation of homogeneous acidic/basic sites has been a challenge. The heterogenisation of catalytic sites in materials, such as those synthesised in this work, provide an opportunity to tackle that problem. Already there are reports of similar organic moieties, immobilised onto SBA-15, which capitalise on this phenomenon. An asymmetric Henry-Michael reaction achieved high yields, d.r., and excellent e.e..[23] Further success was found with an oxa-Michael-Michael cascade reaction, where it was suggested the pendant silanol groups interacted with the substrates in a similar way to that proposed in 5.3.3 Capping the Pendant Silanol Groups.[17]

A domino Michael-aldol reaction has been reported with a J-H catalyst and acetic acid, examples of which are illustrated in Scheme 39.[71,72] Although the yields were reasonable, excellent stereochemical control was managed throughout the reaction, achieving more than 99 % enantioselectivity. Ideally, testing a heterogenised version such as **23c** would permit the removal or reduction of acetic acid, exploiting the inherently acidic silica surface while maintaining the strict stereochemical control.

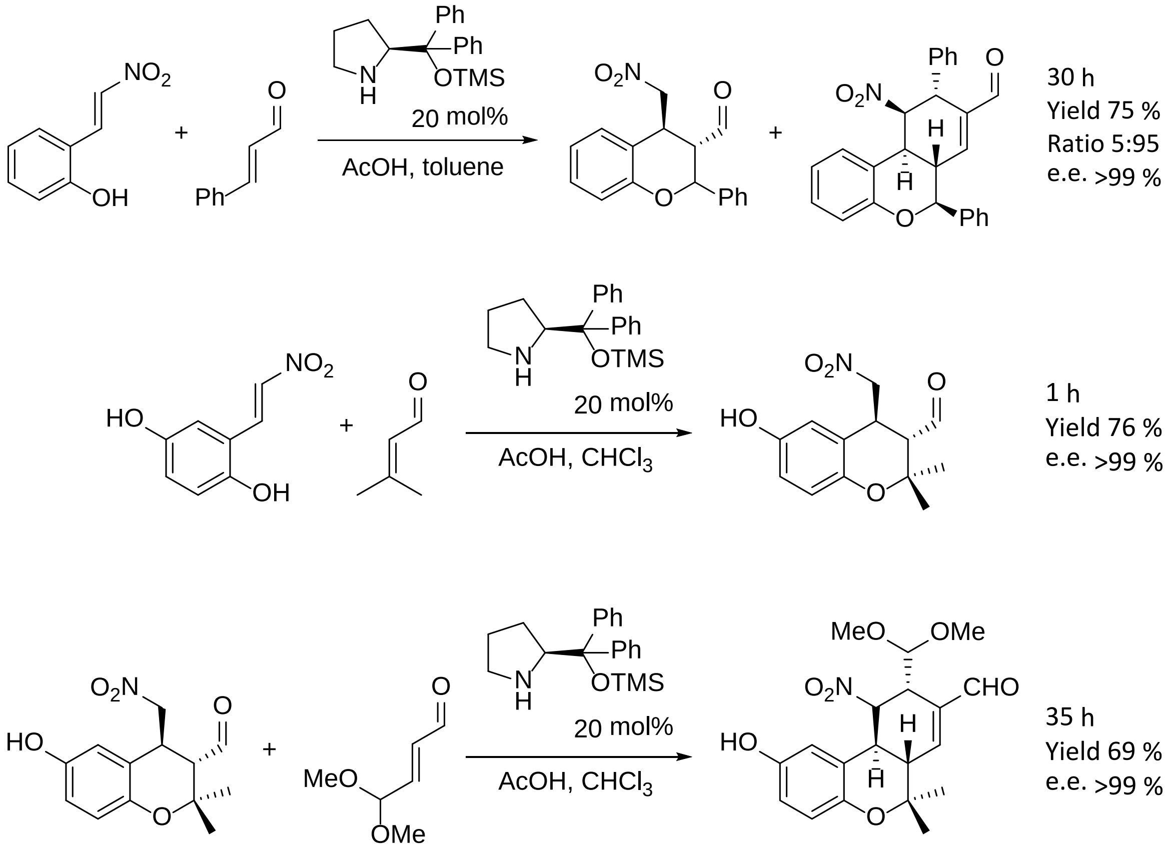

Scheme 39: Tandem oxa-Michael-Michael reaction followed by a domino Michael-aldol condensation with a J-H catalyst.

5.6 Experimental

5.6.1 Anchoring the Catalyst

Amorphous silicas were used directly from commercial sources. Ordered silicas MCM-41 and SBA-15 were kindly provided by fellow PhD students Stephanie Chapman and Matthew Potter respectively.

5.6.1.1 (S)-2-(((Allyldimethylsilyl)oxy)diphenylmethyl)pyrrolidine

The procedure of Yang and He[23] was followed to synthesise the chiral precursor. Triethylamine (0.77 mL, 5.5 mmol) was added to a solution of (S)-diphenylprolinol (1.26 g, 5.0 mmol) in DCM (20 mL). Allyl(chloro)dimethylsilane (0.80 mL, 5.5 mmol) was added dropwise before leaving the reaction to stir between 24-48 hours. To judge when the reaction had reached completion, TLC was used with an eluent of 10:1 hexane/ethyl acetate. Once complete, the reaction mixture was directly purified by column chromatography using the same eluent, whilst increasing in polarity to 100 % ethyl acetate. A yellow oil was collected, typical yield of 1.25 g, 71 %. NMR data was in good agreement with the literature.[23] ^{1}H NMR (400 MHz, $CDCl_3$): δ = 7.48 -7.45(2H, m), 7.37-7.33 (2H, m), 7.31-7.18 (6H, m), 5.85-5.73 (1H, m), 4.87-4.84 (1H, m), 4.84-4.80 (1H, m), 4.02 (1H, t, J = 7.5 Hz), 2.92-2.87 (2H, m), 1.63-1.30 (4H, m), 1.48 (2H, d, J = 8.2 Hz), -0.11 (3H, s), -0.15 (3H, s). ^{13}C NMR (101 MHz, $CDCl_3$): δ = 146.90, 145.83, 135.23, 128.59, 127.78, 127.74, 127.55, 127.16, 126.91, 113.29, 83.24, 65.57, 47.21, 27.54, 26.92, 24.97, 0.24.

5.6.1.2 Functionalising the Silica

Mesoporous silicas were functionalised following the work of Newland et al.[1] Typically (3-mercaptopropyl)triethoxysilane (0.2 mL, 0.83 mmol) was added dropwise to a solution of silica (0.5 g) in toluene (5 mL) and heated to reflux for 20 hours. The white solid was collected by filtration and washed *via* soxhlet extraction with DCM for 6 hours.

5.6.1.3 Immobilised Catalyst (23)

The grafted catalyst was also prepared by adapting the work of Newland et al.[1] The thiol-functionalised silica (0.5 g) was added to a solution of the alkene-functionalised pyrrolidine (74 mg, 0.21 mmol) in chloroform (10 mL). AIBN (35 mg, 0.21 mmol) was then added and the mixture refluxed for 18 hours. The beige/orange solid was collected by filtration and washed *via* soxhlet extraction with DCM for 6 hours.

5.6.2 Control Experiments

5.6.2.1 2-(2,4-Dinitrophenyl)-3-methylcyclopropane-1-carbaldehyde (24)

These control experiments followed the homogeneous reactions run by Meazza et al.[40] The chosen catalyst **23** (20 mol%) and 2,4-dinitrobenzylchloride **21** (100 mg, 0.46 mmol) were set stirring in chloroform (1 mL). The vial was wrapped in aluminium foil and either left at room temp. or cooled to 0 °C. After 15 minutes, mesitylene (50 µL), crotonaldehyde **22a** (mostly *trans*, 77 µL, 0.92 mmol) and DIPEA (89 µL, 0.51 mmol) were added. The reaction was typically left stirring for either 24 or 72 hrs, after which a sample was taken for ^{1}H NMR study to calculate yield and diastereomeric ratios. When the isolated product was desired, the reaction mixture was directly purified by column chromatography (hexane/ethyl acetate = 8:1), affording the products **24a-c** as yellow oils. Enantiomeric excess was calculated by HPLC using a Chiralpak OD-H column (hexane/*i*-PrOH = 80:20, flow rate = 1.0 mL/min, λ = 230 nm). NMR spectra were in good agreement with the literature.[40]

(1*R*,2*S*,3*S*)-2-(2,4-Dinitrophenyl)-3-methylcyclopropane-1-carbaldehyde (**24a**): t_R = 22.4 min, t_R = 24.6 min; ^{1}H NMR (400 MHz, $CDCl_3$) δ = 9.43 (1H, d, J = 2.8 Hz), 8.72 (1H, d, J = 2.3 Hz), 8.37 (1H, dd, J = 8.6, 2.3 Hz), 7.67 (1H, d, J = 8.5 Hz), 2.86 (1H, dd, J = 8.3, 8.2 Hz), 2.46 (1H, ddd, J = 8.8, 5.0, 2.9 Hz), 2.22-2.15 (1H, m), 1.38 (3H, d, J = 6.1 Hz).

(1*S*,2*S*,3*S*)-2-(2,4-Dinitrophenyl)-3-methylcyclopropane-1-carbaldehyde (**24b**) and (1*S*,2*S*,3*R*)-2-(2,4-dinitrophenyl)-3-methylcyclopropane-1-carbaldehyde (**24c**): [Inseparable mixture of diastereoisomers]: **24b**: t_R = 29.1 min, t_R = 26.8 min; **24c**: t_R = 36.6 min, t_R = 43.5 min; ^{1}H NMR (400 MHz, $CDCl_3$) [diastereomer – H (**24b**); diastereomer – H' (**24c**)] δ = 9.66 (1H, dd, J = 4.0, 1.3 Hz), 9.43 (1H', dd, J = 4.2, 1.2 Hz), 8.78 (1H', t, J = 2.0 Hz), 8.72 (1H, t, J = 2.0 Hz), 8.39 (1H', dd, J = 8.6, 2.3 Hz), 8.35 (1H, dd, J = 8.6, 2.3 Hz), 7.61 (1H', d, J = 8.5 Hz), 7.42 (1H, d, J = 8.6 Hz), 3.26 (1H', dd, J = 9.9, 5.4 Hz), 3.15 (1H, dd, J = 6.2, 6.0 Hz), 2.35 (1H, ddd, J = 9.4, 4.8, 4.2 Hz), 2.18 (1H', dd, J = 9.6, 4.6 Hz), 1.97-1.85 (1H, 1H', m), 1.41 (3H, dd, J = 6.3, 0.8 Hz), 0.87 (3H', dd, J = 6.3, 0.4 Hz).

5.6.2.2 2-(2,4-Dinitrophenyl)-3-heptylcyclopropane-1-carbaldehyde (25)

The same procedure as for **24** was applied, using *trans*-2-decenal **22b** (169 µL, 0.92 mmol).

(1*R*,2*S*,3*S*)-2-(2,4-Dinitrophenyl)-3-heptylcyclopropane-1-carbaldehyde (**25a**): t_R = 12.8 min, t_R = 14.1 min; ^{1}H NMR (400 MHz, $CDCl_3$) δ = 9.48 (1H, d, J = 2.6 Hz), 8.75 (1H, d, J = 2.3 Hz), 8.40 (1H, dd, J = 8.6, 2.3 Hz), 7.69 (1H, d, J = 8.6 Hz), 2.89 (1H, dd, J = 8.3, 8.2 Hz), 2.51 (1H, ddd, J = 8.8, 4.9, 2.7 Hz), 2.19 (1H, dq, J = 7.3, 7.0), 1.65-1.55 (2H, m), 1.55-1.45 (2H, m), 1.4-1.25 (8H, m) 0.89 (3H, t, J = 6.7 Hz).

(1*S*,2*S*,3*S*)-2-(2,4-Dinitrophenyl)-3-heptylcyclopropane-1-carbaldehyde (**25b**): t_R = 24.9 min, t_R = 19.4 min; ^{1}H NMR (400 MHz, $CDCl_3$) δ = 9.67 (1H, d, J = 4.1 Hz), 8.77 (1H, d, J = 2.4 Hz), 8.38 (1H, dd, J = 8.7, 2.3), 7.40 (1H, d, J = 8.6 Hz), 3.25 (1H, dd, J = 6.5, 5.9 Hz), 2.34 (1H, ddd, J = 9.0, 4.9, 4.4 Hz), 1.93-1.82 (2H, m), 1.71-1.60 (1H, m), 1.50-1.40 (10H, m), 0.88 (3H, t, J = 6.6).

(1*S*,2*R*,3*R*)-2-(2,4-Dinitrophenyl)-3-heptylcyclopropane-1-carbaldehyde (**25c**): t_R = 16.2 min, t_R = 24.1 min; ^{1}H NMR (400 MHz, $CDCl_3$) δ = 9.45 (1H, d, J = 4.4 Hz), 8.85 (1H, d, J = 2.3 Hz), 8.42 (1H, dd, J = 8.6, 2.4 Hz), 7.58 (1H, d, J = 8.6 Hz), 3.35 (1H, dd, J = 10.0, 5.7 Hz), 2.12-2.04 (1H, m), 1.40-1.12 (12H, m), 0.84 (3H, t, J = 6.9 Hz).

5.7 References

1 S. H. Newland, D. J. Xuereb, E. Gianotti, L. Marchese, R. Rios and R. Raja, *Catal. Sci. Technol.*, 2015, **5**, 660–665.

2 B. Pugin and H.-U. Blaser, in *Topics in Catalysis*, 2010, vol. 53, pp. 953–962.

3 Z. Shen, J. Ma, Y. Liu, C. Jiao, M. Li and Y. Zhang, *Chirality*, 2005, **17**, 556–558.

4 E. Bellis and G. Kokotos, *J. Mol. Catal. A Chem.*, 2005, **241**, 166–174.

5 M. Benaglia, G. Celentano and F. Cozzi, *Adv. Synth. Catal.*, 2001, **343**, 171–173.

6 L. Gu, Y. Wu, Y. Zhang and G. Zhao, *J. Mol. Catal. A Chem.*, 2007, **263**, 186–194.

7 D. Font, C. Jimeno and M. A. Pericàs, *Org. Lett.*, 2006, **8**, 4653–4655.

8 F. Giacalone, M. Gruttadauria, A. M. Marculescu and R. Noto, *Tetrahedron Lett.*, 2007, **48**, 255–259.

9 A. P. Wight and M. E. Davis, *Chem. Rev.*, 2002, **102**, 3589–3614.

10 M. Ferré, R. Pleixats, M. Wong Chi Man and X. Cattoën, *Green Chem.*, 2016, **18**, 881–922.

11 J. Fraile, J. Garcia, J. Mayoral and E. Pires, in *Heterogenized Homogeneous Catalysts for Fine Chemicals Production*, eds. P. Barbaro and F. Liguori, Springer, 2010, pp. 65–121.

12 M. D. Jones, R. Raja, J. M. Thomas, B. F. G. Johnson, D. W. Lewis, J. Rouzaud and K. D. M. Harris, *Angew. Chemie - Int. Ed.*, 2003, **42**, 4326–4331.

13 R. Raja, J. M. Thomas, M. D. Jones, B. F. G. Johnson and D. E. W. Vaughan, *J. Am. Chem. Soc.*, 2003, **125**, 14982–14983.

14 C. Y. Chen, H. X. Li and M. E. Davis, *Microporous Mater.*, 1993, **2**, 17–26.

15 M. Kruk, M. Jaroniec, C. H. Ko and R. Ryoo, *Chem. Mater.*, 2000, **12**, 1961–1968.

16 A. Heckel and D. Seebach, *Helv. Chim. Acta*, 2002, **85**, 913–926.

17 S. Wang, J. He and Z. An, *Chem. Commun.*, 2017, **53**, 8882–8885.

18 C. Baleizão, B. Gigante, H. Garcia and A. Corma, *J. Catal.*, 2003, **215**, 199–207.

19 Y. Hayashi, H. Gotoh, T. Hayashi and M. Shoji, *Angew. Chemie - Int. Ed.*, 2005, **44**, 4212–

4215.

20 M. Lombardo, L. Cerisoli, E. Manoni, E. Montroni, A. Quintavalla and C. Trombini, *European J. Org. Chem.*, 2014, **27**, 5946–5953.

21 I. Mager and K. Zeitler, *Org. Lett.*, 2010, **12**, 1480–1483.

22 K. L. Jensen, G. Dickmeiss, H. Jiang, L. Albrecht and K. A. Jørgensen, *Acc. Chem. Res.*, 2012, **45**, 248–264.

23 S. Yang and J. He, *Chem. Commun.*, 2012, **48**, 10349.

24 M. Gruttadauria, F. Giacalone and R. Noto, in *Polymeric Chiral Catalyst Design and Chiral Polymer Synthesis*, ed. S. Itsuno, John Wiley & Sons, 2011, pp. 63–90.

25 A. Kinting and H. Krause, *J. Mol. Catal.*, 1985, **33**, 215–223.

26 P. Llanes, C. Rodriguez-Escrich, S. Sayalero and M. A. Pericas, *Org. Lett.*, 2016, **18**, 6292–6295.

27 I. Sagamanova, C. Rodríguez-Escrich, I. G. Molnár, S. Sayalero, R. Gilmour and M. A. Pericàs, *ACS Catal.*, 2015, **5**, 6241–6248.

28 R. K. Kunz and D. W. C. MacMillan, *J. Am. Chem. Soc.*, 2005, **127**, 3240–3241.

29 D. Y. K. Chen, R. H. Pouwer and J. A. Richard, *Chem. Soc. Rev.*, 2012, 41, 4631–4642.

30 J. Salaun and M. S. Baird, *Curr. Med. Chem.*, 1995, **2**, 511–542.

31 P. J. Walsh and M. C. Kozlowski, *Fundamentals of Asymmetric Catalysis*, University Science Books, 2009.

32 H. Lebel, J.-F. Marcoux, C. Molinaro and A. B. Charette, *Chem. Rev.*, 2003, **103**, 977–1050.

33 H. E. Simmons and R. D. Smith, *J. Am. Chem. Soc.*, 1959, **81**, 4256–4264.

34 H. E. Simmons and R. D. Smith, *J. Am. Chem. Soc.*, 1958, **80**, 5323–5324.

35 C. D. Papageorgiou, M. A. Cubillo De Dios, S. V. Ley and M. J. Gaunt, *Angew. Chemie - Int. Ed.*, 2004, **43**, 4641–4644.

36 H. Mccooey, T. Mccabe and S. J. Connon, *J. Org. Chem.*, 2006, **71**, 7494–7497.

37 R. Rios, H. Sundén, J. Vesely, G. L. Zhao, P. Dziedzic and A. Córdova, *Adv. Synth. Catal.*, 2007, **349**, 1028–1032.

38 I. Ibrahem, G. L. Zhao, R. Rios, J. Vesely, H. Sundén, P. Dziedzic and A. Córdova, *Chem. - A Eur. J.*, 2008, **14**, 7867–7879.

39 H. Xie, L. Zu, H. Li, J. Wang and W. Wang, *J. Am. Chem. Soc.*, 2007, **129**, 10886–10894.

40 M. Meazza, M. Ashe, H. Y. Shin, H. S. Yang, A. Mazzanti, J. W. Yang and R. Rios, *J. Org. Chem.*, 2016, **81**, 3488–3500.

41 D. Zhao, J. Feng, Q. Huo, N. Melosh, G. H. Fredrickson, B. F. Chmelka and G. D. Stucky, *Science (80-.).*, 1998, **279**, 548–552.

42 S. Sankaranarayanapillai, S. Sreekumar, J. Gomes, A. Grippo, G. E. Arab, M. Head-Gordon, F. D. Toste and A. T. Bell, *Angew. Chemie Int. Ed.*, 2015, **54**, 4673–4677.

43 T. E. Kristensen, K. Vestli, K. A. Fredriksen, F. K. Hansen and T. Hansen, *Org. Lett.*, 2009, **11**, 2968–2971.

44 F. Giacalone, M. Gruttadauria, P. Lo Meo, S. Riela and R. Noto, *Adv. Synth. Catal.*, 2008, **350**, 2747–2760.

45 G. Rulli, K. A. Fredriksen, N. Duangdee, T. Bonge-Hansen, A. Berkessel and H. Gröger, *Synthesis (Stuttg).*, 2013, **45**, 2512–2519.

46 J. M. Notestein and A. Katz, *Chem. - A Eur. J.*, 2006, **12**, 3954–3965.

47 L. Tuchman-Shukron and M. Portnoy, *Adv. Synth. Catal.*, 2009, **351**, 541–546.

48 N. A. Brunelli and C. W. Jones, *J. Catal.*, 2013, **308**, 60–72.

49 X. Fan, G. Zhang and F. Zhang, *Chem. Soc. Rev.*, 2015, **44**, 3023–3035.

50 B. F. MacHado and P. Serp, *Catal. Sci. Technol.*, 2012, 2, 54–75.

51 C. Su and K. P. Loh, *Acc. Chem. Res.*, 2013, **46**, 2275–2285.

52 H. Hu, J. H. Xin, H. Hu, X. Wang and Y. Kong, *Appl. Catal. A Gen.*, 2015, 492, 1–9.

53 H. P. Cong, J. F. Chen and S. H. Yu, *Chem. Soc. Rev.*, 2014, 43, 7295–7325.

54 X. Dong, X. Wang, L. Wang, H. Song, H. Zhang, W. Huang and P. Chen, *ACS Appl. Mater. Interfaces*, 2012, **4**, 3129–3133.

55 Y. Ma, M. Zhao, B. Cai, W. Wang, Z. Ye and J. Huang, *Biosens. Bioelectron.*, 2014, **59**, 384–388.

56 V. Georgakilas, M. Otyepka, A. B. Bourlinos, V. Chandra, N. Kim, K. C. Kemp, P. Hobza, R. Zboril and K. S. Kim, *Chem. Rev.*, 2012, **112**, 6156–6214.

57 Q. Zhao, C. Bai, W. Zhang, Y. Li, G. Zhang, F. Zhang and X. Fan, *Ind. Eng. Chem. Res.*, 2014, **53**, 4232–4238.

58 Q. Zhao, Y. Li, R. Liu, A. Chen, G. Zhang, F. Zhang and X. Fan, *J. Mater. Chem. A*, 2013, **1**, 15039–15045.

59 Q. Zhao, D. Chen, Y. Li, G. Zhang, F. Zhang and X. Fan, *Nanoscale*, 2013, **5**, 882–885.

60 M. Quintana, E. Vazquez and M. Prato, *Acc. Chem. Res.*, 2013, **46**, 138–148.

61 W. Zhang, S. Wang, J. Ji, Y. Li, G. Zhang, F. Zhang and X. Fan, *Nanoscale*, 2013, **5**, 6030–6033.

62 H. Nasrallah, S. Germain, P. Queval, C. Bouvier, M. Mauduit, C. Crévisy and E. Schulz, *J. Mol. Catal. A Chem.*, 2016, **425**, 136–146.

63 D. Ventura-Espinosa, S. Sabater, A. Carretero-Cerdán, M. Baya and J. A. Mata, *ACS Catal.*, 2018, **8**, 2558–2566.

64 S. Sabater, J. A. Mata and E. Peris, *ACS Catal.*, 2014, **4**, 2038–2047.

65 C. Rodríguez-Escrich and M. A. Pericàs, *European J. Org. Chem.*, 2015, **2015**, 1173–1188.

66 I. Atodiresei, C. Vila and M. Rueping, *ACS Catal.*, 2015, **5**, 1972–1985.

67 T. Tsubogo, T. Ishiwata and S. Kobayashi, *Angew. Chemie Int. Ed.*, 2013, **52**, 6590–6604.

68 A. Puglisi, M. Benaglia and V. Chiroli, *Green Chem.*, 2013, 15, 1790–1813.

69 X. Companyó, A. Zea, A.-N. R. Alba, A. Mazzanti, A. Moyano and R. Rios, *Chem. Commun.*, 2010, **46**, 6953.

70 S. Brandau, A. Landa, J. Franzén, M. Marigo and K. A. Jørgensen, *Angew. Chemie - Int. Ed.*, 2006, **45**, 4305–4309.

71 P. Kotame, B. C. Hong and J. H. Liao, *Tetrahedron Lett.*, 2009, **50**, 704–707.

72 B.-C. Hong, P. Kotame, C.-W. Tsai and J.-H. Liao, *Org. Lett.*, 2010, **12**, 776–779.

Appendices

Appendix A relates to Chapter 3, it contains a literature review for the potential products of a CDC reaction with THIQs, and photocatalysts for the aza-Henry reaction. There are also examples of the calculations carried out using the TGA thermogram and NMR spectra.

Appendix B is for Chapter 4, there is a literature review on the different catalysts that have been used to functionalise benzoxazoles in the reactions discussed. In addition to NMR spectra for the novel compounds synthesised.

Appendix C corresponds to Chapter 5, it includes a brief literature review for the variety of proline derivatives and their supports. There are also representative NMR spectra and HPLC traces, as well as the BET isotherm plots for the mesoporous silicas **23a-g** and recycled catalysts.

References have been included at the end in a bibliography.

Appendix A

A.1 Literature Review

Table 32: CDC reaction of tertiary amines with a variety of nucleophiles.[1]

Entry	Product	NMR Yield / %	Temperature
1	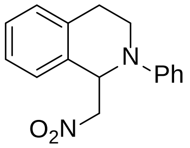	84	r.t.
2	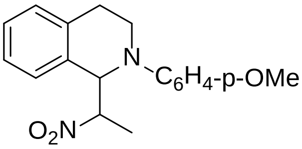	81	r.t.
3	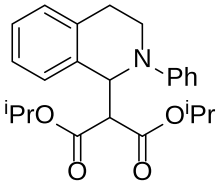	82	r.t.
4[a]	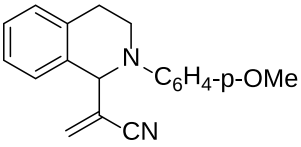	74	50 °C
5[a]	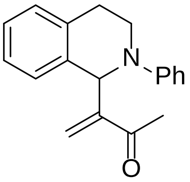	53	50 °C
6	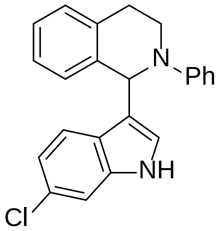	89	50 °C
7	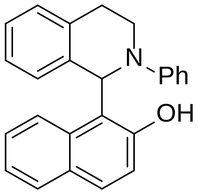	72	50 °C
8[b]	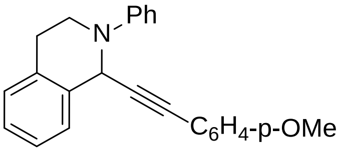	74	100 °C

Reaction conditions: CuBr (5 mol%), TBHP (1.0-1.3 equiv.), stirring overnight. Yield determined by ^1H NMR of reaction mixture, using an internal standard. [a] DABCO (10 mol%). [b] 3 h stirring.

Table 33: Brief summary of literature photocatalytic CDC of *N*-phenyltetrahydroisoquinoline with nitromethane.

Entry	Time / h	Yield[a] / %	Light Source	Catalyst	Conditions
1[2]	10	92	Fluorescent lamp (15 W, distance app. 10 cm)	$Ir(ppy)_2(dtbbpy)PF_6$ (1 mol%)	0.25 M, r.t. air
2[2]	180	{83}		-	
3[2]	24	{20}		-	
4[2]	48	{0}	No light	$Ir(ppy)_2(dtbbpy)PF_6$ (1 mol%)	
5	8	{80}	Green LEDs (1 W, λ = 530 ± 10 nm, 145 lm @ 700 mA)	Eosin Y (2 mol%)	0.25 M, r.t. air
6	180	{78}		-	
7	72	{0}	No light	Eosin Y (2 mol%)	
8	10	92	Green LEDs (0.5-5 W)	Rose Bengal (5 mol%)	0.1 M, r.t.
9	20	{0}	No light		0.25 M, r.t.
10[3]	40	93	Fluorescent bulb (11 W, distance app. 3 cm, cold white, 6400 K)	TiO_2 (1 equiv.)	0.1 M, EtOH, 10 equiv. $MeNO_2$ 0.1 M, EtOH, 10 equiv. $MeNO_2$
11[3]		Traces	No light	TiO_2 (1 equiv.)	

Entry	Time / h	Yield[a] / %	Light Source	Catalyst	Conditions
12[4]	12	{86}	Fluorescent lamp (26 W, distance 5-10 cm)	$[Ru(bpy)_2(dcbpy)]Cl_2$ incorporated into UiO-67 (1 mol %)	0.25 M, r.t. air
13[4]		{19}		-	
14[4]	-	{< 5}	No light	$[Ru(bpy)_2(dcbpy)]Cl_2$ incorporated into UiO-67 (1 mol %)	
15[5]	4	90	Blue LEDs (3 W, λ_{max} = 450)	UiO-68Se (4-5 mg/0.1 mmol THIQ)	9.3 M, r.t., air
16[5]		(Traces)		-	
17[5]	6	(0)	No light	UiO-68Se (4-5 mg/0.1 mmol THIQ)	
18[6]	6	97	No light	Cu^{II} MOF with imidazole carboxylate ligands	0.1 M, r.t., 1.5 equiv. TBHP, MePhTHIQ
19[7]	6	97	No light	ZJU-22	0.1 M, r.t., 1.5 equiv. TBHP, MePhTHIQ
20[7]		11		-	
21[7]	6	76	No light	HKUST-1 (0.01 mmol)	0.1 M, r.t., 1.5 equiv. TBHP, MePhTHIQ
22[1]	overnight	(84)65	No light	CuBr (5 mol%)	9.3 M, r.t., 1.2 equiv. TBHP

[a] Isolated yield given, with calculated yields from NMR in parentheses and conversion in curly brackets.

A.2 TGA Calculations

A.2.1 ZIF-9

Residual mass = 25.67 %

Mass corresponding to Co in Co_2O_3 = 71.06 %

Mass of sample corresponding to Co = 18.2 %

Residual mass discounting DMF 25.67/88.91 x 100 = 28.87 %

Mass of sample (discounting DMF) corresponding to Co = 20.5 %

Theoretical mass of Co in ZIF-9 [Co(PhIm)$_2$] = 20.1 %

Residual mass corresponding to O in Co_2O_3 = 28.94 %

Mass drop discounting DMF 63.45/88.91 x 100 = 71.36 %

Mass corresponding to Organics = 79.72 %

Theoretical mass of organics in ZIF-9 [Co(PhIm)$_2$] = 79.9 %

A.2.2 ZIF-67

Residual mass = 37.59 %

Mass corresponding to Co in Co_2O_3 = 71.06 %

Mass of sample corresponding to Co = 26.7 %

Theoretical mass of Co in ZIF-67 [Co(PhIm)$_2$] = 26.7 %

Residual mass corresponding to O in Co_2O_3 = 10.88 %

Mass drop corresponding to organics = 62.41 %

Mass corresponding to Organics = 73.3 %

Theoretical mass of organics in ZIF-67 [Co(2-Mim)$_2$] = 73.3 %

A.3 EXAFS

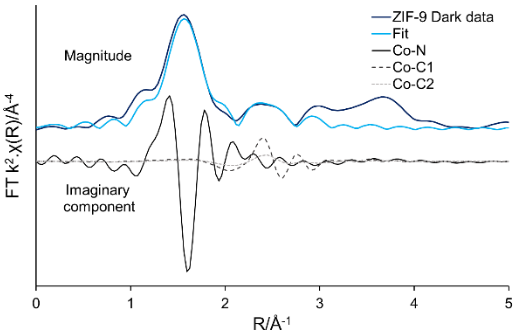

Figure 66: Magnitude and imaginary component of the k^2 weighted Fourier transform EXAFS data, showing the influence of different fitted paths for ZIF-9 under (a) 'dark' and (b) 'hv' conditions.

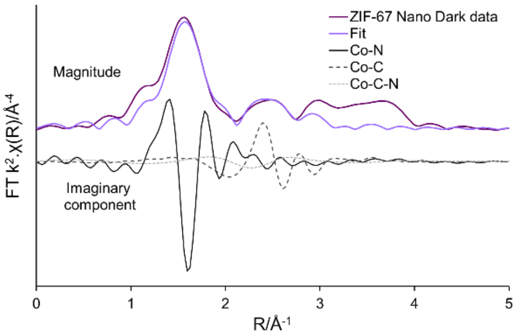

Figure 67: Magnitude and imaginary component of the k^2 weighted Fourier transform EXAFS data, showing the influence of different fitted paths for ZIF-67 under (a) 'dark' and (b) 'hv' conditions.

A.4 NMR Spectra

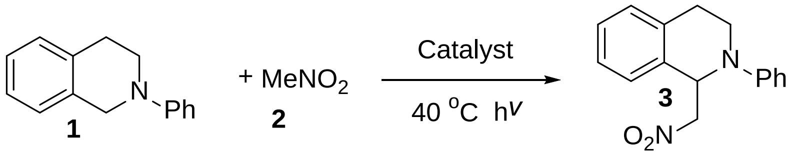

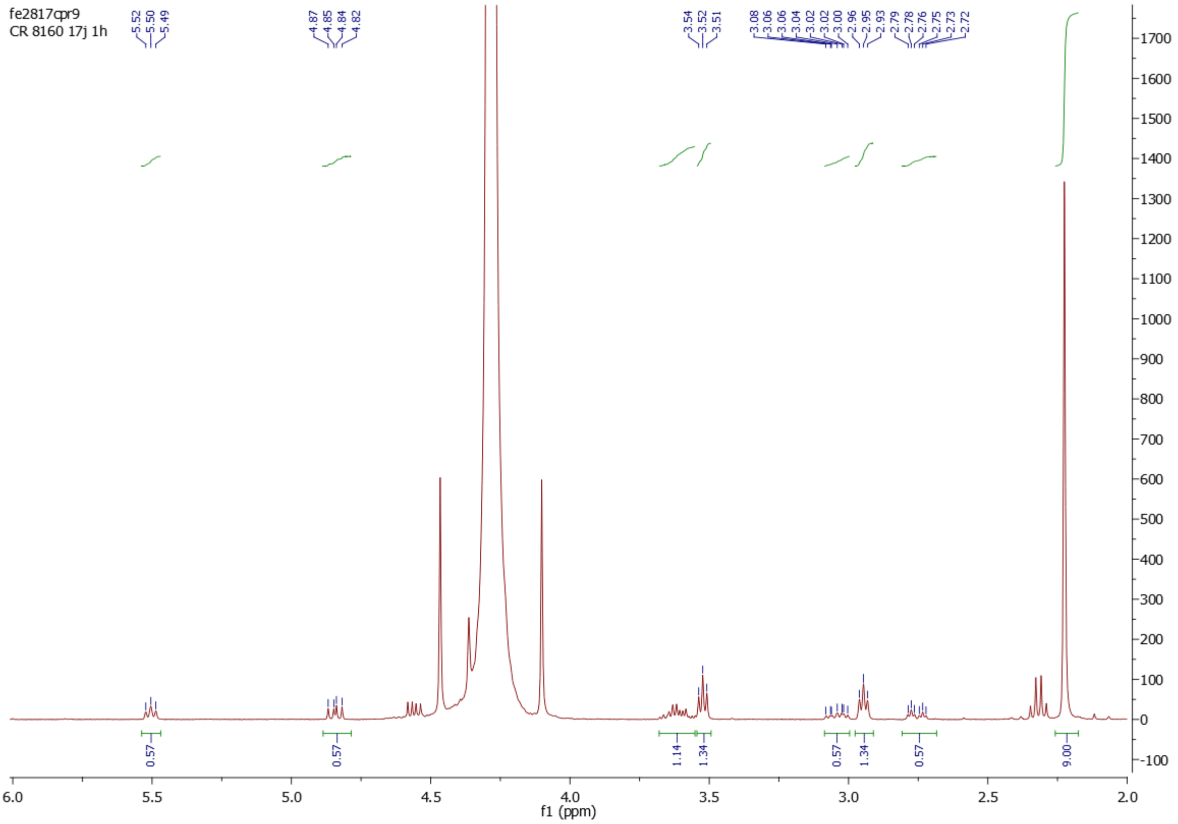

Using mesitylene (10.0 mg, 0.0832 mmol) as an internal standard:

The remaining quantity of starting material can be calculated from the peaks at 3.56 and 2.9 ppm of intensity 1.34, corresponding to two hydrogen atoms each. This represents a value of 0.0580 mmol, from an initial 0.11 mmol, therefore a conversion of 47 %.

The quantity of product is calculated using three peaks, those at 5.5, 4.6 and 2.8 ppm, of intensity 0.57, corresponding to one hydrogen atom each. This represents a value of 0.0483 mmol, from a maximum potential of 0.11 mmol, therefore a yield of 44 %.

No by-products have been identified, total number of moles accounted for is 0.1063 mmol out of a total 0.11 mmol, giving a mass balance of 97 %.

Appendix B

B.1 Literature Review

Table 34: Literature examples for the amination of benzoxazoles.

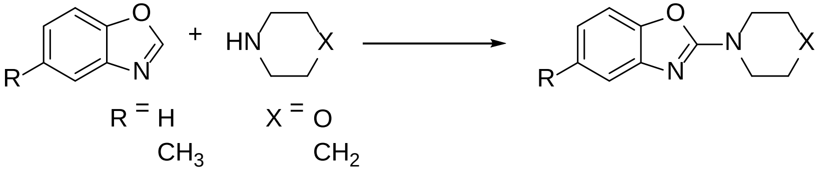

Entry	Product	Yield / %	Time	Conditions	Catalyst	Method	Class
1[8]		99 74	1 h 5 min	r.t., 1h, neat r.t., PhI(OAc)$_2$, DCM		Isolated intermediate. Hypervalent iodine bonds with azole N during ring closure, loss of hydrogen, producing acetic acid and iodobenzene.	Metal-free
2[9]	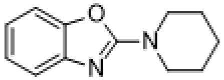	99 93	30 min 5 min	r.t., 30 min, neat 0 °C, KOAc, NBS, H$_2$O/dioxane		Isolated intermediate. Br of NBS bonds with azole N, encouraging ring closure, elimination of HBr with base.	Metal-free

Entry	Product	Yield / %	Time	Conditions	Catalyst	Method	Class
3[10]	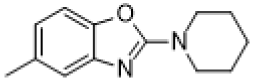	96 91	20 min 6 min	r.t., neat r.t., IBX, DCM		Isolated intermediate. Hypervalent iodine as an oxidising agent	Metal-free
4[11]		 89	4 h 10 min	60 °C, MeCN 60 °C, TEMP, TEMPO$^+$BF$_4^-$, MeCN	TfOH	Formation of intermediate. TEMPO induced radical cyclisation.	Homogeneous
5[12]	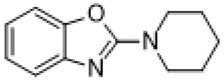	 91	 2 h	r.t., neat r.t., AcOH, TBHP, EtOAc	 *Vitreoscilla* (Haemoglobin VHb)	Isolated intermediate. TBHP and VHb form the radical intermediates which facilitate the reaction.	Metal-free Haemoglobin
6[13]		- 89	10 min 1 h	r.t., neat r.t., Lamp, CBr_4, MeCN, air		Isolated intermediate. Light promotes formation of radical intermediates from CBr_4.	Metal-free Photochemistry
7[14]		- 94	10 min 18 h	r.t., neat r.t., blue LEDs, $MeNO_2$, air	Ru(bpy)$_3$Cl$_2$	Isolated intermediate. Photo-induced SET.	Homogeneous Photocatalytic
8[15]		- 95	30 min 5 min	r.t., neat r.t., H_2O_2, MeCN	$FeCl_2$	Isolated intermediate. Radical induced oxidation.	Homogeneous

Entry	Product	Yield / %	Time	Conditions	Catalyst	Method	Class
9[16]	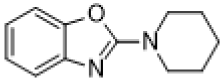	84	12 h	70 °C, AcOH, O_2, MeCN	$Cu(OAc)_2.H_2O$	Cu complexes with amine, then helps to bring the two substrates together.	Homogeneous
10[17]		77	12 h	70 °C, Propanoic acid, TBHP, MeCN	$Ni(OAc)_2.4H_2O$		Homogeneous
11[18]		95	12 h	50 °C, AcOH, air, MeCN	$CuBr_2$	Cu complexes with amine, then helps to bring the two substrates together.	Homogeneous
12[19]	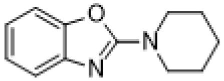	72	12 h	60 °C, Imidazole, air, MeCN	$FeCl_3$	Fe bonds with the azole N, and oxidises the intermediate.	Homogeneous
13[20]		81	12 h	r.t., AcOH, TBHP, MeCN	$Co(OAc)_2$	Co induced radical formation.	Homogeneous
14[21]	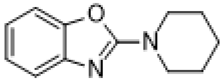	59	8 h	120 °C, NaO^{t}Bu, AgOAc	$Cu@TiO_2$	Cu bonds with azole N, nucleophilic attack from deprotonated amine, oxidation with Ag.	Heterogeneous
15[22]	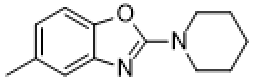	93	12 h	r.t., AcOH, TBHP, MeCN	Co-MOF	Co induced radical formation.	Heterogeneous

Entry	Product	Yield / %	Time	Conditions	Catalyst	Method	Class
16[23]	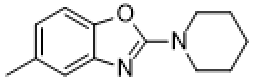	76	24 h	50 °C, O_2, MeCN	γ-MnO_2	Oxidation with Mn	Heterogeneous
17[24]	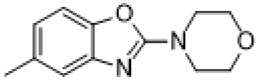	96	-	r.t., AcOH, MeCN	Bu_4NI	Electrolysis. Formation of the intermediate with AcOH, then oxidation facilitated by the halide.	Electrolysis
18	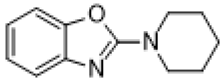	31	-				

Table 35: Literature examples for the formation of 2-phenylbenzoxazole from 2-aminophenol and benzaldehyde.

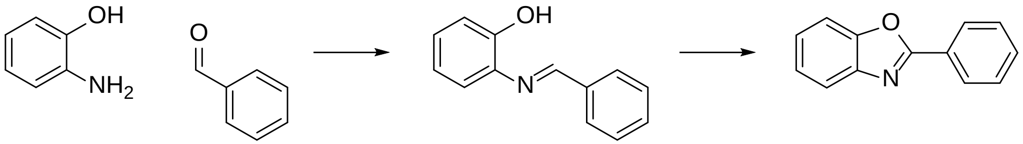

Entry	Yield / %	Time	Conditions	Catalyst	Proposed Mode of Action	Class
1[25]	95	3 min	KCN, DMF, microwave		Formation of benzoin, followed by attack of aminophenol and loss of benzyl alcohol	Homogeneous
2[26]	90	5 h	120 °C, O_2, xylene	4-methoxy-TEMPO	Radical initiated rearomatisation, with regeneration of catalyst using oxygen	Homogeneous
3[27]	93	12 h 2 h	45 °C, MeOH r.t., DDQ, DCE, THF		Formation of intermediate Strong oxidant	Homogeneous
4[12]	93	2 h	r.t., AcOH, TBHP, EtOAc	*Vitreoscilla* (Haemoglobin VHb)	TBHP and VHb form the radical intermediates which facilitate the reaction.	Homogeneous
5[28]	97	8 min	KCN, DMF/H_2O, ultrasonic irradiation	(bmim)PF_6	Formation of benzoin using [bmim]CN, followed by attack of aminophenol and loss of benzyl alcohol	Homogeneous (ionic liquid)
6[29]	78	4 h	120 °C, O_2, xylene	Activated carbon		Heterogeneous
7[30]	95	6 h	140 °C, neat	VNU-11-P-SO_4	Hf-based MOF, solvent free	Heterogeneous

Entry	Yield / %	Time	Conditions	Catalyst	Proposed Mode of Action	Class
8[31]	98	5 h	130 ^{o}C, neat	Brønsted acidic ionic liquid gel grafted onto silica	Acid catalysis, oxidation in air	Heterogeneous
9[32]	98	5 min	r.t., neat	$NH_3(CH_2)_4NH_3.SiF_6$		Heterogeneous
10[33]	95	10 min	r.t., neat	$NiFe_2O_4@SiO_2$ @aminoglucose	Acid/base catalysis with surface alcohol groups. Magnetic recovery.	Heterogeneous
11[34]	96	20 min	r.t., water, sonication	$NiEuFe_2O_4$	Interaction of substrate's N with catalyst aids oxidation	Heterogeneous
12[35]	99	3 min	r.t., ethanol	ZnO NPs	Zinc catalyses the cyclisation, aerobic oxidation to final product	Heterogeneous
13[36]	90	8 min	r.t., neat	$NH_3(CH_2)_5NH_3BiCl_5$		Heterogeneous
14[37]	93	18 h	80 ^{o}C, O_2, DMF,	Pd(II) immobilised into silica-coated magnetic nanoparticles	Pd(II) assisted oxidation	Heterogeneous
15[38]	92	24 h	65 ^{o}C, O_2, 1,4-dioxane	Co-based nanocomposite	Promotes oxidation	Heterogeneous
16[39]	91	15 min	60 ^{o}C, MeCN	TiO_2-ZrO_2		Heterogeneous
17[40]	90	3 h	80 ^{o}C, K_2CO_3, O_2, MeOH	CuNPs		Heterogeneous

B.2 NMR Spectra for Novel Compounds

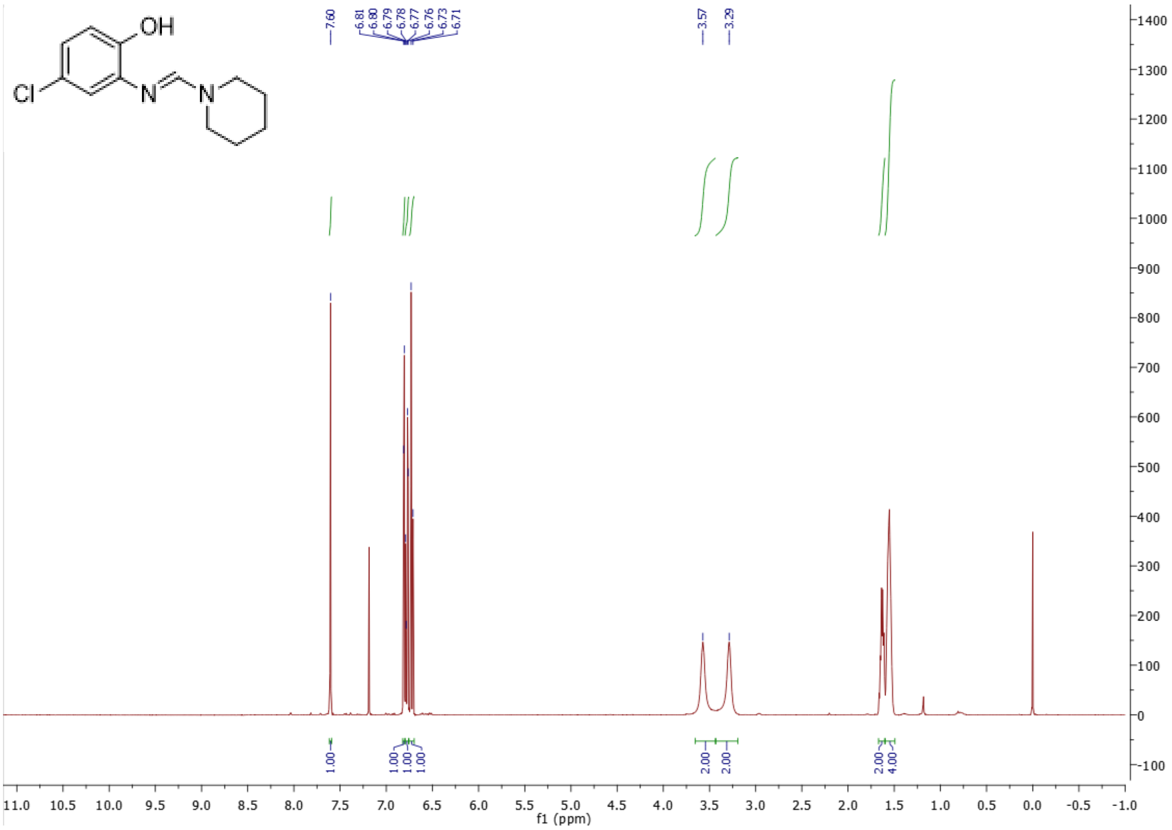

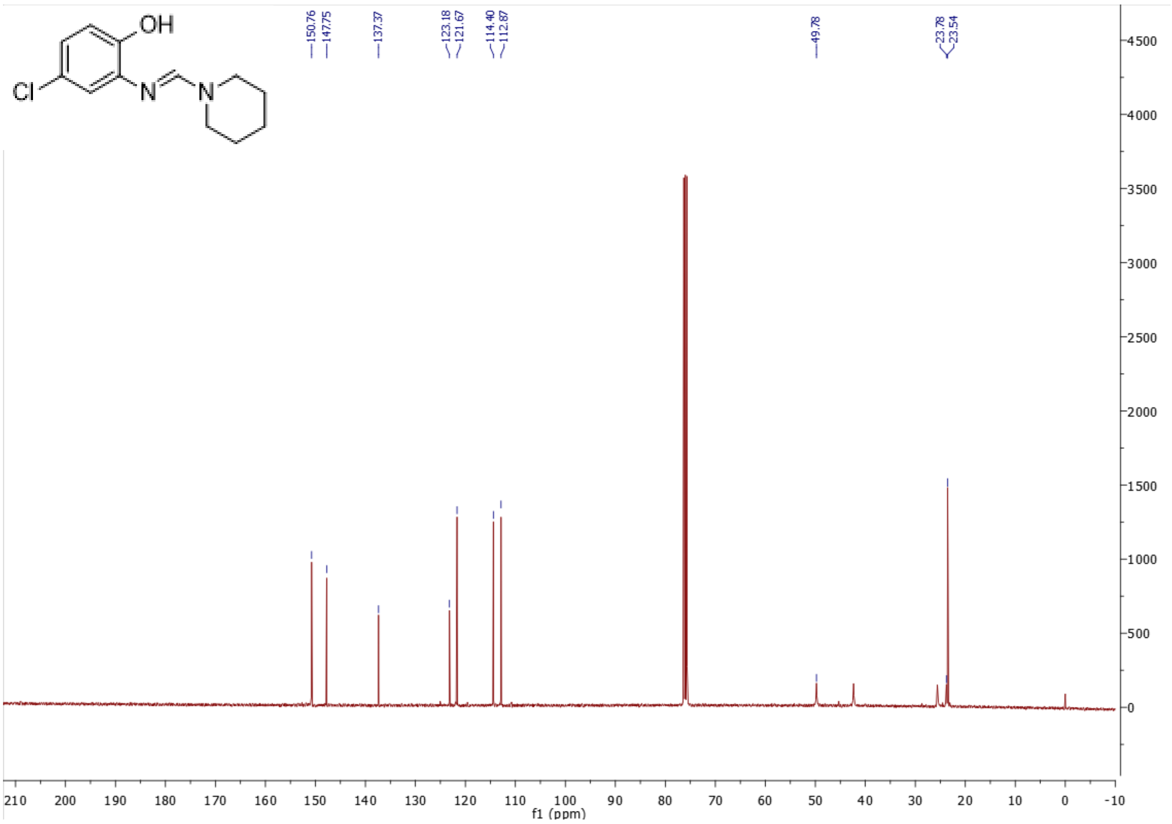

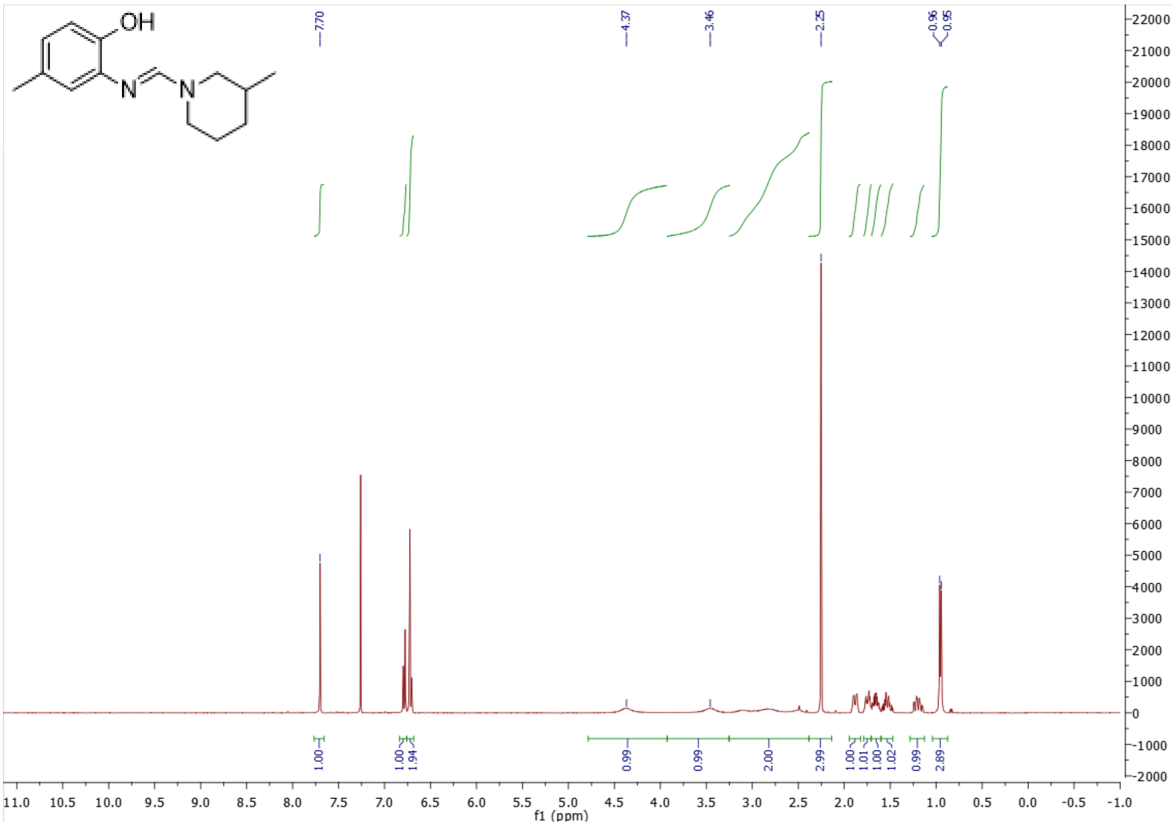
OH
N
N
7.70
4.37
3.46
2.25
0.96
0.95
1.00
1.00
1.94
0.99
0.99
2.00
2.99
1.00
1.01
1.00
1.02
0.99
2.89
11.0
10.5
10.0
9.5
9.0
8.5
8.0
7.5
7.0
6.5
6.0
5.5
5.0
4.5
4.0
3.5
3.0
2.5
2.0
1.5
1.0
0.5
0.0
-0.5
-1.0
f1 (ppm)
22000
21000
20000
19000
18000
17000
16000
15000
14000
13000
12000
11000
10000
9000
8000
7000
6000
5000
4000
3000
2000
1000
0
-1000
-2000

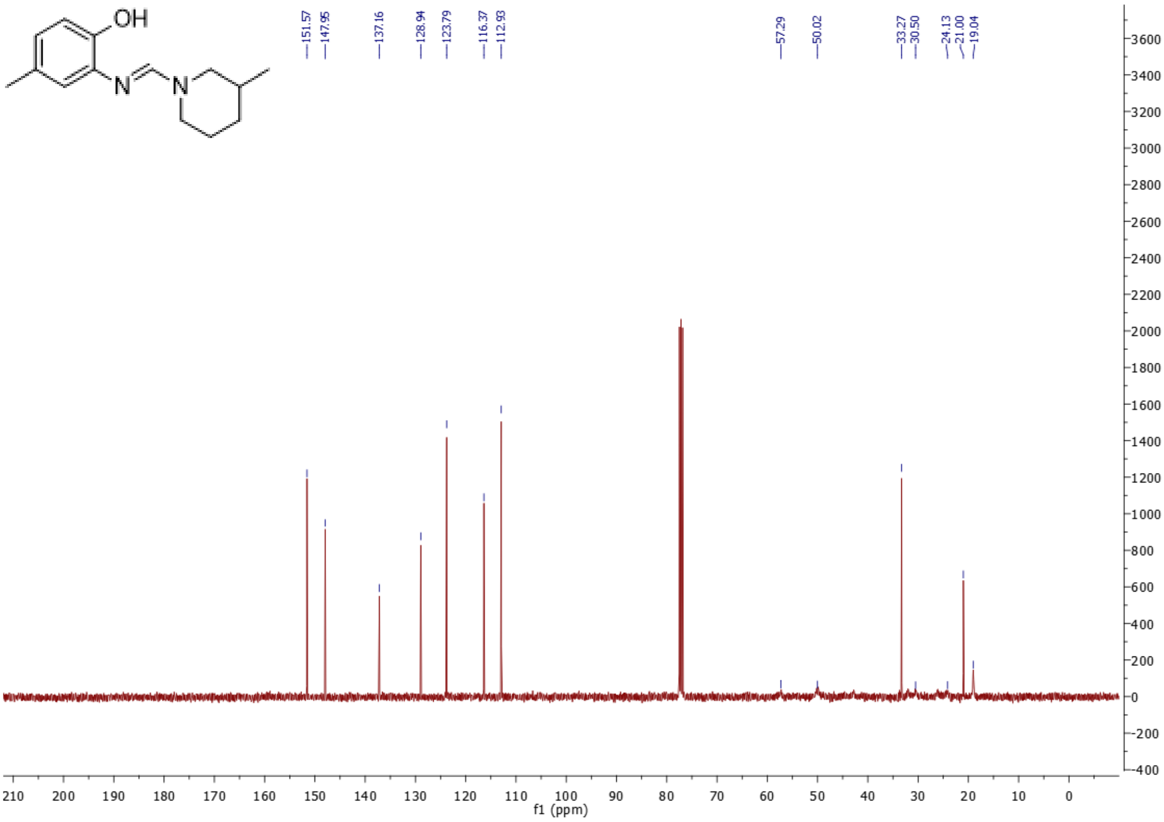
OH
N
N
151.57
147.95
137.16
128.94
123.79
116.37
112.93
57.29
50.02
33.27
30.50
24.13
21.00
19.04
210
200
190
180
170
160
150
140
130
120
110
100
90
80
70
60
50
40
30
20
10
0
f1 (ppm)
3600
3400
3200
3000
2800
2600
2400
2200
2000
1800
1600
1400
1200
1000
800
600
400
200
0
-200
-400

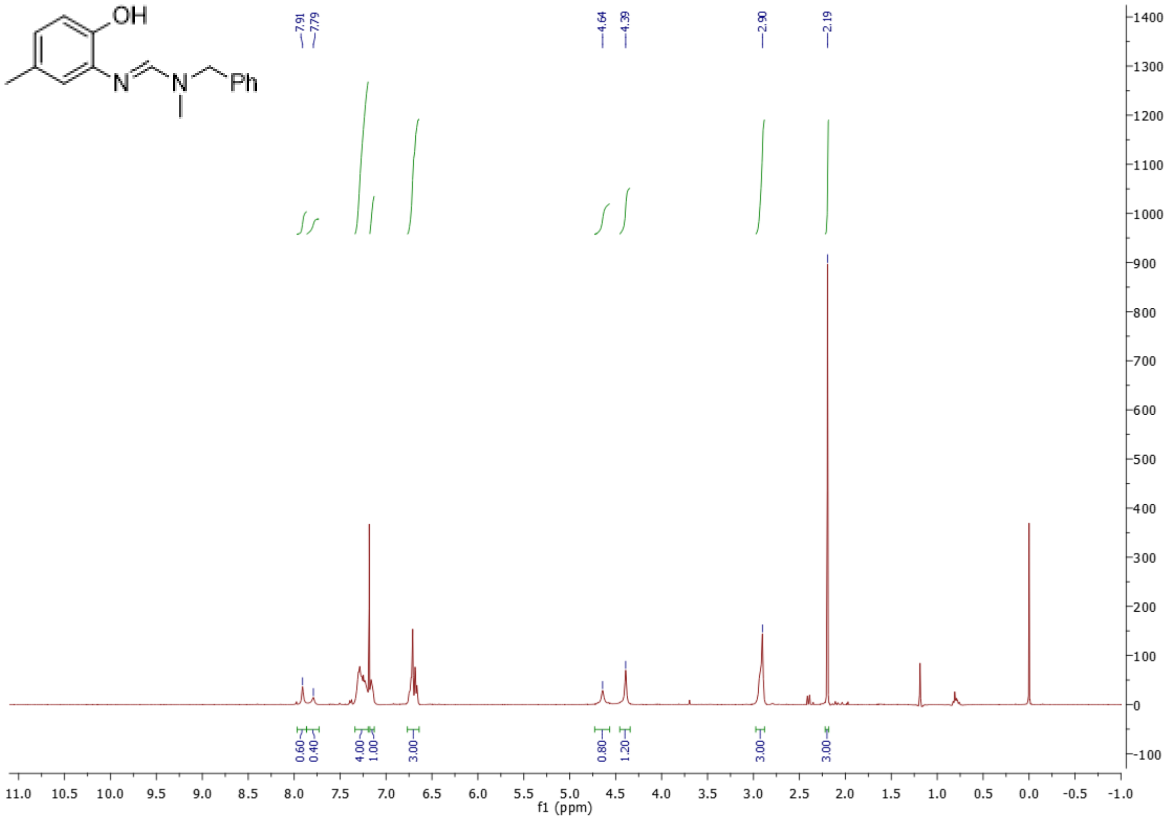
OH
N
N
Ph
7.91
7.79
4.64
4.39
2.90
2.19
0.60
0.40
4.00
1.00
3.00
0.80
1.20
3.00
3.00
11.0 10.5 10.0 9.5 9.0 8.5 8.0 7.5 7.0 6.5 6.0 5.5 5.0 4.5 4.0 3.5 3.0 2.5 2.0 1.5 1.0 0.5 0.0 -0.5 -1.0
f1 (ppm)
1400 1300 1200 1100 1000 900 800 700 600 500 400 300 200 100 0 -100

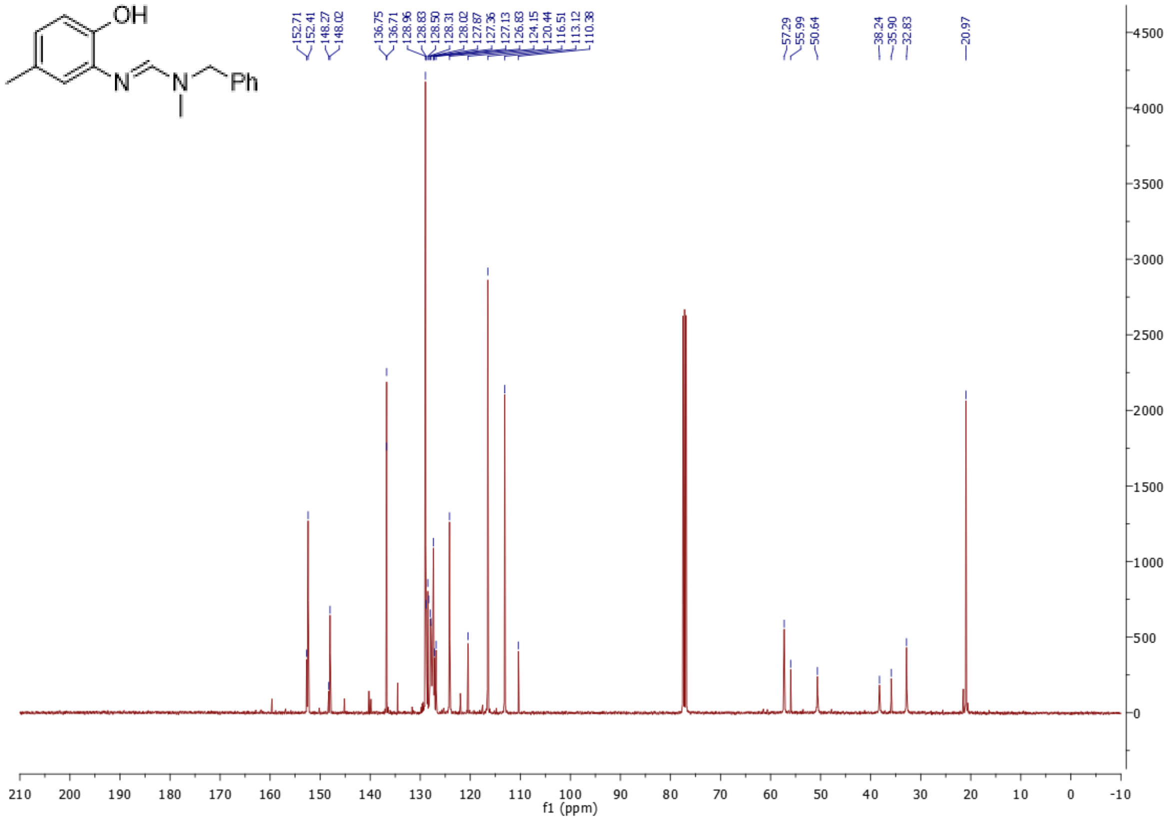
OH
N
N
Ph
152.71
152.41
148.27
148.02
136.75
136.71
128.96
128.83
128.50
128.31
128.02
127.87
127.36
127.13
126.83
124.15
120.44
116.51
113.12
110.38
57.29
55.99
50.64
38.24
35.90
32.83
20.97
210 200 190 180 170 160 150 140 130 120 110 100 90 80 70 60 50 40 30 20 10 0 -10
f1 (ppm)
4500 4000 3500 3000 2500 2000 1500 1000 500 0

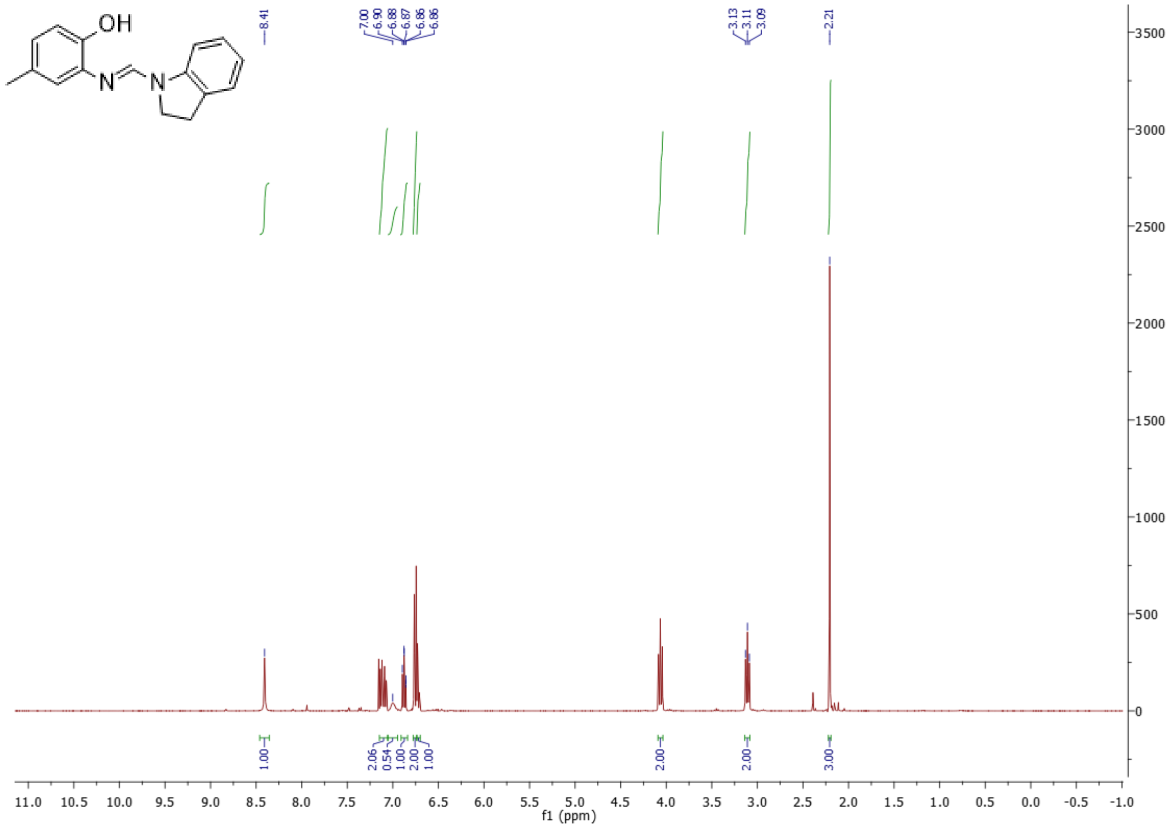
OH
N
N
8.41
7.00
6.90
6.88
6.87
6.86
6.86
3.13
3.11
3.09
2.21
1.00
2.06
0.54
1.00
2.00
1.00
2.00
2.00
3.00
3500
3000
2500
2000
1500
1000
500
0
11.0 10.5 10.0 9.5 9.0 8.5 8.0 7.5 7.0 6.5 6.0 5.5 5.0 4.5 4.0 3.5 3.0 2.5 2.0 1.5 1.0 0.5 0.0 -0.5 -1.0
f1 (ppm)

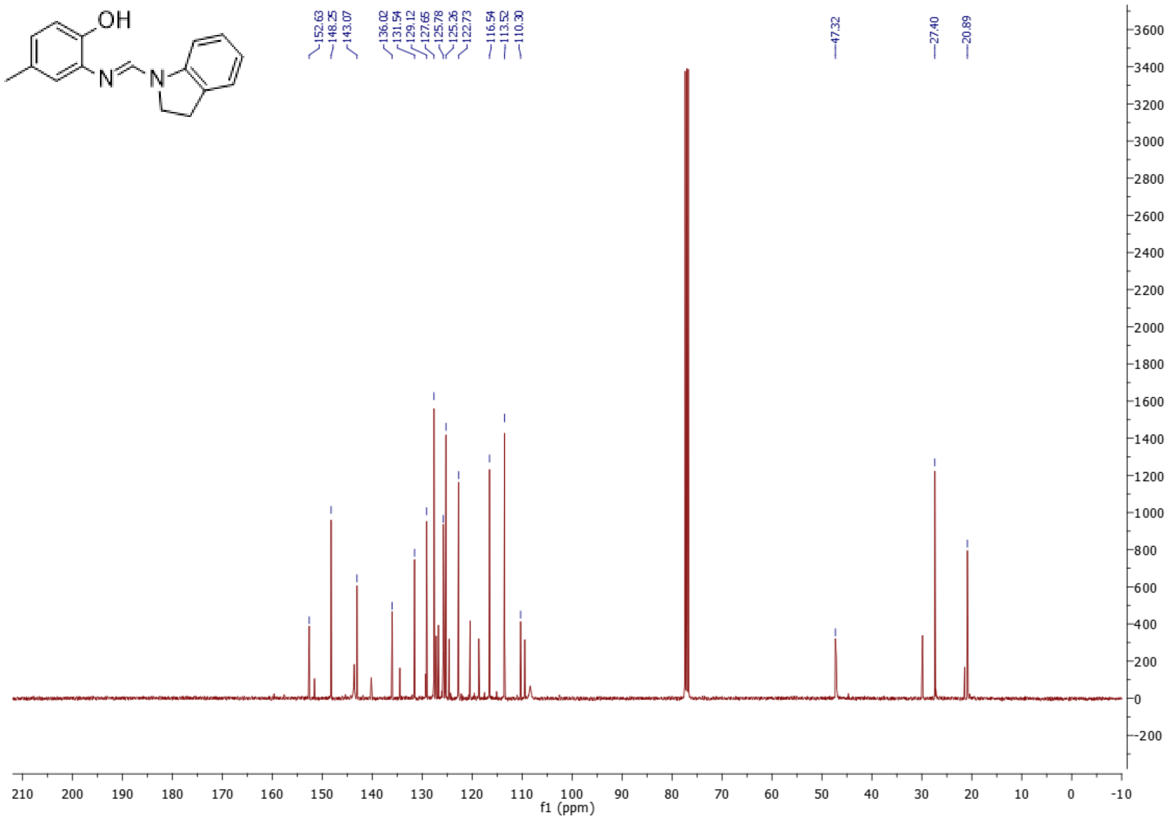
OH
N
N
152.63
148.25
143.07
136.02
131.54
129.12
127.65
125.78
125.26
122.73
116.54
113.52
110.30
47.32
27.40
20.89
3600
3400
3200
3000
2800
2600
2400
2200
2000
1800
1600
1400
1200
1000
800
600
400
200
0
-200
210 200 190 180 170 160 150 140 130 120 110 100 90 80 70 60 50 40 30 20 10 0 -10
f1 (ppm)

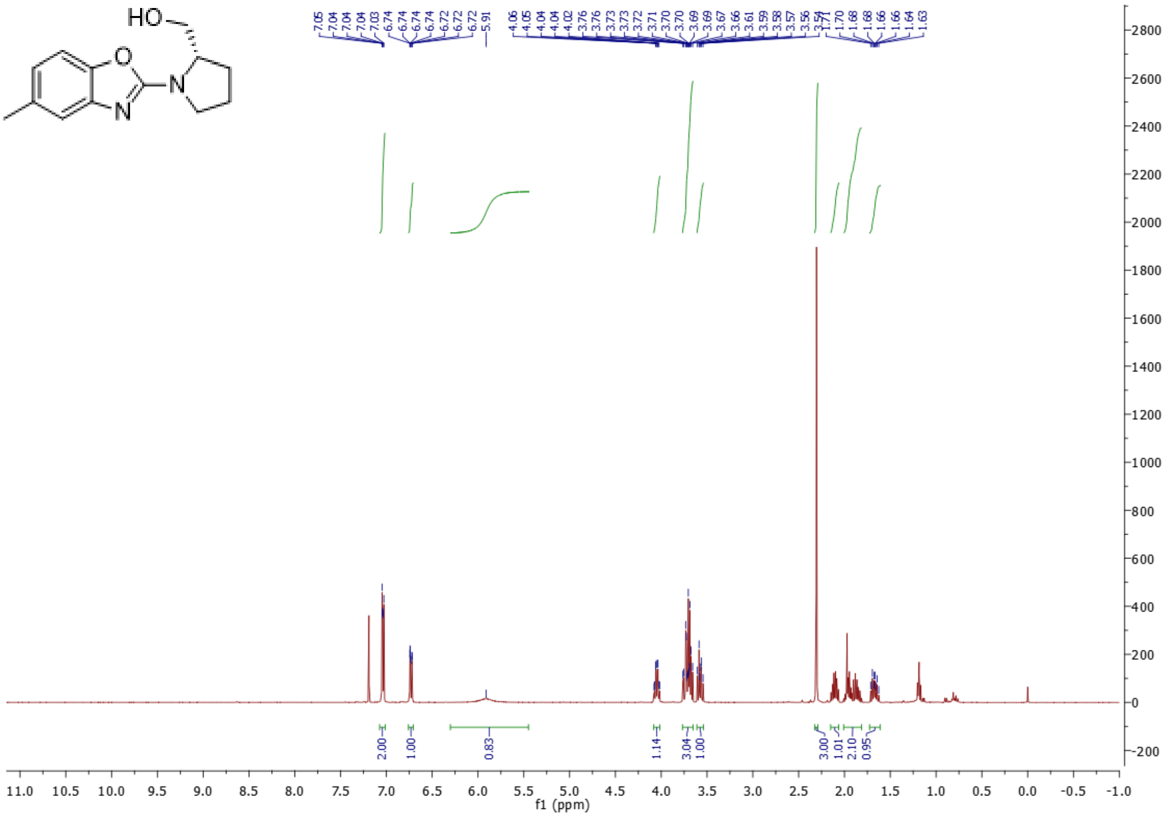
HO
O
N
N
7.05
7.04
7.04
7.04
7.03
6.74
6.74
6.74
6.74
6.72
6.72
6.72
5.91
4.06
4.05
4.04
4.04
4.02
3.76
3.76
3.73
3.73
3.72
3.71
3.70
3.70
3.69
3.69
3.67
3.66
3.61
3.59
3.58
3.57
3.56
3.54
1.71
1.70
1.68
1.68
1.66
1.66
1.64
1.63
2.00
1.00
0.83
1.14
3.04
1.00
3.00
1.01
2.10
0.95
11.0 10.5 10.0 9.5 9.0 8.5 8.0 7.5 7.0 6.5 6.0 5.5 5.0 4.5 4.0 3.5 3.0 2.5 2.0 1.5 1.0 0.5 0.0 -0.5 -1.0
f1 (ppm)
2800 2600 2400 2200 2000 1800 1600 1400 1200 1000 800 600 400 200 0 -200

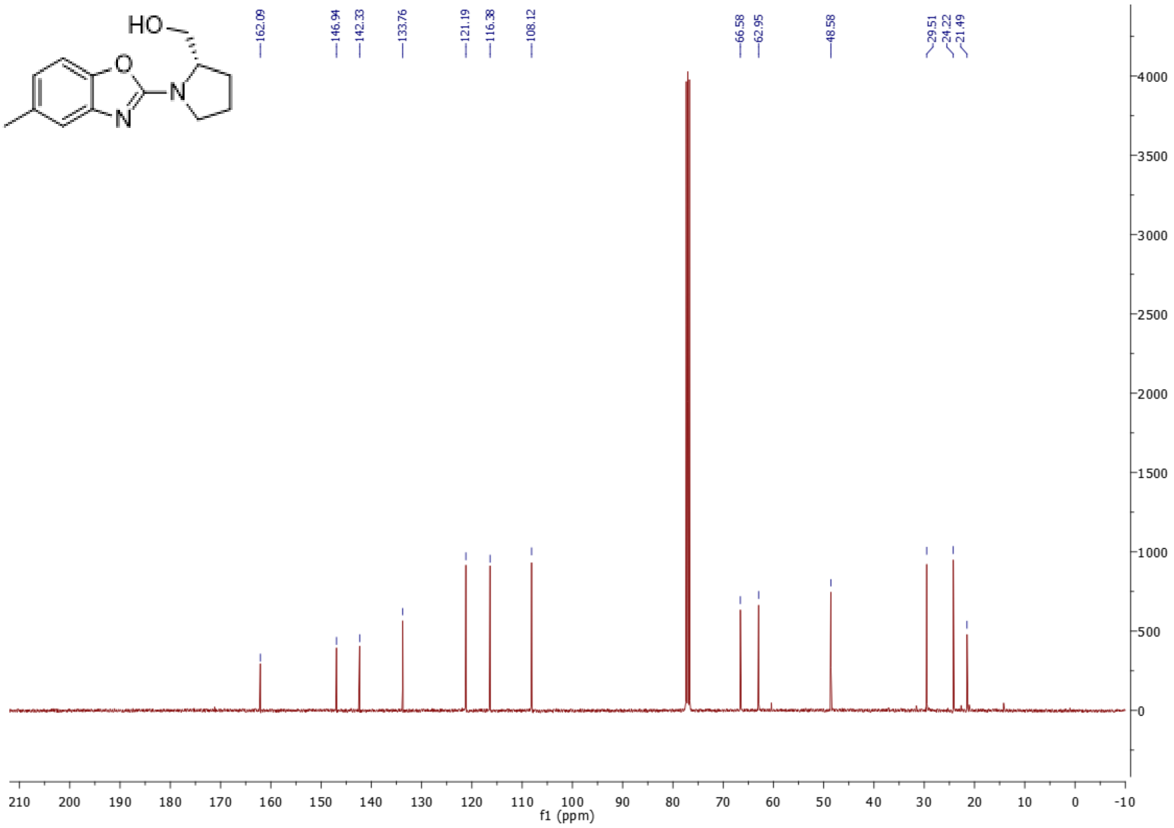
HO
O
N
N
162.09
146.94
142.33
133.76
121.19
116.38
108.12
66.58
62.95
48.58
29.51
24.22
21.49
210 200 190 180 170 160 150 140 130 120 110 100 90 80 70 60 50 40 30 20 10 0 -10
f1 (ppm)
4000 3500 3000 2500 2000 1500 1000 500 0

Appendix C

C.1 Literature Review

Table 36: Brief summary of literature examples immobilising *L*-proline derivatives onto heterogeneous supports.

Entry	Catalyst	Support	Reaction	Yield	d.r.	e.e.
1[41]	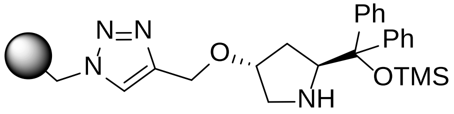	Polystyrene	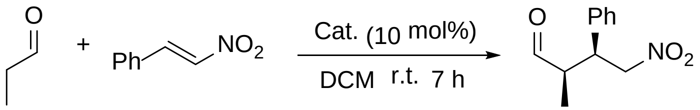	98	>99:1	>99
2[42]	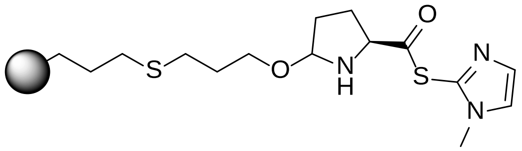	SBA-15	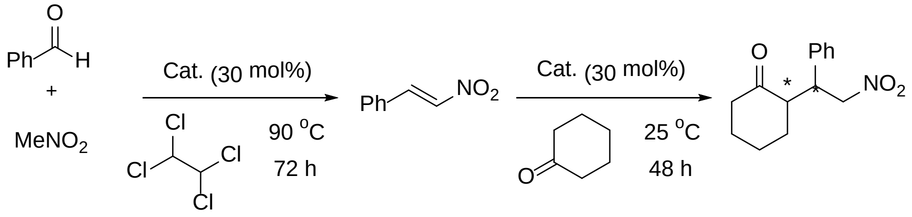	85	4:1	99:95
3[43]	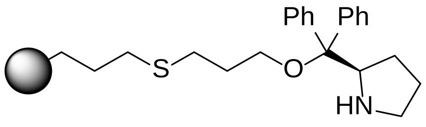	SBA-15	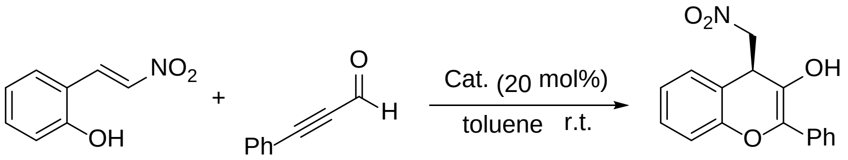	80	94	96

Entry	Catalyst	Support	Reaction	Yield	d.r.	e.e.
4[44]	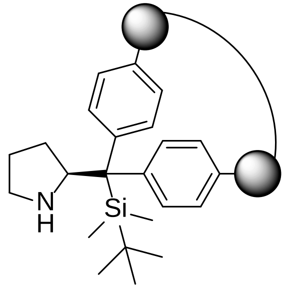	Embedded Polymer	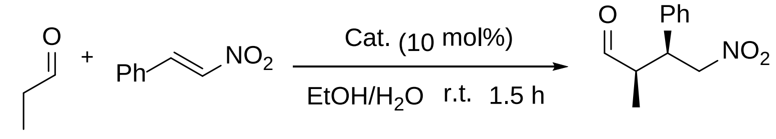	99	12:1	98
5[45]	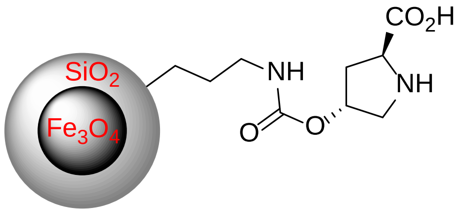	Magnetic Nanoparticle	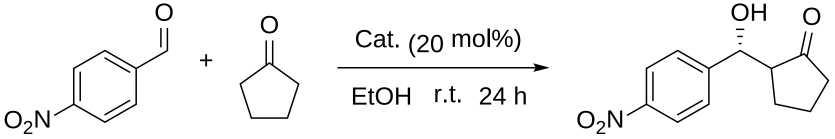	95	-	99

C.2 Sample Calculation with NMR Spectra

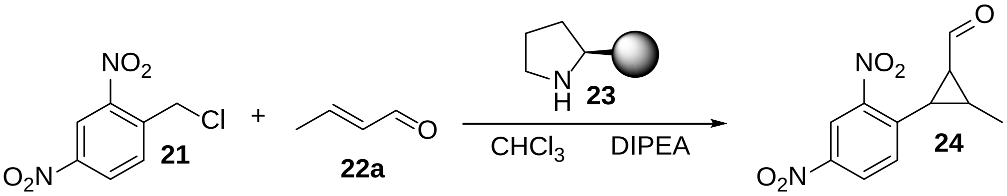

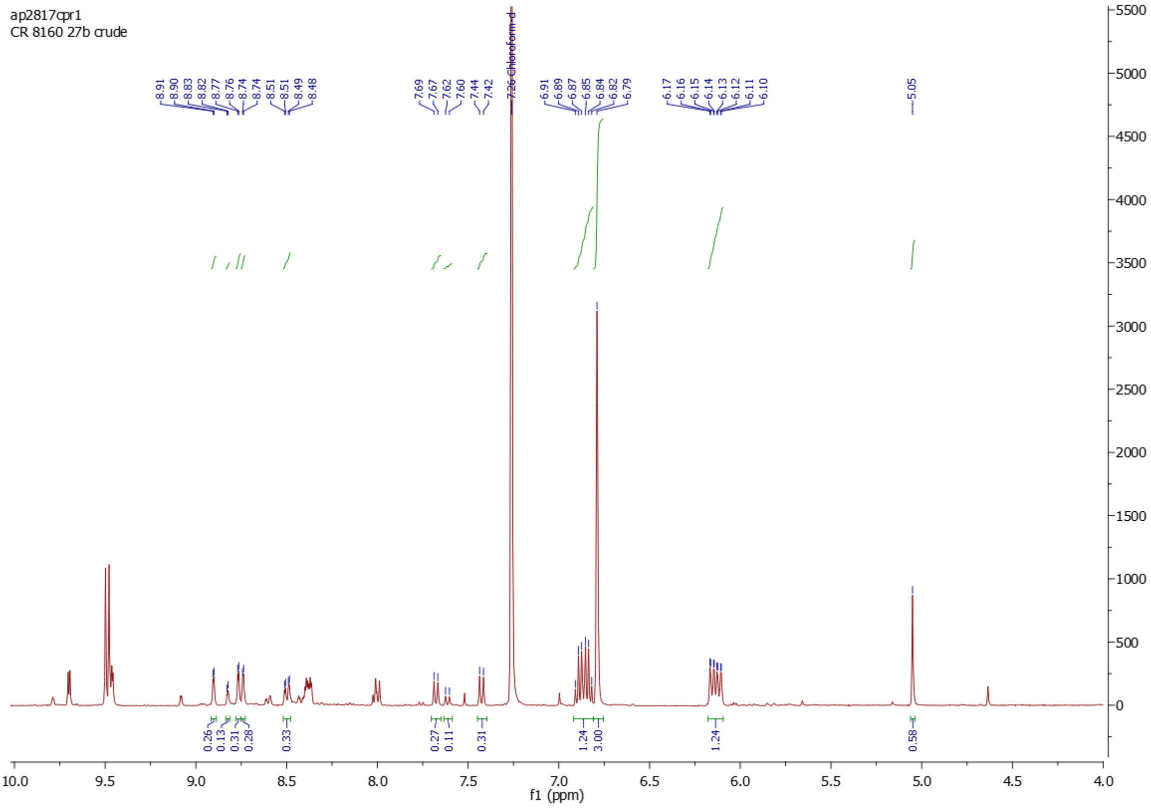

Benzyl chloride (100 mg, 0.4617 mmol) – the peak at 5.05 ppm, with an integral of 0.58, corresponds to two hydrogens

24a – the peak at 7.68 ppm, with an integral of 0.27, corresponds to one hydrogen

24b – the peak at 7.43 ppm, with an integral of 0.31, corresponds to one hydrogen

24c – the peak at 7.61 ppm, with an integral of 0.11, corresponds to one hydrogen

Mesitylene (39 mg, 0.3245 mmol) – the peak at 6.79 ppm, with an integral of 3, corresponds to three hydrogens

Conversion: 0.29 x 0.3245 = 0.3148 mmol, (0.4617 - 0.3148)*100/0.4617 = 80 %

Yield: 0.27 + 0.31 + 0.11 = 0.68, 0.68 x 0.3245 = 0.2207, 0.2207 x 100/0.4617 = 48 %

d.r.: 0.27/0.11 = 2.5, 0.31/0.11 = 2.8 thus a ratio of 2.5 : 2.8 : 1

C.3 BET Isotherms

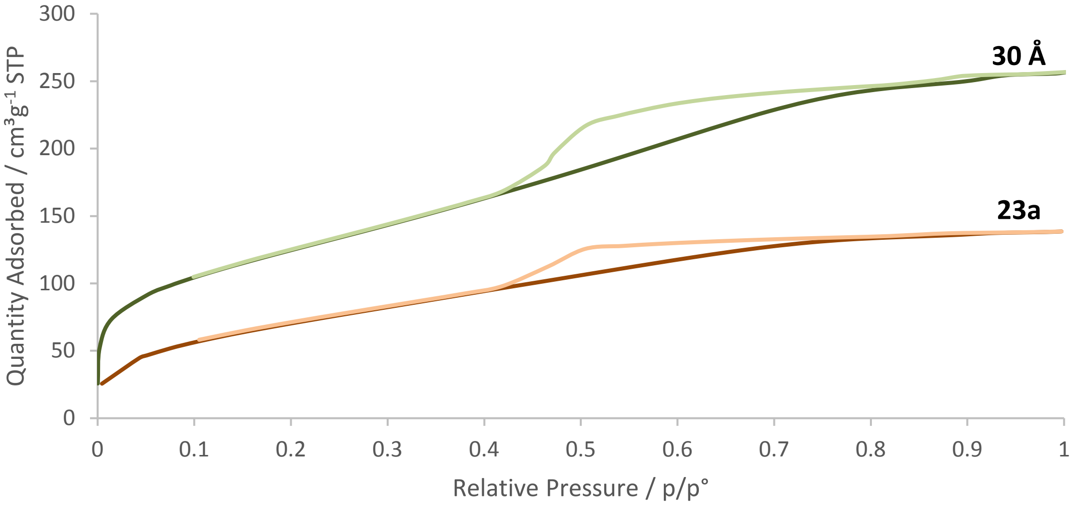

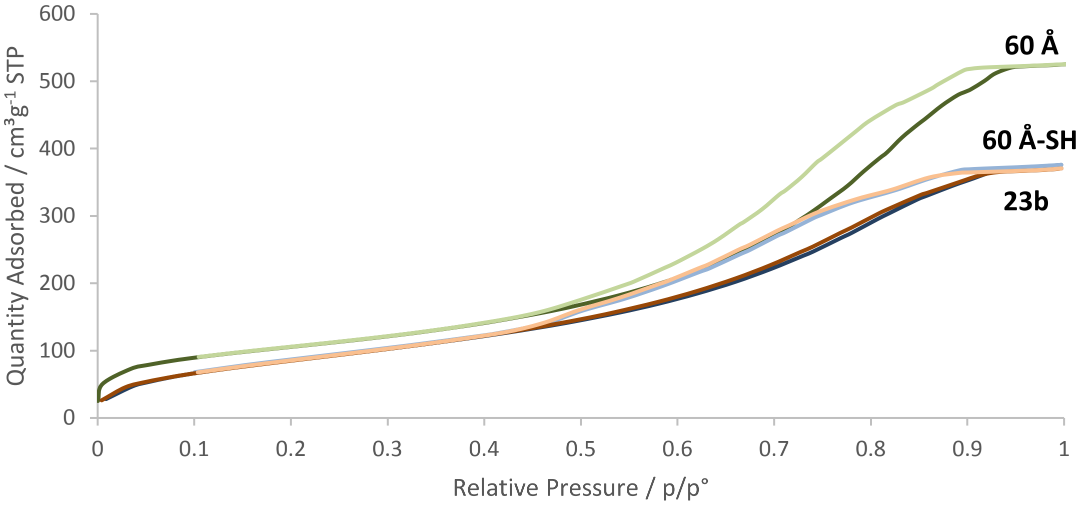

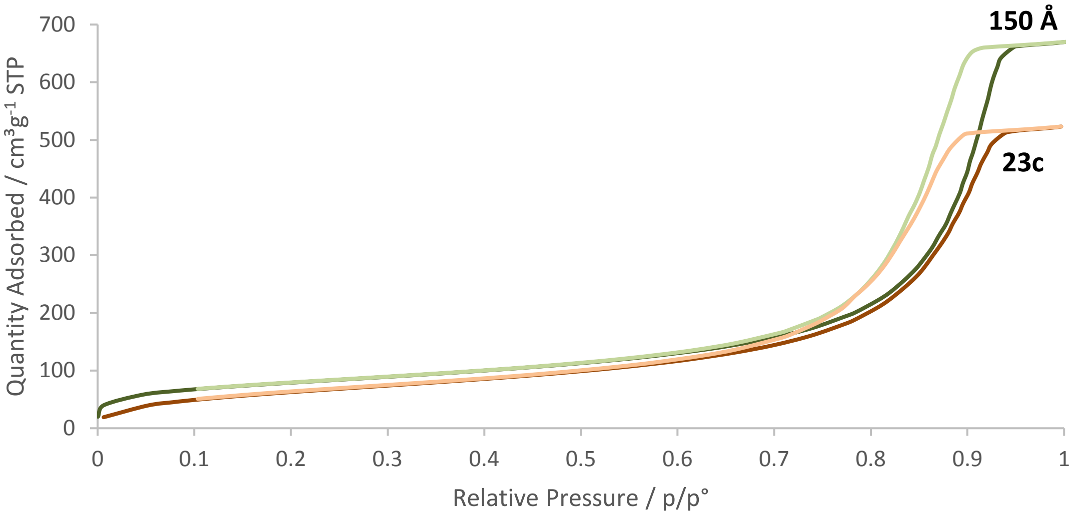

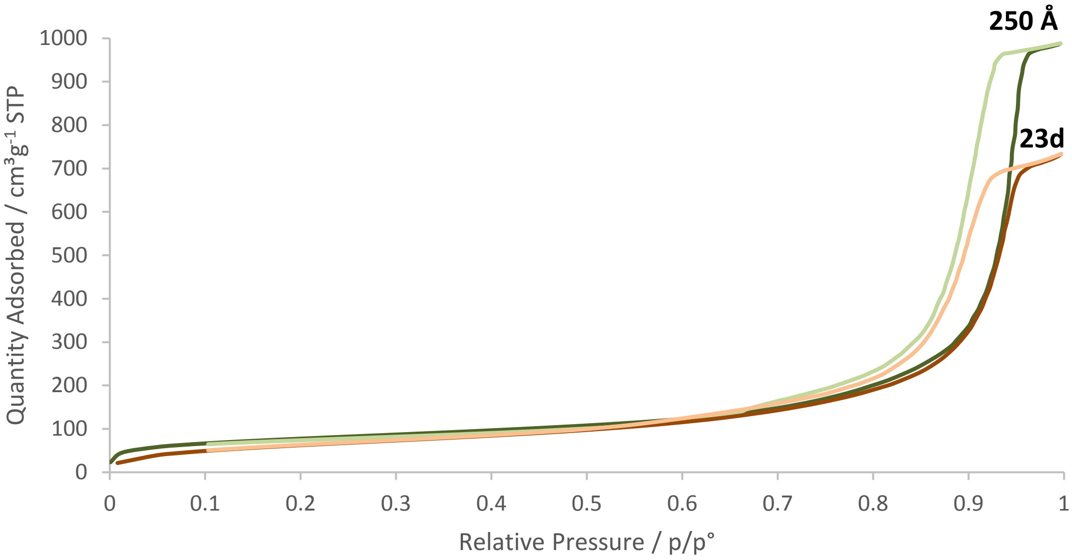
250 Å
23d
Quantity Adsorbed / cm^{3}g^{-1} STP
0
100
200
300
400
500
600
700
800
900
1000
Relative Pressure / p/p°
0
0.1
0.2
0.3
0.4
0.5
0.6
0.7
0.8
0.9
1

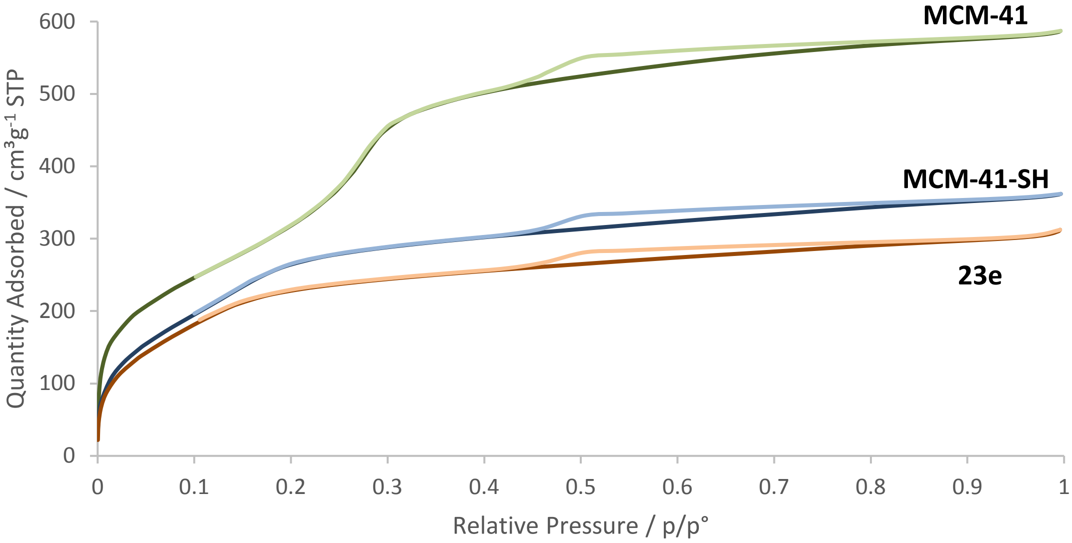
MCM-41
MCM-41-SH
23e
Quantity Adsorbed / cm^{3}g^{-1} STP
0
100
200
300
400
500
600
Relative Pressure / p/p°
0
0.1
0.2
0.3
0.4
0.5
0.6
0.7
0.8
0.9
1

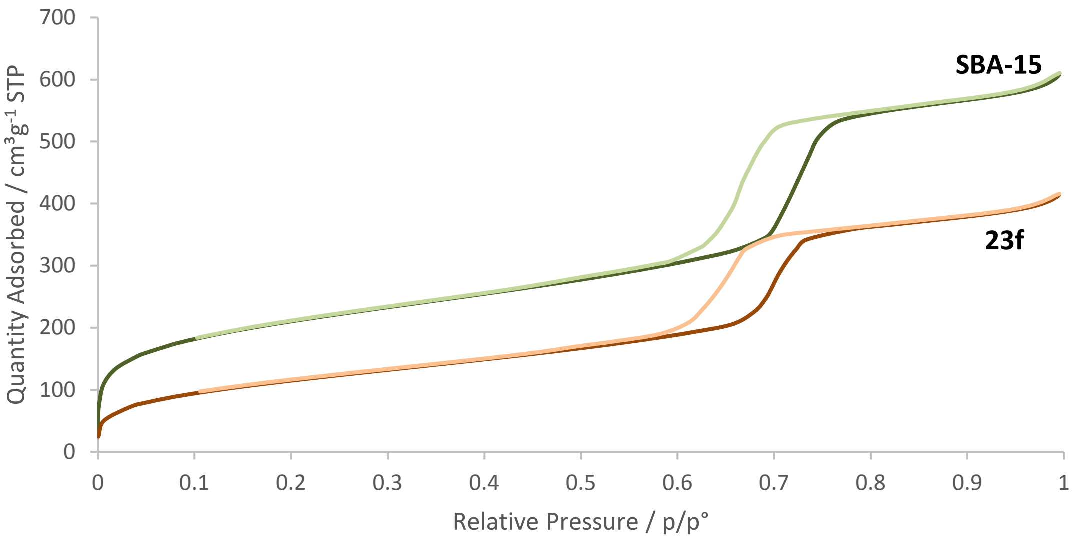
SBA-15
23f
Quantity Adsorbed / cm^{3}g^{-1} STP
0
100
200
300
400
500
600
700
Relative Pressure / p/p°
0
0.1
0.2
0.3
0.4
0.5
0.6
0.7
0.8
0.9
1

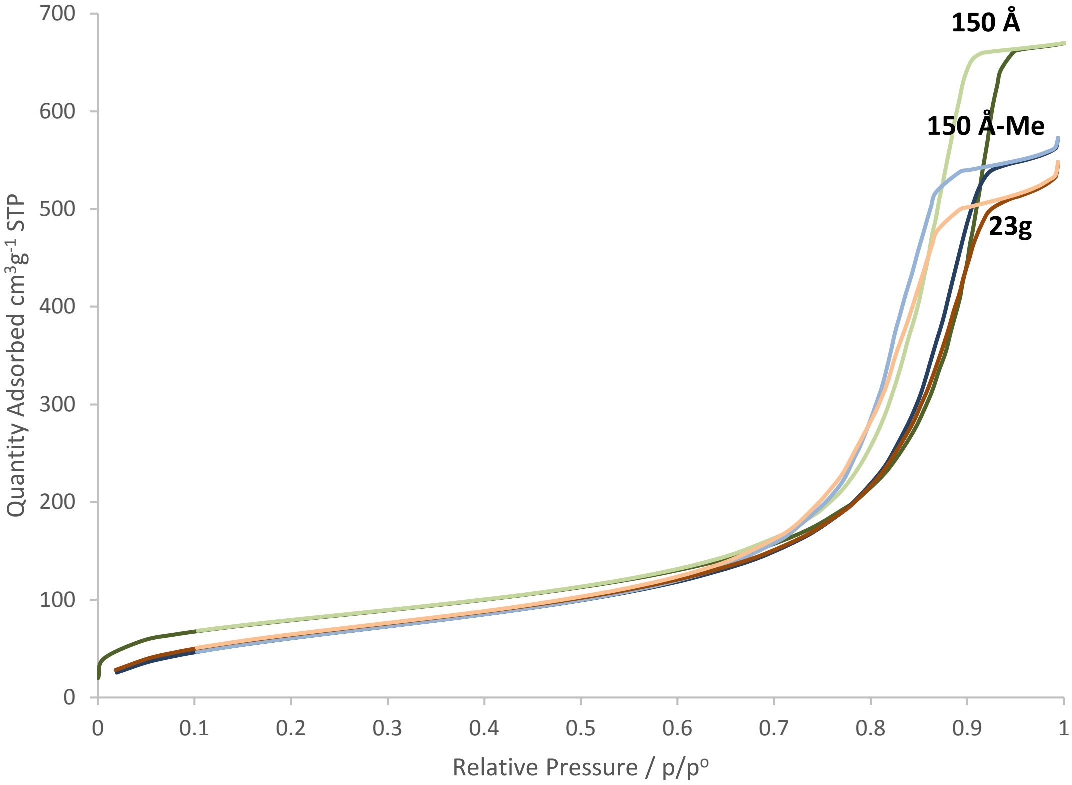
150 Å
150 Å-Me
23g
Quantity Adsorbed cm^3g^{-1} STP
Relative Pressure / p/pº
0
100
200
300
400
500
600
700
0
0.1
0.2
0.3
0.4
0.5
0.6
0.7
0.8
0.9
1

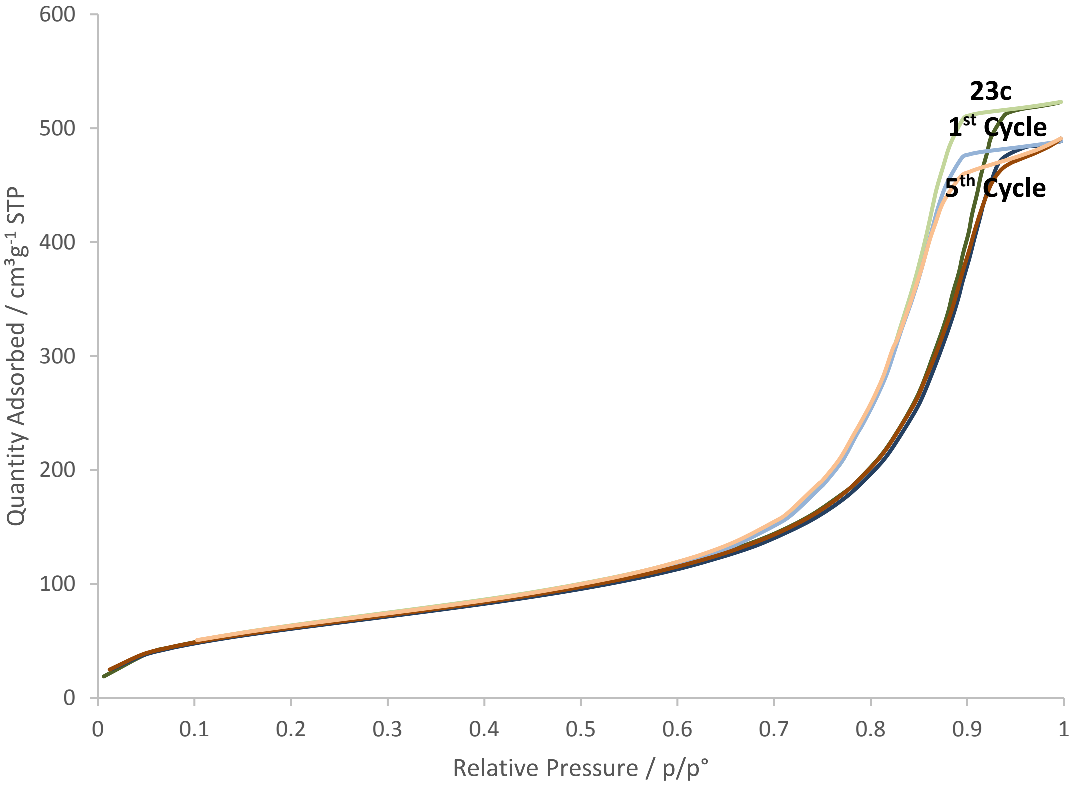
23c
1st Cycle
5th Cycle
Quantity Adsorbed / cm^3g^{-1} STP
Relative Pressure / p/p°
0
100
200
300
400
500
600
0
0.1
0.2
0.3
0.4
0.5
0.6
0.7
0.8
0.9
1

Bibliography

1 Z. Li, D. S. Bohle and C.-J. Li, *Proc. Natl. Acad. Sci. U. S. A.*, 2006, **103**, 8928–8933.

2 A. G. Condie, J. C. González-Gómez and C. R. J. Stephenson, *J. Am. Chem. Soc.*, 2010, **132**, 1464–1465.

3 M. Rueping, J. Zoller, D. C. Fabry, K. Poscharny, R. M. Koenigs, T. E. Weirich and J. Mayer, *Chem. - A Eur. J.*, 2012, **18**, 3478–3481.

4 C. Wang, Z. Xie, K. E. DeKrafft and W. Lin, *J. Am. Chem. Soc.*, 2011, **133**, 13445–13454.

5 W.-Q. Zhang, Q.-Y. Li, Q. Zhang, Y. Lu, H. Lu, W. Wang, X. Zhao and X.-J. Wang, *Inorg. Chem.*, 2016, **55**, 1005–1007.

6 S.-L. Zhu, S. Ou, M. Zhao, H. Shen and C.-D. Wu, *Dalt. Trans.*, 2015, **44**, 2038–2041.

7 X.-L. Yang, C. Zou, Y. He, M. Zhao, B. Chen, S. Xiang, M. O'Keeffe and C.-D. Wu, *Chem. - A Eur. J.*, 2014, **20**, 1447–1452.

8 J. Joseph, J. Y. Kim and S. Chang, *Chem. - A Eur. J.*, 2011, **17**, 8294–8298.

9 X. Wang, D. Xu, C. Miao, Q. Zhang and W. Sun, *Org. Biomol. Chem.*, 2014, **12**, 3108–3113.

10 Y. S. Wagh, N. J. Tiwari and B. M. Bhanage, *Tetrahedron Lett.*, 2013, **54**, 1290–1293.

11 S. Wertz, S. Kodama and A. Studer, *Angew. Chemie Int. Ed.*, 2011, **50**, 11511–11515.

12 F. Li, Z. Li, X. Tang, X. Cao, C. Wang and J. Li, *ChemCatChem*, 2019, **11**, 1192–1195.

13 T. Keshari, V. P. Srivastava and L. D. S. Yadav, *RSC Adv.*, 2014, **4**, 5815–5818.

14 V. P. Srivastava and L. D. S. Yadav, *Synlett*, 2013, **24**, 2758–2762.

15 D. Xu, W. Wang, C. Miao, Q. Zhang, C. Xia and W. Sun, *Green Chem.*, 2013, **15**, 2975–2980.

16 Y. Li, Y. Xie, R. Zhang, K. Jin, X. Wang and C. Duan, *J. Org. Chem.*, 2011, **76**, 5444–5449.

17 Y. Li, J. Liu, Y. Xie, R. Zhang, K. Jin, X. Wang and C. Duan, *Org. Biomol. Chem.*, 2012, **10**, 3715–3720.

18 K. Cao, J. Wang, L. Wang, Y. Li and X. Yu, *Synth. Commun.*, 2014, **44**, 2848–2853.

19 J. Wang, J. Hou, J. Wen, J. Zhang and X. Yu, *Chem. Commun.*, 2011, **47**, 3652–3654.

20 J. Y. Kim, S. H. Cho, J. Joseph and S. Chang, *Angew. Chemie Int. Ed.*, 2010, **49**, 9899–9903.

21 P. K. Dutta, S. Sen, D. Saha and B. Dhar, *European J. Org. Chem.*, 2018, 657–665.

22 S. C. Chen, N. Li, F. Tian, N. N. Chai, M. Y. He and Q. Chen, *Mol. Catal.*, 2018, **450**, 104–111.

23 P. Pal, A. K. Giri, H. Singh, S. C. Ghosh and A. B. Panda, *Chem. - An Asian J.*, 2014, **9**, 2392–2396.

24 W. Gao, W. Li, C. Zeng, H. Tian, L. Hu and R. D. Little, *J. Org. Chem.*, 2014, **79**, 9613–9618.

25 H. Naeimi and S. Rahmatinejad, *Synth. React. Inorganic, Met. Nano-Metal Chem.*, 2016, **46**, 471–476.

26 Y.-X. Chen, L.-F. Qian, W. Zhang and B. Han, *Angew. Chemie Int. Ed.*, 2008, **47**, 9330–9333.

27 J. Chang, K. Zhao and S. Pan, *Tetrahedron Lett.*, 2002, **43**, 951–954.

28 H. Naeimi and S. Rahmatinejad, *Polycycl. Aromat. Compd.*, 2016, **36**, 773–788.

29 Y. Kawashita, N. Nakamichi, H. Kawabata and M. Hayashi, *Org. Lett.*, 2003, **5**, 3713–3715.

30 L. H. T. Nguyen, T. T. Nguyen, H. L. Nguyen, T. L. H. Doan and P. H. Tran, *Catal. Sci. Technol.*, 2017, **7**, 4346–4350.

31 T. T. Nguyen, X.-T. T. Nguyen, T.-L. H. Nguyen and P. H. Tran, *ACS Omega*, 2019, **4**, 368–373.

32 Z. Benzekri, H. Serrar, S. Sibous, S. Boukhris, A. Ouasri, A. Rhandour and A. Souizi, *Green Chem. Lett. Rev.*, 2016, **9**, 223–228.

33 L. Z. Fekri, M. Nikpassand, S. Shariati, B. Aghazadeh, R. Zarkeshvari and N. Norouz, *J. Organomet. Chem.*, 2018, **871**, 60–73.

34 A. Ziarati, A. Sobhani-Nasab, M. Rahimi-Nasrabadi, M. R. Ganjali and A. Badiei, *J. Rare Earths*, 2017, **35**, 374–381.

35 S. Banerjee, S. Payra, A. Saha and G. Sereda, *Tetrahedron Lett.*, 2014, **55**, 5515–5520.

36 Z. Benzekri, S. Sibous, H. Serrar, A. Ouasri, S. Boukhris, A. Rhandour and A. Souizi, *J. Iran. Chem. Soc.*, 2018, **15**, 2781–2787.

37 F. M. Moghaddam, V. Saberi, S. Kalhor and N. Veisi, *Appl. Organomet. Chem.*, 2018, **32**, 4240.

38 J. He, F. Lin, X. Yang, D. Wang, X. Tan and S. Zhang, *Org. Process Res. Dev.*, 2016, **20**, 1093–1096.

39 M. R. Patil, J. T. Bhanushali, B. M. Nagaraja and R. S. Keri, *Comptes Rendus Chim.*, 2018, **21**, 399–407.

40 M. Kidwai, V. Bansal, A. Saxena, A. Swati and S. Mozumdar, *Tetrahedron Lett.*, 2006, **47**, 8049–8053.

41 E. Alza, S. Sayalero, P. Kasaplar, D. Almaşi and M. A. Pericàs, *Chem. - A Eur. J.*, 2011, **17**, 11585–11595.

42 S. Yang and J. He, *Chem. Commun.*, 2012, **48**, 10349.

43 S. Wang, J. He and Z. An, *Chem. Commun.*, 2017, **53**, 8882–8885.

44 C. A. Wang, Z. K. Zhang, T. Yue, Y. L. Sun, L. Wang, W. D. Wang, Y. Zhang, C. Liu and W. Wang, *Chem. - A Eur. J.*, 2012, **18**, 6718–6723.

45 H. Yang, S. Li, X. Wang, F. Zhang, X. Zhong, Z. Dong and J. Ma, *J. Mol. Catal. A Chem.*, 2012, **363**–**364**, 404–410.